

On the Exploration of Electrochemical Reaction Cascades

By

Evan Walter Clark Spotte-Smith

A dissertation submitted in partial satisfaction of the

requirements for the degree of

Doctor of Philosophy

in

Engineering — Materials Science and Engineering

in the

Graduate Division

of the

University of California, Berkeley

Committee in charge:

Professor Kristin Aslaug Persson, Chair

Professor Gerbrand Ceder

Professor Bryan D. McCloskey

Fall 2023

On the Exploration of Electrochemical Reaction Cascades

Copyright 2023
by
Evan Walter Clark Spotte-Smith

Abstract

On the Exploration of Electrochemical Reaction Cascades

by

Evan Walter Clark Spotte-Smith

Doctor of Philosophy in Engineering — Materials Science and Engineering

University of California, Berkeley

Professor Kristin Aslaug Persson, Chair

Anthropogenic climate change represents one of the greatest present threats to human society and global ecology. Rapid and dramatic reductions in greenhouse gas emissions are essential to avoid catastrophic global warming and environmental collapse. Although renewable energy from solar and wind resources is cheap and widely available, these resources are intermittent, and energy storage is needed to reliably supply renewable energy to the electrical grid and power vehicles. In particular, electrochemical energy storage in batteries can be highly efficient and energy-dense, showing tremendous promise to decarbonize the energy and transportation industries.

Metal-ion batteries like lithium-ion batteries (LIBs) are the current state of the art for commercial and research energy storage technologies. To achieve high energy density, metal-ion batteries typically operate at voltages outside of the electrochemical stability window of their electrolytes. As a result, electrolyte components react electrochemically, reducing and/or oxidizing to trigger a complex reaction cascade. In some batteries, such as LIBs with graphitic negative electrodes and electrolytes with certain cyclic and linear carbonate solvents, electrolyte degradation is managed by the formation of a passivation film known as an interphase. Once an interphase forms, these batteries are extremely stable over many years and thousands of charge-discharge cycles. To realize the goal of next-generation energy storage technologies with higher energy densities, including lithium-ion batteries with lithium metal or silicon electrodes as well as multivalent batteries (e.g. magnesium-ion batteries or MIBs), electrolytes must be designed either to avoid decomposition altogether or to react in a controlled manner such that they form stable interphase films.

Herein, I discuss efforts to predict the behavior of reactive electrochemical systems such as battery electrolytes using computational simulations and data science. I begin (Chapter 1) with an introduction to battery electrochemistry, focusing primarily on the role of electrolytes and interphase formation, as well as the inherent challenges of interphase engineering. In Chapter 2, I review the literature on analysis of interphase films using both

experimental and theoretical approaches. As I will show, there are few techniques available that can provide mechanistic explanations for electrochemical reactivity accounting for the complex interactions between electrodes, electrolyte species, impurities, and decomposition intermediates and products.

Chapter 3 details a traditional study of electrolyte decomposition using a first-principles quantum chemical method: density functional theory (DFT). Specifically, I use DFT to explain the chemical and thermal instability of lithium hexafluorophosphate (LiPF_6) salt in terms of elementary reaction mechanisms. This study highlights the limitations of chemical intuition in understanding reaction cascades and the need for new methods to broadly explore diverse (electro)chemical interactions.

In Chapter 4, I describe such a methodology that combines high-throughput DFT, chemical reaction networks (CRN), and stochastic simulations to predict reaction outcomes and pathways in complex systems with minimal prior knowledge. As a proof of concept (Chapter 5), I apply this approach to reductive electrolyte decomposition and interphase formation in LIBs with ethylene carbonate as a solvent. I recover most previously reported interphase products and predict several new, previously unreported, but chemically plausible species. From this starting point, I apply a kinetic Monte Carlo (kMC) algorithm to construct a model of LIB interphase formation and evolution (Chapter 6). This model successfully captures the expected bilayer structure of the interphase without relying on adjustable parameters or fitting to experiment.

Finally, in Chapter 7, I apply the previously described CRN methods to a new system where significantly less information is known: electrolyte decomposition and gas evolution in MIBs. I show how CRNs can help to interpret experimental spectra (in this case differential electrochemical mass spectroscopy or DEMS) and explain not only why certain species form in abundance but also why other species cannot form due to kinetic limitations.

I conclude (Chapter 8) by highlighting opportunities to apply computational modeling — in particular using CRNs — to understand complex (electro)chemical systems. The developments laid out here represent a significant step forward towards the rational design of reactive processes not only in the world of batteries and energy storage but also in electrochemical synthesis, pollution management, and much more. I also point out remaining challenges to studies of reactivity — both experimental and computational — and suggest possible avenues for future research to alleviate them.

My journey to study batteries began in Otubet, Uganda, a community that was completely without access to electricity. I dedicate this dissertation to the people there, and to all people with a desperate need for power – electrical, social, and political.

And to the brighter minds who will prove me wrong and find better paths than I could dream up. I left you plenty of fuel. Find something fun to burn.

Contents

Contents	ii
List of Figures	v
List of Tables	xiii
1 Introduction	1
1.1 Battery Basics	1
1.2 Electrolyte Degradation and Interphases	2
1.3 The Challenge of the SEI	4
2 Literature Review: Methods to Interrogate Electrolyte Decomposition and Interphase Formation	6
2.1 Experimental Methods	7
2.2 Computational Methods	9
2.3 What Do We Need?	16
3 First-Principles Explanation of Lithium Hexafluorophosphate Decomposition in Li-Ion Batteries	18
3.1 The Importance and Challenges of LiPF ₆	18
3.2 Questioning the hydrolysis hypothesis	20
3.3 Reactions with Li ₂ CO ₃	21
3.4 An atomistic mechanism for POF ₃ autocatalysis	23
3.5 Conclusions	25
4 Methods to Construct and Analyze Electrochemical CRNs Based on High-Throughput DFT	28
4.1 Generating Datasets of Challenging Reactive Molecules Using High-Throughput DFT	29
4.2 Generating and Analyzing (Electro)chemical Reaction Networks	38
5 Predicting Electrolyte Decomposition Products and Their Formation Mechanisms Using CRNs	46

5.1	Developing LIBE	46
5.2	Description of the LIBE dataset	49
5.3	Automatic Identification of Battery SEI Network Products	54
5.4	CRN-Derived Elementary Mechanisms to Form Unexpected Network Products	56
5.5	CRN Pathways and Products Guide Investigation of Expanded Mechanisms	60
6	A Mechanistic Model of SEI Formation and Evolution in Li-Ion Batteries	61
6.1	Computational Methods	62
6.2	Recovering the Peled Model	64
6.3	Effect of Varying Electrolyte Impurities	67
6.4	Exploring SEI Decomposition and Growth	68
6.5	A Mechanistic Model of SEI Reactivity	70
7	Combining CRN Analysis and Experimental Spectroscopy to Explain Gas Evolution in Mg-Ion Batteries	72
7.1	OEMS	73
7.2	Identifying Observed Gases	75
7.3	The role of TFSI ⁻	78
7.4	Summary	79
8	Conclusions	84
8.1	Even More Complicated Than We Imagined	84
8.2	A New Approach to Studying Electrochemical Reactivity	86
8.3	CRNs Beyond Metal-Ion Batteries	87
8.4	Final Reflections	90
A	Data Availability	93
A.1	Data associated with Chapter 3	93
A.2	Data associated with Chapter 5	94
A.3	Data associated with Chapter 7	94
B	Additional Methods	95
B.1	Methods associated with Chapter 3	95
B.2	Methods associated with Chapter 5	96
B.3	Methods associated with Chapter 6	114
B.4	Methods associated with Chapter 7	117
C	Software Availability	125
C.1	LIBE Usage Notes	125
C.2	Generating LIBE	126
C.3	CRN generation and reaction pathways	126
D	Principal Molecules Used to Generate LIBE	128

E Average Monte Carlo Trajectories	136
E.1 Trajectories associated with Chapter 5	136
E.2 Average trajectory associated with Chapter 6	136
E.3 Trajectories associated with Chapter 7	136
F Understanding Differences in SEI Formation	147
G Species and Reactions for kMC in Chapter 6	150
G.1 Molecules Included in kMC Simulations	150
G.2 Reactions Included in kMC Simulations	155
H Supplemental Information for Chapter 7	182
H.1 Demonstration of Reversible Mg Plating and Stripping	182
H.2 Snapshot OEMS Spectra	184
H.3 Solvation Correction	186
H.4 Reduction Potentials	187
H.5 Network Products	188
H.6 Scanning Electron Microscopy	191
Bibliography	192

List of Figures

2.1	a) Cartoon depiction of a chemical reaction network (CRN) as a directed graph, where edges lead from reactant nodes to products; b) depiction of important (blue, green, purple) and unimportant network species; c) identifying reaction pathways to species of interest by tracing connections in the CRN.	15
3.1	Hydrolysis of PF ₅ to form POF ₃ and 2 HF. This mechanism is overall thermodynamically unfavorable and involves two reactions with high barriers ($\Delta G^\ddagger > 1.00$ eV).	20
3.2	Energy diagrams for the formation of POF ₃ from PF ₅ and Li ₂ CO ₃ . a) LiPOF ₄ forms via by simultaneous elimination of LiF and CO ₂ from a PF ₅ -Li ₂ CO ₃ adduct; LiPOF ₄ can then eliminate LiF to form POF ₃ . b) Alternate, less favorable mechanisms in which LiF is eliminated from the adduct without simultaneously eliminating CO ₂	22
3.3	Reactions between POF ₃ and simple inorganic carbonates a) H ₂ CO ₃ , b) LiHCO ₃ , and c) Li ₂ CO ₃) to form CO ₂ and either PF ₂ OOH or LiPF ₂ O ₂ . A trend between the partial charge of the reacting oxygen(s) and the reaction energies with POF ₃ for each carbonate considered is shown in d). A linear fit, $\Delta G = 4.39q + 4.47$, where q = the most negative oxygen partial charge, shows strong correlation ($R^2 = 0.96$) among the three carbonates.	24
3.4	Possible routes for the reformation of POF ₃ from PF ₂ OOH (a) and LiPF ₂ O ₂ (b). Both mechanisms are kinetically limited due to an extremely unfavorable intramolecular fluorine transfer step (M ₂₆ → M ₂₇ , M ₃₀ → M ₃₁), which makes POF ₃ autocatalysis unlikely at modest temperatures. Rate coefficients for the fluorine transfer step are provided in c) for the PF ₂ OOH pathway and in d) for the LiPF ₂ O ₂ pathway.	26
4.1	Examples of molecules with various Li ⁺ coordination environments: monodentate (a), bidentate (b), tridentate (c), and tetradentate (d). White atoms are hydrogen, gray atoms are carbon, red atoms are oxygen, blue are fluorine, and pink are lithium.	30

4.2 A flowchart for correcting an SCF convergence error. When the error is encountered, only a single remedy will be applied. If there is no possible remedy, or if too many errors have already been encountered, then the error handler will quit, and the calculation will be allowed to fail.	32
4.3 The frequency-flattening optimization (FFOpt) procedure. In the initial step, the geometry is optimized and a vibrational frequency calculation is performed. If there are no imaginary frequencies, or if there is a single imaginary frequency with very small magnitude, the calculation completes successfully. Otherwise, the Hessian from the vibrational frequency calculation will be used to inform the next cycle of optimization.	34
4.4 A schematic overview of a molecular fragmentation process. For a single-step fragmentation (a), a principal molecule is selected. Each bond is broken, generating a collection of molecular fragments. These fragments are then filtered to generate a set of unique (non-isomorphic) molecules. In an n-step fragmentation (b), this process is repeated in a recursive fashion. At each step, all fragments from the previous step are collected and undergo a single-step fragmentation. If the fragment is a single atom with no bonds or if all fragments generated are already present in the collection, then the process terminates (red "X"). When the maximum number of steps has been reached, or when no new fragments can be generated, the n-step fragmentation terminates.	36
4.5 A simplified depiction of the recombination process. First (1), two fragments - in this case, from lithium ethylene carbonate, or principal molecule 1 in Appendix D - are selected. The heavy atoms in these molecules that can form additional bonds (shown in purple) are identified using valence rules (2), and finally, bonds (also in purple) are added between all combinations of these connectable heavy atoms (3) to form a set of unique recombinant molecules (gray box).	37

5.2	The 36 total collected network products from four different initial conditions (+0.0V vs. Li/Li ⁺ with Li ⁺ and EC as starting species; +0.0V vs. Li/Li ⁺ with Li ⁺ , EC, and CO ₂ as starting species; +0.5V vs. Li/Li ⁺ with Li ⁺ and EC as starting species; and +0.5V vs. Li/Li ⁺ with Li ⁺ , EC, and CO ₂ as starting species). The 16 network products outlined in green have previously been experimentally identified in the SEI; these include the major gaseous products, molecular inorganic components, and organic components (including lithium methyl carbonate or LMC, vinyl carbonate, lithium ethyl carbonate or LEC, ethylene monocarbonate, lithium ethylene dicarbonate or LiEDC ⁻ , and lithium butylene dicarbonate or LiBDC ⁻). Six of the network products, outlined in dotted light green, are species which have very similar spectroscopic signatures to the dominant organic components, and thus may be present in the SEI in small quantities without being detected. Two of the network products outlined in dashed purple, lithium 2-(formyloxy)ethan-1-olate or LFEO and 4,4',5,5'-tetrahydro-2,2'-bi(1,3-dioxolylidene) or bi-dioxolylidene, have not been previously reported and were subjected to further mechanistic analysis. Finally, the remaining 12 network products (which have also not been previously reported as SEI products) may be kinetically inaccessible, may indicate that our CRN is missing species or reactions, or may be true SEI products, motivating future study.	55
5.3	Comparison of network-identified reaction pathways and elementary mechanisms obtained from kinetic refinement to form (a) lithium 2-(formyloxy)ethan-1-olate (LFEO) and (b) 4,4',5,5'-tetrahydro-2,2'-bi(1,3-dioxolylidene) (bi-dioxolylidene). For elementary steps involving a transition-state, energy barriers (ΔG^\ddagger) and reaction free energies (ΔG) are provided. Corresponding reaction steps between the network-identified pathways and elementary mechanisms are indicated via line color and style. Coordination and reduction steps are combined for brevity; in reality, these occur as separate steps in both network-identified pathways and elementary mechanisms.	57
5.4	Extended mechanisms based off of network-identified pathways: a) formation of LVC, a known SEI product, via the ring-opening of the deprotonated Li ⁺ EC-H ⁻¹ , a byproduct of LFEO formation; b) two possible catalytic cycles yielding ethylene gas and reforming dioxolylidene via the production of either CO ₂ or Li ⁺ CO ₂ ⁻¹ . For elementary steps involving a transition-state, energy barriers (ΔG^\ddagger) and reaction free energies (ΔG) are provided. Green boxes indicate species that have been experimentally identified as products or byproducts of SEI formation. . . .	59
6.1	Select reaction pathways involving key SEI products, including inorganic carbonates (a, b, d, e), LEDC (a, b, e), DLEMC (a, c), lithium oxalate (d), and LEMC (c). Gases CO ₂ (a, d, e), C ₂ H ₄ (a), CO (a, d), and H ₂ (c) are also highlighted. A complete set of reactions included in the microkinetic simulation are listed in Appendix G	63

7.1 OEMS measurements on a Mg(TFSI) ₂ /G2 electrolyte during a potentiostatic hold at a cell potential of -1.0 V. a) The applied current density during potentiostatic hold; b) integrated relative OEMS intensity (in log scale) after approximately four hours of measurement, with major peaks indicated; c) time-resolved flow for several major peaks ($M/Z = 18, 28, 32, 36$) demonstrating continuous evolution; d) time-resolved flow for $M/Z = 45$ with initially high partial pressure that rapidly decays.	74
7.2 Gases predicted to evolve from Mg(TFSI) ₂ /G2 electrolytes, based on CRN analysis and prediction of solubility S_{G2} . The mass of each CRN product (rounded, in amu) is shown next to the 2D structure in gray.	76
7.3 Elementary reaction mechanisms for the formation of a) C ₂ H ₄ , b) CH ₃ OH, and c) H ₂ O. Reaction energies and energy barriers marked with an asterisk (*) were taken from Seguin et al.[368]	81
7.4 Elementary reaction mechanisms for the formation of a) CH ₄ , b) C ₂ H ₆ , and c) CH ₃ OCH ₃ . Reaction energies and energy barriers marked with an asterisk (*) were taken from Seguin et al.[368]	82
7.5 a) Progressive cyclic voltammetry cycling behavior (10 cycles) on a fresh Pt electrode in electrochemically conditioned 0.3M Mg(TFSI) ₂ /G2 at a scan rate of 10 mV/s. b) XPS-derived composition of the Pt electrode surface as a function of cycle number. A cycle number of 0 indicates that the measurement was taken before any potential had been applied.	83
8.1 Stages of LMEAS: i) electrochemical lithium plating; ii) chemical reaction of lithium and N ₂ to form Li ₃ N; iii) protonation of Li ₃ N to form NH ₃ . In this example, the electrode is copper (Cu) the solvent is tetrahydrofuran (THF), the salt is lithium bistriflimide (LiTFSI), and the proton donor is ethanol.	88
B.1 Conformations of LEDC. The linear conformer (libe-115795, a) is less stable than the puckered conformer (libe-652486, b) by 0.68 eV, although the linear conformer is more commonly observed in all-atom molecular dynamics simulations. When the Li ⁺ are removed from the puckered conformer and the structure is re-optimized (charge -2), a roughly linear conformer is again obtained (c), indicating that the puckered conformer is only preferred because of the insufficient stabilization of Li ⁺ in implicit solvent.	98
B.2 Relative stabilization of Li ⁺ by increasing numbers of EC.	99
B.3 Solvation corrections applied to reactions with bonds changing. a) When the number of coordinate bonds in the reactants and the products are the same, then the correction to the reaction free energy is 0 eV. b) However, when there is a change in the number of coordinate bonds (here, there are two coordinate bonds in the reactants and only one in the products), then the reaction free energy changes based on the change in coordinate bonds.	100

B.4	Star examples. a) The stars of methanol. b) The stars of two product molecules following the breakage of the CO bond in methanol.	104
B.5	The star count difference of the reaction breaking the CO bond in methanol.	105
B.6	Generating fragments from the breakage of one bond for a molecule and then comparing reactant and product fragments for a reaction.	108
B.7	Unphysical single step formation of LEDC that motivated the non-hydrogen transfer filter.	110
B.8	Unphysical single step decomposition of LEDC that motivated the ring closing filter.	110
B.9	Schematic drawing of the OEMS system used in this study.	122
C.1	An overview of our automated high-throughput molecular DFT framework, as implemented in <code>pymatgen</code> (blue), <code>custodian</code> (green), and <code>atomate</code> (yellow) (a); an example calculation (Firework) for geometry optimization (b), indicating the different steps and the ways in which <code>pymatgen</code> , <code>custodian</code> , and <code>atomate</code> interact. First, the input file is written using default parameters defined in <code>pymatgen</code> . Then, the geometry optimization calculation is performed using the Q-Chem interface in <code>custodian</code> and an automated error handler. Finally, once the calculation is finished, the input and output files are parsed using <code>pymatgen</code> , and the results from the calculation are added to a database.	127
E.1	Average trajectory from 100,000 stochastic trajectories of our network with electron free energy -1.4 and initial condition 30 Li^+ ions and 30 EC. Only network products are shown.	137
E.2	Average trajectory from 100,000 stochastic trajectories of our network with electron free energy -1.4 and initial condition 30 Li^+ ions, 30 EC and 30 CO_2 . Only network products are shown.	138
E.3	Average trajectory from 100,000 stochastic trajectories of our network with electron free energy -1.9 and initial condition 30 Li^+ ions and 30 EC. Only network products are shown.	139
E.4	Average trajectory from 100,000 stochastic trajectories of our network with electron free energy -1.9 and initial condition 30 Li^+ ions, 30 EC and 30 CO_2 . Only network products are shown.	140
E.5	Average trajectory for simulations conducted at an applied potential of $+0.0$ V vs. Li/Li^+ with a tunneling barrier $D = 10.0 \text{ \AA}$, simulating a regime far from the negative electrode. It can be seen that starting species such as CO_2 are consumed over time, leading to the formation of SEI products, such LEDC, as well as gases, such as C_2H_4 and CO	141
E.6	Average of 50,000 Monte Carlo trajectories beginning with Mg^{2+} , G2, and TFSI^- subjected to a potential of 0V vs. Mg/Mg^{2+} . Predicted gaseous products are highlighted.	142

E.7	Average of 50,000 Monte Carlo trajectories beginning with Mg^{2+} , G2, $TFSI^-$, and CO_2 subjected to a potential of 0V vs. Mg/Mg^{2+} . Predicted gaseous products are highlighted.	143
E.8	Average of 50,000 Monte Carlo trajectories beginning with Mg^{2+} , G2, $TFSI^-$, and OH^- subjected to a potential of 0V vs. Mg/Mg^{2+} . Predicted gaseous products are highlighted.	144
E.9	Average of 50,000 Monte Carlo trajectories beginning with Mg^{2+} , G2, $TFSI^-$, OH^- , and H^\bullet subjected to a potential of 0V vs. Mg/Mg^{2+} . Predicted gaseous products are highlighted.	145
E.10	Average of 50,000 Monte Carlo trajectories beginning with Mg^{2+} , G2, $TFSI^-$, CO_2 , OH^- , and H^\bullet subjected to a potential of 0V vs. Mg/Mg^{2+} . Predicted gaseous products are highlighted.	146
H.1	Cyclic voltammogram showing two plating-stripping cycles for a DEMS cell containing a 0.5M $Mg(TFSI)_2/G2$ electrolyte, an Au working electrode, and Mg foil reference electrode. The scan rate was 100 mV s^{-1}	183
H.2	Snapshot OEMS spectrum taken at the beginning of a potentiostatic experiment.	184
H.3	Snapshot OEMS spectrum taken one hour into a potentiostatic experiment.	184
H.4	Snapshot OEMS spectrum taken two hours into a potentiostatic experiment.	185
H.5	Snapshot OEMS spectrum taken three hours into a potentiostatic experiment.	185
H.6	Snapshot OEMS spectrum taken four hours into a potentiostatic experiment.	186
H.7	Relative stabilization of Mg ions (Mg^{2+} , a-b; Mg^{1+} , c-d) by dimethoxyethane (DME) (a, c) and G2 (b, d) in terms of electronic energy (in eV). Equations for lines of best fit (solid black lines) are provided.	187
H.8	Oligomer and other chain hydrocarbon network products.	189
H.9	Salt network products.	190
H.10	Other network products.	190
H.11	SEM images of remnant Mg and electrolyte ($TFSI^-$ and G2) decomposition products after 1 (a) and 10 (b) deposition and stripping cycles.	191

List of Tables

1.1	Intercalation, plating, or conversion potentials for common negative electrodes in metal-ion batteries.	3
5.1	Solvent parameters for use in the SMD implicit solvent model. The dielectric constant ϵ represents a 3:7 weight blend of EC and EMC; all other parameters are for pure EC.	47
5.2	Description of keys present in LIBE dataset entries.	50
5.3	Number of different types of bonds present in the LIBE dataset.	53
B.1	: Comparison of computed and experimental reduction potentials for lithium-ion battery electrolyte solvents coordinated with Li^+	100
B.2	: Comparison of computed and experimental oxidation potentials for lithium-ion battery electrolyte solvents.	101
D.1	Principal molecules used for fragmentation, including depth of fragmentation. A fragmentation depth of “MAX” indicates that all possible combinations of bonds were broken during fragmentation.	135
F.1	SEI species commonly identified in the experimental literature from EC-based electrolytes at graphite, lithium metal, and silicon negative electrodes.	149
G.1	Molecules included in kMC simulations. For molecules included in the LIBE dataset, molecule IDs are provided.	155
G.2	Reduction and oxidation reactions included in kMC simulations. The Gibbs free energy ΔG reported here does not account for the electron free energy, which will vary with potential; energy barriers and rate constants, which also depend on potential, are not reported. However, the inner reorganization energy, λ_{in} is independent of potential, and so is general to all simulations. Where relevant, all values are calculated at $T = 298.15\text{K}$	156

G.3 Coordination and re-coordination reactions included in kMC simulations. For coordination reactions, if the reaction is exergonic ($\Delta G < 0$), then the reaction is taken to be barrierless; otherwise, the free energy defines the effective barrier. For re-coordination reactions, there is a minimum energy barrier, which we take in most simulations to be $\Delta G_{recoord}^\ddagger = 0.266$ eV. The units of the rate constant k depend on if the reaction is unimolecular or bimolecular. Where relevant, all values are calculated at $T = 298.15K$	178
G.4 Barrierless reactions included in kMC simulations. These reactions either have no transition-state (as reported from the literature and confirmed at the ω B97X-V/def2-TZVPPD/SMD level of theory) or a transition-state was found and the calculated free energy barrier was negative in one or both directions. In general, the effective free energy barrier is calculated from the reaction free energy ΔG . However, for select reactions (such as the dissociation of water, which occurs essentially barrierlessly on a bare surface but not in solution),[212] the barrier was set to 0 by fiat. All values are calculated at $T = 298.15K$	179
G.5 Other reactions included in kMC simulations. All values are calculated at $T = 298.15K$. ^a this value is modified from the calculated value of 0.685 eV.	181
H.1 Reduction potentials of Mg-coordinated species with and without explicit solvation. All potentials are reported referenced to the reduction potential of Mg. * = The reduced molecule dissociated during geometry optimization.	188

Acknowledgments

First, my professional colleagues:

I would not have come to the University of California – Berkeley without Dr. Anubhav Jain taking a chance on an undergraduate student who had never touched computational research before. After three months working with Anubhav and with DFT, I was hooked, and my career and research plans changed completely. I may also not have chosen Berkeley – or my research group – had I not received such warmth and kindness from Dr. Matthew Horton and Dr. Samuel Blau (Sam), both of whom I continue to hold as dear friends.

Sam has been with me from my internship at Lawrence Berkeley National Laboratory to today, serving as a mentor, a thought partner, a sounding board, a strategist, a sharp editor, a co-conspirator, and a fellow loud-mouth shit-talker. I could call Sam my “factotum”, which, to the best of my knowledge of Latin, translates to something like “one who does everything”. Working with Sam hasn’t always been easy, but his constant presence was often the anchor that I needed to go on in my research. And besides, when Sam’s bothering me, I know I can always tell him straight to his face, that he’ll always listen to me. Sam, I hope I’ve been fair for you as you’ve been to me, and I look forward to strengthening the Spotte-Blau collaboration in the years to come.

There are many things that I can say about Prof. Kristin Aslaug Persson, my advisor. I’ll keep it to the two most important. First, Kristin made it possible to keep going in the dark, early days of the COVID-19 Pandemic. I was afraid, I was deeply unwell, and I felt the entire world collapsing. I still see the cracks sometimes. If I had any other advisor - any normal advisor - I probably would have quit, or worse. But Kristin tried her best to create peace and hope. I’ll always be grateful for that. Second, Kristin never said no. And I do mean literally never. Never “no” to a conference, to a paper, to a new research project, to hiring an undergraduate mentee. This hasn’t always been good for me – my office wall, containing my list of active projects, was called the “Wall of Death” for a reason – but Kristin gave me almost full control of my research direction. She let me make my own mistakes and build my own successes. It was a rare opportunity, and one that I took full advantage of.

Speaking of undergraduate researchers, I would be remiss if I did not acknowledge my mentees: Ronald L. Kam, Aniruddh Khanwale, Nikita S. Redkar, Thea Bee Petrocelli, and Laura Zichi. Several of the projects described in this dissertation would never have been started without these brilliant, passionate minds, let alone completed so successfully. More importantly, my PhD would have been less full of excitement and joy. Working with and mentoring these five – as researchers and as people – was one of the most important things that I’ve done in the last four-and-a-half years. To the “Spotte-Smith Sub-sub-group”, I thank you, and I hope we all stay in touch. I’m sorry that I never made team swag.

During my doctoral research, I worked with a huge number of scientists in Berkeley and around the United States. The list is too long – and my memory too poor – for me to try and list them all out here, but I hope to name all of the collaborators who have been most essential to my core research projects. Ronald Kam began the work on kMC modeling of interphase formation as his undergraduate honors thesis in Chemical and Biomolecular Engineering,

and Thea Petrocelli initiated our studies on LiPF₆ decomposition under my guidance during her Community College Internship (CCI). Dr. Daniel Barter's work designing the core algorithms for CRN construction and analysis were essential to much of my research. I have never been more grateful to have a mathematician in my life. Prof. Mingjian Wen showed me that machine learning can actually be useful. I'm grateful for that, and I'm grateful that he let me help out writing a perspective on CRNs. Dr. Chen Liao performed all of the DEMS experiments that I describe in Chapter 6 on Mg-ion electrolyte degradation and gas evolution.

In addition to these colleagues, whose work with me entered this dissertation, I must highlight several others whose efforts are not mentioned here but were nonetheless important parts of my PhD. Hetal Patel and Dr. Rachel Woods-Robinson were solid friends and supports throughout my time in grad school. I always knew I could come complain to them or ask them for advice. Likewise, Prof. Ryan Kingsbury was an ever-smiling face and a source of stability and wisdom when I needed it. Dr. Alexander R. Epstein helped me to appreciate polymer chemistry and the importance of hydrolysis. Dr. Sudarshan Vijay and Dr. Bernardine "Didi" Rinkel were both hugely important in helping me to understand electrolyte oxidation processes. Without Santiago Vargas, I would have large piles of data and no way to use them; for his expertise in machine learning and his eagerness to apply it to every problem I could throw at him, I'm grateful. And last but not least, Orion Archer Cohen and Dr. Jason M. Munro somehow turned me into a Web designer and supported me in making molecules first-class citizens of the Materials Project (or should I say the Molecules Project?).

And now, on a personal note:

To the friends who have never left my side, who saw me develop as person, into an adult, who watered the seed that grew into who I am today: Laura Rieck, Carmelina Elizabeth Palmer, Alexandra "Kiss" Kissilenko, and Rachael Katherine "Death" "Whittles" Whitley. No matter how often we find time to talk, my heart will be full of love for y'all.

To the teachers who saw my wit in my challenges, my determination in my stubbornness, my passion in the chaos that I brought to the classroom: Mrs. McKenna (hope I'm spelling that right), Mr. MacGregor, Dr. Collins, Ms. Krummel, Mrs. Erin Radebe, Ms. Beth (Just Beth) Dungee, thank you. I needed you.

To all of my students at The Brooklyn Latin School, who taught me how to make the classroom into a community. I especially thank Kali Hough, Esela Segbefia, Clara Park, Quinn Accardi, Mason James Bunker, Cooper Glick, and Nazahah Hasan. You'll always be my students, my family, and I'll always be your Evan.

To my first good therapist, Rachelle Michaud. I would probably be dead without you, and even if I weren't, I would know myself far less well.

To the ones I loved deeply. It may be weird to give your exes a shout-out in your dissertation, but I have to do it. Y'all showed me kindness when I couldn't show it to myself, and each relationship left shards buried that are now parts of me. Vulnerability

leads to growth, and I was vulnerable with all of you. Rylie Winona Taylor, Sophia Gabrielle Kielar (née Weinstock), Olivia Carolina Bianchi, and Krystal Garcia-Hearn. For some of you, I know our paths will cross again, and I hope to embrace you and see you smiling. For others, I hope you're whole, healthy, and happy.

To Julia Isabelle McKeown. Thank you for giving me a chance. The last two and a half years have been incredible, full of laughter, silliness, singing, poetry, dancing, strange noises, learning, growth, wonder, and love. So much love. Some day we will break up, or we will die, but now, I live in our tree-house with you, with our plants and our books and our birb-friends and our art, and I am so excited for what our next chapter will bring, what our queer, trans, poly life will look like. Together. Thank you for being with me through the worst of this. I promise, it's almost done.

Chapter 1

Introduction

1.1 Battery Basics

Fundamentally, a battery can be thought of as an electrochemical cell with five main parts: two electrodes — the negative electrode (called the “anode” in the battery community) and the positive electrode (called the “cathode”) — where charge is transferred and electrochemical reactions occur; the electrolyte, which transports redox-active species while preventing electronic conduction; a separator, which prevents the two electrodes from coming into contact and shorting the cell; and various electrical components such as current collectors and wiring that complete the electrical circuit and allow the cell to function.

In this work, I am concerned with metal-ion batteries, with a primary focus on Li-ion and Mg-ion chemistries. As the name suggests, metal-ion batteries operate by shuttling metal ions (e.g. Li^+ or Mg^{2+}) from one electrode to the other; depending on the type of electrode, the metal ions can be plated as metals (e.g. Li or Mg), intercalated into a host structure, or else form a new phase through a conversion reaction.

Modern Li-ion batteries (LIBs) consist of graphitic negative electrodes, intercalation-type positive electrodes such as lithium iron phosphide (LiFePO_4 or LPF)[1] or lithium nickel manganese cobalt oxide ($\text{LiNi}_x\text{Mn}_y\text{Co}_{1-x-y}\text{O}_2$, NMC abc , where a , b , and c are the fractions of Ni, Mn, and Co, or simply NMC),[2] and liquid electrolytes comprised of carbonate solvents (primarily mixtures of ethylene carbonate (EC), ethyl methyl carbonate (EMC), dimethyl carbonate (DMC), and diethyl carbonate (DEC)) and lithium hexafluorophosphate (LiPF_6) salt, often with small additive concentrations on the order of $\sim 1 - 5\%$.[3] In such a battery, the main electrochemical reaction on both sides of the battery is intercalation. For instance, for a graphite (C_6) negative electrode and an LFP positive electrode, the main reaction can be written as $\text{LiC}_6 + \text{FePO}_4 \longleftrightarrow \text{C}_6 + \text{LiFePO}_4$, where the forward direction represents a galvanic (discharge) process. Lithium is deintercalated from graphite and intercalated into the FePO_4 host.

Though current LIBs have many attractive features, including relatively long lifetimes[4] and low cost,[5] they also have a number of considerable drawbacks. Perhaps most impor-

tantly, LIBs with graphitic negative electrodes have relatively low specific capacity ($\sim 370 \text{ mAh g}^{-1}$) and, as a result, low energy density.[6] This has motivated considerable research into adopting alternative negative electrodes, most notably silicon and related oxides ($\sim 4200 \text{ mAh g}^{-1}$)[6] and lithium metal (3860 mAh g^{-1}).[7] Another strategy to increase energy density is to use positive electrodes that reach higher potentials (energy density $D_E = \Delta V C$, where ΔV is the battery's voltage or potential difference, and C is the specific capacity) such as disordered rock salt (DRX) materials.[8, 9]

All Li-based batteries, including those with graphite, Si, and lithium metal negative electrodes, suffer from two additional, significant limitations: resource abundance[10] and safety.[11] Li is a relatively rare metal in the Earth's crust and is geographically concentrated, with the largest reserves being found in South America (specifically Bolivia, Argentina, and Chile) and Australia.[12, 13] This presents significant geopolitical risk for battery manufacturing and calls into question the feasibility of many aspirations of the LIB industry, for instance, replacing all automobiles powered by internal combustion engines with electric vehicles. In terms of safety, it has been widely reported that LIBs often form dendrites of Li metal that can pierce through battery separators, short-circuit cells, and cause fires.[14] This problem is exacerbated by the fact that common commercial Li-ion electrolytes are flammable and thermally unstable.[15]

Non-Li metal-ion batteries offer natural and in many cases intrinsic solutions to the problems of Li-ion technologies. Sodium, magnesium, and calcium are all much more abundant in the Earth's crust than lithium,[16] minimizing geopolitical and resource availability risks. Magnesium and calcium offer higher theoretical specific capacities than Li if pure metal negative electrodes can be used.[17] Mg-ion batteries (MIBs) are also typically viewed as safer than LIBs; Mg most often plates in uniform hemispherical deposits,[18] effectively preventing battery shorting.

1.2 Electrolyte Degradation and Interphases

Batteries operate in both galvanic and electrolytic modes. When a battery is discharged, it acts as a galvanic cell; energy is released as the electrochemical reaction proceeds in the thermodynamically favorable direction. To charge a battery, an electrochemical potential is applied and energy is input into the system, driving the reaction in the opposite (electrolytic) direction. In an ideal battery, the amount of charge put into a battery during electrolytic charging would be exactly equal to the amount of charge released during galvanic discharge. In other words, the round-trip efficiency of charge transfer (the Coulombic efficiency) would be 1.0 or 100%. However, perfect Coulombic efficiency is never achieved, because there are always parasitic reactions — electrochemical reactions which consume current but which do not participate in energy storage or release.[19]

These parasitic side reactions are rooted in the chemistry of the electrodes and the electrolytes. Existing and next-generation metal-ion batteries operate at extreme potentials at the negative electrode and also in many cases at the positive electrode. In part, high

operating cell voltages are desirable from an engineering perspective, as they increase the battery’s energy density. And to a certain extent, highly reducing potentials are unavoidable because of the working ions being used. Table 1.1 lists the intercalation and plating potentials for common negative electrode materials in metal-ion batteries. Notably, Li has the lowest reduction potential of any metal (0 V vs. Li/Li⁺), and all alternatives in Li-ion, Mg-ion, Ca-ion, and Na-ion batteries intercalate at less than 1 V above this highly reducing potential.

Working Ion	Negative Electrode	Working Potential (vs. Li/Li⁺)	Reference
Li ⁺	Li metal	0.0	[20]
Li ⁺	Si	0.0 – 0.4	[21]
Li ⁺	graphite	~ 0.1	[22]
Mg ²⁺	Mg metal	0.67	[20]
Ca ²⁺	Ca metal	0.17	[20]
Na ⁺	Na metal	0.33	[20]
Na ⁺	graphite	~ 0.7	[22]

Table 1.1: Intercalation, plating, or conversion potentials for common negative electrodes in metal-ion batteries.

Many electrolyte components — solvents, salts, and additives — are unstable under the extreme reducing (at the negative electrode) and/or oxidizing (at the positive electrode) conditions reached during battery cycling.[23–26] As a result, these components will react electrochemically, participating in charge transfer at the electrode in parasitic reactions and lowering the Coulombic efficiency.[27, 28] In many cases, the products of these electrolyte decomposition reactions involve the working ion,[29, 30] which means that there may be fewer ions available to transport across the cell. Rather than simply lowering the efficiency for a single cycle of the battery, this irreversibly decreases the total capacity of the battery.

Electrolyte decomposition can result in diverse chemical products. We can classify these by phase: gas, liquid, and solid. Products such as CO₂, CO, PF₃, and C₂H₄[31, 32] can evolve out of solution and significantly increase pressure inside a cell,[33] potentially compromising the cell mechanically and increasing the risk of fire and explosion. Other products, including various acids (e.g. HF, PF₂OOH, CHOOH) and other small molecules (e.g. water, methanol, and ethylene glycol, and POF₃), remain in solution. These products could be chemically innocent or could participate in further reactions. Liquid-phase products can also participate in “cross-talk”[34, 35] these molecules form on one electrode and then diffuse or migrate to the other electrode. In particular, water and HF, which can form on the positive electrode,[36, 37] can have deleterious effects on the negative electrode.[38] Finally,

solid products are those that precipitate out of solution, depositing on the electrode surfaces. These solid products can be inorganic species (e.g. Li₂CO₃, Li₂O, and LiF), small organic molecules (e.g. lithium ethylene dicarbonate or LEDC, lithium ethylene monocarbonate or LEMC), or polymers such as poly(ethylene oxide) (PEO) or poly(ethylene carbonate) (PEC).[39]

If the electrode surface is not effectively passivated, then electrolyte degradation will continue unabated, and the battery capacity will fade rapidly. This was a ubiquitous problem in early LIBs with Li metal[40] and Si negative electrodes,[41, 42] for instance. On the other hand, if the electrolyte decomposes to form products that are impermeable to the working ion, then the battery must face a high overpotential to charge or discharge, or else cease functioning altogether. Most Mg-ion and Ca-ion cells suffer from this problem,[17, 43, 44] as electrolytes in these systems typically form inorganic surface films with low ionic conductivity.

Alternatively, an electrolyte can react to form a film that is electronically insulating — passivating the electrode and preventing continued parasitic reactions — and yet ionically conductive. Such passivation films, called “solid electrolyte interphases” (SEIs) because they function much like solid-state electrolytes, were initially discovered by Peled and Yamin in 1979 in the context of aqueous Li electrodes.[45, 46] Since their initial discovery, SEIs have been widely observed on electrode surfaces, particularly in metal-ion batteries.[47–51] The development of SEI-forming electrolytes in LIBs is the main reason that commercial Li-ion cells maintain their capacity over thousands of cycles.[52] While it was once believed that multivalent metal-ion batteries could not form effective SEI layers, this conventional wisdom has recently been overturned. The first passivating SEI layers in MIBs were discovered towards the end of the last decade.[53–55] As a result, though most multivalent-ion research still focuses on the design of nonreactive electrolytes,[56, 57] there has recently been renewed interest in SEI formation in Mg and Ca chemistries.[58, 59]

A note on terminology: though Peled and Yamin’s original language is general and does not refer to either a positive or a negative electrode, the battery community has adopted the term “SEI” to refer primarily to passivation films on battery negative electrodes. The term “cathode electrolyte interphase” (CEI) is instead used to refer to passivation films on positive electrodes. To avoid confusion, I will use the word “interphase” when speaking generally about battery electrode passivation and will use the abbreviations “SEI” and “CEI” as they are commonly used by battery researchers.

1.3 The Challenge of the SEI

In an early review on the subject, German battery researcher Martin Winter called the SEI the “most important and least understood” solid electrolyte.[60] The SEI is important because of its role in preventing capacity loss and stabilizing metal-ion batteries; it remains poorly understood because of its extreme chemical complexity and sensitivity.

Once a sufficiently low electrochemical potential is applied, electrolyte molecules take part in a reaction cascade. In the cascade,[61, 62] individual reactions and intermediates cannot be effectively separated. Rather, many competing and interacting reactions occur simultaneously, leading to a diverse distribution of products. In LIBs with carbonate-LiPF₆ electrolytes, dozens of decomposition products and interphase species have been positively identified,[29, 39] and these species are formed from perhaps hundreds or even thousands of significant reaction mechanisms. To design an SEI, one would need to first understand the roles of these different species — which lead to improved performance, which lead to worse performance, and why — and then understand how to selectively form certain species over others by disentangling the decomposition cascade.

SEI engineering is made even more challenging by the fact that extremely small chemical changes to battery electrolytes can have dramatic impacts on the SEI. In a classic example, consider the difference between EC and propylene carbonate (PC)-based LIBs. EC and PC have similar chemical structures. They are both 5-membered cyclic organic carbonates, differing only by the substitution of one hydrogen for a methyl group. However, whereas EC forms a highly stable, primarily organic SEI on graphite negative electrodes, PC fails to passivate graphite and instead can contribute to electrode exfoliation.[63, 64] In additive design, similar effects can often be observed; small changes in functional group can dramatically alter interphase chemistry and battery capacity.[25] Moreover, the effects of additives are often non-monotonic and nonlinear, with the maximum benefit for a given additive being achieved at some empirically-determined, typically moderate concentration.[65, 66] Finally, it is well known that battery electrolytes are sensitive to impurities. While some impurities such as water are accounted for in battery electrolyte research through rigorous drying protocols and careful titration measurements,[67, 68] other impurities (e.g. organic impurities in electrolyte solvents)[69] are often neglected.

In sum, a major aim of the battery community — and the most significant goal of this dissertation — is this: to be able to predict *a priori* how a given electrolyte component or electrolyte formulation will participate in a complex reaction cascade, considering the impact of small chemical modifications and impurities. Only once this goal is achieved will the rational design of battery electrolytes and SEI layers be possible; until then, the field must rely on intuition and guesswork.

Chapter 2

Literature Review: Methods to Interrogate Electrolyte Decomposition and Interphase Formation

Given the importance of interphases for long-term battery cycling, it is unsurprising that considerable effort has been expended to characterize these layers and reveal their secrets. Of greatest interest are the following questions:

1. Composition: What is the interphase made of?
2. Structure: What is the morphology of the interphase?
3. Origin & mechanism: What electrolyte components form what products, and how are those products formed?
4. Impact: How do composition, structure, and mechanisms affect the properties of the interphase, and how do those properties impact overall battery performance?

Often, analysis of interphase layers is indirect. Electrochemical measurements such as cyclic voltammetry (CV)[70, 71] and electrochemical impedance spectroscopy (EIS)[72–74] provide general information about battery performance, such as the internal resistance in a cell. From this information, one can infer how the interphase is behaving, if it is effectively passivating the negative electrode, and how its properties change over time. However, these techniques can only provide partial answers regarding impact and cannot directly address questions of composition, structure, or origin.

Here, we focus on experimental and theoretical methods that directly interrogate either electrolyte reactivity (including decomposition to gaseous or soluble products) or interphases in battery environments. This chapter is not meant to provide a complete overview of these techniques, as several reviews (primarily but not exclusively focusing on Li-ion technologies) have previously been published.[39, 52, 75–80] Rather, this chapter serves as a brief overview to orient the reader and motivate the methodological choices described in later chapters.

2.1 Experimental Methods

X-ray Methods

One of the most widely used characterization techniques in battery interphase studies is X-ray photoelectron spectroscopy (XPS). In XPS, a sample is bombarded with X-rays, which cause electrons to be ejected from the sample. The energies of the ejected electrons can then provide information regarding the sample's elemental composition.[81, 82] Because photoelectron energy levels are somewhat dependent on bonding, XPS can be used in battery environments to distinguish between simple inorganic species (e.g. LiF, Li₂CO₃) as well as identify bonding motifs in organic products (e.g. C–H or C–O bonds).[42]

Alternatively, one can use an absorption technique such as X-ray absorption spectroscopy (XAS)[53, 57] or X-ray absorption near edge structure (XANES) spectroscopy.[83, 84] These techniques provide complementary information to XPS, probing the unoccupied rather than occupied electron energy levels.

X-ray techniques typically require extremely high vacuum; they are also most often conducted *ex situ*. Because interphase components are often sensitive, prone to evaporation as well as reaction with moisture and air, XPS is likely to cause changes to the interphase composition even before the X-rays start shining. The situation is worsened when samples are washed prior to characterization, which may dissolve interphase components or else mechanically damage the fragile passivation film.[85] However, there have been efforts to perform x-ray characterization *in situ*, for instance by Nandasiri et al.[86] While an *in situ* approach cannot overcome the fundamental limitations of X-ray characterization, sample damage by the environment, vacuum, or washing can be minimized.

Electron Microscopy

Scanning electron microscopy (SEM) is commonly used to observe materials on the micro- or nanoscale. In the context of batteries, SEM can reveal electrode morphology, which can be important for e.g. understanding electrode cracking,[87, 88] dendrite formation,[89, 90] or the smoothness of metal plating.[91] Because interphase layers are extremely thin (typically $\sim 1 - 10$ nm for CEI layers[92, 93] and on the order of 10 – 100 nm for SEI layers),[94, 95] SEM is not well suited to directly observe interphase structure. However, when SEM is used with techniques such as energy dispersive spectroscopy (EDS), it can help to provide limited information about interphase composition.[47, 96] EDS and related techniques reveal the spatially resolved elemental composition of the sample surface.[97] Because SEM requires high-energy electrons and a high vacuum environment, sample damage is essentially guaranteed.

For higher-resolution analysis of interphase structure, transmission electron microscopy (TEM) is used instead of SEM. In particular, cryo-EM, in which samples are flash-frozen and sectioned by e.g. a focused ion beam before being introduced to high-energy electrons, is attractive for battery interphases and electrolytes.[98–100] By freezing the sample, one

prevents interphase components from evaporating in vacuum and moreover limits the extent of sample damage from the electron beam. Cryo-EM is therefore one of the best tools available to examine interphase structure and morphology.

Vibrational Spectroscopy

Fourier transform infrared (FT-IR) and Raman spectroscopy both use infrared light to excite molecular vibrational modes.[101] Because vibrational modes are nonlocal,[102] depending often on the motion of functional groups or the entire molecule, rather than individual atoms, vibrational techniques like FT-IR and Raman spectroscopy can provide more detailed information about molecular structure than X-ray or electron microscopy methods. Vibrational signals are not specific or unique - that is, signals from multiple different functional groups or from multiple different molecules often appear in the same region of the spectrum.[103, 104] Nonetheless, vibrational spectra are attractive for their ease of acquisition and their ability to probe *in situ* without sample damage. In addition, FT-IR and Raman signals are somewhat sensitive to the local environment around a molecule (e.g. the effect of neighboring ions), which makes these techniques helpful in understanding electrolyte solvation structures.[105–107]

Like X-ray methods, vibrational spectra alone cannot be used to positively identify organic interphase products,[39] though information about functional groups can be helpful in generating plausible hypotheses for product identification. Enhanced Raman techniques, such as surface enhanced Raman spectroscopy (SERS)[108] and shell-isolated nanoparticle-enhanced Raman spectroscopy (SHINERS),[109] can provide further time-resolved information regarding the compositional and structural evolution of interphases.

Nuclear Magnetic Resonance Spectroscopy

Nuclear magnetic resonance (NMR) spectroscopy is a gold-standard characterization technique in organic chemistry. NMR, which probes the local magnetic field around atomic nuclei with spin, is highly sensitive to the local environment of an atom and provides information regarding each symmetrically inequivalent nucleus of a particular element, which means that it can be used to effectively differentiate molecules with even very similar chemical structures and functional groups.[110] In addition to chemical specificity, NMR is attractive because it can be used *in situ*[111] or even *in operando*,[112, 113] preventing sample damage.

Most commonly, liquid-phase NMR is used to probe battery electrolytes. As the name implies, liquid-phase NMR cannot probe solid-state interphases directly but is nonetheless valuable for understanding electrolyte degradation processes, in particular characterizing soluble electrolyte degradation products.[114] Recently, liquid-phase NMR has been applied to understand cross-talk in Li-ion batteries,[29] disentangling what species arise at the positive or the negative electrode and suggesting how they may react at the opposite side of the battery. The use of solid-state NMR to more directly probe battery interphases is also growing in popularity.[115–117]

As powerful as NMR is, it has several serious drawbacks. First, to achieve reasonable signal, NMR spectroscopy requires either a relatively large volume of sample (often as much as mLs), long acquisition times (sometimes as long as weeks), or both.[118] In addition to being often costly and laborious to produce, NMR spectra can be difficult to interpret, requiring databases of reference spectra (either experimental or computed) and considerable domain expertise.

Mass Spectroscopy and Gas Characterization

Most of the techniques discussed so far probe either the liquid or the solid phase, though some techniques like NMR can be used for either. But, as mentioned in Chapter 1, electrolyte decomposition also results in the production of gases. These gases are intrinsically important — gas evolution needs to be minimized to prevent battery swelling and rupture — but they can also provide some clues as to the mechanisms of electrolyte decomposition and interphase formation.[119]

Gas chromatography mass spectroscopy (GC-MS) and differential electrochemical mass spectroscopy (DEMS) can be used to probe gaseous products in batteries. In both techniques, a (typically inert) gas such as Ar or He flows into the electrochemical cell. This carrier gas picks up any volatile components that may be dissolved in the electrolyte or may have built up in the headspace of the cell. In GC-MS, the gases are separated via chromatography before being analyzed by a mass spectrometer,[120] whereas in DEMS, no such separation occurs, and the different mass signals are distinguished only by time-of-flight analysis after ionization.[121] GC-MS and DEMS are complementary. With appropriate calibration, GC-MS can determine specifically what gases are present in a sample,[122, 123] which can be difficult to accomplish in DEMS (multiple molecules could produce fragments with the same or very similar mass-to-charge ratios). On the other hand, DEMS excels at real-time data acquisition;[124] while *in operando* GC-MS in batteries is possible,[125] GC-MS analysis is often done *post mortem*. Both DEMS and GC-MS can measure gases with high precision and resolution. In particular, DEMS can detect gases with parts-per-billion concentrations.[121]

Mass spectroscopy can also be used to analyze solid products. Matrix assisted laser desorption/ionization (MALDI) mass spectroscopy has specifically been used to identify organic interphase components. In contrast to secondary ion mass spectroscopy (SIMS), in which ions are used to eject species from a surface, MALDI uses a laser for surface ejection and ionization.[126] MALDI is somewhat more gentle than SIMS, minimizing fragmentation, which makes it helpful for positively identifying large (e.g. oligomeric or polymeric) and fragile molecular products.[127]

2.2 Computational Methods

Experimental characterization can provide in-depth analysis of interphase structure (via e.g. electron microscopy or SERS). Though positive identification of interphase components can

be challenging, it is also possible through careful experimental design to determine interphase composition and identify related gaseous and soluble electrolyte decomposition products. At the most basic level, this can be accomplished via elemental analysis, though techniques like NMR and mass spectroscopy make positive identification of molecular components possible.

However, existing experimental methods are generally unable to capture short-lived intermediate species or track individual reactions in electrochemical environments,[128] making direct observation of interphase formation mechanisms impossible. Additionally, it can be extremely difficult to disentangle the effects of electrode materials, electrolyte components, additives, impurities, potential or current conditions, and more in a realistic battery environment. Together, this means that experiments alone are unable to directly address interphase origins and are often unable to provide thorough structure-property-function relationships linking electrolytes, interphases, and battery performance. As a result, mechanisms or explanations proposed in experimental studies are usually intuitive guesses without significant direct evidence.

Theoretical and computational modeling can supplement experimental characterization. In particular, models can provide precise mechanisms and cause-and-effect explanations for observed phenomena. Appropriate models can also address questions of interphase composition, structure, and morphology.

All models must be based on assumptions, or “first principles”. These assumptions are crucial, often making impossible calculations tractable, but they also critically limit the applicability of a model. If the assumptions do not apply to the system of interest, then the model may produce misleading or incorrect results. When discussing different modeling methods in this and subsequent chapters, I try to point out model assumptions and limitations.

Static Quantum Chemistry

The most fundamental models available treat battery components, including electrodes, electrolytes, and decomposition products, using quantum mechanics. Due to its reasonable balance between accuracy and cost, Kohn-Sham density functional theory (DFT)[129, 130] is the most widely used quantum chemistry method. Conventional DFT employs the Born-Oppenheimer approximation,[131] treating atomic nuclei as slow-moving particles that are analyzed separately from the fast-moving electrons. This lowers the degrees of freedom in a given problem and, thereby, significantly simplifies calculations. As an additional simplification to the many-body Schrödinger equation for electrons, DFT solves for the total electron density, rather than treating each electron individually. Less commonly, wavefunction methods such as Møller-Plesset perturbation theory (e.g. MP2) and coupled-cluster theory (e.g. coupled-cluster singles, doubles and quasiperturbative triplets or CCSD(T)) have been employed to study battery electrolytes and interphases.[132–134] Due to their high computational cost and unfavorable scaling with the number of electrons in the system, these methods are often prohibitively expensive. Moreover, for many systems and properties of interest, well-designed density functionals approach the accuracy of gold-standard

CCSD(T) in the complete basis set (CBS) limit,[135] meaning that the benefit of using such expensive wavefunction methods may not be significant.

To understand electrolyte decomposition and interphase formation, often the most important quantities to calculate using quantum chemistry are reduction and oxidation potentials (E^0), reaction thermodynamics (e.g. ΔG), and reaction kinetics (e.g. energy barriers ΔG^\ddagger or rate coefficients k). However, as a quantum chemical technique, DFT can provide information about much more than reactivity and (electro)chemical stability. As but one example, calculated infrared[136] and NMR spectra[137, 138] can be used to help interpret experimental signals.

The main drawback to using DFT (or any other quantum chemical technique) alone is that it cannot capture dynamic effects. DFT can speak to what processes are thermodynamically accessible and what processes may be fast or slow, but it cannot directly address *what will happen* in a real battery, where different species and reaction pathways are in complex competition. In addition, computational cost is often a problem for DFT studies. Even after making significant simplifying assumptions, DFT has unfavorable computational scaling. In principle, hybrid DFT using exact Hartree-Fock exchange scales as $O(n^4)$, where n is the number of basis functions.[139] This means that, to ensure reasonable computational cost, low levels of theory must be used (involving e.g. small basis sets), or system size must be restricted. As a result, it is common to neglect explicit solvent effects and the effect of an explicit electrode surface.

Molecular Dynamics

Rather than treating nuclei as static, as is done in a DFT calculation, one can allow nuclei to move as classical particles according to Newton's laws of motion. Such approaches, called molecular dynamics (MD) simulations, can be used to observe chemical dynamics, competition, and (in some cases) reactivity.

There are two main types of MD: classical and *ab initio*. In classical MD, electrons are either completely ignored or (less commonly) are treated as classical particles.[140] Rather than being described by a functional of the electron density, energy and forces are defined by a “force-field”, which is almost always empirically determined and is often fitted to e.g. DFT or wavefunction calculations.[141–143] Most force-fields rely on static definitions of bonding; while these force-fields can provide potentially important information regarding electrolyte speciation,[144, 145] transport,[146, 147] and even double-layer effects at and near electrode interfaces,[148] they can provide no information regarding electrolyte degradation and interphase formation. Notably, there have been classical MD studies examining transport (especially of Li^+ ions) through interphase products, including that of Muralidharan et al.,[149] which can provide some information regarding what interphase compositions may be desirable to enable e.g. low overpotential and impedance.

With a sufficiently flexible description of chemical bonding, it is possible to use classical MD to simulate chemical reactions. Perhaps the most common reactive force-field is ReaxFF,[150, 151] which is trained on DFT simulations. ReaxFF has been used to directly

simulate SEI formation in LIBs[152–154] and to estimate reaction energy barriers.[155] Alternatively, one can use a conventional, non-reactive force-field but dynamically adjust bonds during the course of a simulation in response to structural triggers. This approach was recently taken by Alzate-Vargas et al.[156] to study SEI formation in LIBs at a silicon electrode.

A new approach to classical MD has recently gained considerable attention: machine learned force-fields (MLFF).[157] MLFFs are much like other force-fields, in that they are empirical, trained on quantum chemical data, and treat atoms as classical, non-quantum particles. However, recent MLFFs, especially those trained using equivariant neural network methods,[158–162] can achieve extraordinary accuracy with respect to their DFT training data. Though little work has been done so far to apply MLFFs to electrolyte degradation and interphase formation problems[163] (especially with liquid electrolytes), I suspect that MLFFs will soon become a standard method of choice for MD studies in batteries.

In contrast with all of the classical MD methods described thus far, *ab initio* MD (AIMD) treats electrons explicitly, using quantum chemistry (e.g. DFT) directly to calculate energies and forces.[164, 165] AIMD is an ideal method to study electrolyte reactivity in an unbiased manner,[166–170] as it does not rely on any empirical fitting beyond what parameterization may be involved in density functional design.

The main limitation of MD approaches, as with the static quantum chemical methods described above, is computational cost. A typical AIMD run lasts on the order of 10-100 ps,[171] even when small basis sets, cheap functionals (typically of the generalized gradient approximation or GGA family), and loose convergence criteria are used. Classical MD using traditional force-fields is regularly able to simulate 10-100 ns,[172, 173] but not much beyond this limit. Unfortunately, interphase formation in commercial batteries takes hours to days to complete,[174, 175] and it is well known that interphases — and especially SEI layers — continue to evolve after this initial formation.[176] Even if significant acceleration can be achieved, for instance by coupling MLFFs with MD codes running on graphical processing units (GPUs), it is unlikely that MD will ever be able to provide accurate descriptions of interphase formation on all experimentally relevant time scales.

An additional problem concerns simulation setup. Typical reactive classical MD and AIMD simulations begin with an electrolyte (often without any impurities) in contact with a pristine electrode. In almost all cases, this is an unrealistic description. Even with battery-grade electrolytes and electrodes, impurities are ubiquitous[69, 177] and can have significant effects on interphase formation.[38] Metal electrodes like Li and Mg will be covered with a native surface film, if not prior to the introduction of the electrolyte, then immediately following.[178–180] Even less reactive electrodes like Si can have native surface films and variable surface terminations.[181] Typical MD simulations ignore these entirely or else make significant simplifying assumptions. Voids, grain boundaries, and defects in electrodes are likewise mostly ignored in literature MD simulations. While highly idealized MD simulations are certainly not useless for understanding interphasial chemistry, it is unclear how well they connect to experimental results.

Continuum-Scale Models

Modeling at the continuum scale entirely eliminates atomic and molecular detail in order to access longer time and length scales and more directly compare to experimental observables. When we speak of “the continuum scale”, however, we could be referring to a number of different scales. The smallest continuum model relevant to battery interphase research would be a single-particle model, which considers electrochemistry, transport, and interphase formation at a single electrode particle in contact with an electrolyte. Such models essentially operate on the micron length scale and are typically 1D, treating the electrode particle as spherically symmetric.[182–184] Phase-field models[185, 186] are concerned with the nucleation and growth of different phases and therefore can at least consider multiple grains of a single composition. At the most extreme, a continuum level model could consider an entire battery device, including both positive and negative electrodes. For instance, Katařník et al.[187] recently developed a continuum model to study thermal transport between electrodes in an LIB.

Regardless of the exact scale and scope, most continuum-scale models are set up and behave somewhat similarly. As the name implies, continuum models consider continuous variables, such as concentrations, fluxes, or currents. At their core, continuum models involve 1) setting up spatial grids, 2) defining boundary conditions and constraints (e.g. electroneutrality or no-slip transport) and systems of differential equations (related to e.g. chemical kinetics, mass, charge and thermal tranport, or phase transformations), and 3) solving the system of equations based on a predetermined initial condition.

Continuum-level models are among the best computational tool available to understand interphase structure and to observe the impact of electrolyte and interphase properties on battery performance via such metrics as parasitic current over time. Because, for simplicity and model stability, continuum approaches tend to minimize the number of species and reactions considered, interphase composition and reaction mechanisms should not be analyzed using continuum methods.

Mesoscale Modeling

The term “mesoscale” is ill-defined and depends strongly on the problem in question. In the case of batteries, the “nanoscale” is atomistic or molecular (described by atomistic simulations like DFT and MD) and the “macroscale” is on the level of electrodes, half-cells, or full-cell devices (described by continuum-level models). The mesoscale is the middle ground, considering length and time scales beyond those accessible to atomistic models while trying to link fundamental molecular features to macroscopic phenomena. Note that the term “mesoscale modeling” is sometimes used to describe continuum models below the device scale, such as phase-field models.[185] However, I prefer to group all continuum models together, as they are alike in terms of level of abstraction (not directly treating molecules or abstracting away molecular-level descriptions) and mathematical formalism (solving systems of equations).

A representative technique for mesoscale modeling is kinetic Monte Carlo (kMC).[188, 189] In kMC, one defines a set of “reactions” or “events” — which could be conventional chemical reactions, diffusion or other transport events, or other chemical interactions — and their associated rate coefficients. At each step of the discrete simulation, an event is selected from a statistical distribution, where events with higher propensities (defined by the rate coefficient and the amount of “reactants” or species involved in the event) are more likely than events with lower propensities.[190] From this basic starting point, many different kinds of kMC simulations are possible - for instance, simulations on a 3D lattice[191, 192] or 2D surface lattice[193] or in a well-mixed homogeneous medium.[194] kMC can access time scales much longer than MD but still shorter than experiments, ranging from microseconds[195] to a few seconds.[196] Events in kMC simulations are often linked to molecular or atomistic reaction mechanisms, but kMC simulations do not need to consider every atom or every possible molecular vibration. In this way, kMC can be thought of as a form of coarse-graining.

Alone, kMC simulations cannot address questions of origins, because specific species, events, and kinetics are usually required as input to the model. However, because they access relatively long time scales, they can provide crucial insights into what mechanisms are important, not only in the very early stages of electrolyte degradation, but potentially throughout interphase formation. kMC and other mesoscale techniques can also provide an improved structural description of battery interphases,[197–199] revealing spatial inhomogeneity, different phases, and more. These structural outputs are unique to mesoscale modeling; atomistic methods typically cannot access length and time scales long enough for such structural phenomena to emerge, while continuum-level models tend to simplify interphases, reducing them to a small number of homogeneous or quasi-homogeneous phases.

Chemical Reaction Networks

A chemical reaction network (CRN) is a simple mathematical object, consisting of a set of species (**S**), a set of “reactions” between those species (**R**), where “reaction” can be interpreted broadly like “events” in kMC simulations, and (optionally) a set of properties describing the species or reactions (**P**).[200] Using this fundamental definition, it appears that CRNs are everywhere, emerging out of a number of the methods that I have already discussed. Reactive classical or *ab initio* MD can be thought of as sampling or exploring a CRN, where **S**, **R**, and **P** are not known *a priori*. DFT calculations of reaction mechanisms can be said to produce CRNs as outputs, and kMC simulations require CRNs as inputs, where the main properties included in **P** are the reaction rate coefficients.

When speaking of CRNs as a method of their own, I am referring to approaches that automatically leverage CRNs to obtain chemical insights.[201–203] In addition to enabling dynamical simulations, as already discussed, CRNs can provide information about important species as well as mechanisms. To understand how CRNs can furnish these insights, one can think of a CRN as a graph (Figure 2.1a), where the nodes are species and the edges are reactions. I note that CRNs are distinct from graphs and do not need to be represented

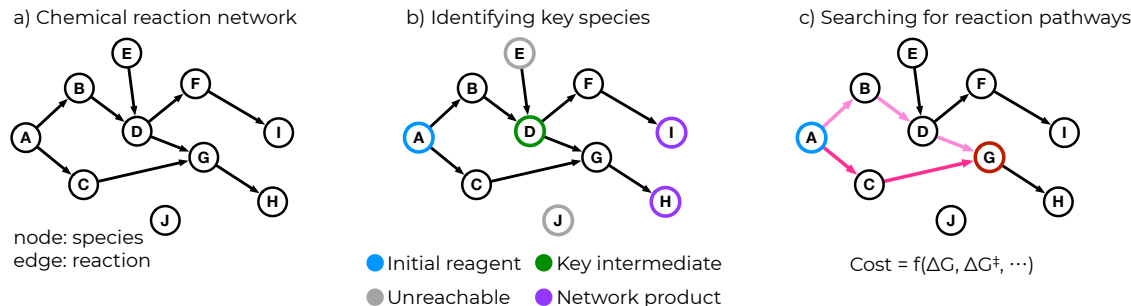


Figure 2.1: a) Cartoon depiction of a chemical reaction network (CRN) as a directed graph, where edges lead from reactant nodes to products; b) depiction of important (blue, green, purple) and unimportant network species; c) identifying reaction pathways to species of interest by tracing connections in the CRN.

as such algorithmically, as I will discuss later, but a graph representation is helpful for visualization.

Important species emerge from the structure of the network (Figure 2.1b). Key intermediates (node D) are species that are connected to many other species and that participate in many reaction pathways, while products (nodes I and H) are those species that can be formed from given starting species but are not easily consumed. Some species are completely disconnected from the rest of the graph (node J) or otherwise cannot be reached from the initial reagent species (node E), so we can consider these unimportant in the system being studied.

Identifying reaction mechanisms can be thought of as a pathfinding exercise (Figure 2.1c) — one simply traces from reactants of interest to products, or vice versa. Where multiple paths are available, one can define a cost function based on e.g. reaction thermodynamics or kinetics to weigh different paths and identify which are “best” or have minimal cost.

CRNs have been used successfully for years in organic chemistry,[204, 205] prebiotic and biochemistry,[206–208] and in fields like combustion[209, 210] where reaction mechanisms are relatively well understood and there is extensive knowledge of reaction products and intermediates from the prior literature. In contrast, the application of CRNs in electrochemistry (let alone in the field of batteries) is nascent. The first studies of CRNs in batteries were performed by Blau, Xie, and coworkers.[211, 212] In this early work, we represented CRNs as graphs and used well-established shortest-path algorithms, namely Dijkstra’s algorithm[213] to find the single path with the lowest cost between two nodes and Yen’s algorithm[214] to find the N paths with the lowest cost, to identify formation mechanisms for two known interphase products, LEDC[215] and LEMC.[116] Though this early work provided some useful insights — for instance, revealing that LEMC could not be formed without water or hydroxide being present — the methods that we initially designed were severely limited. We found that computational scaling was problematic, and networks larger than several million

reactions were completely intractable, even using supercomputing facilities. Moreover, the graph-based method required that endpoints be known *a priori*, which means that we could not be fully predictive and reveal mechanisms to unknown or novel reaction products.

2.3 What Do We Need?

There is no one technique, experimental or theoretical, that can address questions of composition, structure, origin/mechanism, and impact. Speaking broadly, experimental techniques can provide detailed information regarding interphase structure and composition (though I note that identification of electrolyte decomposition and interphase products is consistently challenging), yet even the best characterization technique can only hint at the mechanisms underlying interphase formation or the underlying structure-property-function relationships. Atomistic computational techniques can provide detailed mechanistic explanations for electrolyte and interphase behavior if appropriate assumptions are made and cost barriers can be overcome, while mesoscale and continuum models can do a good job of reflecting interphase structure. Because simulation methods often allow for more direct control than experiments, questions of impact are also more tractable with modeling than with experiments.

If nothing that we have now is good enough to answer all of our questions, we need to imagine new methods that would fill the gaps in the current available tools. Thinking of modeling specifically, an ideal tool would be predictive, requiring little or no knowledge about how a system will behave. It should retain molecule-level resolution so that it can speak to questions of composition and origin, but in order to address questions of structure and impact, it must either be able to coarse-grain this molecular detail or else interface with mesoscale and continuum-scale simulations. Even the best model cannot be trusted without experimental validation. As such, an ideal method would be able to produce results that can be compared to experiment and verified. Finally, just as this ideal tool should be able to have its results checked by experiment, it should also be able to check the experiment, aiding in e.g. spectroscopic interpretation and providing explanations for experimental observations.

Automated CRN methods have the potential to serve as this ideal tool. A CRN can hold molecular information, if the reactions contained within reflect elementary processes. As I discussed above, CRN structures implicitly encode species importance, allowing one to perform detailed analysis without necessarily knowing what one is looking for. At the same time, CRNs are effectively the input to kMC models and could also be thought of as one component of a reaction-diffusion continuum-level model. This means that, once a CRN has been constructed, it can be leveraged to obtain structural information and connect to experimental observables. Because existing CRN techniques are insufficient, in particular lacking the desired predictivity, I will spend Chapter 4 describing a new approach to constructing and analyzing CRNs that enable predictive analysis of complex electrochemical reaction cascades.

But first, to further motivate these methodological developments and to more directly contrast automated CRN analysis with more conventional methods, I will provide in the next

chapter an example of a more traditional analysis based on by-hand reaction mechanism discovery with DFT.

Chapter 3

First-Principles Explanation of Lithium Hexafluorophosphate Decomposition in Li-Ion Batteries¹

3.1 The Importance and Challenges of LiPF₆

As I discussed in Chapter 1, today's commercial LIBs typically use electrolytes comprised of LiPF₆ dissolved in blends of cyclic carbonates.[217–221] Carbonate/LiPF₆ electrolytes have many desirable properties, including weak ion association and high Li⁺ conductivity,[136, 145, 222] but they are reactive at low potentials. When paired with graphite negative electrodes, carbonate/LiPF₆ electrolytes decompose to form a relatively stable SEI layer,[23, 39, 96, 223–225] which prevents continual electrolyte degradation while allowing reversible charging and discharging. On the other hand, conventional electrolytes based on carbonates and LiPF₆ are essentially incompatible with high-energy density negative electrodes (e.g. Li metal[52, 226] and Si[47, 227]), where they form unstable SEIs resulting in comparatively poor cycle and calendar life.[228, 229]

Due to the significance of the SEI in preserving battery capacity, SEI formation from carbonate/LiPF₆ electrolytes has been extensively studied for decades.[60, 230, 231] Such studies have sought to reveal the fundamental processes involved in the exemplar system and to identify opportunities for improvement through electrolyte engineering. An understanding of the decomposition of carbonate solvents, particularly EC, has been developed via a combination of experiment and theory. A wide range of decomposition products - including gases,[232, 233] short-chain organic molecules, oligomers/polymers, and inorganic carbonates (e.g. Li₂CO₃) and oxides (e.g. Li₂O)[39] - have been experimentally characterized, and plausible elementary mechanisms for EC decomposition have been identified using

¹This chapter is closely adapted from Ref [216]: Spotte-Smith*, E.W.C.; Petrocelli*, T.B; Patel, H.D.; Blau, S.M.; Persson, K.A. Elementary decomposition mechanisms of lithium hexafluorophosphate in battery electrolytes and interphases. *ACS Energy Letters* **2023**, 8(1), 347–355.

DFT,[169, 234, 235] AIMD,[166, 236, 237] and CRN analysis.[211, 212]



In comparison, there are many open questions concerning the decomposition of LiPF₆. It is widely accepted that LiPF₆ reacts to form LiF, which precipitates and contributes to the SEI.[230, 231, 238, 239] A range of other products, including POF₃,[240] difluorophosphoric acid (PF₂OOH),[241] and some organophosphorus compounds[242] have been identified by experimental spectroscopy. Moreover, LiPF₆ demonstrates thermal instability,[243, 244] and it has long been suggested that an autocatalytic mechanism involving POF₃ (Equations 3.1-3.2) is responsible.[15] However, mechanistic explanations for LiPF₆ reactivity remain lacking. Most commonly, hydrolysis[238, 239, 244–246] is invoked to explain observed PF₆⁻ decomposition products (Equations 3.3-3.4 show an example mechanism). LiPF₆ has been shown to be unstable in the presence of water,[221] yet hydrolysis alone is insufficient to explain the significant role of LiPF₆ in SEI formation. The DFT study of Okamoto[247] suggests that PF₆⁻ hydrolysis should be extremely slow, in agreement with longstanding experimental evidence.[248] Moreover, LIB electrolytes used in laboratory studies are often rigorously dried, allowing ~10 ppm H₂O. Though exposure to high potentials on the positive electrode can both enable the formation of H₂O by reactions with EC[29] and accelerate PF₆⁻ hydrolysis,[37] this cannot explain LiF formation or further LiPF₆ decomposition during early SEI formation before high potentials have been reached or in batteries without high-voltage positive electrodes.



In this Chapter, we explore the decomposition mechanisms of LiPF₆ using DFT (see Appendix B.1 for details on our computational methods). We find that water is not necessary to explain the formation of LiF or POF₃, but rather that PF₅ can react rapidly with readily available Li₂CO₃ during early SEI formation. This mechanism is entirely chemical in nature; it does not depend on electrochemical reduction or oxidation of LiPF₆ and can occur at any depth of the SEI as long as the transport of PF₆⁻ to inorganic carbonate domains is feasible. Hence, the porosity, morphology, and transport properties of the SEI also become relevant factors. We then study POF₃ autocatalysis, using PF₂OOH and LiPF₂O₂ as model intermediates. Because POF₃ adds selectively to highly charged oxygens in oxyanions, LiPF₂O₂ is preferred over PF₂OOH in the absence of an oxidizing potential. Our calculations indicate that overall, the POF₃ autocatalytic cycle is limited by a slow intramolecular fluorine transfer step. These findings answer longstanding questions regarding the decomposition of LiPF₆ and suggest new routes for controlling salt reactivity during SEI formation.

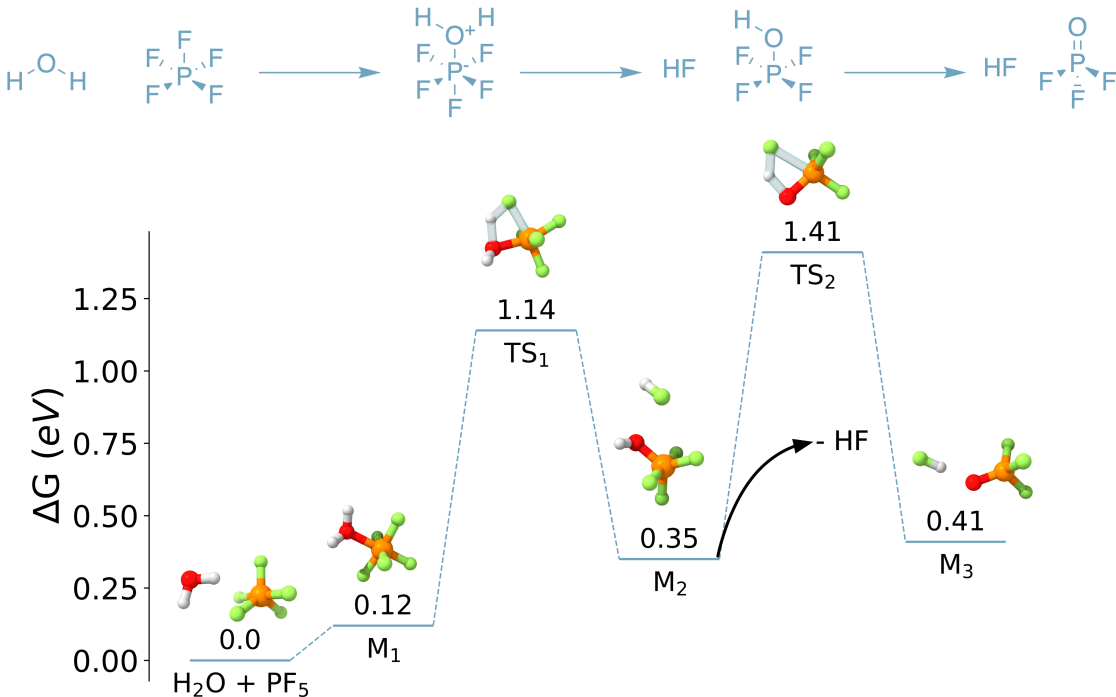


Figure 3.1: Hydrolysis of PF_5 to form POF_3 and 2 HF . This mechanism is overall thermodynamically unfavorable and involves two reactions with high barriers ($\Delta G^\ddagger > 1.00$ eV).

3.2 Questioning the hydrolysis hypothesis

We begin by considering the formation of PF_5 , which is a key intermediate in essentially all LiPF_6 reaction routes considered in the literature and in this work. We find that the elimination of LiF from LiPF_6 to form PF_5 (Equation 3.3) has no transition-state (TS) but is endergonic, with $\Delta G = 1.04$ eV. However, we note that the product in this reaction is a solution-phase molecule of LiF , whereas we expect that LiF will precipitate, forming solid deposits within the SEI. The elimination of LiF is more likely to occur when considering the possibility that LiF could be stabilized by precipitation. Okamoto[247] previously found that the deposition of solid LiF ($\text{LiF}(\text{solv}) \longrightarrow \text{LiF}(\text{solid})$) has $\Delta G = -1.17$ eV, which would make Equation 3.3 overall exergonic. More recently, Cao et al.[249] used DFT and AIMD to show that LiPF_6 decomposition by either chemical or electrochemical means is greatly accelerated in the presence of existing LiF . Here, we report the reaction energies and energy barriers of LiF elimination reactions like Equation 3.3 without including the effect of a surface or LiF precipitation. However, we emphasize that these reactions, in general, should be more favorable than what is predicted based on calculations with molecular LiF in solution.

Even once PF_5 is formed, Figure 3.1 confirms that, at our chosen level of theory, the direct hydrolysis of PF_5 by H_2O is unfavorable. Each of the three hydrolysis steps — the addition of H_2O to PF_5 ($\text{H}_2\text{O} + \text{PF}_5 \longrightarrow M_1$), the elimination of HF to form PF_4OH ($M_1 \longrightarrow M_2$), and the elimination of another HF from PF_4OH to form POF_3 ($M_2 \longrightarrow M_3$) — is predicted to be endergonic. Further, the latter two steps both have energy barriers $\Delta G^\ddagger > 1.00$ eV, agreeing with the experimental observation that hydrolysis is slow at room temperature. Significant thermal activation beyond temperatures reached in normal LIB cycling conditions would be required to enable LiPF_6 hydrolysis.

3.3 Reactions with Li_2CO_3

An alternate mechanism involves the reaction of PF_5 with Li_2CO_3 (Figure 3.2). Reactions between LiPF_6 and inorganic carbonates have been proposed in the past[177, 250] on the basis of the observed evolution of CO_2 and POF_3 upon mixing of LiPF_6 and Li_2CO_3 , but this route has largely been neglected in favor of hydrolytic mechanisms. Moreover, no elementary mechanism for the reaction between LiPF_6 -like species and Li_2CO_3 has been reported.

We find that PF_5 reacts vigorously with Li_2CO_3 . An initial addition step between the two reactants ($M_4 \longrightarrow M_5$) has a low barrier of $\Delta G^\ddagger = 0.04$ eV. Following reorganization of Li^+ ($M_5 \longrightarrow M_6$), the adduct (M_6) then dissociates in a single concerted reaction, yielding LiF , CO_2 , and LiPOF_4 with $\Delta G^\ddagger = 0.19$ eV. Finally, to form POF_3 , LiPOF_4 eliminates an additional molecule of LiF ($M_7 \longrightarrow \text{LiF} + \text{POF}_3$), with $\Delta G^\ddagger = 0.63$ eV, $\Delta G = 0.28$ eV. We again note that we expect both ΔG and ΔG^\ddagger for LiF elimination reactions to be lowered if precipitation of LiF on a surface is allowed. Even without any corrections for the instability of molecular LiF produced in $M_6 \longrightarrow M_7$ and $M_7 \longrightarrow \text{LiF} + \text{POF}_3$, this mechanism represents one of the most kinetically favorable elementary mechanisms for PF_5 decomposition yet reported.

If it does not dissociate completely, the adduct M_5 may instead eliminate LiF ($M_5 \longrightarrow M_8$), though this reaction suffers from a high predicted barrier of $\Delta G^\ddagger = 1.34$ eV. After LiF elimination, an additional oxygen from the carbonate group binds to phosphorus to form a ring complex M_9 . By eliminating CO_2 , either immediately ($M_9 \longrightarrow M_{11}$, $\Delta G^\ddagger = 0.81$ eV) or following the elimination of another LiF ($M_{12} \longrightarrow M_{13}$, $\Delta G^\ddagger = 0.36$ eV), this ring complex also forms LiPOF_4 (M_{11}) or POF_3 (M_{13}).

The proposed mechanisms shown in Figure 3.2 rely only on Li_2CO_3 , which should be abundant at the negative electrode, especially during early SEI formation.[75, 96, 166, 231, 250, 251] The reaction of PF_5 and Li_2CO_3 is also entirely chemical in nature; none of the reactions in Figure 3.2 depend on electrochemical oxidation or reduction. As a result, the decomposition should not depend explicitly on applied potential, the proximity to the negative electrode surface, or the availability of electrons. We therefore predict that the decomposition of PF_5 can occur anywhere in the SEI, so long as inorganic carbonates like Li_2CO_3 are present. This being said, because Li_2CO_3 is formed in the SEI as a result of electrochemical

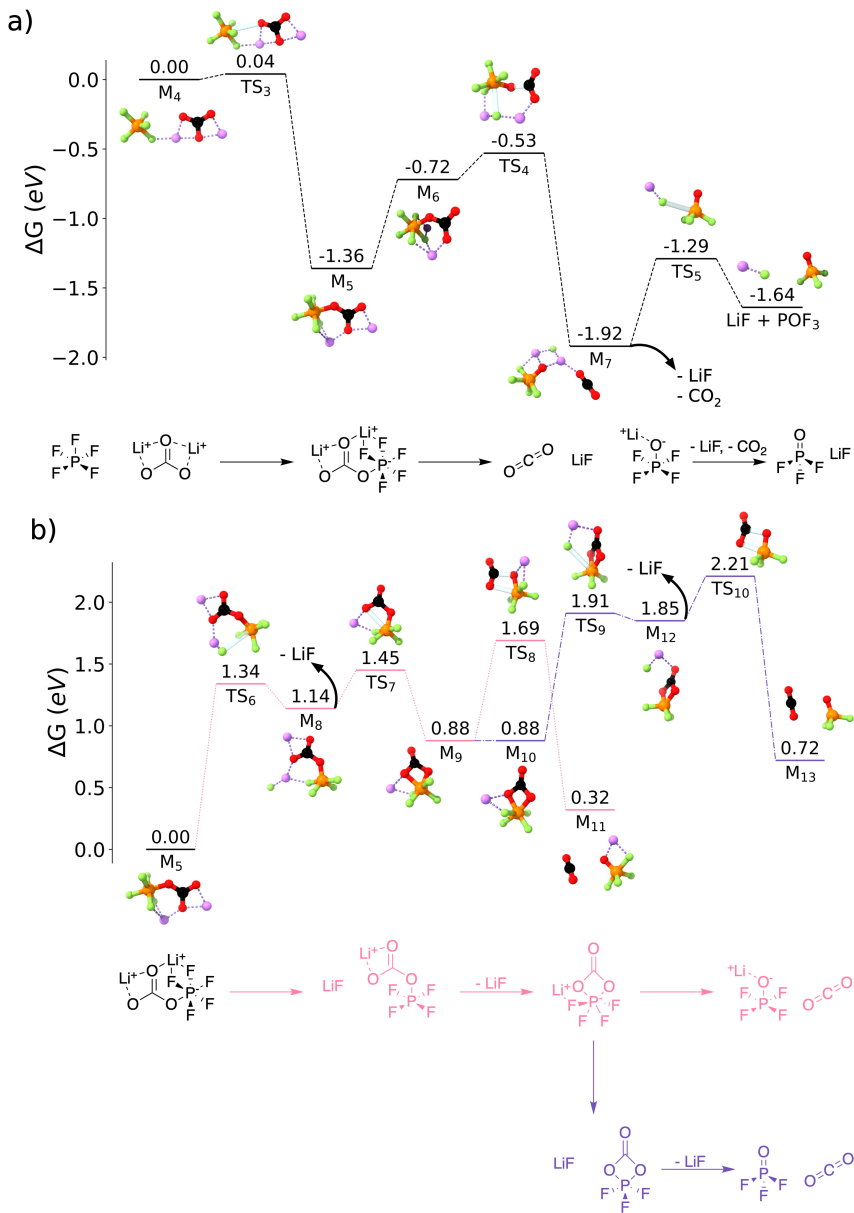


Figure 3.2: Energy diagrams for the formation of POF_3 from PF_5 and Li_2CO_3 . a) LiPOF_4 forms via simultaneous elimination of LiF and CO_2 from a $\text{PF}_5\text{-Li}_2\text{CO}_3$ adduct; LiPOF_4 can then eliminate LiF to form POF_3 . b) Alternate, less favorable mechanisms in which LiF is eliminated from the adduct without simultaneously eliminating CO_2 .

reduction of EC,[166] the overall rate of POF_3 formation via the reaction of PF_5 with Li_2CO_3 will implicitly have a potential dependence.

While our focus in this work is on LiPF_6 decomposition during SEI formation, it is worth noting that Li_2CO_3 is an impurity formed during the synthesis of common transition metal oxide positive electrodes.[177] Accordingly, the mechanisms described in Figure 3.2 could occur at the positive electrode as well as at the negative electrode or the SEI.

3.4 An atomistic mechanism for POF_3 autocatalysis

Figure 3.2 indicates that POF_3 emerges rapidly by reaction with Li_2CO_3 during SEI formation. This hints that the proposed autocatalytic mechanisms for POF_3 (re)formation (Equations 3.1-3.2), which rely on POF_3 and carbonate species, are chemically plausible.

To confirm the mechanism of POF_3 autocatalysis at elevated temperature, we first consider the formation of $\text{PF}_2\text{O}_2\text{R}$ species, namely PF_2OOH , which can emerge from reactions with H_2CO_3 (Figure 3.3a) and LiHCO_3 (Figure 3.3b), and LiPF_2O_2 , which forms from reactions with Li_2CO_3 (Figure 3.3c). In addition to their relevance for POF_3 formation and LiPF_6 decomposition, $\text{PF}_2\text{O}_2\text{R}$ species and in particular PF_2OOH have been blamed as major contributors to the decomposition of SEI species and the loss of battery capacity.[35, 252] Jayawardana et al. have argued that PF_2OOH should form at the positive electrode as a result of PF_6^- oxidation.[35] If PF_2OOH and related species could form at the negative electrode without high potentials, it could have significant implications for the stability of the SEI.

Figure 3.3a shows a mechanism for a chemical reaction between H_2CO_3 and POF_3 . The initial addition reaction between POF_3 and H_2CO_3 ($\text{H}_2\text{CO}_3 + \text{POF}_3 \longrightarrow M_{14}$) is thermodynamically unfavorable ($\Delta G = 1.62$ eV). Subsequent reactions to form HF, CO_2 , and PF_2OOH do not face significant barriers and should occur rapidly. The reaction between POF_3 and LiHCO_3 (Figure 3.3b) follows a similar mechanism. The addition step ($M_{17} \longrightarrow M_{18}$) is also endergonic ($\Delta G^\ddagger = 0.48$ eV, $\Delta G = 0.52$ eV), though we suggest that it could be accessed at moderate temperatures. Addition by LiHCO_3 is followed by the elimination of LiF ($M_{19} \longrightarrow M_{20}$), which is analogous to the elimination of HF in Figure 3.3a, ($M_{14} \longrightarrow M_{15}$). Following the complete removal of LiF, M_{20} can undergo the same concerted proton transfer and CO_2 elimination shown in Figure 3.3a ($M_{15} \longrightarrow M_{16}$).

In contrast, POF_3 adds easily to Li_2CO_3 (Figure 3.3c, $M_{21} \longrightarrow M_{22}$), with $\Delta G^\ddagger = 0.15$ eV and $\Delta G = -0.01$ eV. We explain the difference in the thermodynamics of the reactions between POF_3 and H_2CO_3 , LiHCO_3 , and Li_2CO_3 by considering acid-base chemistry. POF_3 and PF_5 are both Lewis acids. Li_2CO_3 is a Lewis base, while LiHCO_3 is, depending on context, either a weak acid or a weak base, and H_2CO_3 is an acid. The differences in basicity of Li_2CO_3 , LiHCO_3 , and H_2CO_3 are reflected in the atomic partial charges of their reacting oxygens (Figure 3.3c); oxygens in Li_2CO_3 are significantly more anionic than those in LiHCO_3 or H_2CO_3 , suggesting a greater proclivity to donate electrons. Though PF_2OOH formation via LiHCO_3 is possible, the difficulty of addition with protonated carbonates

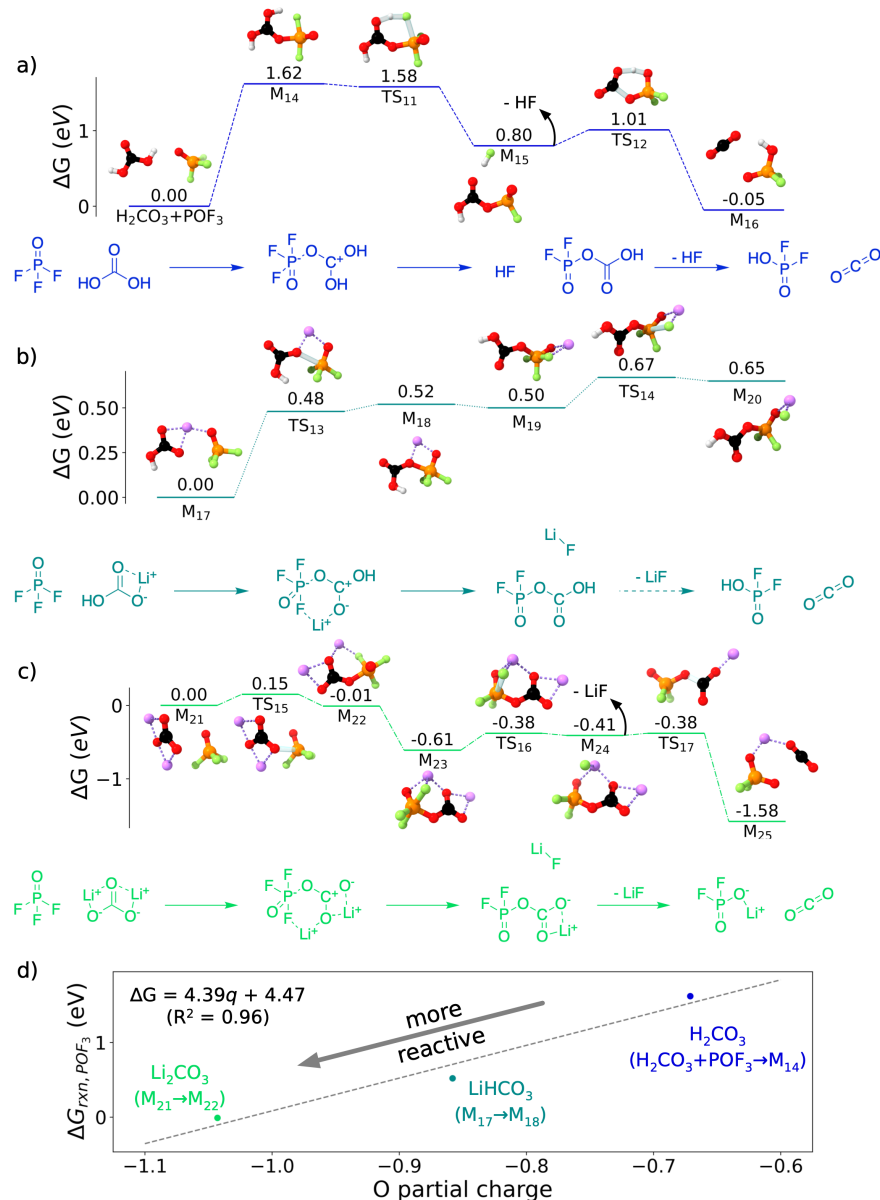


Figure 3.3: Reactions between POF_3 and simple inorganic carbonates a) H_2CO_3 , b) LiHCO_3 , and c) Li_2CO_3 to form CO_2 and either PF_2OOH or LiPF_2O_2 . A trend between the partial charge of the reacting oxygen(s) and the reaction energies with POF_3 for each carbonate considered is shown in d). A linear fit, $\Delta G = 4.39q + 4.47$, where q = the most negative oxygen partial charge, shows strong correlation ($R^2 = 0.96$) among the three carbonates.

suggests that, barring electrochemical processes, LiPF₂O₂ should be more abundant at the negative electrode than PF₂OOH. Nonetheless, the prediction that PF₂OOH and LiPF₂O₂ can form at or near the SEI without the need for cross-talk from the positive electrode motivates further efforts to understand the interactions between these species and other SEI components.

Mechanisms for the reformation of POF₃, completing the autocatalytic cycle in Equation 3.2, are shown in Figure 3.4. Following a similar trend to that shown in Figure 3.3d, the attack of PF₅ by the acidic PF₂OOH (Figure 3.4a, PF₂OOH + PF₅ → M₂₆) is thermodynamically unfavorable, while LiPF₂O₂ can favorably add to PF₅ (Figure 3.4b, LiPF₂O₂ + PF₅ → M₂₉). After the initial addition, an intramolecular fluorine transfer is required; for both PF₂O₂R species considered, this step is thermodynamically unfavorable and suffers from a high barrier (M₂₆ → M₂₇, ΔG‡ = 0.95 eV; M₃₀ → M₃₁, ΔG‡ = 1.76 eV). While both intramolecular fluorine transfer reactions are kinetically limited at room temperature (Figure 3.4 c-d), the reaction without Li⁺ can occur at elevated temperature (especially T > 150 °C). After fluorine transfer, the two mechanisms in Figure 3.4a-b diverge. In Figure 3.4a, a concerted proton transfer and elimination step occurs (M₂₇ → M₂₈), yielding POF₃ and PF₄OH. PF₄OH can subsequently eliminate HF to form POF₃, as shown in Figure 3.1. In Figure 3.4b, a four-member O-P-O-P ring is formed (M₃₂ → M₃₃) and POF₃ is eliminated (M₃₃ → M₃₄), leaving LiPOF₄ which could then form LiF and POF₃ as previously discussed.

Our mechanism confirms the previously reported autocatalytic formation of POF₃. We find, in agreement with earlier experimental studies,[15, 243] that this cycle requires significant thermal activation (T ~ 150 °C). This is primarily due to a sluggish intramolecular fluorine transfer and, specifically for the mechanism requiring PF₂OOH as an intermediate, the high barrier for HF elimination to reform POF₃. While we have found a mechanism for POF₃ autocatalysis that does not require any water, the significantly lower barrier for the pathway involving PF₂OOH indicates that LiPF₆ thermal decomposition could be initiated and accelerated by LiPF₆ hydrolysis,[240] which is accessible at elevated temperature.

3.5 Conclusions

To conclude, LiPF₆ is an exceptional salt that is likely to play a major role in the LIB market for years to come. While some decomposition of LiPF₆ is desirable to form a functional SEI, continued breakdown can severely limit the life of LiBs. In this work, we identified a novel and facile elementary decomposition mechanism of LiPF₆ using first-principles DFT simulations. Our results imply that under normal battery cycling conditions, the major decomposition mechanism of LiPF₆ does not depend on water or on electrochemical salt reduction. Rather, LiPF₆ forms the expected products LiF, POF₃, LiPF₂O₂, and potentially PF₂OOH via entirely chemical reactions with inorganic carbonates (especially Li₂CO₃). These reactions can likely occur in the solution phase or in nanocrystalline or amorphous regions of the SEI. PF₅ and POF₃ show a strong affinity to react with highly anionic oxygens and Lewis

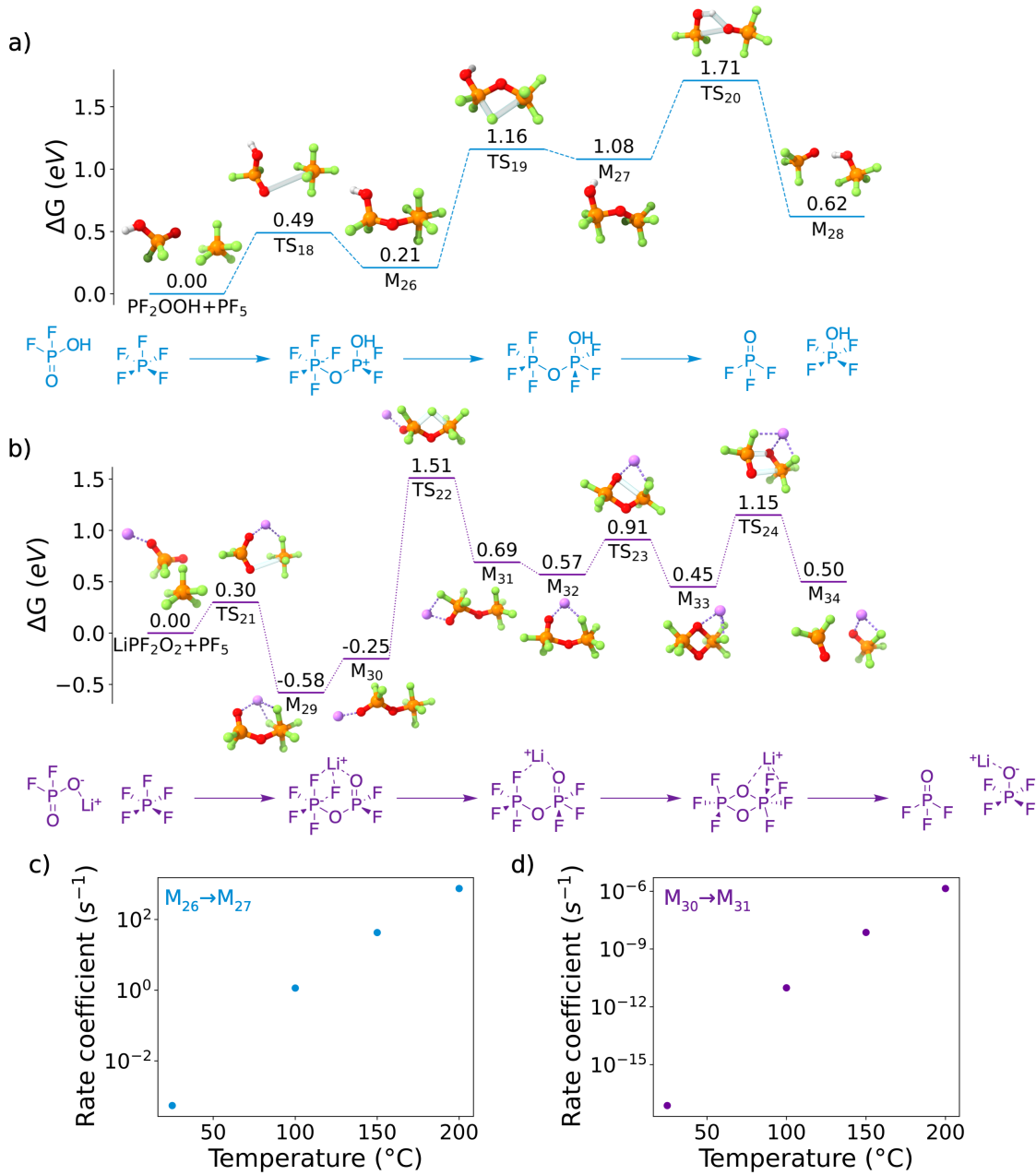


Figure 3.4: Possible routes for the reformation of POF_3 from PF_2OOH (a) and LiPF_2O_2 (b). Both mechanisms are kinetically limited due to an extremely unfavorable intramolecular fluorine transfer step ($M_{26} \rightarrow M_{27}$, $M_{30} \rightarrow M_{31}$), which makes POF_3 autocatalysis unlikely at modest temperatures. Rate coefficients for the fluorine transfer step are provided in c) for the PF_2OOH pathway and in d) for the LiPF_2O_2 pathway.

bases, suggesting that efforts to control the reactivity of LiPF₆ should focus on limiting the exposure of PF₅ to oxyanion and other basic species, including and especially inorganic carbonates like Li₂CO₃, in the SEI as well as on the surface of positive electrodes. This consideration may include morphological control, such as reducing porosity and/or abundance of inorganic species in the outer regions of the SEI.

In the future, theoretical studies should be combined with experimental spectroscopy to validate the mechanisms reported here. It should be possible to compare rate laws obtained by experiment (via e.g. time-resolved spectroscopy with varying amounts of inorganic carbonates and LiPF₆) and theory (via kinetic simulations, e.g. kinetic Monte Carlo). More challenging, but no less worthwhile, would be to confirm if the decomposition of LiPF₆ in a battery is primarily chemical or electrochemical in nature. This could be accomplished by tracking the rate of decomposition of LiPF₆ in the presence of inorganic carbonate species in a reductively stable solvent under varying applied potentials. While we have focused here primarily on LiPF₆ decomposition in EC-based electrolytes, we suspect that LiPF₆ could chemically react in a range of solvents via mechanisms similar to what we have described, provided that those solvents reduce and decompose to form oxyanions with highly charged reactive oxygens or sufficiently strong Lewis bases. The extent of LiPF₆ decomposition will depend on the availability of these basic and oxyanion species. Additional investigations into solvent degradation and SEI formation in EC-free (and especially carbonate-free) electrolytes should be conducted to assess if the mechanism that we have described here is general or specific to carbonate-based solvents. Detailed study of the elementary reaction mechanisms between LiPF₆ decomposition products (especially PF₂O₂R species) and other SEI species (e.g. organic carbonates), as well as the formation mechanisms of organophosphorus compounds and phosphate polymers in the SEI, should also be conducted.

Chapter 4

Methods to Construct and Analyze Electrochemical CRNs Based on High-Throughput DFT¹

Through the DFT study presented in Chapter 3, we learned much about salt reactivity in LIBs, including the interactions of LiPF₆ with water and inorganic carbonates as well as the temperature-dependent autocatalysis of LiPF₆ decomposition that leads to the salt's thermal instability. However, that study was significantly limited by its approach. Using by-hand or even semi-automated DFT required considerable time: three months of full-time effort from an undergraduate student (Thea Bee Petrocelli) who I mentored part-time, plus roughly two more months of my own concerted effort.² At this rate, it is reasonable to expect that a thorough description of electrolyte degradation and SEI formation in a given electrolyte system could take many years, even with a larger, fully dedicated team of experts. Moreover, as discussed in Chapter 2, relying entirely on static DFT obscures reactive competition and the complex interplay of intermediates and products during the SEI formation cascade.

The goal of this Chapter is to present an alternative method to study (electro)chemical cascades such as SEI formation combining high-throughput DFT, CRNs, and stochastic dynamic simulations. Though I will describe applications of these methods to batteries in subsequent chapters, none of the methods that I describe here are specific to battery chemistry. Rather, we designed these methods to explore (electro)chemical systems where i) a strong driving force such as an applied potential triggers a mostly spontaneous cascade; ii)

¹This chapter is adapted from the following references: [253]: Spotte-Smith*, E.W.C.; Blau*, S.M.; Xie, X.; Patel, H.D.; Wen, M.; Wood, B; Dwaraknath, S.; Persson, K.A. Quantum chemical calculations of lithium-ion¹ battery electrolyte and interphase species. *Scientific Data* **2021**, *8*(203); [254]: Barter*, D.; Spotte-Smith*, E.W.C.; Redkar, N.S.; Khanwale, A.; Dwaraknath, S; Persson, K.A.; Blau, S.M. Predictive stochastic analysis of massive filter-based electrochemical reaction networks. *Digital Discovery* **2023**, *2*, 123–137.

²Note that this only counts data acquisition and analysis and does not count labor required to, for instance, write a manuscript.

chemical intuition is limited because basic mechanisms are unknown or poorly understood; and iii) it is not known *a priori* what species or reactions are most important to the overall process. I describe an application of the methods described here in Chapter 5.

4.1 Generating Datasets of Challenging Reactive Molecules Using High-Throughput DFT

Reactive organic and organometallic molecules present significant challenges for computational analysis. Conventional methods to define molecular graph representations — necessary to define bonding and study molecular reactivity — are insufficient to capture coordinate bonds between metals such as Li and Mg and heavy atoms like O, F, and N. In addition, DFT calculations involving highly reactive charged, radical, and metal-coordinated molecules frequently encounter errors or fail to converge to stable potential energy surface minima. Here, we describe methods to address both of these challenges.

Dataset construction begins with a small set of molecules that are known to be important. These “principal molecules” could include reagents, reactants, catalysts, known or suspected products, etc. From the principal molecules, we generate a set of molecular fragments by recursively breaking bonds in the molecular graph representations. To explore molecular formation beyond what is currently known, we then recombine a subset of these molecular fragments, adding bonds between fragments to create new molecules. Through the application of fragmentation and recombination methods, we generate a collection of molecules that could connect starting species to final products, allowing for the exploration of reactive chemistry.

Determination of bonding and molecular graph representations

Initially, bonding for all molecules is determined from 3D atomic coordinates using the bond detection algorithm defined in OpenBabel.[255, 256] While this algorithm is well suited to the detection of covalent bonds, it is not designed to capture ionic bonds or coordinate bonds between metal ions and molecules.[257] Specifically, it is assumed in OpenBabel that Li^+ will only form one bond and that Mg^{2+} will only form two bonds. This is a critical issue due to the important and diverse coordination behavior of metal ions. As an example, Li^+ generally seeks to form between 4 and 6 coordinate bonds when in an electrolyte solution.[136, 258, 259] While often, Li^+ forms only one coordinate bond with each coordinated molecule (Figure 4.1a), cases where two (Figure 4.1b), three (Figure 4.1c), and even four (Figure 4.1d) or more coordinate bonds form can occur. Because the thermodynamics of monodentate, bidentate, tridentate, and tetradentate configurations can vary significantly, it is essential to be able to distinguish between these bonding motifs. A modified bond detection algorithm is therefore required.

A heuristic method is used to add neglected coordinate bonds between Li and electronegative coordinating atoms, namely N, O, F, and S. If an N, O, F, or S atom is less than 2.5 Å

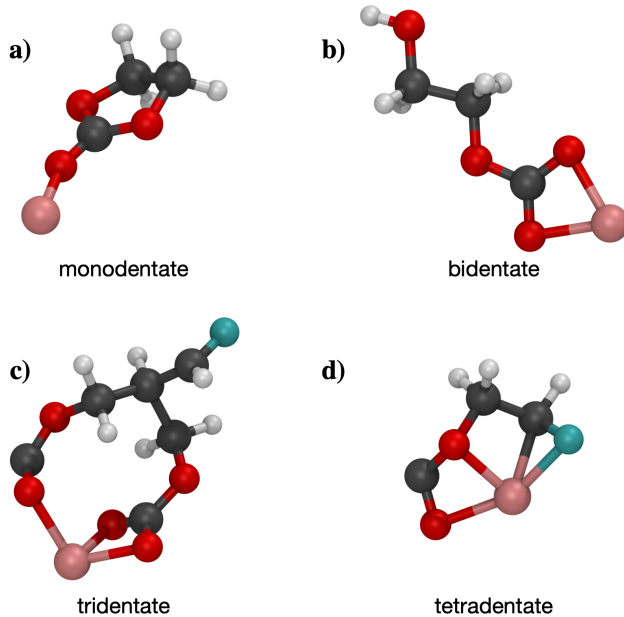


Figure 4.1: Examples of molecules with various Li^+ coordination environments: monodentate (a), bidentate (b), tridentate (c), and tetradentate (d). White atoms are hydrogen, gray atoms are carbon, red atoms are oxygen, blue are fluorine, and pink are lithium.

away from a Li atom, then those two atoms are considered to be bonded. If, after this procedure, there are Li atoms in a molecule with no bonds, then the cutoff is increased from 2.5 Å to 3.5 Å, and the procedure is repeated. Prior to performing any DFT calculations, molecular connectivity is defined first using OpenBabel and then by applying this heuristic method to add missing coordinate bonds.

After DFT calculations are completed, a quantum chemical method is also used to identify bonds. The **Critic2** program[260, 261] is employed to identify bonding interactions in the electron densities of the optimized molecular geometries. **Critic2** identifies critical points in the molecular electron density, which correspond to interatomic interactions. If the calculated field at a critical point between two atoms is greater than 0.02 (in atomic units) and if the distance between atoms is less than 2.5 Å, then the two atoms are considered to be bonded. An exception is made for bonds between Li and C, for which a smaller field (greater than 0.012) is allowed. The final bonding for a molecule is defined by the union of the sets of bonds identified using OpenBabel, the heuristic coordinate bond detection method, and **Critic2**.

High-throughput computational methods

In order to be able to compute the properties of arbitrary molecules, including highly reactive fragments, radicals, and charged species, an automated framework has been developed for

high-throughput molecular DFT. This framework, which incorporates methods to correct common errors and ensure convergence to potential energy surface (PES) minima during molecular DFT calculations on the fly, is used to optimize geometries and compute a range of properties, including total electron densities, vibrational frequencies, thermochemistry (e.g. electronic energy, enthalpy, entropy, and Gibbs free energy), atomic partial charges and spins, etc. Here, we describe the computational methods used for high-throughput DFT calculations; we provide an overview of how these methods are implemented in open source code bases in Appendix C.

Error correction

Once a DFT calculation has terminated, its output file is parsed for errors. If any errors are detected, an empirically designed recipe-based error correction process is conducted. If the error handler recognizes the error and an appropriate remedy is available, then that remedy will be employed and the calculation will be restarted automatically, generally with some alteration to the input parameters. If an error is encountered in the re-started calculation, the same recipe-based error correction procedure is applied. If the error handler is unable to interpret the error, if all possible remedies have been exhausted, or if no remedy has been implemented for a particular error type, then the calculation fails.

Even if there are several possible remedies, only one remedy is applied at a time. The appropriate remedy for a given error may be sensitive to the parameters with which the calculation was run. Those parameters, in turn, may depend on the type and number of errors that the calculation has encountered previously.

To illustrate the error-correction process, Figure 4.2 depicts the logic dictating how a convergence error for a self-consistent field (SCF) calculation should be remedied.³ The first possible remedy involves increasing the number of SCF cycles allowed; if the number of SCF cycles is lower than some maximum value (typically 200), then the number of cycles are increased to that maximum. If that remedy cannot be applied, either because it has already been applied or because the user specified a large number of SCF cycles initially, then the next remedy is to alter the SCF algorithm. The geometric direct minimization (GDM) method[262] tends to be highly robust at converging SCF calculations even for challenging molecules. However, because of its higher cost, the more rapid Direct Inversion of the Iterative Subspace method (DIIS)[263, 264] or a combination of the two methods (DIIS-GDM in the Q-Chem electronic structure code[265]) are used first, with GDM serving as a method of last resort. Finally, the SCF settings are altered such that an initial guess electron density is generated for each SCF calculation, with no knowledge of prior calculations. Using the previous solution as a starting point for an SCF calculation can improve efficiency, but it can also fail to capture electronic state reordering in a newly visited region of the PES, occasionally resulting in SCF convergence problems. If none of these remedies can be applied,

³Note that this procedure is out-of-date, and different error handlers have been implemented in the `custodian` package. I have chosen to present the error handlers as they were during the time when the datasets discussed in subsequent Chapters were developed.

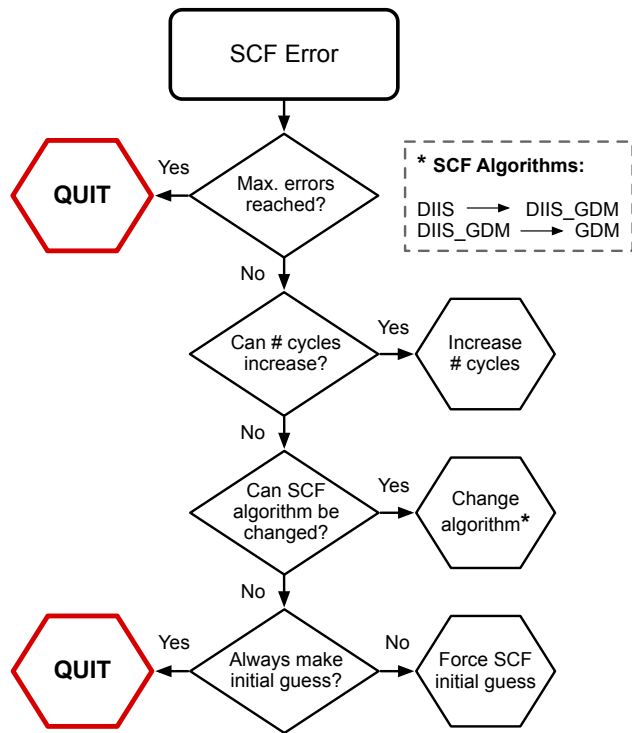


Figure 4.2: A flowchart for correcting an SCF convergence error. When the error is encountered, only a single remedy will be applied. If there is no possible remedy, or if too many errors have already been encountered, then the error handler will quit, and the calculation will be allowed to fail.

if all of them have been applied already, or if the number of errors encountered in total has exceeded a user-defined limit (e.g. five), then the calculation will fail without further attempt to remedy the error.

In addition to SCF convergence errors, remedies have been implemented for a range of errors that might arise during a calculation (failing to optimize the molecular geometry, failing to transform from internal to Cartesian coordinates, failing to calculate the Hessian eigenvalues for a vibrational frequency calculation, etc.) or while preparing a calculation (failing to parse the input file, failing to access the DFT code executable file, failure to access a license file, etc.).

Convergence to potential energy surface minima

The goal of geometry optimization is to minimize the energy and to determine the stable molecular geometry. Generally, an optimizer will seek to reduce the gradient to zero, indicating that a stationary point has been found. However, convergence to a stationary point

does not guarantee convergence to a local minimum of the PES; it is also possible to converge to an n th-order saddle point, where n is the number of imaginary frequencies. It is important to know when a calculation has converged to a saddle point and how to remedy it. Saddle points may provide poor approximations to the nearest minimum energy structure. Furthermore, saddle points can exhibit different bonding behavior from the minimum.

Most often, geometry optimization in DFT is conducted using a quasi-Newton-Raphson method; at each step, the energy and gradient are calculated, and the gradient is used to generate an approximation of the second derivative (Hessian) matrix.[266] While, in some methods, the exact Hessian is calculated at each step, this is prohibitively expensive in most cases and is therefore inappropriate for high-throughput applications. Because the Hessian used in quasi-Newton-Raphson optimization is not exact, the optimizer's knowledge of the curvature of the PES is limited. This makes it relatively common for geometry optimization algorithms to converge to saddle points instead of minima, perhaps especially for large molecules, complex reactive fragments, and/or species in an implicit solvent environment.

A method of “Frequency Flattening Optimization”, or FFOpt, is used to eliminate imaginary frequencies. As illustrated in Figure 4.3, successive optimization calculations are conducted until the structure has converged to a local minimum of the PES. In order to determine if a converged structure is a PES minimum or a saddle point, a vibrational frequency calculation is performed following each completed optimization calculation. Frequency calculations serve a dual purpose, simultaneously providing information about the curvature of the PES (the exact Hessian) and the nature of the converged stationary point while also providing some thermodynamic information, including the molecular enthalpy and entropy. If there are no imaginary frequencies, then the structure is confirmed to be a PES minimum, and no further calculations are needed. If there are imaginary frequencies, then the structure is a PES saddle point. The exact Hessian reported by the frequency calculation is then used as input to the subsequent optimization calculation in order to provide a better description of the local PES and allow the optimizer to move away from the saddle point and towards a true minimum. This procedure can be repeated as many times as needed until a minimum is found. We emphasize that the FFOpt procedure, like most geometry optimization methods, aims to optimize to a local minimum and does not guarantee convergence to the global minimum of the PES.

In order to limit the computational cost of an individual calculation, we recommend that no more than 10 frequency flattening cycles are allowed. Moreover, additional cycles should not be pursued if there is only one imaginary mode with a very small frequency magnitude ($|\nu| \leq 15 \text{ cm}^{-1}$) or if the energy has changed by less than 10^{-7} Hartree (Ha) from the previous cycle to the current cycle, indicating that knowledge of the exact Hessian did not allow the optimization to leave the saddle point. Very small, singular imaginary frequencies are allowed because they may not correspond to true transition states; rather, they could be artifacts of numerical noise in the frequency calculation. If there is a single imaginary mode with a small frequency magnitude, the calculation is still considered a success; otherwise, a calculation which terminates with at least one imaginary frequency is considered a failure.

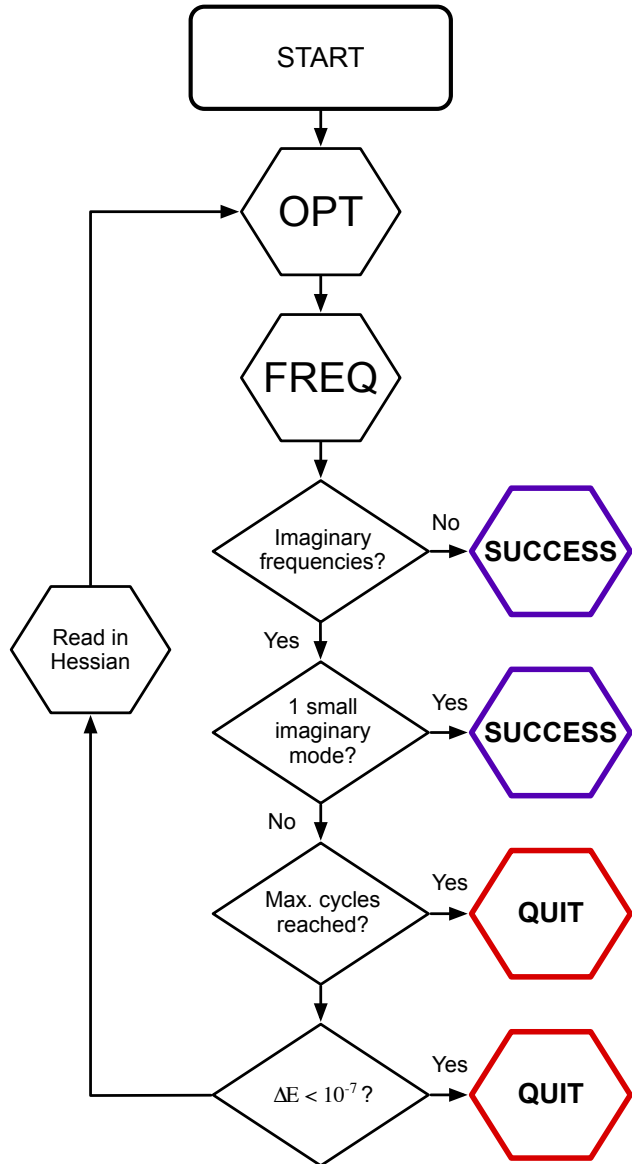


Figure 4.3: The frequency-flattening optimization (FFOpt) procedure. In the initial step, the geometry is optimized and a vibrational frequency calculation is performed. If there are no imaginary frequencies, or if there is a single imaginary frequency with very small magnitude, the calculation completes successfully. Otherwise, the Hessian from the vibrational frequency calculation will be used to inform the next cycle of optimization.

General calculation procedure

For a given set of unique molecular structures (as defined by the graph representations), FFOpt calculations are conducted at multiple charge states (e.g. -1, 0, and 1). For a

particular charge state, when an even number of electrons is present, the molecule is initially assumed to be in a singlet state, and when an odd number of electrons is present, a doublet state is assumed.

Most commonly, low-spin states are preferred for molecular ground states, and stable high-spin states are rare.[267] This implies that one could expect that most molecules with even numbers of electrons should be in singlet states, rather than triplet states. However, triplets cannot be completely ignored, as there are exceptions (most notably diatomic oxygen) where triplet states are preferred at modest temperatures.[268, 269] It is also possible that there exist species that are relevant to a particular chemistry (e.g. SEI formation) which exhibit connectivity that can only exist as a triplet.

Unless the preferred ground-state spin of a given molecule is known *a priori*, all molecules with even numbers of electrons should be subjected to DFT analysis via FFOpt in both the singlet and triplet state. However, depending on the number of molecules being considered, this could be computationally prohibitive, and so practical considerations must be taken into account.

For all molecules for which the FFOpt procedure succeeds in identifying a PES minimum, a single-point calculation is conducted on the optimized geometry in order to produce a “cube” file of the electron density.[270] This cube file is then analyzed using Critic2 to determine the critical points and improve the determination of the molecular bonding.

For single atoms (Li, H, F, etc.), a different procedure is used. Because geometry optimization is unnecessary for such molecules, only single-point calculations to determine the energy and frequency calculations to determine the translational enthalpy and entropy components are conducted.

This general procedure of conducting FFOpt singlet and doublet calculations, and (potentially selective) triplet calculations, followed by single-point calculations, is used in several stages to build a dataset, as described below.

Dataset generation

Molecular fragmentation

Fragmentation begins with the molecular graph representation and 3D structure of a principal molecule. In a single fragmentation step (Figure 4.4a), each individual bond in the molecular graph is broken, generating either one or two fragments. In the case of a single fragment - indicating that the bond is part of a ring - an initial structure for the ring-opened fragment is generated using a low-cost optimization with the UFF force field as implemented in OpenBabel. This preliminary optimization is conducted with the aim of preventing the ring from immediately re-closing during geometry optimization. In the case of two fragments, the coordinates associated with the atoms in each fragment were used as the initial structure. After all bonds have been broken, all unique fragments - defined by their graph representations - are collected.

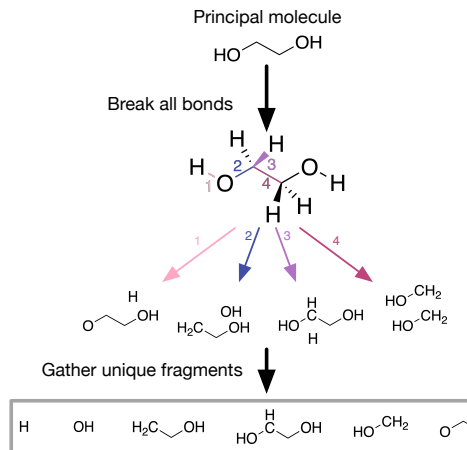
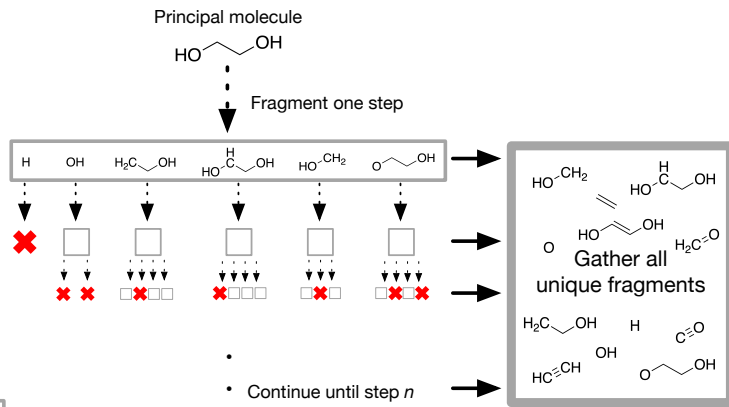
a) One-step fragmentation:

b) n -step fragmentation:


Figure 4.4: A schematic overview of a molecular fragmentation process. For a single-step fragmentation (a), a principal molecule is selected. Each bond is broken, generating a collection of molecular fragments. These fragments are then filtered to generate a set of unique (non-isomorphic) molecules. In an n -step fragmentation (b), this process is repeated in a recursive fashion. At each step, all fragments from the previous step are collected and undergo a single-step fragmentation. If the fragment is a single atom with no bonds or if all fragments generated are already present in the collection, then the process terminates (red "X"). When the maximum number of steps has been reached, or when no new fragments can be generated, the n -step fragmentation terminates.

In many cases, it is desirable to not only obtain the products of single-bond cleavage, but all possible sub-fragments of a given molecule. This can be done by recursively applying the above single-step fragmentation method (Figure 4.4b). At the n th step, all new structures from the $n - 1$ th step undergo a single-step fragmentation if possible (single atoms, which have no bonds, cannot be fragmented); the final set of fragments at that step is the union of the sets of unique fragments from each such single-step fragmentation. This recursive fragmentation can be continued until all fragments contain no bonds (at which point until only single atoms remain).

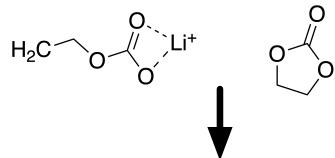
After fragmenting each principal molecule using the appropriate number of steps, all unique fragments - defined by graph connectivity - are analyzed using DFT.

Generation of recombinant molecules

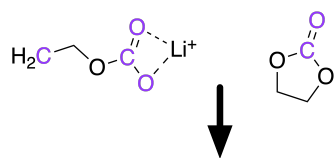
Reaction cascades most often involve bonds being formed as well as broken. The set of principal molecules could include known products, implicitly accounting for some bond for-

mations between possible fragments. However, fragmenting these principal molecules does not guarantee that all important intermediates or even all products are included. To improve coverage of possible intermediate and product species, some fragments are allowed to recombine to form new molecules.

1. Select two fragments



2. Identify connectable heavy atoms



3. Generate recombinant molecules

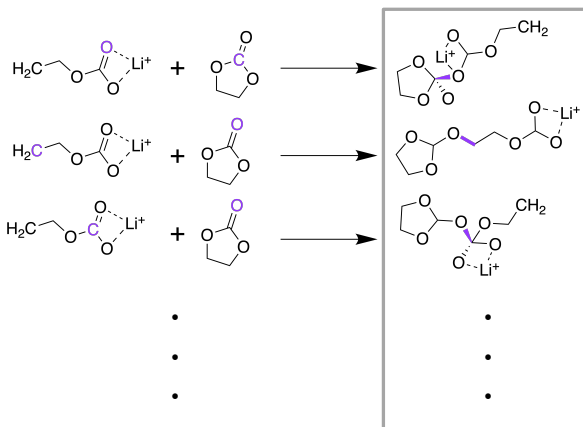


Figure 4.5: A simplified depiction of the recombination process. First (1), two fragments - in this case, from lithium ethylene carbonate, or principal molecule 1 in Appendix D - are selected. The heavy atoms in these molecules that can form additional bonds (shown in purple) are identified using valence rules (2), and finally, bonds (also in purple) are added between all combinations of these connectable heavy atoms (3) to form a set of unique recombinant molecules (gray box).

After all fragment species have been analyzed using DFT, a subset are selected for recombination. All combinations of two allowed fragments are recombined by adding a single bond in all possible ways that respect the typical valence rules of different atoms (Figure 4.5). For instance, if one fragment has an oxygen connected to only one atom and one fragment has

a carbon connected to only three atoms, then they would be allowed to combine. On the other hand, that same oxygen would not be allowed to combine with a carbon connected to four atoms. In applying these bonding rules, we do not count metal coordinate bonds and do not consider bond order (a single bond is treated on the same footing as a double or triple bond), but only consider the number of non-metal atoms connected to a given atom.

The recombinant molecules generated in this manner are further filtered by considering the reaction free energies of the recombination reactions. The BonDNet neural network[271] is employed to predict the bond formation energies of recombinant molecules. If the formation of the bond is predicted to be endergonic (i.e. the recombinant molecule is less stable than the constituent fragments), then the recombinant molecule can be discarded. Initial guess structures of all remaining molecules are produced using a force field such as OPLS,[272] and these initial structures are analyzed using DFT.

Note that the numerous stages of filtering used here - beginning with a small number of fragment molecules, requiring valence rules to be obeyed, and screening by bond formation energy - are necessary to limit the number of recombinant molecules considered. Recombination, as described here, is an inherently combinatorial process. Without appropriate filters, massive numbers of recombinant molecules can be generated, far too many to be calculated using high-accuracy DFT methods.

4.2 Generating and Analyzing (Electro)chemical Reaction Networks

Developing a CRN Methodology for Complex Reaction Cascades

CRNs are often generated[201] by applying quantum chemical methods to explore a potential energy surface (PES).[273] PES exploration techniques – including *ab initio* molecular dynamics,[165] artificial force-induced reactions,[274] and stochastic surface walking,[275] among others – are useful for exploring a chemical space. PES exploration requires minimal initial information (e.g. a set of initial species) and allows for the identification of intermediates, reactive products, and elementary reaction steps (including energy barriers). Unfortunately, PES exploration techniques typically suffer from prohibitively high cost, limiting their application to simple systems involving only small molecules or exploring reactivity over very short (~ 10 ps) time scales. While applications of semi-empirical methods[276, 277] and machine learning[158, 278] could soon alleviate this limitation in some domains, the ongoing challenges in simulating electrochemical dynamics even for simple systems (e.g. the hydrogen evolution reaction)[279] suggest that PES exploration remains unsuitable for studies of complex electrochemistry.

When PES exploration is not used, CRNs are most commonly constructed based on human chemical intuition. By applying reaction templates to include only commonly observed mechanisms[208, 280–283] or pruning by the “chemical distance” between species (the number of bonds that must change for a reaction to occur, or the number of reactions required

to transform reactants to products) to focus only on starting species and known products of interest,[284] it is possible to create networks capable of elucidating reaction pathways. However, chemical intuition is limited and unreliable when describing new reactive spaces.[285] In electrochemistry, studies of reaction mechanisms[286, 287] and characterization of reaction products[116] are very challenging. Additionally, the linear scaling relations (*i.e.* Bell-Evans-Polanyi[288, 289]) that are widely used to predict the rates of families of similar reactions in thermochemistry have not been well established in electrochemistry. As a result, CRN methods that rely on templates or the chemical distance to known products cannot yet be used to study electrochemical reactivity.

Aiming to bypass both the cost of PES exploration and the intuition required for template-based CRN generation, we recently developed the first method to construct and analyze electrochemical CRNs, which we used to study the formation of the SEI in LIBs. In this prior work on graph-based CRNs,[211, 212] the networks that we studied were limited by the computational cost of network analysis, in particular due to the poor scaling of shortest-path graph algorithms. These costs constrained the number of species as well as the number and types of reactions contained in the networks. Even more critically, our prior graph-based analysis approach was limited in its predictive capacity; in order to apply shortest-path algorithms, products of interest had to be known *a priori*. Here we confront the more challenging problem of exploring a reactive space without significant knowledge of end products. Specifically, we seek to search for many feasible pathways under various starting conditions to a range of products, byproducts, and intermediates, including species that might not be known to be important at the time of network construction.

We present a new approach to construct and explore CRNs in challenging domains such as electrochemistry that is capable of extracting unique insights and generating hypotheses to guide further in-depth analysis. First, we describe our method of **High-Performance Reaction Generation** (HiPRGen). Beginning with a set of possible species that could contribute to the chemistry of interest (\mathbf{S}_{init}), HiPRGen enumerates all stoichiometrically valid reactions and employs user-defined filters to eliminate reactions based on physical or practical criteria while aiming to retain a diverse and chemically reasonable set \mathbf{R} . To overcome the scaling limitations of graph-based pathfinding, we explore CRNs with a stochastic approach, sampling the reactive space without knowledge of reaction kinetics. We can then extract paths to any molecule formed in the trajectories and heuristically identify the products of the network as a function of initial conditions. The combination of HiPRGen with stochastic network analysis allows for the investigation of electrochemical reactivity without prior knowledge of reaction mechanisms or end products for the first time.

Template-Free Reaction Network Generation

Inspired by the previous work of Kim[284] and Xie[212] where the chemical distance between species was used to selectively include reactions in a CRN without employing templates, we have devised HiPRGen to construct CRNs by applying filters to initial collections of species and reactions.

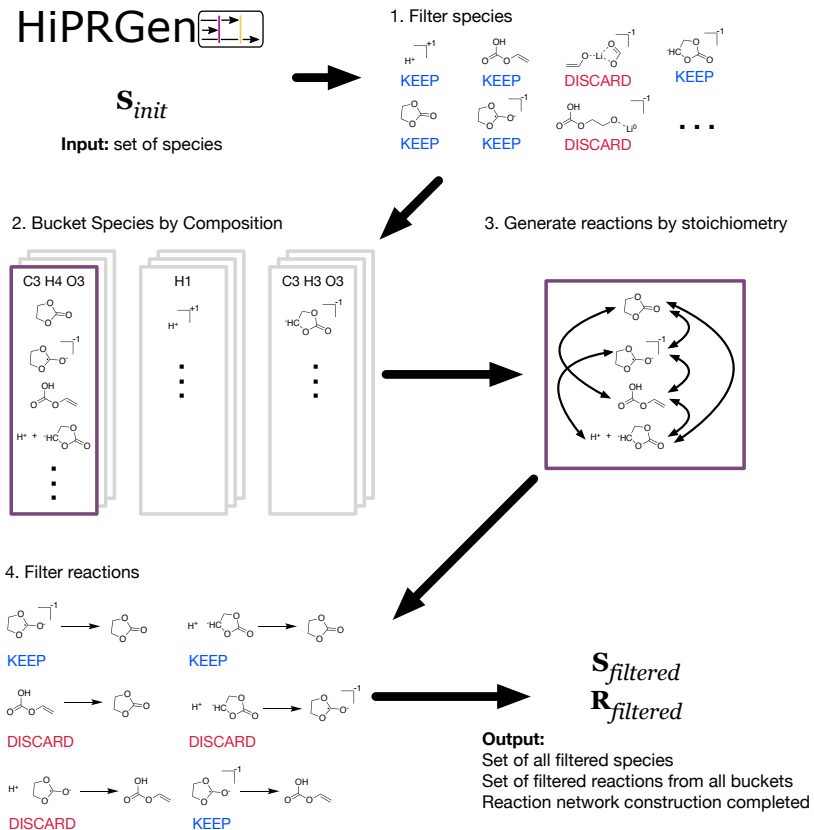


Figure 4.6: A schematic overview of the High-Performance Reaction Generation (HiPRGen) method. A set of species S_{init} is provided as input. This set of species could come from a high-throughput DFT campaign using the methods described earlier in this Chapter. 1. The species contained in S_{init} are filtered via user-defined criteria. Here, species including neutral or negatively charged metals (e.g. Li⁰) and species where multiple fragments are connected only by coordination bonds are removed. 2. Species are grouped and bucketed based on composition. Each bucket is populated by entries that contain either a single molecule or a pair of molecules that together have the composition of the bucket. 3. Within each bucket, all stoichiometrically valid reactions are generated. This corresponds to generating all combinations of two members of the bucket. 4. The generated, stoichiometrically valid reactions are then passed through user-defined reaction filters. Here, dissociative redox reactions (where changes in bonding occur simultaneously with reduction or oxidation) and reactions involving more than two bonds changing are removed. After aggregating the reactions generated from each bucket, the end result of the HiPRGen procedure is a set of filtered species $S_{filtered}$ and a set of filtered reactions $R_{filtered}$ constituting a reaction network.

HiPRGen begins with some large dataset of species. In principle, these species could come from any source, but in practice, our species and their properties come from the fragmentation, recombination, and high-throughput DFT methods described earlier in this Chapter. We then apply a series of filters, where each filter can remove species that are chemically unreasonable or otherwise undesirable under the conditions studied (Figure 4.6-1). A list of species filters that we have employed is described in Appendix B.2. HiPRGen has been designed such that users can easily include additional filters, which might be necessary to apply HiPRGen to diverse chemistries.

The filtered set of species $\mathbf{S}_{filtered}$ is then used to populate buckets that are each defined by a unique composition (Figure 4.6-2). Buckets are populated by members containing either one or two species where the total composition of each member matches the composition of the bucket. This means that any pair of members in a given bucket define the reactants and products of a stoichiometrically balanced chemical reaction containing one or two reactants and one or two products. In order to reduce the number of possible reactions, we do not presently allow ternary reactions. While some elementary reactions with three products are possible, we expect them to be rare, and we do not generally believe that elementary reactions with three reactants are meaningful in electrochemistry. For each bucket, all combinations of two unique members yield unique reactions (Figure 4.6-3). Note that, because we allow for electrochemical reactions, charge is not necessarily balanced in these reactions. For a system of several thousand species, there can easily be hundreds of billions or even trillions of stoichiometrically valid reactions. Reaction filters are therefore employed to remove reactions that, despite being stoichiometrically valid, are chemically implausible or otherwise undesirable (Figure 4.6-4). All reaction filters that we have implemented are also described in Appendix B.2. Finally, the reactions from each bucket that pass all filters are aggregated. The result of HiPRGen is a set of filtered species $\mathbf{S}_{filtered}$ and filtered reactions $\mathbf{R}_{filtered}$, which constitute a CRN.

HiPRGen can enumerate and filter all possible reactions between up to approximately 10,000 species, overcoming the scaling limitations of our previous approach.[212] Further, to the best of our knowledge, HiPRGen is the first method that combines an exhaustive enumeration of stoichiometrically valid reactions with a range of chemically-motivated filters that leverage pre-computed molecular properties. HiPRGen has the benefit that the filtering infrastructure was designed to be easily modified and extended by future users, making it facile to apply HiPRGen to new chemical domains.

It is worth briefly comparing HiPRGen to template-based methods of reaction enumeration. HiPRGen is inherently inefficient compared to template-based CRN generation. Many of the reactions generated by HiPRGen may not occur in a single step, may not be kinetically accessible (due to excessively high energy barriers), or may not ever occur in the chemical system of interest because they require a reactant that will never form. While we are continuing to improve HiPRGen's filters in order to better avoid non-elementary or inaccessible reactions, in the absence of a general method to robustly identify plausible species and reactions in electrochemistry and other complex domains, this inefficiency cannot presently be avoided. Templates can also produce unreasonable reactions, and it can be difficult even for

experts to identify such exceptions to chemical rules.[290] Nonetheless, this problem is likely more severe for filter-based than template-based reactions. Where HiPRGen excels is in the inclusion of exceptional reactions that do not follow normal trends or patterns. Moreover, HiPRGen’s method of bucketing ensures that no duplicate reactions will ever be added to a CRN (a particular reactant-product pair is only considered once), while in a naive template-based approach, duplicate reactions could easily be produced if multiple templates convert a set of reactants to the same products.

From the CRN generated by HiPRGen, it becomes possible to search for diverse products and reaction pathways to those products. However, even after filtering the set of stoichiometrically valid reactions, the number of remaining reactions can be so vast that a highly scalable method of network analysis is required.

Stochastic Network Analysis

While it might be desirable to use shortest-path algorithms to identify reaction pathways in graph-based CRNs, as we did previously,[211, 212] such algorithms become computationally intractable as network size increases. We therefore turn to the kMC algorithm of Gillespie,[188] which, with appropriate modifications,[291] can scale sublinearly with number of reactions. In a kMC simulation, a system evolves from some user-defined initial state in a manner that is non-deterministic but consistent with the rate coefficients provided to the model.

When templates are viable and accurately describe the reactivity in a system, they can be used to approximate reaction kinetics with minimal cost.[280, 283] In a template-free network of potentially millions of reactions, it is presently impossible to include accurate rate coefficients for all reactions. For the purposes of stochastic network exploration and analysis, we therefore assign rate coefficients by fiat. All unimolecular reactions are given the same rate coefficient k_0 ; to ensure appropriate units, all bimolecular reactions have the rate coefficient k_0/V , where V is a spatial term related to the (in this case fictitious) system volume.[188, 190]

A critical note: Most commonly, the Gillespie algorithm and kMC are used to study the time evolution of a reacting system. In such a case, the use of fiat rate coefficients would be inappropriate, as it likely would not lead to even qualitatively accurate dynamics. However, in this work we are not interested in reactive time evolution. Rather, we use the Gillespie method in a somewhat unorthodox manner to obtain insights into reactivity that, while dynamic in nature, do not necessarily reflect *chemical dynamics*. Rather, our analysis focuses mainly on which reactions proceed (without concern for how quickly they proceed or when they proceed in time) and which species form (without concern for quantitatively accurate ratios of products, which would require a notion of relative rates). Given sufficient sampling, all reactions included in the network that would occur given accurate kinetics will be observed in kMC simulations with fixed rate coefficients. In sum, **because our aims do not include accurate time evolution or quantitative competition between possible products, we can employ kMC with arbitrary rate coefficients.** We further note that the

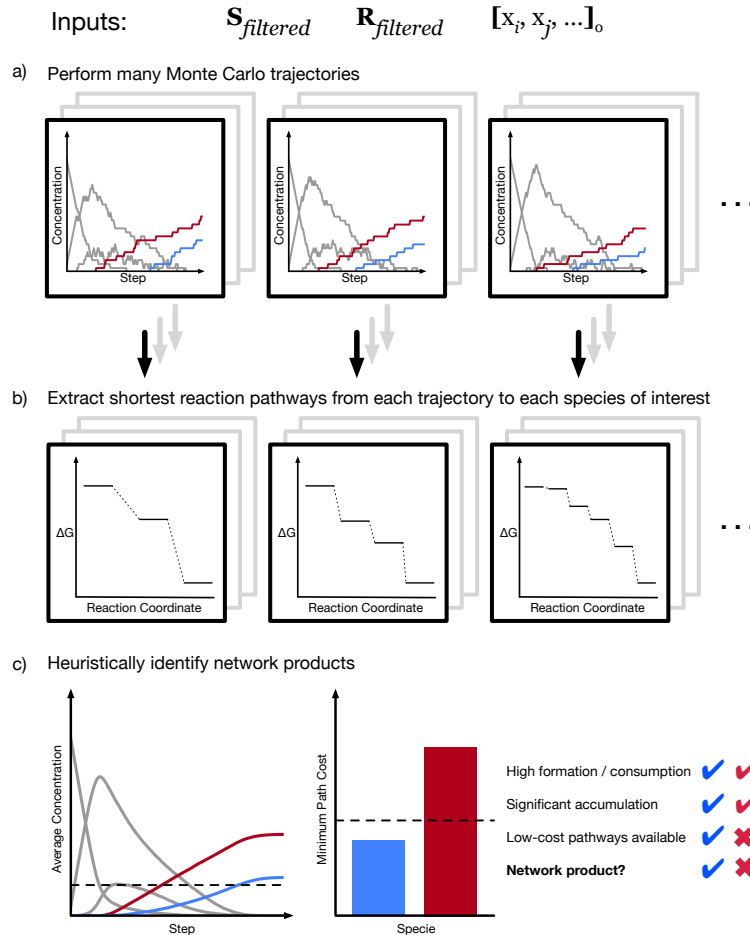


Figure 4.7: Methods for analyzing CRNs from stochastic simulations. a) A large number of kinetic Monte Carlo trajectories with fixed rates are calculated, beginning with the same network (defined by $\mathbf{S}_{\text{filtered}}$ and $\mathbf{R}_{\text{filtered}}$) and the same initial state ($[x_i, x_j, \dots]_0$, where x_q is the quantity of species q). b) In each trajectory, the shortest reaction pathway to some species of interest can be identified. Note that because these trajectories are stochastic, different trajectories will often yield different shortest pathways to the same product. c) To identify products of the network, a set of heuristics are applied. In order to be considered a product of the CRN, a species must be formed substantially more than it is consumed and must accumulate to a significant degree on average (that is, its average final concentration must be higher than some threshold). In addition, a product species must be reachable by some low-cost path. In the example provided, both the red and the blue species are formed significantly more than they are consumed, and both accumulate, but only the blue species can be reached by a low-cost pathway. Therefore, by this heuristic, the blue species is a network product, while the red species is not.

analysis of CRNs without kinetic information is not without precedent; for instance, Stocker et al.[292] have previously used reaction thermodynamics and arbitrary energy barriers to explore a CRN describing combustion.

In addition to providing arbitrary and fixed rate coefficients, we consider only reactions with $\Delta G < 0$ eV. This latter simplification is necessary to eliminate cycles or loops from the network. In reality, depending on temperature, reactions with ΔG above zero can occur. Furthermore, the inherent uncertainty in calculated reaction thermodynamics likely means that some number of reactions that we calculate to have ΔG slightly above zero (endergonic) in reality have ΔG slightly below zero instead (exergonic). However, the elimination of loops is practically necessary to enable CRN analysis. If all reactions have the same rate coefficient, then the presence of loops effectively ensures that any kMC simulation will be dominated by unimportant back-and-forth processes. This dramatically increases the noise in the simulations, making identification of important species and reactions difficult (see below). Beyond such practical and technical considerations, the elimination of endergonic reactions is reasonable on a physical basis within our main domain of interest, electrochemistry. Electrochemical reaction cascades are often dominated by ion- and radical-driven reactions.[293, 294] Such cascades should, in general, be comprised entirely or almost entirely by (often rapid) exergonic steps, meaning that the elimination of endergonic steps should not significantly affect the predictions of our simulations.

To analyze a CRN, we perform a large number of kMC simulations in parallel (Figure 4.7a). The result of each simulation is a series of reactions defining a trajectory of the system state. If a molecule of interest is known, we can use these trajectories to identify potential formation pathways to that molecule. We trace each trajectory; if the molecule of interest is formed at any point, we then identify the shortest sequence of reactions leading to its first formation (Figure 4.7b). Performing this method of stochastic pathfinding over many trajectories, we identify a range of possible pathways to the molecule of interest. We then rank the identified paths in order to identify the “best” paths among those observed, as defined by some cost function. The thermodynamic pathways obtained from network analysis can then be subjected to further analysis to identify complete mechanisms, including TS and energy barriers.

However, pathfinding is useful only if one already knows what molecule to search for. Stochastic sampling with kMC, unlike graph-based pathfinding, enables the exploration of a reactive space without a specific target. This is because, while kMC trajectories can be used to search for a specific species, they are neither produced with any species in mind, nor are they biased towards any species. As a result, a unique capability of our approach is the ability to identify products of a CRN with minimal prior knowledge. To do this, we apply a set of heuristic criteria to the collection of trajectories (Figure 4.7c). In line with the common-sense notion of a reaction product, we define a network product as any species that i) is on average formed significantly more than it is consumed; ii) accumulates significantly in the final state of an average trajectory; and iii) can be reached by low-cost reaction pathways. We note that the specific products that are identified depend on threshold values for these heuristics, which are arbitrarily selected. We further emphasize that the heuristics

just described essentially require the elimination of endergonic reactions and reactive loops, as described above. If a species is involved in one or many loops, then the back-and-forth reactions would make exact counts of formation and consumption reactions meaningless. In addition, with loops present, a kMC simulation can in principle proceed indefinitely, which makes definition of accumulation in a “final” state problematic.

Using this heuristic method, we are able to analyze the structure of the CRN itself. The average trajectory (Figure 4.7c) satisfies a rate equation of the system.[295, 296] We observe that the average trajectories of our simulations are smooth, indicating convergence to the exact expected dynamics. Because the rates used in our simulations are arbitrary, the dynamics themselves are not physically meaningful, but the trajectory smoothing ensures that we have sufficiently sampled reactive trajectories. Therefore, the identified products are well defined and invariant to changes in e.g. random seeds. The products of the network are not necessarily the metastable or stable products that would be observed experimentally, nor are they necessarily exhaustive. Nonetheless, the network products provide useful hypotheses regarding what might form in an actual reactive system. We can then interrogate these hypotheses and validate them by either theoretical or experimental means. We note that in addition to the choice of heuristic thresholds, the choice of initial state can affect the network products identified via this method.

Chapter 5

Predicting Electrolyte Decomposition Products and Their Formation Mechanisms Using CRNs¹

Here, I elaborate how the methods described in the previous chapter can be used to understand electrochemical reaction cascades. Specifically, in this Chapter, I will discuss the development of the **Lithium-Ion Battery Electrolyte** (LIBE) dataset and how this dataset enables the discovery of new, chemically plausible electrolyte decomposition mechanisms and potentially important intermediates and products in LIB SEIs.

5.1 Developing LIBE

LIBE includes non-polymeric and non-oligomeric molecules relevant to SEI formation in LIBs, with molecular properties such as optimized geometries, molecular thermochemistry, and vibrational spectra calculated using DFT. These molecules, which include both species previously reported in the literature as well as many novel species, could form at the SEI as a result of electrolyte decomposition or the recombination of electrolyte fragments. The main purpose of LIBE is for studies of SEI formation and reactivity.

Far from being a single-use dataset of relevance only to SEI researchers, LIBE has the possibility of being used for broader studies of chemical reactions. For instance, the diverse molecules included in LIBE, including highly reactive and unstable species, provide an excellent dataset for ML models. We have recently used a subset of LIBE, which we called the “Bond Dissociation of Neutral and Charged Molecules” (BDNCM) dataset, to train a

¹This chapter is adapted from the following references: [253]: Spotte-Smith*, E.W.C.; Blau*, S.M.; Xie, X.; Patel, H.D.; Wen, M.; Wood, B; Dwaraknath, S.; Persson, K.A. Quantum chemical calculations of lithium-ion battery electrolyte and interphase species. *Scientific Data* **2021**, *8*(203); [254]: Barter*, D.; Spotte-Smith*, E.W.C.; Redkar, N.S.; Khanwale, A.; Dwaraknath, S; Persson, K.A.; Blau, S.M. Predictive stochastic analysis of massive filter-based electrochemical reaction networks. *Digital Discovery* **2023**, *2*, 123–137.

graph neural network called BonDNet.[271] BonDNet was able to predict heterolytic and homolytic bond dissociation energies with mean absolute error (MAE) far below chemical accuracy (0.022 eV vs. chemical accuracy of 0.043 eV).

Calculation parameters

All calculations discussed in this Chapter were performed using version 5.2.2 of the Q-Chem electronic structure code.[265] A large quadrature grid (SG-3) was used for all calculations,[297] and the cutoff for the neglect of two-electron integrals is set to the tightest possible value (10^{-14}). Molecular symmetry was not used to improve calculation efficiency. Unless otherwise noted, with this exception, all Q-Chem default values (as of the 5.2.2 version) were used for initial calculations, though during error-correction these default values might be changed.

This dataset employs a level of theory based on the ω B97X-V density functional,[298] which leverages the VV10 nonlocal van der Waals density functional[299] to accurately model noncovalent interactions. The def2-TZVPPD basis set [300, 301] is employed, and solvation effects were included implicitly by means of the SMD method,[302] which adds short-range energy contributions to the polarizable continuum model (PCM).[303, 304] The dielectric constant used ($\epsilon = 18.5$) is that of a 3:7 EC:EMC mixture (a commonly used solvent blend for LIB electrolytes). All other solvent parameters (see Table 5.1) are for pure EC.[305, 306]

Parameter	Meaning	Value
ϵ	Dielectric constant	18.5
n	Refractive index	1.415
$\sum \alpha_2^H$	Abraham's hydrogen-bond acidity	0.0
$\sum \beta_2^H$	Abraham's hydrogen-bond basicity	0.735
γ	Relative surface tension	20.2
ϕ	Carbon aromaticity	0.0
ψ	Electronegative halogenicity	0.0

Table 5.1: Solvent parameters for use in the SMD implicit solvent model. The dielectric constant ϵ represents a 3:7 weight blend of EC and EMC; all other parameters are for pure EC.

For all unique structures generated by fragmentation and recombination, FFOpt calculations were conducted at the -1 , 0 , and $+1$ charge states. As discussed in Chapter 4, singlet or doublet states were generally assumed, depending on whether the number of electrons in the molecule was even or odd. To balance computational cost and dataset diversity, only successfully optimized singlet molecules with less than 50 electrons were re-calculated as triplets. We note that this choice of cutoff is arbitrary, and there may be larger triplet

species that are important to electrolyte or SEI formation reactions. Expanding the number of triplet species considered will be a future effort.

Selection of principal molecules

The set of principal molecules was designed to adequately cover initial electrolyte molecules, experimentally identified SEI components, and other plausible intermediates or products that could arise during SEI formation in common LIB electrolytes. While many electrolyte chemistries have been developed for use in LIBs, the most widely used formulations involve a fluorinated salt such as LiPF₆,[96, 215, 247, 250, 307] lithium bis(trifluoromethanesulfonyl)imide (LiTFSI),[32, 259] or lithium bis(flurosulfonyl)imide (LiFSI)[308, 309] dissolved in a solvent blend of cyclic carbonates such as EC,[215, 305] or fluroethylene carbonate (FEC)[136, 310–312] and linear carbonates like DMC,[23, 313] DEC,[230, 231] or EMC.[215, 305] At the current stage, LIBE contains molecules relevant to the electrolyte systems mentioned above (LiPF₆, LiTFSI, LiFSI, EC, FEC, DMC, DEC, EMC).

The general strategy for selecting principal molecules was as follows: a set of electrolyte molecules and non-polymeric SEI products related to those electrolytes were selected from the literature. In some cases (especially for products derived from EC), these molecules were then modified in two ways: hydrogen atoms and lithium atoms bonded to oxygen could be substituted for one another, and hydrogen atoms bonded to carbon could be replaced by fluorine. The former substitution was guided by proposed reaction pathways in which hydrogen fluoride can attack Li-O bonds to produce -OH groups and LiF; the latter modification was chosen because of the inclusion of FEC, which can participate in many similar reaction pathways as EC. No conformer searching was conducted on principal molecules; initial structures that minimized steric hindrance were posed by hand and optimized. During initial geometry optimization, there were some cases in which multiple conformers with different Li coordination environments were identified. In such cases, all identified conformers were accepted as distinct principal molecules.

Representations of all principal molecules are provided in Appendix D. These can be grouped into solvent molecules (Molecule numbers 1-13), salt molecules (14-16), inorganic SEI products (17-26), possible dissolved minority species, including gases (27-35), lithium ethylene dicarbonate (LEDC) and related derivatives (36-39), lithium butylene dicarbonate (LBDC) and related derivatives (40-47), lithium ethylene monocarbonate (LEMC) and related derivatives (48-60), ethanol and related derivatives (61-62), ethylene glycol (EG) and related derivatives (63-70), 1,4-butanediol and related derivatives (71-73), other molecules related to LiEC decomposition (74-77), and other molecules related to PF₆⁻ decomposition (78-87).

Fragmentation and Recombination

Appendix D also includes the number of fragmentation steps allowed for each principal molecule. In most cases, the number of steps was chosen such that all possible bonds were broken, indicated with “MAX”. For larger molecules (with 20 or more atoms), computing the properties of all possible sub-fragments would be too computationally costly, hence a smaller number of steps was used.

After all fragment species had been analyzed using DFT, a subset were selected for recombination. Specifically, all fragments from a two-step fragmentation of LiEC (principal molecule 1 in Appendix D) that could be formed exergonically from LiEC were included, as well as all fragments of H₂O.

Data Analysis

Molecular enthalpies, entropies, and free energies at 298.15 K were calculated in multiple ways. The raw electronic energies, enthalpies, and entropies calculated in Q-Chem were used and are provided in the given units (Ha for electronic energy, kcal · mol⁻¹ for enthalpy, and cal · mol⁻¹ · K⁻¹ for entropy), as well as in eV (or eV · K⁻¹ for entropy). In addition, two different methods to correct for errors in the rigid-rotor harmonic oscillator (RRHO) approximation (used in Q-Chem) are employed: that of Ribiero et al.,[314] in which low-frequency vibrational modes are shifted to some higher frequency (100 cm⁻¹) and that of Grimme,[315] in which low-frequency modes are treated not as vibrations but as rotations. In all cases, imaginary frequencies are ignored for the purposes of calculating enthalpy, entropy, and free energy.

The point groups of all molecules were identified using the `PointGroupAnalyzer` tool implemented in `pymatgen`.[316]

5.2 Description of the LIBE dataset

Data Format

Table 5.2 describes the keys in each entry of LIBE file. Note that in some cases, keys may have no associated value; for instance, a single atom has no bonds.

Validation

Justifying Level of Theory

In order to maximize the utility of the LIBE dataset, a relatively costly but accurate level of theory was chosen. In an extensive benchmark study of density functionals by Mardirossian and Head-Gordon,[135] ω B97X-V was found to be the most suitable hybrid generalized gradient approximation (hybrid GGA) functional, with exceptional accuracy for bonded

Key	Description
molecule.id	Unique identifier (format: libe-XXXXXX, where XXXXXX is a 6-digit number)
bonds	List of pairs (a, b), where a and b are the 0-based indices of bonded atoms
charge	Charge of the molecule
chemical_system	Collection of elements present (ex: “C-H” for a molecule with C and H present)
composition	Keys are elements; values are the number of atoms of those elements present
elements	List of elements present
formula_alphabetical	Simple chemical formula, with elements in alphabetical order (ex: “C4 H8 O1”)
molecule	Serialized <code>pymatgen Molecule</code> object
molecule_graph	Serialized <code>pymatgen MoleculeGraph</code> object; molecule with graph representation
number_atoms	Number of atoms in the molecule
number_elements	Number of unique elements present in the molecule
partial_charges	Atomic partial charges based on the Mulliken, RESP, and Critic2 methods
partial_spins	Atomic partial spins, calculated with Mulliken population analysis
point_group	Molecular point group in Schönflies notation
species	Elements present at each atom in the molecule, in order
spin_multiplicity	Spin multiplicity ($2S + 1$) of the molecule
thermo	Molecular thermodynamics
vibration	Calculated vibrational spectra and normal modes
xyz	3D coordinates of the atoms in the molecule, in same order as “species”

Table 5.2: Description of keys present in LIBE dataset entries.

interactions and noncovalent interactions. It is worth noting that ω B97X-V also displays high accuracy for calculation of barrier heights; while no transition states are included in LIBE, this is still beneficial, as it implies that the kinetic properties of reactions between molecules within the dataset could be reliably calculated without modification to the level of theory. While, to the best of our knowledge, no benchmark study has systematically examined how ω B97X-V performs for calculations involving charged, radical, and metal-coordinated species in solution, ω B97X-V has been shown to exhibit exceptional performance for calculations involving transition metal complexes[317] and metal-organic reactions[318] in gas phase. Additionally, a previous *ab initio* molecular dynamics study[319] found that ω B97X-V was able to model aqueous solutions of NaCl more accurately than most density functionals, producing results in qualitative agreement with experiment. The benchmark study by Mardirossian and Head-Gordon found using a limited set of density functions that the def2-TZVPPD basis set performed nearly as well as the much larger def2-QZVPPD basis set,[135] which makes it especially useful for high-throughput studies involving many thousands of calculations.

Generally, it should be expected that the use of an implicit solvation model should improve the accuracy of calculations involving molecules in solvent. Specifically, the SMx family of models, including the SMD model shown here, have been shown to accurately predict solvation free energies[302, 320, 321] as well as redox potentials,[322] improving upon the more simple PCM models due to their inclusion of non-electrostatic effects.

We also justify our choice of level of theory by noting that similar levels of theory have previously been used to generate datasets used to study reactivity. In particular, Grambow et al.[323] recently used the ω B97X-D3 density functional[324] (which is closely related to ω B97X-V and differs primarily in the choice of dispersion correction) and the def2-TZVP basis set (which is part of the same family as def2-TZVPPD but contains no diffuse functions and fewer polarization functions) to create a dataset of over 12,000 organic reactions (including optimized reactants, products, and transition states) in vacuum. The solution-phase charged and radical organometallic chemistry involved in SEI formation is more complex than the gas-phase organic reactions considered by Grambow et al., necessitating both the inclusion of an implicit solvent model and the use of a larger basis set including diffuse functions.

Data Filtering

We note that the error correction procedures that we have employed are successful in decreasing the likelihood of failure in FFOpt calculations. Without intervention, roughly 25% of all calculations fail due to an error (for instance, inability to achieve a converged SCF solution or an inability to optimize a molecular geometry in the allowed number of steps), encounter a significant imaginary frequency (with magnitude $> 15 \text{ cm}^{-1}$), or optimize to a structure with multiple disconnected fragments. With our error-handling procedures employed, this failure rate drops below 5% on average. In cases where error correction procedures were unable to eliminate issues, the calculations were not included in LIBE. While, in principle, single-point and Critic2 calculations could also be a source of failure, in practice such calculations almost never failed when applied to optimized molecular structures.

Of the successful calculations that produced PES minima with connected structures, additional filters were put in place to ensure data quality and prevent duplicate molecules from being included in LIBE. First, molecules were eliminated if the energy of the molecule at the end of the geometry optimization differed from the energy calculated from the subsequent single-point calculation by more than 0.001 Hartree. Such a disagreement in energy suggests that the single-point calculation converged to a different minimum of the electron density than was found at the end of the geometry optimization, potentially leading to inaccurate or inconsistent determination of bonding or atomic partial charges. Additionally, duplicate molecules were removed from the dataset. If two or more sets of calculations produced molecules that were non-equivalent (had different 3D coordinates) but with identical bonding, charge, and spin multiplicity, then only the molecule with the lowest calculated electronic energy was included in LIBE. Note that, while we did not explicitly perform any conformer searches, this filter implicitly selects the lowest-energy conformer that had been calculated.

Dataset Diversity

The LIBE dataset is designed for the study of (electro)chemical reactivity in LIB. As such, the most important consideration is whether the dataset adequately captures the possible

molecules that could form in a LIB as a result of electrolyte decomposition. Considering that many common electrolyte molecules and most reported non-oligomeric/non-polymeric products derived from those molecules are among the principal molecules used to generate LIBE, we believe this is the case.

For uses outside of this domain, it is worth examining the chemical diversity of the LIBE dataset. While the dataset skews towards small molecules by design (both because most molecules examined are fragments of larger molecules and because large molecules would be computationally expensive), Figure 5.1a shows that the distribution of molecules by size (measured by number of electrons) is wide; similar distributions are found when the size is measured by number of atoms and number of bonds.

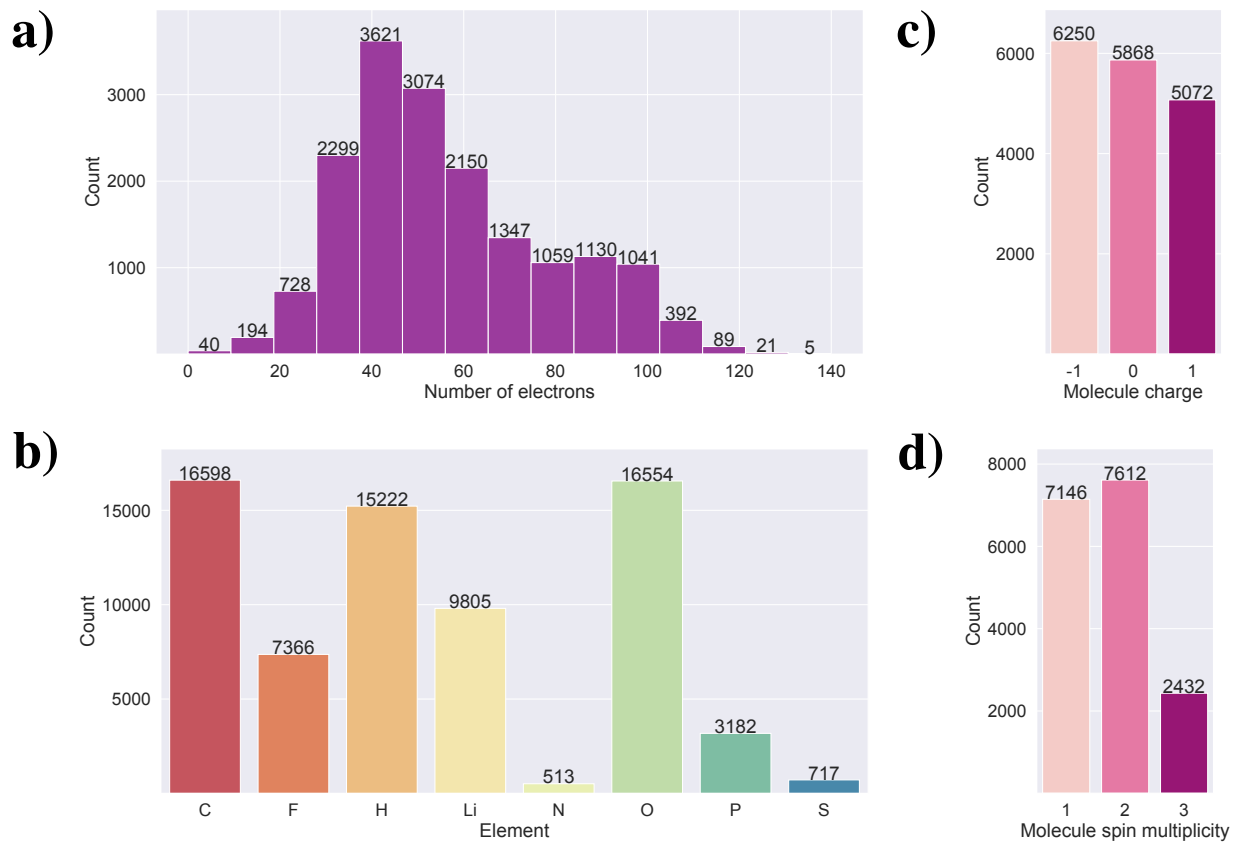


Figure 5.1: An analysis of the composition of the LIBE dataset in terms of: number of molecules with different numbers of electrons (a); number of molecules with various elemental species (b); number of molecules with charges -1 , 0 , and 1 (c); and number of molecules with spin multiplicity 1 , 2 , and 3 (d).

Because most principal molecules are organic in nature and more specifically are derived from lithiated organic carbonates, the dataset is biased towards the C-H-O-Li chemical system, though with many (7,366) fluorine-containing molecules present as well (see Figure 5.1b). While many phosphorus-containing molecules (3,182) are included, the bonding motifs (see Table 5.3) observed for phosphorus are limited (only F-P, O-P, and a small number of C-P, H-P, and Li-P bonds are present) because these molecules are all derived from PF₆ and related molecules. We further note that the diversity in nitrogen- and sulfur-containing species is lacking because they are present only from TFSI- and FSI-based fragments.

Bond Type	Number of Bonds
C-C	25,744
C-F	6,002
C-H	53,178
C-Li	2,626
C-N	129
C-O	55,186
C-P	256
C-S	636
F-F	10
F-H	74
F-Li	1,285
F-O	150
F-P	4,604
F-S	195
H-H	4
H-Li	9
H-O	4,266
H-P	21
Li-Li	1
Li-N	53
Li-O	18,821
Li-P	19
Li-S	89
N-O	28
N-S	867
O-O	346
O-P	4,925
O-S	1,387
S-S	34

Table 5.3: Number of different types of bonds present in the LIBE dataset.

While there are similar numbers of neutral molecules (5,868) and molecules with charge -1 (6,250), there are somewhat fewer molecules with charge $+1$ (5,072) (Figure 5.1c). Because calculations were attempted for all initial molecule structures at charges -1 , 0 , and $+1$, this implies that the cationic species were more likely to fail than the anions or neutral

species. There are slightly more doublet species (7,612) than singlets (7,146) (Figure 5.1d). As discussed above, the number of triplets was intentionally kept low to reduce computational cost. We note that of the 1,961 pairs where singlet and triplet calculations optimized to isomorphic structures, the triplet was lower in electronic energy in 11.98% (235) of cases. Further, there are 471 triplet molecules for which no isomorphic singlet with the same charge exists. Thus, it is possible that some number of unique structures, and some stable ground-states for existing structures, may be missing from LIBE. Because most often, the singlet structure is more stable than the triplet structure in the ground state, this lack of triplets should not be a significant detriment to the quality of the data.

5.3 Automatic Identification of Battery SEI Network Products

Using HiPRGen, we constructed a reaction network that seeks to describe SEI formation in lithium-ion batteries. An initial set of species were taken from the LIBE dataset; specifically, network construction began with a subset of LIBE containing all species comprised of only carbon, hydrogen, oxygen, and/or lithium. This subset, which we call LIBE-CHOLi, contains 8,904 species. Importantly, no knowledge of SEI formation mechanisms was used to generate LIBE, though some known SEI products are included in the dataset.

Network construction with HiPRGen resulted in a CRN containing 5,193 filtered species and 86,001,275 filtered reactions. With this network, we conducted 100,000 stochastic trajectories under four conditions, with combinations of two different applied potentials (+0.0V vs. Li/Li⁺ and +0.5V vs. Li/Li⁺) and two different initial states (one consisting only of Li⁺ and EC and the other consisting of Li⁺, EC, and CO₂). Average trajectories for each condition are shown in Appendix E.1. We emphasize that our goal is not to compute and observe the dynamics of SEI formation, but rather to identify key species and reaction pathways. We further note that we do not consider the effect of the electrode surface in our simulations. However, since the SEI can grow to a thickness of ~ 10 – 100nm, the effect of the electrode on the SEI chemistry should be small after the first reactions occur. Moreover, the products of the SEI are in general insensitive to the identity of the anode, as we discuss in Appendix F.

The utility of our approach is demonstrated through analysis of the 36 network products collected from the set of four conditions previously described (Figure 5.2). We first note that our automated procedure recovers 16 species that include a majority of the experimentally observed products of SEI formation (Fig. 5.2 solid dark green). These include gases (H₂, C₂H₄, CO),[232] inorganic species (lithium carbonate (Li₂CO₃) and lithium oxalate (Li₂C₂O₄)),[29, 39] and alkyl carbonates (including species closely related to LEDC[29, 39, 75] and LEMC,[29, 116] as well as lithium methyl carbonate or LMC, LBDC,[29] and lithium vinyl carbonate or LVC).[325] We emphasize that these species are recovered even though reaction kinetics are entirely ignored in network exploration.

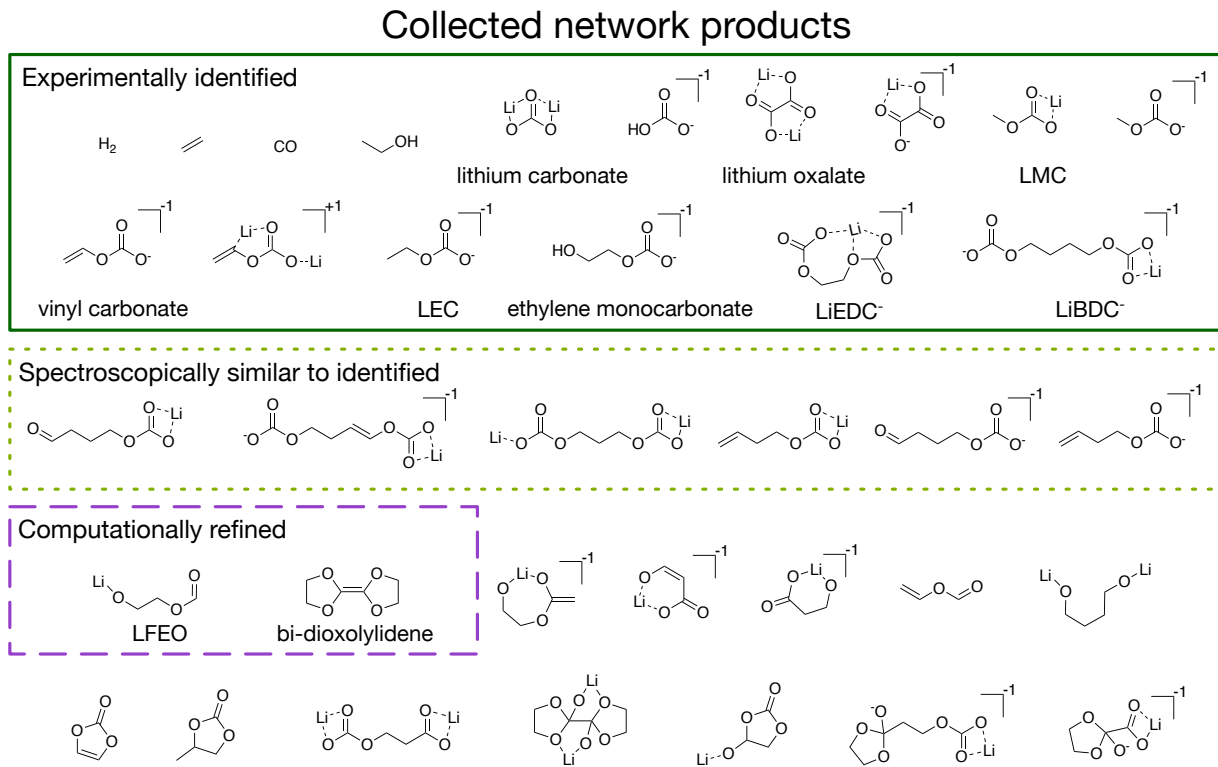


Figure 5.2: The 36 total collected network products from four different initial conditions (+0.0V vs. Li/Li^+ with Li^+ and EC as starting species; +0.0V vs. Li/Li^+ with Li^+ , EC, and CO_2 as starting species; +0.5V vs. Li/Li^+ with Li^+ and EC as starting species; and +0.5V vs. Li/Li^+ with Li^+ , EC, and CO_2 as starting species). The 16 network products outlined in green have previously been experimentally identified in the SEI; these include the major gaseous products, molecular inorganic components, and organic components (including lithium methyl carbonate or LMC, vinyl carbonate, lithium ethyl carbonate or LEC, ethylene monocarbonate, lithium ethylene dicarbonate or LiEDC $^-$, and lithium butylene dicarbonate or LiBDC $^-$). Six of the network products, outlined in dotted light green, are species which have very similar spectroscopic signatures to the dominant organic components, and thus may be present in the SEI in small quantities without being detected. Two of the network products outlined in dashed purple, lithium 2-(formyloxy)ethan-1-olate or LFEO and 4,4',5,5'-tetrahydro-2,2'-bi(1,3-dioxolylidene) or bi-dioxolylidene, have not been previously reported and were subjected to further mechanistic analysis. Finally, the remaining 12 network products (which have also not been previously reported as SEI products) may be kinetically inaccessible, may indicate that our CRN is missing species or reactions, or may be true SEI products, motivating future study.

In addition to these well-known species, there are also a number of novel products that have not previously been proposed to participate in SEI formation. Among these are six additional alkyl carbonates (Fig. 5.2 dotted light green) which are each very similar to known products in molecular size, composition, bonding, and contained functional groups. Due to the extreme difficulty of experimentally characterizing the SEI and the resulting limited ability to resolve small signal to noise,[326] the likely spectroscopic similarity[327] of these species to the known products means that they may be present in the SEI in small quantities but that they could not easily be positively identified.

Other network products include species with ester, carboxylate, and oxide functional groups, such as lithium 2-(formyloxy)ethan-1-olate, which we abbreviate as LFEO, as well as a number of cyclic species, such as 4,4',5,5'-tetrahydro-2,2'-bi(1,3-dioxolylidene), which we abbreviate as bi-dioxolylidene. LFEO and bi-dioxolylidene (Fig. 5.2 dashed purple) were particularly unexpected given how distinct they are from other predicted SEI products and, in particular, the experimentally identified products. Evaluating whether or not these products will actually form in the SEI necessitates considering energy barriers, kinetics, and reactive competition. Using the shortest paths from stochastic network analysis to guide automated transition-state calculations, we identified elementary formation mechanisms to both LFEO and bi-dioxolylidene to evaluate their potential to participate in SEI formation (see 5.4).

On the other hand, there are some network products which do not reflect the corresponding chemical system in a real battery. Specifically, both vinylene carbonate (VC) and propylene carbonate (PC) are known to rapidly decompose when included in battery electrolytes.[328, 329] This contradiction indicates that there are reactions or species that are necessary to facilitate the decomposition of VC and PC must be missing from the network. The identification of this gap through the use of CRN analysis and network product prediction provides a tractable path forward to expand the CRN via selective addition of missing molecules that enable redox, decomposition, or recombination of network products with other abundant intermediate or product species.

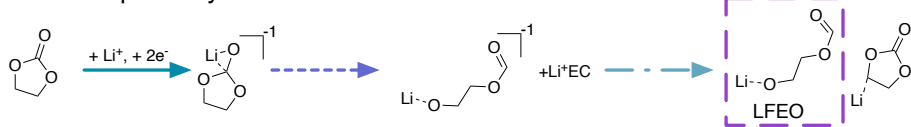
5.4 CRN-Derived Elementary Mechanisms to Form Unexpected Network Products

The reaction pathways produced by our stochastic approach involve no knowledge of reaction kinetics. In actuality, the dominant reaction pathways are heavily dependent on reaction energy barriers ΔG^\ddagger and rate coefficients. In order for our approach of using kMC with arbitrary rate coefficients to provide useful chemical insights, it is critical that the predicted reaction pathways can be reasonably translated into elementary reaction mechanisms including TS and energy barriers.

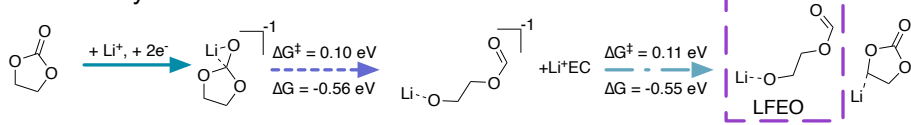
Using our stochastic approach, we can identify the N lowest-cost reaction pathways to the network products, ranked by a cost function that we have employed previously[211] (see B.2).

a) lithium 2-(formyloxy)ethan-1-olate (LFEO)

Network pathway:

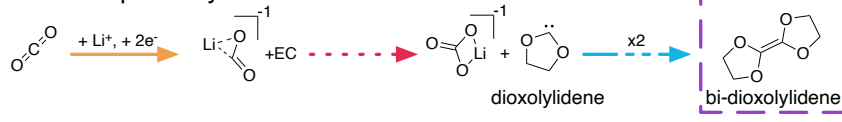


Elementary mechanism:



b) 4,4',5,5'-tetrahydro-2,2'-bi(1,3-dioxolylidene) (bi-dioxolylidene)

Network pathway:



Elementary mechanism:

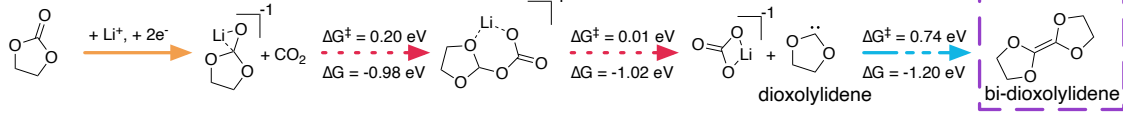


Figure 5.3: Comparison of network-identified reaction pathways and elementary mechanisms obtained from kinetic refinement to form (a) lithium 2-(formyloxy)ethan-1-olate (LFEO) and (b) 4,4',5,5'-tetrahydro-2,2'-bi(1,3-dioxolylidene) (bi-dioxolylidene). For elementary steps involving a transition-state, energy barriers (ΔG^\ddagger) and reaction free energies (ΔG) are provided. Corresponding reaction steps between the network-identified pathways and elementary mechanisms are indicated via line color and style. Coordination and reduction steps are combined for brevity; in reality, these occur as separate steps in both network-identified pathways and elementary mechanisms.

We selected two unexpected network products — LFEO and bi-dioxolylidene — and subjected their shortest pathways in order of cost to an automated procedure to identify the TS for each step along each pathway, allowing for the construction of complete reaction mechanisms. Figure 5.3 highlights two formation paths obtained using this procedure, emphasizing the utility of network-generated reaction pathways to construct elementary mechanisms.

The network pathway shown in Figure 5.3a has the 12th lowest cost with only Li^+ and EC as starting species (no CO_2) at +0.0V vs. Li/Li^+ . In this pathway, Li^+ coordinates with EC, and the Li^+EC reduces twice. The doubly reduced $\text{Li}^+\text{EC}^{-2}$ then ring-opens at the shoulder bond, after which this shoulder-ring-opened species can abstract a proton from an additional Li^+EC , forming LFEO with a $\text{Li}^+\text{EC-H}^-$ as a byproduct. The identified elementary mechanism follows this path exactly, with two TS — one for the ring-opening of $\text{Li}^+\text{EC}^{-2}$ with a barrier $\Delta G^\ddagger = 0.10 \text{ eV}$ and one for proton abstraction from EC to form LFEO with $\Delta G^\ddagger = 0.11 \text{ eV}$.

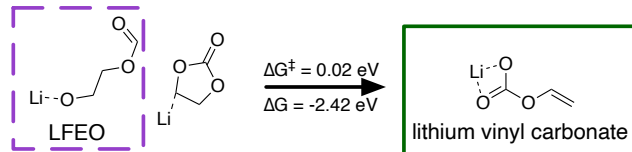
A path to form bi-dioxolylidene is shown in Figure 5.3b. This network pathway has the 3rd lowest cost for simulations with CO_2 was present as a starting species at 0.0V vs. Li/Li^+ . In the pathway, CO_2 reduces twice and coordinates with Li^+ , forming $\text{Li}^+\text{CO}_2^{-2}$. This $\text{Li}^+\text{CO}_2^{-2}$ species reacts with EC to form $\text{Li}^+\text{CO}_3^{-2}$ and the 1,3-dioxolylidene carbene, which we abbreviate as dioxolylidene. Two of these carbenes can then combine to form the dimer bi-dioxolylidene. The identified elementary mechanism follows the same general steps as the network pathway — coordinate and reduce, form dioxolylidene, and then dimerize two carbenes — but differs in two main ways. First, it is more favorable to reduce EC than CO_2 , which changes the initial steps of the mechanism. Second, we found that the carbene formation actually occurs via an addition-elimination mechanism with two elementary steps. The addition, which results in an EC-CO_2 adduct, has a barrier $\Delta G^\ddagger = 0.20 \text{ eV}$, and the elimination to produce $\text{Li}^+\text{CO}_3^{-2}$ and dioxolylidene has a barrier $\Delta G^\ddagger = 0.01 \text{ eV}$.

The identified elementary mechanisms to LFEO and bi-dioxolylidene involve steps that are predicted to be competitive with other known SEI formation processes. Both mechanisms rely on $\text{Li}^+\text{EC}^{-2}$, which can form easily at low potentials.[251, 330] After breaking the shoulder bond, the ring-opened $\text{Li}^+\text{EC}^{-2}$ is known to decompose unimolecularly to $\text{Li}^+\text{OCH}_2\text{CH}_2\text{O}^{-2}$ and CO with a predicted energy barrier between 0.09 eV[330] and 0.22 eV[251] depending on the level of theory used. Considering that the necessary precursor to LFEO formation, Li^+EC , should be present in abundance during early SEI formation, this implies that LFEO could actually be a significant product during early SEI formation at low potentials.

The formation of bi-dioxolylidene is predicted to be less kinetically favorable than that of LFEO. The dimerization reaction has an energy barrier that is considerably higher than many major SEI formation pathways,[169, 235, 251, 330, 331] implying that bi-dioxolylidene should not be a significant product. The formation of the carbene monomer, on the other hand, is plausible. Using the Eyring equation,[332] the addition of CO_2 to $\text{Li}^+\text{EC}^{-2}$ with a 0.20 eV barrier has a predicted rate coefficient roughly 70 times lower than that of the shoulder ring-opening of $\text{Li}^+\text{EC}^{-2}$ with a 0.09 eV barrier. However, dioxolylidene formation could be significant if CO_2 is abundant, a plausible scenario considering that CO_2 can form

at either the anode[119] or the cathode[29] in LIBs. On this basis, we predict that while LFEO, $\text{Li}^+\text{OCH}_2\text{CH}_2\text{O}^{-2}$, and CO will be favored, dioxolylidene should at least form as a short-lived minority intermediate.

a) Byproducts of LFEO formation



b) Carbene catalysis

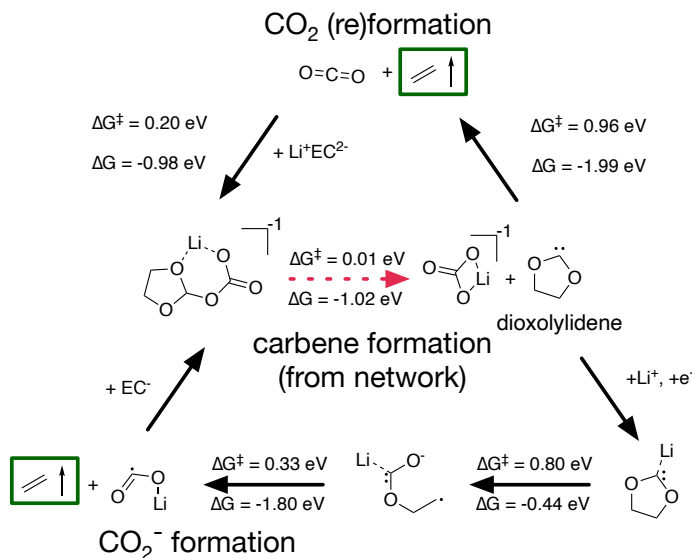


Figure 5.4: Extended mechanisms based off of network-identified pathways: a) formation of LVC, a known SEI product, via the ring-opening of the deprotonated $\text{Li}^+\text{EC}-\text{H}^{-1}$, a byproduct of LFEO formation; b) two possible catalytic cycles yielding ethylene gas and reforming dioxolylidene via the production of either CO_2 or $\text{Li}^+\text{CO}_2^{-1}$. For elementary steps involving a transition-state, energy barriers (ΔG^\ddagger) and reaction free energies (ΔG) are provided. Green boxes indicate species that have been experimentally identified as products or byproducts of SEI formation.

5.5 CRN Pathways and Products Guide Investigation of Expanded Mechanisms

Leveraging CRN analysis, we have predicted network products and reaction paths that could be important to a complex electrochemical system but which have not been seriously studied in the literature before. We can now expand on these paths, using the calculated elementary formation mechanisms of LFEO and bi-dioxolylidene as starting points for studying how species along these paths may further react. In doing so, we demonstrate the utility of CRN-generated pathways as a tool for hypothesis generation to guide follow-up investigation (see Figure 5.4).

In the mechanism for LFEO formation identified in Figure 5.3a, a byproduct is the deprotonated EC species $\text{Li}^+\text{EC}-\text{H}^{-1}$. We suspected that this byproduct would be highly reactive and would likely decompose. Indeed, we found (Figure 5.4a) that $\text{Li}^+\text{EC}-\text{H}^{-1}$ can open at the waist bond with an extremely low barrier ($\Delta G^\ddagger = 0.02 \text{ eV}$), forming LVC. We note that LVC has previously been identified as an SEI product,[325] though its formation mechanism has not been thoroughly studied. Therefore, not only is the formation of LFEO plausible on the basis of the low reaction barriers identified, but LFEO formation can potentially help to explain the formation of another SEI product.

We also considered the reactivity of the dioxolylidene carbene (Figure 5.4b). In addition to the dimerization shown in Figure 5.3b, we found that dioxolylidene could react in two other ways, either decomposing in a single step to form CO_2 and C_2H_4 or decomposing to $\text{Li}^+\text{CO}_2^{-1}$ and C_2H_4 via a two-step process after coordination with Li^+ and reduction. All reactions identified — dimerization and both decomposition mechanisms — involve relatively high energy barriers. Our understanding of the role of dioxolylidene in SEI formation remains incomplete, and further work must be done to elucidate its decomposition routes. However, if the barriers to dioxolylidene decomposition were lowered by e.g. a solvent effect[333] or a reactive surface,[237] the possibility exists for a catalytic loop in which dioxolylidene is repeatedly reformed via the reaction of CO_2 with $\text{Li}^+\text{EC}^{-2}$ or $\text{Li}^+\text{CO}_2^{-1}$ with EC^{-1} .

Chapter 6

A Mechanistic Model of SEI Formation and Evolution in Li-Ion Batteries¹

SEI layers in LIBs with EC-based electrolytes are made up of inorganic species — including inorganic carbonates (*e.g.* lithium carbonate (Li_2CO_3)) and lithium oxalate ($\text{Li}_2\text{C}_2\text{O}_4$) — as well as organic species like LEDC and LEMC.[29, 39, 47, 116, 215, 230] The Peled model[334] first proposed that the SEI, though highly inhomogeneous, is comprised of a primarily inorganic inner layer and a primarily organic outer layer. It has also been observed that gases (particularly H_2 , C_2H_4 , CO , and CO_2) are produced as byproducts of SEI formation.[232, 335] However, in spite of decades of careful study, a mechanistic explanation of SEI composition and structure remains elusive. A range of theoretical techniques such as DFT,[331, 336] reactive classical MD [155, 235] and AIMD[166, 337], and CRNs[211, 212] have all revealed plausible reaction pathways to key SEI components. These contributions include the results presented in Chapters 3 and 5. Yet the combination of these methods has been unable to move beyond the identification of specific mechanisms towards the true formation process which involves multi-product dynamics and competitive pathways occurring on timescales ranging from picoseconds[251] to days.[225]

Here, we describe the first mechanistic, first-principles microkinetic model of SEI formation and find that it explains fundamental, observed reactive and structural trends in the LIB SEI. Figure 6.1 shows select mechanisms to form and decompose potential SEI products LEDC, LEMC, dilithium ethylene monocarbonate (DLEMC), inorganic carbonates, and $\text{Li}_2\text{C}_2\text{O}_4$. These mechanisms were obtained from essentially the same CRN discussed in Chapter 5 (further methodological details are provided in Appendix B.3). With rate constants derived from high-throughput transition-state calculations and Marcus theory[338], we perform kinetic Monte Carlo (kMC) simulations to study SEI formation under varying

¹This chapter is adapted from reference [330]: Spotte-Smith*, E.W.C., Kam*, R.L., Barter, D., Xie, X., Hou, T., Dwaraknath, S., Blau, S.M., Persson, K.A. Toward a Mechanistic Model of Solid-Electrolyte Interphase Formation and Evolution in Lithium-Ion Batteries. *ACS Energy Letters* 7(4), 1446–1453.

chemical and electrochemical conditions. Previously, kMC simulations using empirical rates have been used to study SEI formation,[339, 340] and recently, DFT and *ab initio* MD were used to inform first-principles kMC simulations of lithium plating and stripping from copper.[341] kMC simulations are highly attractive for modeling SEI reactivity, especially when based on high-quality thermochemical and kinetic data,[169] because they can study much longer time scales than are accessible through other molecular-scale dynamical methods while retaining more mechanistic detail than other mesoscale and continuum-level models.[79, 342]

6.1 Computational Methods

We perform kMC simulations using the discrete time Gillespie algorithm[189, 343] under diverse chemical and electrochemical conditions in order to understand how competition between various reaction pathways could change over the course of SEI formation cycling (Figure 6.2). Most simulations begin with an initial state consisting of some amount of EC, Li^+ , CO_2 , and water. Because water will readily reduce during and even before SEI formation,[344, 345] we include the reduction products OH^- and H rather than H_2O . Simulations of SEI evolution after initial formation begin with Li^+ and EC as well as LEDC, LEMC, Li_2CO_3 , and $\text{Li}_2\text{C}_2\text{O}_4$. To simulate SEI formation at various points during Li^+ intercalation (for instance in graphite[346] or Si[347] negative electrodes), we vary the electron free energy G_{elec} from -2.1 eV to -1.4 eV in 0.1 eV increments, corresponding to a change in the applied potential V from +0.7V (roughly the reduction potential of Li^+/EC)[348] to +0.0V vs. Li/Li^+ (the point of lithium plating). We additionally vary the electron transport rates through application of a tunneling barrier with thickness D . Specifically, we perform simulations with $D = 0.0 \text{ \AA}$, indicating that the electrolyte is in contact with a bare negative electrode, and with $D = 10.0 \text{ \AA}$, indicating an existing SEI layer. Each individual simulation is spatially homogeneous; however, by including a varying thickness D , we effectively simulate a one-dimensional (1D) system. Note that the rates of redox reactions $A + e^- \rightleftharpoons A^-$ depend on both the applied potential V and the tunneling barrier thickness D . Previous simulations have suggested that direct tunneling from the negative electrode is likely not the dominant mechanism of charge transfer during SEI growth,[236, 349] and as a result, the variation in electron transport rate with SEI thickness D in our model is not quantitatively accurate. However, this simple method does allow for a qualitative understanding of how SEI formation varies in regimes with rapid or slow electron transport, which is a goal of this work. For each set of simulation conditions, we construct an average kMC trajectory from 30 simulations of 10,000,000 steps each. We assess reactive competition by analyzing and comparing the relative occurrences of reactive events in the average trajectories (an example average trajectory is shown in E.2). Simulations are performed at 298.15 K (25 °C) unless otherwise noted.

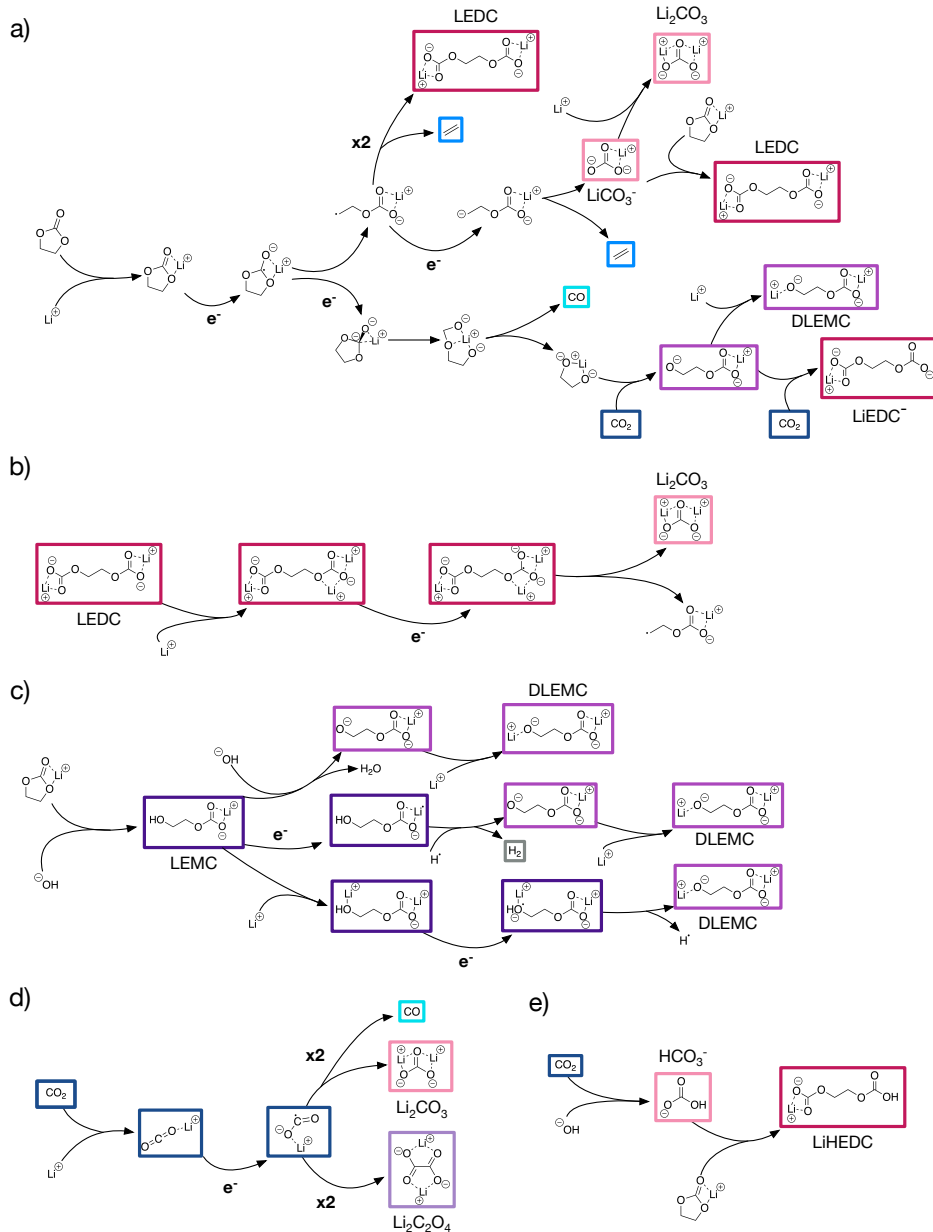


Figure 6.1: Select reaction pathways involving key SEI products, including inorganic carbonates (a, b, d, e), LEDC (a, b, e), DLEM (a, c), lithium oxalate (d), and LEMC (c). Gases CO_2 (a, d, e), C_2H_4 (a), CO (a, d), and H_2 (c) are also highlighted. A complete set of reactions included in the microkinetic simulation are listed in Appendix G.

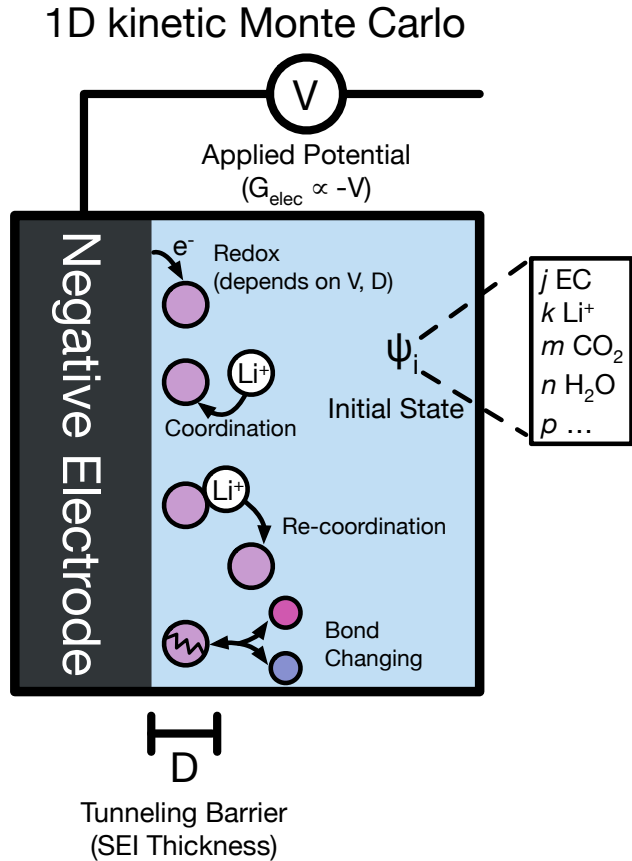


Figure 6.2: A schematic depiction of the inputs to the kMC model described here. Reactions considered in the microkinetic model include redox reactions $A + e^- \rightleftharpoons A^-$, coordination reactions $A + M \rightleftharpoons AM$ (where M is a metal, e.g. Li^+), re-coordination reactions $AM + B \rightarrow A + BM$, and bond-changing reactions e.g. $A + B \rightarrow C + D$. We vary the applied potential V , which is equivalent to varying the electron free energy G_{elec} , the electron tunneling barrier thickness D , which is associated with the SEI thickness, and the initial state ψ_i , which typically consists of EC, Li^+ , and impurity species CO_2 and H_2O .

6.2 Recovering the Peled Model

Figure 6.3 shows the average fractional quantities of SEI products (a, d) and gas molecules (b, e) as a function of applied potential and tunneling barrier thickness for a simulation beginning with 1M Li^+ in a 15M EC electrolyte with $\approx 5\text{ppt}$ CO_2 and $\approx 1\text{ppt}$ H_2O . Because the negative electrode can be rapidly covered by the SEI even at relatively high potentials, the electrolyte will likely not be in direct contact with the negative electrode at low potentials. Data for applied potentials below $+0.5\text{V}$ vs. Li/Li^+ with $D = 0.0\text{\AA}$ are nonetheless included

in Figure 6.3 a-b; however, the low-potential region is shaded to reflect that they may not be accessible under actual battery cycling conditions.

The observed electrochemical competition results in a bilayer SEI structure that is in qualitative agreement with the Peled model. When the SEI initially forms — at high potential and close to the negative electrode surface (Figure 6.3 a) — carbonates are the major product, with LEMC and LEDC as minority products. When reactions occur further from the negative electrode surface after this initial carbonate layer forms (Figure 6.3 d), LEMC and LEDC are the majority components, with inorganic carbonates as the minority components. To our knowledge, this is the first time that the varying composition of the SEI with thickness has been directly simulated from first principles. Beyond simply reproducing this structure, our microkinetic analysis is also able to suggest a mechanistic explanation for its emergence.

Competition between reductive processes controls the ratio of products. When reduction rates are moderate — at high potentials close to the negative electrode (Figure 6.3 a-b) or at low potentials far from the negative electrode (Figure 6.3 d-e) — EC reduction occurs in two stages. After Li^+EC reduces once, EC ring-opens and only then reduces again, ultimately producing an inorganic carbonate species (most directly LiCO_3^-) and C_2H_4 (Figure 6.1 a). In the regime close to the negative electrode, the LiCO_3^- prefers to coordinate with Li^+ , forming Li_2CO_3 , while in the regime far from the negative electrode, LiCO_3^- often reacts with Li^+EC to form LEDC (Figure 6.1 a). When reduction is more facile, a rapid two-electron reduction of EC (Figure 6.1 a) can occur, resulting in CO and $\text{Li}^+\text{OCH}_2\text{CH}_2\text{O}^{-2}$. This pathway is dominant at moderate potentials (beginning around +0.5V vs. Li/Li⁺) close to the negative electrode, but it can also occur to a lesser extent at extremely low potentials (+0.0V vs. Li/Li⁺) far from the negative electrode. The $\text{Li}^+\text{OCH}_2\text{CH}_2\text{O}^{-2}$ intermediate can react with one CO_2 to form DLEMC, which then reacts further with CO_2 to form LEDC. While CO_2 may form at the positive electrode and diffuse to the negative electrode as part of a cross-talk mechanism,[29] for these simulations we limit CO_2 to the amount that would be present in a saturated EC solution, reflecting early SEI formation conditions. Because of the limited amount of CO_2 , few DLEMC or LEDC are produced by the rapid two-electron reduction mechanism. EC reduction also competes with the direct reduction of CO_2 to form carbonates as well as oxalates in small quantities (Figure 6.1 d).

Interestingly, we observe that the formation of LEMC is essentially unaffected by these competing reductive processes. In agreement with our recent findings based on analysis of CRNs,[212] the most facile path for LEMC formation is direct basic hydrolysis of Li^+EC (Figure 6.1 d). Since we assume that water reduces before significant SEI formation begins, this means that LEMC can form under any electrochemical conditions studied here. However, because we limit the initial amount of water (like CO_2) to impurity concentrations, LEMC is a minority component except when reduction is very slow (at high potentials far from the negative electrode).

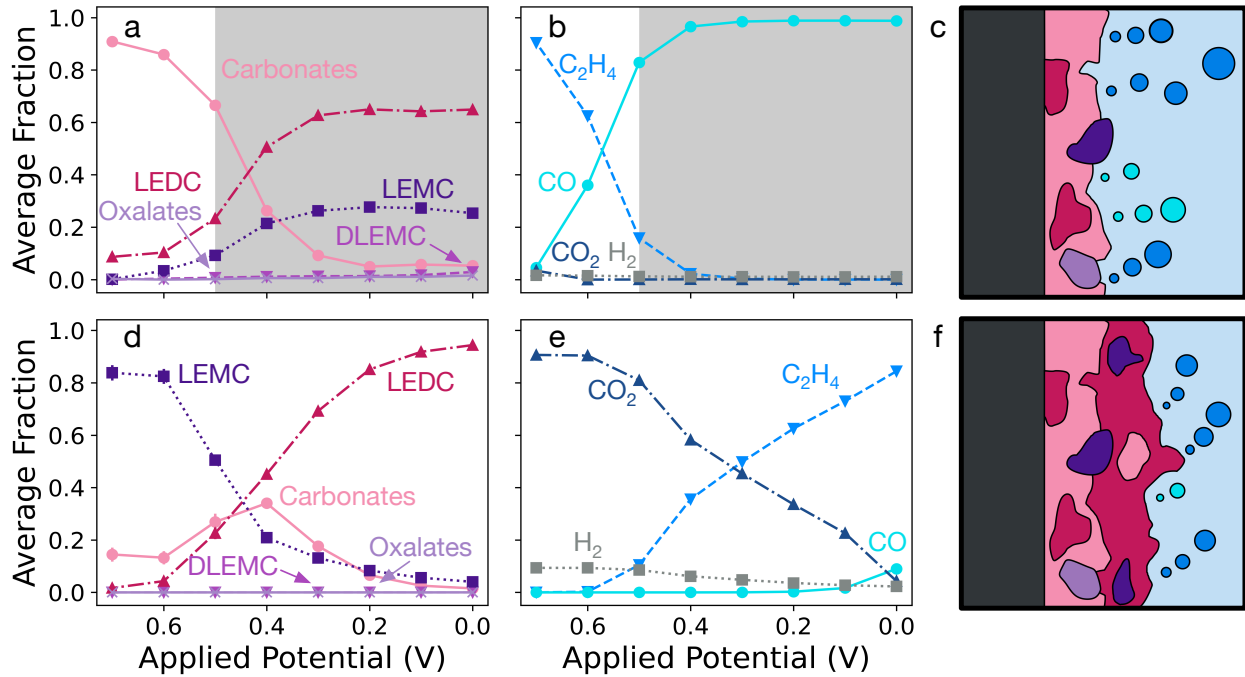


Figure 6.3: Average fractions of SEI products (a, d) and gaseous byproducts (b, e) at the end of kMC simulations as a function of applied potential referenced to an Li/Li⁺ electrode. Simulations were conducted under two conditions reflecting different regimes of SEI formation. To simulate SEI formation close to the negative electrode, before a significant interphase layer has formed (a-c), reduction was allowed to proceed in the absence of a tunneling barrier ($D = 0.0 \text{ \AA}$). Because the electrode will likely be covered at high applied potentials, the low-potential region (below an applied potential of +0.5V vs Li/Li⁺) is likely not accessible in an actual battery environment. This region has therefore been shaded. To simulate SEI formation far from the negative electrode (d-f), in the presence of an existing, partially electronically insulating interphase layer, reduction was slowed by a relatively thick tunneling barrier ($D = 10.0 \text{ \AA}$). Error bars representing the standard error of the mean are provided but are generally too small to be seen. Cartoons (c, f) depict the formation of SEI layers reflecting the kMC results.

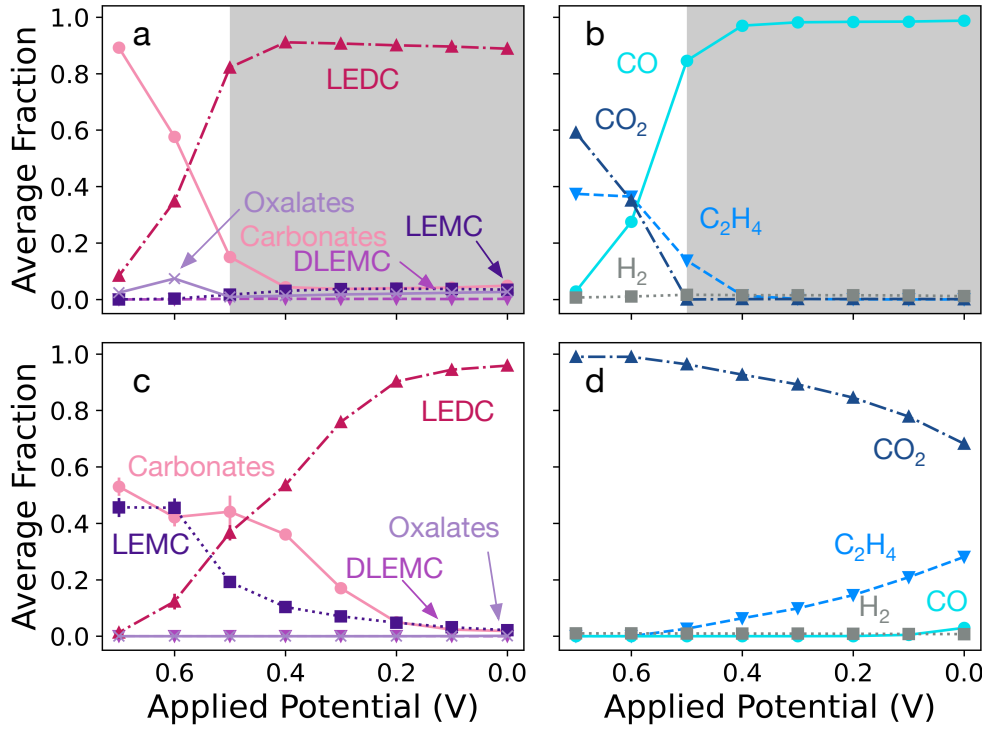


Figure 6.4: Average fraction of SEI products (a, c) and gaseous byproducts (b, d) at the end of kMC simulations under various applied potentials referenced to an Li/Li⁺ electrode with an increased initial quantity of CO₂ (\approx 50ppt, 10x as much as in Figure 6.3). Simulations were otherwise conducted under the same conditions considered in Figure 6.3. Because the electrode will likely be covered at high applied potentials, the low-potential region close to the electrode (below an applied potential of +0.5V vs Li/Li⁺) is likely not accessible in an actual battery environment. This region has therefore been shaded. Error bars representing the standard error of the mean are provided but are generally too small to be seen.

6.3 Effect of Varying Electrolyte Impurities

In Figure 6.3, we find that even a small amount of CO₂ is important in determining SEI composition. The critical role of impurity species in general, and CO₂ specifically, has long been recognized in the literature.[350] For EC-based electrolytes, it has been shown that the intentional addition of CO₂ leads to increased Li₂CO₃ formation and improved surface passivation.[230, 351–354] More recently, in the context of Li-ion batteries with Si negative electrodes, Schwenke et al.[355] found that CO₂ reduction prevented solvent decomposition and actually lowered the LEDC fraction in the SEI.

To further explore the effect of CO₂ concentration on SEI composition, we conducted

additional simulations with an increased initial quantity of CO₂ (10x the amount in the initial simulations). Simulations with increased water content were not pursued because the initial water content of our simulations is already significantly higher than what would be expected in a rigorously dried battery electrolyte.

Figure 6.4 shows the average fraction of SEI products after simulations with elevated initial CO₂. In agreement with the early observations of Aurbach et al.,[230] the quantity of inorganic carbonates produced increases significantly. With augmented CO₂, carbonates are a major SEI component in the regime far from the negative electrode at moderate to high potentials (above +0.3V vs. Li/Li⁺). We also observe a modest increase in the formation of lithium oxalate, though it remains a minority component. In contrast with Schwenke et al., the amount of LEDC produced increases with additional CO₂, especially close to the negative electrode where the additional CO₂ can react with the Li⁺OCH₂CH₂O⁻² anion along the rapid two-electron reduction mechanism of Li⁺EC. However, as we demonstrate below (see Section 6.4), LEDC that is exposed to a reducing environment should be expected to eventually decompose to form Li₂CO₃. Moreover, as Schwenke notes, the additional inorganic carbonate production during early SEI formation may effectively passivate the electrode surface (an effect that we have not included in our model but aim to incorporate in future work), preventing LEDC formation at lower applied potentials.

6.4 Exploring SEI Decomposition and Growth

The time scale accessible in a kMC simulation is limited by the fastest reactions that can occur. In our simulations — which are able to proceed 10⁻⁷ to 10⁻⁵s in 10,000,000 steps depending on simulations conditions — the fastest reactions are typically re-coordination reactions of the type $AM + B \rightarrow A + BM$, where A and B are coordinating molecules and M is a metal (Li⁺). Very fast reactions also limit the sampling of rare events. In practice, these limitations prevent SEI product decomposition from being observed in our kMC trajectories. However, it is known that the SEI continues to evolve after initial formation,[356] and that many SEI products[225] are actually metastable on the time scale of battery operation. In fact, previously developed SEI formation protocols involve holding cells at elevated temperatures for hours to optimize this evolution for improved battery cell performance.[357]

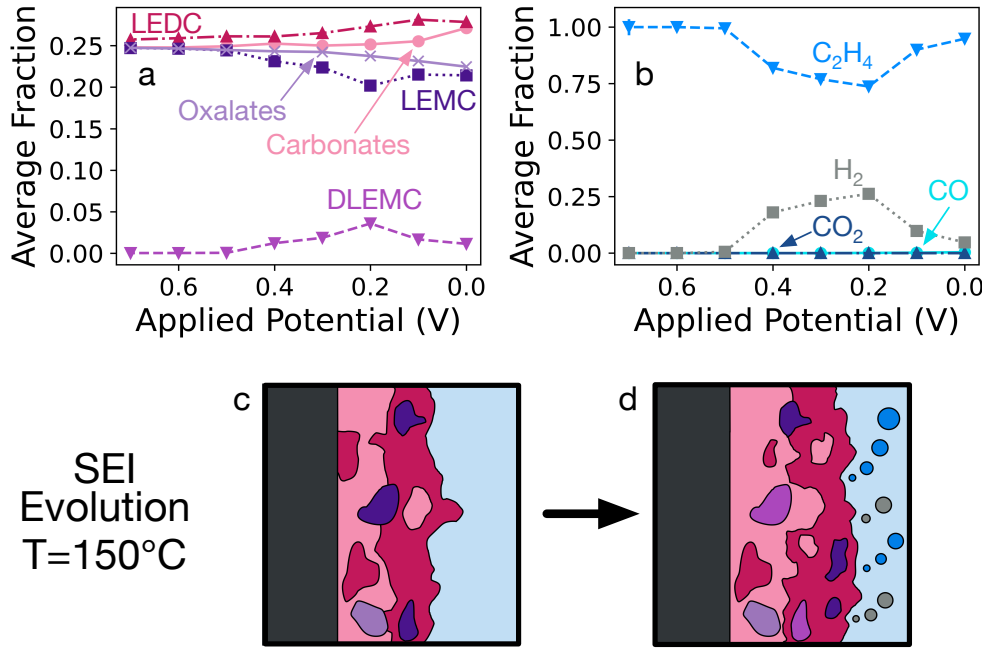


Figure 6.5: Average fraction of SEI products (a) and gaseous byproducts (b) at the end of kMC simulations under various applied potentials referenced to an Li/Li⁺ electrode with an initial state beginning with equal amounts of LiEC⁺, LEDC, LEMC, Li₂C₂O₄, and Li₂CO₃. Simulations were conducted with an electron tunneling barrier of $D = 10.0 \text{ \AA}$ to approximate the effect of a partially passivated SEI layer, which should slow reduction. To accelerate the simulation and allow for the decomposition of SEI components, an elevated temperature (423.15 K, or 150 °C) was used, and no metal re-coordination reactions were included. Error bars representing the standard error of the mean are provided but are generally too small to be seen. Cartoons (c, d) depict the evolution of an existing SEI layer, reflecting the kMC results.

In order to probe SEI evolution, we performed simulations beginning with equal amounts of Li⁺EC, LEDC, LEMC, Li₂CO₃, and Li₂C₂O₄ at an elevated temperature of 423.15K (150 °C) to accelerate decomposition reactions with a tunneling barrier of $D = 10 \text{ \AA}$, approximating an already-formed and partially electronically insulating SEI. The rapid re-coordination reactions with Li⁺ were removed in order to allow us to access longer time scales of $\approx 1\text{s}$; because all initial species are fully lithiated, this should not adversely affect the availability of Li⁺ in the simulation. In Figure 6.5, it can be seen that all products are relatively thermally stable at the chosen temperature (they do not react significantly at high applied potentials), though Li⁺EC reduces and reacts to form some C₂H₄ and additional LEDC. Under a strongly reducing potential close to the negative electrode surface, however, both LEDC and LEMC are electrochemically unstable. As has been previously observed,[225] LEDC decomposes to form inorganic carbonates and C₂H₄ (Figure 6.1 b); note that the average fraction of LEDC

is not lowered because of the continual formation of LEDC by Li^+EC . Additionally, LEMC decomposes to form DLEMC and H_2 (Figure 6.1 d). $\text{Li}_2\text{C}_2\text{O}_4$ and Li_2CO_3 are predicted to be relatively electrochemically stable in our simulations; the reduced fraction of $\text{Li}_2\text{C}_2\text{O}_4$ at low applied potentials is a result of additional LEDC forming via Li^+EC reduction, not $\text{Li}_2\text{C}_2\text{O}_4$ decomposing.

We emphasize that while the reduction of LEMC to form DLEMC and H_2 was previously postulated,[116] DLEMC has never before been conclusively identified by experimental spectroscopy, and this is the first direct observation of DLEMC formation by kinetic simulations. Our findings suggest that DLEMC may not be present in the SEI initially but could form over time if an SEI containing LEMC is exposed to low potentials for a prolonged period (particularly at high temperature) or cycled repeatedly. Given that previous simulations have suggested that DLEMC could be a fast Li^+ conductor[116] and thus a beneficial SEI component, this motivates further experimental studies to confirm under what conditions DLEMC could be preferentially formed in the SEI.

6.5 A Mechanistic Model of SEI Reactivity

We now summarize the findings of our first-principles microkinetic modeling, using them to draw conclusions about SEI formation and evolution. Beginning charging in the first cycle with a pristine electrode in contact with an EC electrolyte, we find that as the potential is lowered past the reduction potential of Li^+EC , EC reduces to form inorganic carbonates with some LEDC and LEMC, which we assume precipitate onto the surface. During this surface film formation, C_2H_4 and CO are released. After an initial layer has formed, the potential is continually lowered over time, causing the SEI to continue to grow outward, with LEDC being the main component, C_2H_4 being the major gaseous byproduct, and LEMC and inorganic carbonates being significant minority components.

After initial SEI formation is complete, the SEI can continue to evolve if exposed to low applied potentials through a potentiostatic hold or repeated cycling. Until the SEI is thick enough to be completely electronically insulating, we expect the inorganic inner region of the SEI to grow as LEDC decomposes to form inorganic carbonates and C_2H_4 ; the minority LEMC will also decompose to form DLEMC and H_2 . At the same time, Li^+EC reduction can continue at the electrolyte-SEI interface, leading to the formation of fresh LEDC, LEMC (if additional water is present), and inorganic carbonates.

In this Chapter, we used kMC simulations based on reaction mechanisms obtained via automated CRN analysis and *ab initio* calculations to study SEI formation and evolution. By conducting simulations over a range of applied potentials and with varying electron tunneling barriers, we observe the formation of distinct inorganic and organic layers in the SEI, recovering and elucidating the origins of the Peled model from first principles. Competition between organic and inorganic SEI products is driven primarily by the different reduction mechanisms of Li^+EC , as well as the direct reduction of CO_2 . Simulations with varying initial conditions highlight the importance of impurity species in controlling SEI formation and sup-

port the observation that CO₂ concentration in the electrolyte can be modified to tune SEI composition. By performing simulations at elevated temperature, we observe the expected electrochemical decomposition of LEDC to form inorganic carbonates, as well as the formation of DLEMC through the reductive decomposition of LEMC. Our work demonstrates the promise of combining first-principles and data-driven simulations with microkinetic models towards explaining the formation process of one of the most impactful passivation layers in our modern technology: the Li-ion battery SEI.

Chapter 7

Combining CRN Analysis and Experimental Spectroscopy to Explain Gas Evolution in Mg-Ion Batteries¹

In previous Chapters, I have focused primarily on LIBs for two main reasons. First, LIBs are perhaps the most commercially and industrially important battery technology today, and it is unlikely that this present market dominance will be challenged in the near future. Second, while there exist many remaining questions regarding electrolyte degradation and SEI formation in LIBs, there is a large body of prior experimental and theoretical research on the subject. This means that, by studying LIB SEI formation, my colleagues and I could consistently validate our DFT, CRN, and kMC results against prior findings *ex post facto*.

In order to meet growing global demand for energy storage while mitigating resource scarcity as well geopolitical supply chain risk,[10, 359] alternatives to LIBs are needed. MIBs present one such possible beyond-Li-ion technology, alleviating some of the inherent limitations of current LIBs. However, the potential of MIBs is presently unrealized because of comparatively poor cycling behavior and unfavorable electrode passivation. Most electrolytes decompose at Mg negative electrodes during MIB charging. But, as I discussed in Chapter 1, many MIB electrolytes degrade to produce ionically insulating films which prevent reversible Mg plating and stripping.[360, 361]

Previous studies have provided relatively little detail regarding either reaction mechanisms or decomposition products involved in MIB electrolyte decomposition and interphase formation. In most cases where MIB interphases have been characterized,[53–55, 362–365] the techniques used have identified simple inorganic components (e.g. MgO, MgS, or MgCO₃) or bonding motifs (e.g. C–O or C=O groups), unable to provide specific insight into organic speciation. Theoretical studies using DFT and AIMD can provide more detailed insight into electrolyte reactivity. However, previous DFT studies have primarily or exclusively consid-

¹This chapter is adapted from reference [358]: Spotte-Smith, E.W.C., Blau, S.M., Barter, D., Leon, N.J., Hahn, N.T., Redkar, N.S., Zavadil, K.R., Liao, C., Persson, K.A. *Journal of the American Chemical Society* 145(22), 12181–12192.

ered the initial steps of electrolyte decomposition,[366–368] while AIMD is generally limited to extremely short time scales ($\sim 10\text{ps}$) at idealized interfaces.[168, 363]

In this Chapter, we conduct a combined theoretical-experimental analysis to probe electrolyte degradation and gas evolution in a model MIB electrolyte — magnesium bis triflimide ($\text{Mg}(\text{TFSI})_2$) dissolved in diglyme (G2). We perform online electrochemical mass spectroscopy (OEMS), a kind of differential electrochemical mass spectroscopy (DEMS), to detect gaseous byproducts of MIB electrolyte decomposition *in situ*. DEMS is a useful tool for instantaneous and quantitative detection of gaseous species evolved from solution during electrochemical testing,[124, 369] and it has previously been used to quantitatively diagnose the gaseous species generated during LIB cycling.[121, 370, 371] However, DEMS has not been extensively applied to study gas evolution in MIBs. Due to the limited understanding of electrolyte decomposition in MIBs, spectroscopic interpretation for MIBs is more challenging than for LIBs.

Computational modeling can aid in the interpretation of experimental spectra. In particular, CRNs are natural tools for combined theoretical-experimental studies, as they can be applied to identify important species in a reactive system and even study reactive dynamics.[200] Here, for the first time, we combine our platform for high-throughput DFT and CRNs (described in Chapter 4) with experimental characterization techniques to understand reactivity in batteries. We construct the first ever CRN describing MIB electrolyte decomposition and SEI formation at the Mg plating potential. By screening the predicted products of this CRN by their calculated liquid-gas solubility, we are able to identify possible evolved gases and from these positively identify the gases observed experimentally in OEMS. Analyzing elementary reaction mechanisms for the formation of these possible gases, we explain why some gases form while others do not. Our approach of combining CRN analysis with experimental spectroscopy provides a path forward for the in-depth analysis of chemical transformations in next-generation electrochemical systems with minimal prior knowledge.

7.1 OEMS

A 0.5M $\text{Mg}(\text{TFSI})_2/\text{G2}$ electrolyte was used to plate Mg onto Au at a cell voltage of -1.0 V for approximately four hours in the OEMS system described above (experimental methods are provided in Appendix B.4). The electrochemical and OEMS measurements are shown in Figure 7.1; cyclic voltammetry data is shown in Figure H.1 in Appendix H.1. The current density during the potentiostatic hold (Figure 7.1a) is initially high (-2.65 mA/cm²) but gradually decreases in magnitude over time as a result of increased resistance caused by electrode passivation. The dynamic resistance of the electrode interfaces is also evident from the sudden changes in current which occur at varying intervals.

The OEMS signal over the course of the experiment was integrated in order to identify the major peaks (Figure 7.1b; snapshot OEMS spectra are presented in Appendix H.2). We ignore peaks at $\text{M/Z} = 2, 4, 20$, and 40, as these correspond to the carrier gas (He, M/Z

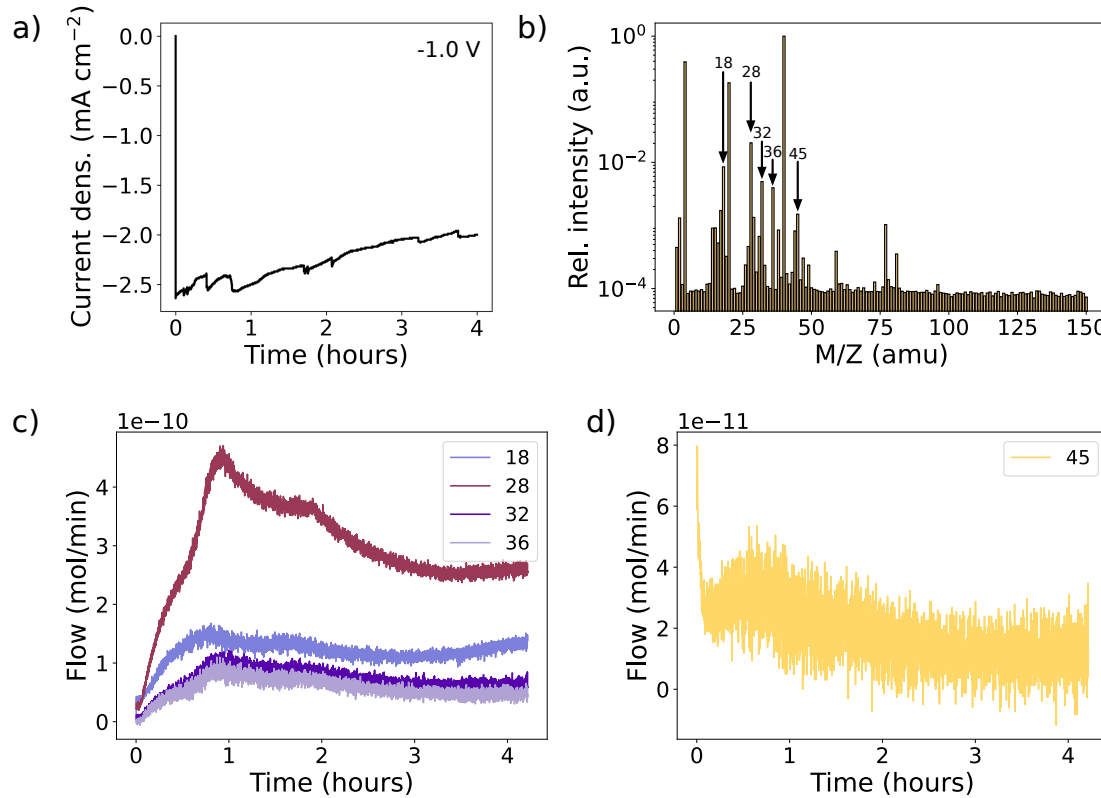


Figure 7.1: OEMS measurements on a $\text{Mg}(\text{TFSI})_2/\text{G2}$ electrolyte during a potentiostatic hold at a cell potential of -1.0 V. a) The applied current density during potentiostatic hold; b) integrated relative OEMS intensity (in log scale) after approximately four hours of measurement, with major peaks indicated; c) time-resolved flow for several major peaks ($\text{M/Z} = 18, 28, 32, 36$) demonstrating continuous evolution; d) time-resolved flow for $\text{M/Z} = 45$ with initially high partial pressure that rapidly decays.

= 2, 4) or Ar ($M/Z = 20, 40$) that was trapped in the $Mg(TFSI)_2/G2$ electrolyte after the electrolyte was distilled and the DEMS cell was assembled in an Ar-filled glovebox. Other major peaks include those at $M/Z = 18, 28, 32, 36$, and 45.

From the time-resolved measurements (Figure 7.1c), we find that the signal at $M/Z = 18$ is relatively stable after an initial increase, while the signal at $M/Z = 28, 32$, and 36 all reach a maximum at ~ 1 hour and afterwards gradually decrease. In contrast (Figure 7.1d), the $M/Z = 45$ flow rapidly decays to a near-zero signal in the first few minutes of the experiment.

This initial difference in signal over time suggests that the species detected at $M/Z = 18, 28, 32$, and 36 are products of ongoing reactivity, while the species detected at $M/Z = 45$ is either a decomposition product that can only form under highly specific conditions or is not indicative of a decomposition product at all. Given that this OEMS experiment was conducted in a constant-potential regime in which Mg is consistently plated, we believe that the latter possibility is more likely. We suggest that the $M/Z = 45$ signal is likely indicative of G2 itself, rather than a product of G2 decomposition formed at the Mg electrode. The initially high $M/Z = 45$ signal reflects evaporated G2 that built up in the DEMS cell during preparation; after this initial G2 is purged, evaporation continues slowly, resulting in a lower signal during the remainder of the experiment. We note that OEMS is typically not sufficiently specific to allow positive identification of specific gases or molecular fragments. $M/Z = 28$, for instance, could indicate diatomic nitrogen (N_2 , $M = 28$ amu), carbon monoxide (CO, $M = 28$ amu), or ethylene (C_2H_4 , $M = 28$ amu), among other possibilities.

7.2 Identifying Observed Gases

In order to determine the identity of the major observed species, we constructed a CRN containing species that could be relevant to the decomposition of $Mg(TFSI)_2/G2$ electrolytes and subsequent interphase formation (computational details are provided in Appendix B.4). Using stochastic simulations under five different initial conditions, we identified 85 of an initial 6,469 species as CRN products (see Appendix H.5 for more discussion). We believe that most electrolyte decomposition products will either precipitate and contribute to an interphase layer, or else will be soluble in the electrolyte. Therefore, we filtered the predicted CRN products by their predicted solubility in G2 (S_{G2}), using Equation B.9 (Appendix B.4). Expecting considerable error in the prediction of S_{G2} , we remove any predicted CRN product with a predicted solubility $> 5M$. We also remove ionic CRN products and CRN products containing Mg, as we expect such species to be considerably more stable in solution than in the gas phase.

With these criteria, we predict that 14 of the 85 CRN products could evolve out of solution and be detected by OEMS (Figure 7.2). These predicted gaseous CRN products enable the unambiguous assignment of the major observed OEMS peaks. For most peaks, there is exactly one gas that would be consistent with the signal. Specifically, the $M/Z =$

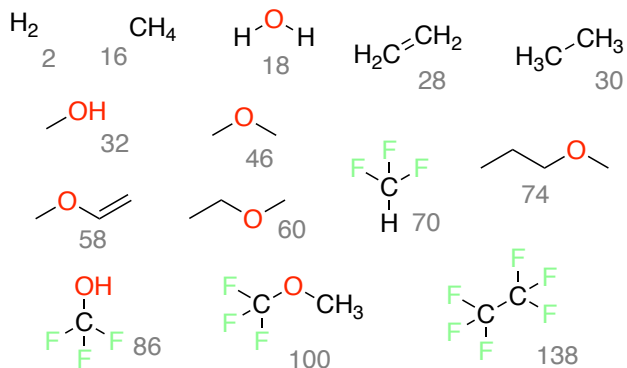


Figure 7.2: Gases predicted to evolve from $\text{Mg}(\text{TFSI})_2/\text{G2}$ electrolytes, based on CRN analysis and prediction of solubility S_{G2} . The mass of each CRN product (rounded, in amu) is shown next to the 2D structure in gray.

18 peak can be assigned to water (H_2O), the $\text{M/Z} = 28$ peak can be assigned to ethylene (C_2H_4), and the $\text{M/Z} = 32$ peak can be assigned to methanol (CH_3OH).

Notably, there are no predicted gaseous CRN products with masses consistent with $\text{M/Z} = 36$ and $\text{M/Z} = 45$ (though several species could produce fragments with $\text{M} = 45$ amu). This supports our previous suggestion that the $\text{M/Z} = 45$ signal does not correspond to a decomposition product but instead comes from another source such as evaporated G2. We further suggest that the $\text{M/Z} = 36$ signal corresponds to an impurity species, rather than a decomposition product of either G2 or TFSI^- . Considering that chloride (Cl^-) is an impurity in commercial $\text{Mg}(\text{TFSI})_2$,^[372] we tentatively assign the $\text{M/Z} = 36$ peak to hydrogen chloride (HCl). This assignment is also consistent with the presence of a minor $\text{M/Z} = 38$ signal. The ratio of the integrated $\text{M/Z} = 36$ signal and the $\text{M/Z} = 38$ signal is 4.67, which is close to the ratio of the natural abundances of ^{35}Cl to ^{37}Cl (3.17).^[373]

Validating Predicted Major Products

To confirm that the peak assignments based on CRN products are reasonable, we identified formation pathways to several CRN products using the previously constructed CRNs and then used DFT to construct elementary reaction mechanisms.

There are several plausible pathways that lead to the formation of C_2H_4 (Figure 7.3a). All identified pathways initialize with Mg^{2+} being partially reduced in the presence of G2 ($\text{M}_1 \longrightarrow \text{M}_2$). It has previously been reported that the partial reduction of Mg^{2+} ions to highly reactive radical Mg^{1+} can promote electrolyte decomposition.^[366, 368] We predict that this reduction can occur at 0.64 V vs. Mg/Mg^{2+} ; however, this and all other reported reduction potentials with Mg ions present depend on the solvation environment of the metal ion (see Appendix H.3). Seguin et al.^[368] previously showed that the partially reduced com-

plex M₂ can cleave either of the internal C-O bonds with $\Delta G^\ddagger = 0.42$ eV due to a bifurcation of the potential energy surface. If a methoxide ion (CH_3O^- , M₃) is eliminated, we find that the remaining Mg-coordinated fragment (M₄) can subsequently reduce ($E^\circ = 3.51$ V) and eliminate C₂H₄ with a low barrier $\Delta G^\ddagger = 0.15$ eV. Alternatively, a radical CH₃OCH₂CH₂• (M₆) can be eliminated. CH₃OCH₂CH₂• can then coordinate with an additional Mg²⁺ and reduce (M₆ → M₈, $E^\circ = 3.89$ V), producing C₂H₄ with another low barrier ($\Delta G^\ddagger = 0.27$ eV). Though this latter mechanism involving CH₃OCH₂CH₂• is more difficult, we nonetheless believe that it could occur, given that M₃ + M₄ and M₅ + M₆ are essentially equally likely to form from the initial cleavage of C-O bonds in G2.

If methoxide is present, for instance because of the mechanisms reported in Figure 7.3a, then the formation of methanol is facile and straightforward (Figure 7.3b). M₃ can attack either methylene group in Mg-coordinated G2 (M₁), abstracting a proton to form methanol (M₃ + M₁ → M₁₁ + M₁₂, $\Delta G^\ddagger = 0.46$ eV; M₃ + M₁ → M₁₁ + M₁₃, $\Delta G^\ddagger = 0.22$ eV). The deprotonated Mg-coordinated G2 species (M₁₂, M₁₃) are reactive and can further decompose. M₁₂ can form M₁₄, methoxyethene, (M₁₂ → M₅ + M₁₄, $\Delta G^\ddagger = 0.25$ eV). While we predict M₁₄ to be a potential gaseous product (Figure 7.2), we do not find evidence for significant methoxyethene evolution, perhaps because the deprotonation leading to M₁₂ is slower than that leading to M₁₃. The decomposition of M₁₃ instead produces magnesium methoxide (M₁₃ → M₁₀ + M₁₅, $\Delta G^\ddagger = 0.26$ eV), which could generate further methanol by the mechanism just described. This suggests that methanol formation in G2 electrolytes may be autocatalytic; once methoxide is initially formed, it can be continually reformed via chemical reactions with G2.

Hydroxide ions can react with Mg-coordinated G2 similarly to methoxide, abstracting a proton to form water (M₁ + M₁₆ → M₁₃ + M₁₇, $\Delta G^\ddagger = 0.23$ eV). We note that this hydroxide could be free in the electrolyte solution (due to trace water) or could be present in the form of Mg(OH)₂, which should be expected on Mg electrodes. Hydroxide could also potentially arise from the reduction and decomposition of CH₃OH. The finding that G2, upon chelating Mg, can be deprotonated by hydroxide is in agreement with the prior work of Yu et al.[363] We note that the reduction potential of water is >1.5 V vs. Mg/Mg²⁺,[374] hence we expect that during charging of an MIB, water should quickly reform hydroxide, creating yet another potential autocatalytic loop.

Explaining Absent Gases

While several of the gases predicted to form via CRN analysis appear to be likely major products of G2 decomposition — namely, C₂H₄, CH₃OH, and H₂O — many of the predicted gaseous CRN products are not observed by OEMS. Just as we have used elementary reaction mechanism analysis to validate our spectroscopic peak assignment, indicating pathways that could reasonably lead to the identified gaseous CRN products, we can also suggest mechanistic explanations for why other gases are not evolved. Here, we consider three gases that were not observed experimentally in significant quantities: methane (CH₄), ethane (C₂H₆), and dimethyl ether (CH₃OCH₃).

Reaction mechanisms leading to CH₄ are shown in Figure 7.4a. Seguin et al. previously predicted that a methyl radical (CH₃•, M₁₈) could be eliminated from M₂ with a moderate barrier ($\Delta G^\ddagger = 0.67$ eV).[368] This reaction is accessible at room temperature but is several orders of magnitude slower than the other C-O cleavage reactions discussed previously (e.g. M₂ → M₃ + M₄). Even once M₁₈ forms, the abstraction of H to form CH₄ is difficult. We have identified four different H abstraction reactions involving either Mg-coordinated G2 (M₁) or a reduced and partially decomposed Mg-coordinated G2 (M₁₉). The most facile abstraction (M₁₈ + M₁₉ → M₂₀ + M₂₂) has a barrier of 0.83 eV; all others have barriers of ~1 eV.

The formation of ethane (Figure 7.4b) is also kinetically limited. Like CH₄, C₂H₆ requires methyl radicals via the reaction M₂ → M₁₈ + M₁₉. M₁₈ could directly attack either M₁₉ or M₁, transferring another methyl group to form C₂H₆. However, these reactions suffer from extremely high barriers ~ 1.8 eV, and we therefore do not believe that they will occur under normal battery cycling conditions. If the methyl group reduces ($E^\circ = 0.91$ V vs. Mg/Mg²⁺) to form a methanide anion (M₂₇, CH₃⁻), a similar methyl transfer reaction can occur (M₂₇ → M₂₅ + M₂₈); while this reaction is considerably more facile than those involving M₁₈, it is still sluggish at room temperature, with $\Delta G^\ddagger = 0.87$ eV. DFT is known to exhibit deficiencies in the prediction of energy barriers for radical-radical reactions, which is why we did not consider the reaction CH₃• + CH₃• → C₂H₆ (or M₁₈ + M₁₈ → M₂₅). Intuitively we believe that this reaction has a low barrier or is perhaps even barrierless. However, it would require two methyl radicals to form separately in close proximity, which seems unlikely considering that the decomposition of G2 to form CH₃• is not preferred.

We find that dimethyl ether can form via methoxide (Figure 7.4c). The methoxide ion can attack a Mg-coordinated G2 in a single step (M₁ + M₃ → M₁₉ + M₃₀, $\Delta G^\ddagger = 0.82$ eV). Because the formation of methanol by proton abstraction (e.g. M₁ + M₃ → M₁₁ + M₁₃) is considerably more facile, dimethyl ether should not be expected to form, or should form only as a minority product.

7.3 The role of TFSI⁻

Bistriflimide anions are known from both theoretical and experimental studies to be reductively unstable under MIB charging conditions.[55, 364, 366, 375] It might therefore be expected that some fragments of TFSI⁻ will be involved in gas evolution. Indeed, of the 14 potential gaseous products shown in Figure 7.2, four of them contain trifluoromethyl groups (-CF₃) derived from TFSI⁻. Trifluoromethyl groups in TFSI⁻ can easily be eliminated under reducing conditions,[366] making it reasonable to think that CF₃ might react to form various small molecules. However, none of the major gases identified in OEMS contain -CF₃ or any other structural motif from bistriflimide. Moreover, none of the reaction mechanisms to form C₂H₄, CH₃OH, or H₂O require TFSI⁻ or any related fragment. Although the concentration of TFSI⁻ in our OEMS experiment (1M for a 0.5M Mg(TFSI)₂ electrolyte) is considerably lower than that of G2, it should be high enough for any gaseous decomposi-

tion products to be detected by OEMS.[376–378] It therefore appears that TFSI⁻ is not significantly involved in forming any evolved gases, in spite of its observed reactivity.

If bistriflimide is not forming gases or assisting in the decomposition of G2, it raises the question of what happens to the TFSI⁻ decomposition fragments. Recent AIMD results from Agarwal et al.[168] suggest that TFSI⁻ might catastrophically decompose and even atomize at Mg interfaces, particularly if coordinated with Mg²⁺. The results of Agarwal, which are based on simulations in the presence of an idealized, completely clean Mg electrode surface (with highly undercoordinated and therefore reactive Mg), may not explain TFSI⁻ reactivity in all cases, for instance if a robust SEI layer or even thin oxide layer is present to shield the electrolyte from a Mg metal electrode. However, in our experiment, we continuously plate Mg metal, potentially exposing fresh interfaces that can react with the electrolyte. We suggest that TFSI⁻ decomposes at this newly formed metal interface, forming primarily solid deposits, rather than small molecules and gases.

Surface analysis provides further evidence that TFSI⁻ forms solid deposits on the metallic Mg surface. We cycled a 0.3M Mg(TFSI)₂/G2 electrolyte between -0.6V and 3.0 V vs. Mg/Mg²⁺ 10 times on a Pt WE (Figure 7.5a) to determine if accumulation of a reaction product occurs with Mg deposition. During cycling, we used XPS to analyze the elemental composition of the surface film on the electrode (Figure 7.5b). Before cycling, the surface film was primarily composed of carbon (84.5%), with some oxygen (12.7%) and Mg (2.7%) and essentially no fluorine or sulfur. These results suggest that whereas G2 (containing C, O, and H, the latter of which cannot be detected by XPS) or G2 decomposition products from conditioning might be inherently unstable at a Pt surface, TFSI⁻ (containing C, O, F, N, and S) is not inherently reactive. After the first cycle, some F (1.6%) and S (1.9%) are observed, indicating that TFSI⁻ reacts electrochemically and that the products of TFSI⁻ decomposition deposit on the electrode surface. The extent of TFSI⁻ decomposition increases upon cycling, and by the 10th cycle, the surface film is 12.2% F and 6.5% S indicating accumulation of TFSI⁻ reaction products. Notably, the atomic fraction of Mg in the surface film also increases with cycling, reflecting a degree of passivation-induced Mg stranding (Figure H.11 in Appendix H.6) as well as a loss of Mg inventory and battery capacity during cycling.

In addition to precipitated solid species, there is some evidence that TFSI⁻ decomposition could result in products which are soluble in G2. A recent study on the effect of impurities in MIBs with glyme solvents by Yang et al.[69] applied electrospray ionization mass spectroscopy (ESI-MS) to study electrolyte speciation. The authors observed several F- and N-containing species in the electrolyte; because these were seen only in the conditioned electrolytes, these species could only come from TFSI⁻ decomposition.

7.4 Summary

In this work, we used OEMS, CRNs, and DFT to identify gaseous byproducts of electrolyte decomposition in MIBs. Using a CRN, we identified 14 possible gaseous species which

could form from Mg(TFSI)₂/G2 electrolytes. Of these, three (C₂H₄, CH₃OH, and H₂O) were consistent with major peaks in the observed OEMS spectra. We validated our peak assignments by identifying elementary reaction mechanisms to these three species, finding in all cases that the species could be easily formed via Mg-coordinated G2 (and, in the case of H₂O, hydroxide ions). On the basis of reactive competition, we rationalized why other gases (CH₄, C₂H₆, and CH₃OCH₃) which were predicted to form may not actually emerge during MIB cycling. Although TFSI⁻ decomposes at Mg metal electrodes and during Mg plating, we find that TFSI⁻ does not itself form any gaseous species, nor is it necessary to assist in the decomposition of G2. Rather, we suggest that TFSI⁻ primarily forms solid deposits on the electrode and potentially forms some products that are soluble in G2.

The methodology described here enables facile, in-depth analysis of *in situ* spectroscopy in electrochemical systems via powerful computational tools. While we have here focused on a model system in order to compare our results with previous experimental and theoretical findings, we believe that an approach mixing first-principles simulations, CRN exploration, and spectroscopy is especially well suited to allow for the characterization of completely novel electrolytes in which nothing is known regarding reactivity, decomposition products, and SEI formation. DEMS is a highly attractive point of comparison due to its high resolution, but CRN-assisted analysis of other spectroscopic measurements, such as infrared and nuclear magnetic resonance spectroscopies, should also be considered.

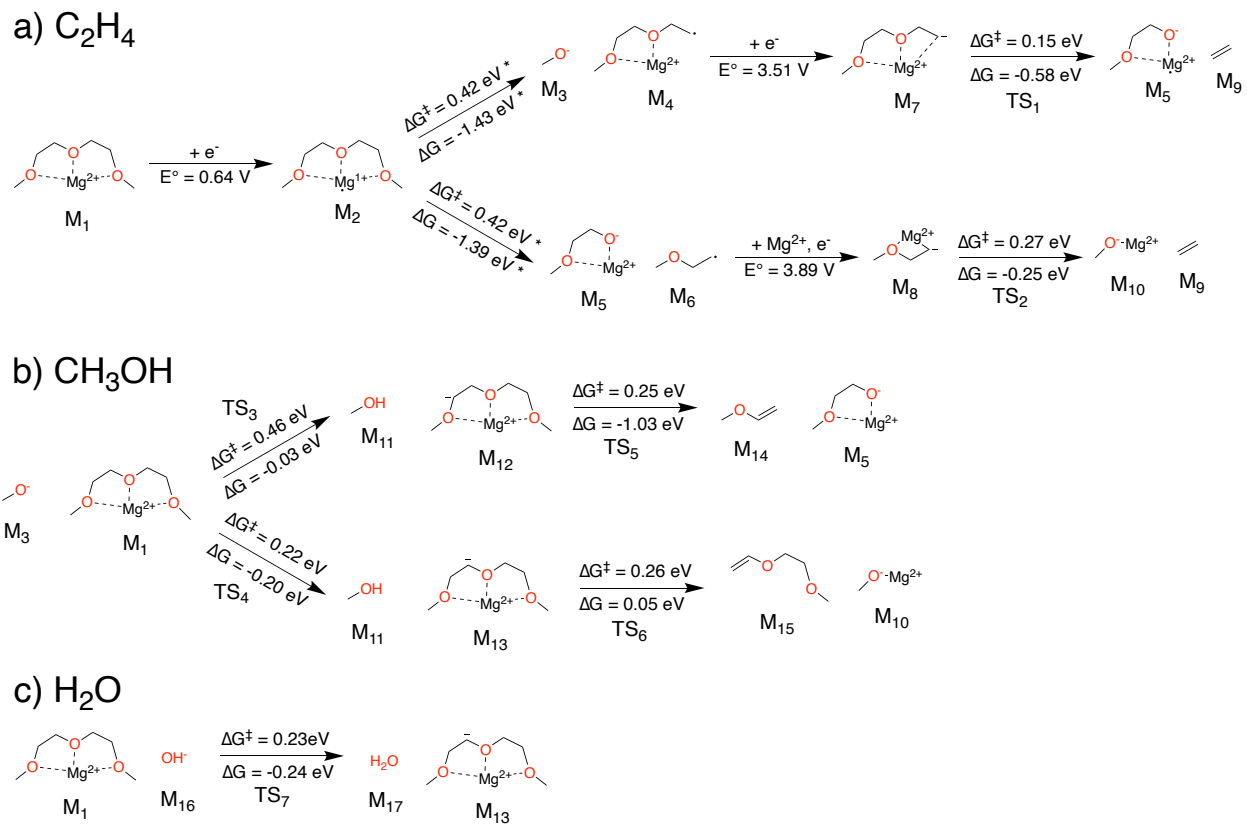
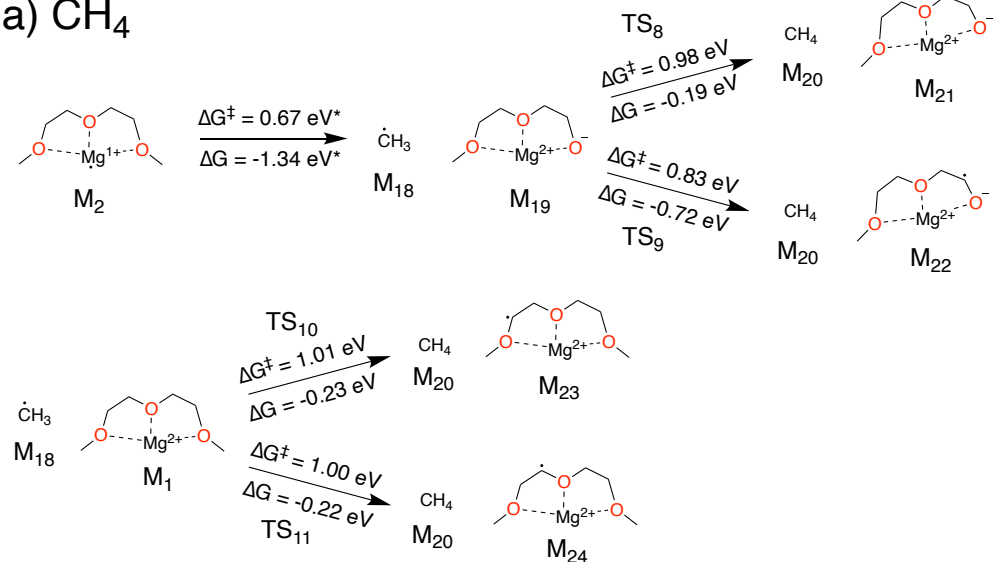
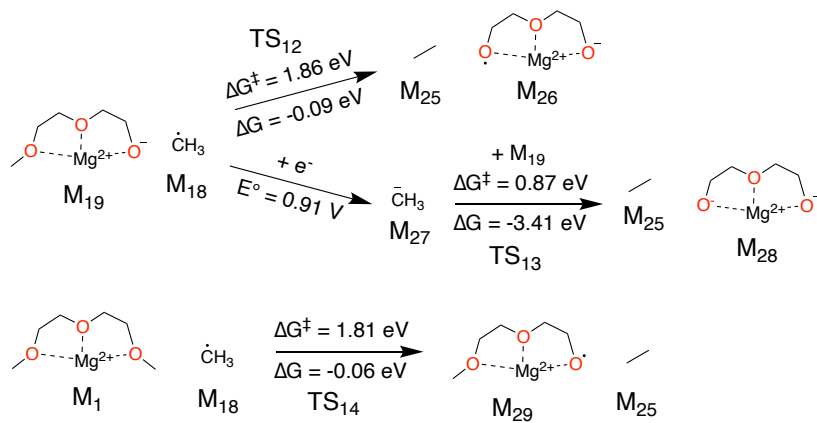


Figure 7.3: Elementary reaction mechanisms for the formation of a) C_2H_4 , b) CH_3OH , and c) H_2O . Reaction energies and energy barriers marked with an asterisk (*) were taken from Seguin et al.[368]

a) CH₄



b) C₂H₆



c) CH₃OCH₃

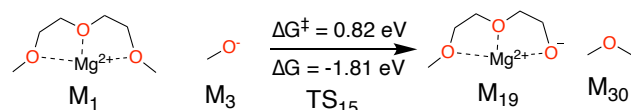


Figure 7.4: Elementary reaction mechanisms for the formation of a) CH₄, b) C₂H₆, and c) CH₃OCH₃. Reaction energies and energy barriers marked with an asterisk (*) were taken from Seguin et al.[368]

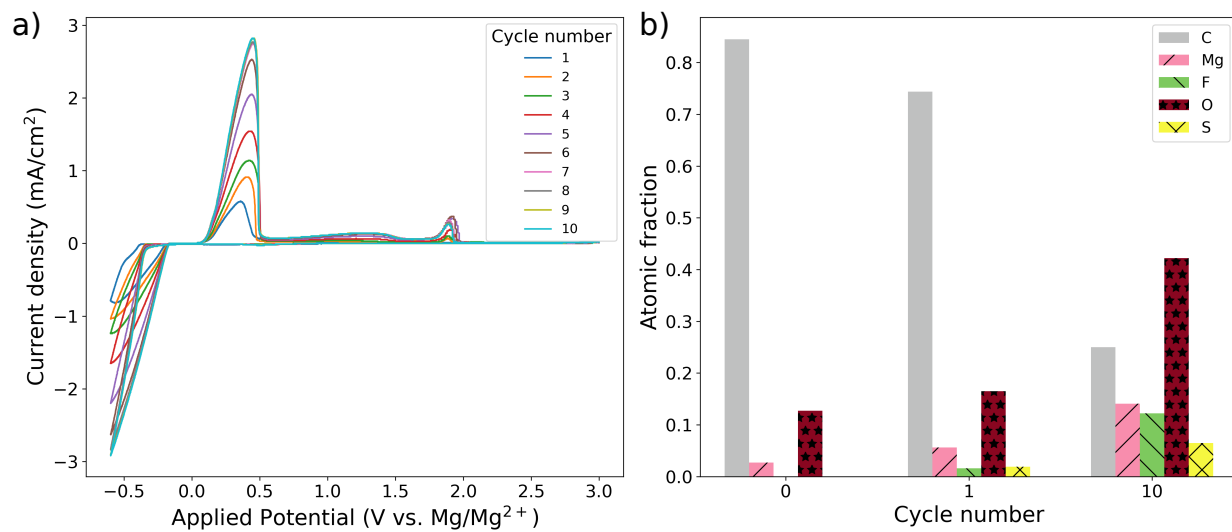


Figure 7.5: a) Progressive cyclic voltammetry cycling behavior (10 cycles) on a fresh Pt electrode in electrochemically conditioned 0.3M $\text{Mg}(\text{TFSI})_2/\text{G2}$ at a scan rate of 10 mV/s. b) XPS-derived composition of the Pt electrode surface as a function of cycle number. A cycle number of 0 indicates that the measurement was taken before any potential had been applied.

Chapter 8

Conclusions

In general, battery electrolytes are (electro)chemically unstable. At the extreme potentials necessary to achieve high energy density, electrolyte salts, solvents, additives, and impurities react and decompose, leading to gas evolution[232, 313] and (in the best case) the formation of passivating interphases.[39, 77] These processes — electrolyte degradation and interphase formation — are the life and death of modern batteries, which led me to the goal that I laid out in Chapter 1:

to be able to predict *a priori* how a given electrolyte component or electrolyte formulation will participate in a complex reaction cascade, considering the impact of small chemical modifications and impurities.

I defined the questions guiding analyses of electrolyte decomposition and interphase formation more broadly in Chapter 2: what are the composition, structure, origins, and impact of an interphase? Now, I can look back and assess the extent to which I was able to meet this goal and answer these questions.

In the previous five chapters (Chapters 3–7), I described a series of efforts aiming to meet this goal and answer these questions, starting from the tried-and-true methods of quantum chemistry and developing new approaches combining network theory, statistical mechanics, and microkinetic modeling. In this Chapter, I will briefly summarize my findings, summarizing the key bits of wisdom that my efforts have earned and further indicating where my colleagues and I have succeeded in meeting our goals and where we still fall short. I will share some directions for future work that I believe will be important to drive progress in the analysis of complex (electro)chemical processes.

8.1 Even More Complicated Than We Imagined

It has long been recognized that electrolyte decomposition and interphase formation are highly complex processes.[60] However, in spite of this, many battery scientists have historically insisted on making a wide range of assumptions in order to simplify their analysis.

This is perhaps especially true for studies seeking to explain the mechanism of a process (for instance, the decomposition of an electrolyte component, the formation of a particular product, or the origin of a particular failure mode). Through my work, I have found that many of these simplifications are inappropriate and can lead to results that are likely incorrect and are perhaps even unreasonable. Here I point out a few of these simplifications and explain how, in my own research, progress could only be made by making contrary assumptions.

Each Reacting Component Can Be Considered In Isolation

It is widely viewed as a best practice for scientists to separate variables, to (where possible) consider only one effect at a time. Perhaps for this reason, studies of electrolyte reactivity often focus only on one molecule at a time and consider only linear pathways from the pure, unreacted molecule to known or predicted products.[15, 23, 247, 251, 331, 379] In reality, it is often impossible to disentangle different reaction pathways in batteries; indeed, this is one of the defining features of a reaction cascade. As we described in Chapter 3, this one-at-a-time approach was used for many years to explain the reactivity of LiPF₆. Although there is experimental evidence that LiPF₆ forms organic phosphate and fluorophosphate species,[250] implying reactions with organic electrolyte components such as EC, the most widely cited reaction mechanism for LiPF₆ decomposition, including the formation of LiF and POF₃, was a hydrolytic process that involved no electrolyte component other than LiPF₆ and the impurity H₂O.[238, 239, 244–246] While I cannot say for certain why this reaction was favored, it may well be because this reaction was simple and straightforward to understand.

As we have shown, this hydrolytic mechanism is highly implausible when considering DFT-calculated reaction energies and energy barriers, typical water concentrations in laboratory LIBs, and long-standing experimental evidence. We believe, based on first-principles reaction mechanisms, that LiPF₆ primarily reacts with inorganic carbonates and potentially other Lewis bases, which are mainly formed from the reduction of CO₂ and EC. This reaction mechanism likely could not be discovered without acknowledging possible interactions between different electrolyte species and between electrolyte species and pre-existing interphase components. In future studies of electrolyte decomposition, I hope that researchers take pains to consider such interactions when proposing reaction mechanisms. In addition to potentially providing more satisfying and chemically reasonable explanations, this approach can potentially reveal new routes for battery design that had not previously been considered. For instance, through our work on the decomposition of LiPF₆, we realized that to stop PF₅ from reacting would be to limit its contact with Li₂CO₃; this suggests that mass transport through the growing SEI should be considered when designing and engineering interphase-forming electrolytes.

Electrolyte Decomposition is Electrochemical

Even the most basic and seemingly innocuous assumption can lead us as researchers astray. It is perhaps obvious and intuitive to think that electrolyte decomposition and interphase

formation in batteries are electrochemically driven. And, ignoring native passivation films on reactive electrode materials like Li and Mg metals, this is probably true to some extent. However, it would be an error to think that *all* electrolyte reactivity is electrochemical in nature.

In our work, we identified two important cases where electrochemistry has little or nothing to do with important electrolyte decomposition reactions. In Chapter 3, we found that LiPF₆ could react to form LiF, POF₃, LiPO₂F₂, CO₂, and more through purely chemical reactions with Li₂CO₃. While it is true that, during SEI formation, Li₂CO₃ itself can be formed initially by electrochemical reduction, even Li₂CO₃ does not *necessarily* form electrochemically, as it is an impurity formed when synthesizing oxide positive electrodes. We also found in Chapter 7 that G2 could catalytically decompose via a chemical mechanism involving methoxide. Again, this methoxide could and likely does initially form electrochemically, but the main catalytic mechanism is entirely chemical in nature. I strongly suspect that many other important, non-electrochemical reaction pathways are taking place in current commercial and next-generation batteries, and that we as a field are missing them because we are only looking for processes driven by charge transfer.

8.2 A New Approach to Studying Electrochemical Reactivity

CRNs are an extremely powerful and promising tool in the tool-belts of electrochemists, with the potential to either directly answer or assist in answering all of the key questions surrounding electrolyte reactivity. With the work presented in this dissertation, the promise of CRNs is closer to being realized. Whereas the earlier work of Blau et al.[211] and Xie et al.[212] were able only to identify pathways to known products (limiting their predictive and exploratory capacity), the methods developed by my colleagues and me in Chapter 4 and demonstrated in Chapter 5 enables for the first time the simultaneous prediction of electrolyte degradation products and formation mechanisms. Combining CRN analysis with microkinetic modeling in Chapter 6, we were able to not only reproduce an experimentally observed bilayer interphase structure but explain the origins of that structure and how it was affected by the presence of impurity and additive species.

CRNs should not be considered only as tools for computationalists. Rather, I am excited by the possibility of CRNs being used alongside experimental characterization. As we demonstrated in Chapter 7, there is natural synergy between experimental spectroscopy and CRN analysis. CRNs can be used to predict what species might be detected in spectra and explain their mechanistic origins. At the same time, experimental spectra can provide necessary validation for CRN predictions and potentially reveal gaps in CRN construction or analysis. Thus far, we have only explored using CRNs alongside DEMS characterization, but in the near future, I hope that CRNs will be used with NMR and FT-IR spectroscopy.

At this point, I believe that we have the necessary tools to make *a priori* predictions

of (electro)chemical reaction cascades and interphase formation, but this goal has not been met in full. First and perhaps most importantly, the current methods available fall short of being truly predictive. In the two applications that I discussed in this dissertation – SEI formation in LIBs and MIBs – there was either extensive prior knowledge available in the literature which informed our analysis or experimental evidence available for comparison and validation. Even in these cases, we were not able through CRN analysis alone to exactly reproduce experimental findings, predicting spurious network products that do not actually emerge in real battery systems. Likely, the main weakness of our current approach for CRN analysis is that it relies exclusively on reaction thermodynamics and ignores kinetic barriers. This presents two new avenues for CRN method development:

1. Limiting the scope of CRN construction such that high-throughput DFT can be used to calculate the energy barriers of all reactions in the network
2. Leveraging ML to predict cheaply calculate approximate energy barriers, allowing for kinetic information to be included in even very large networks containing many millions of reactions

In addition to potentially aiding in the predictive capacity of CRNs, advances in either of these areas would lower the high computational barrier to CRN studies.

A less severe limitation of my work up to now is that my colleagues and I have not yet proven the ability of our CRN methodology to compare the reactive behavior of different electrolyte components. This ability will be important for applications such as high-throughput screening of electrolyte additives, where many (often chemically similar) species are compared to determine which candidates perform best for a given application. Future work should focus on comparative CRN studies. In addition to being practically useful, I suspect that such efforts may reveal additional areas for methodological improvement.

8.3 CRNs Beyond Metal-Ion Batteries

Complex, difficult-to-characterize reaction cascades are not unique to batteries. Many technologically relevant processes, in electrochemistry and elsewhere, involve such messy reactivity. But automated CRN analysis has only been widely applied in a small number of chemical domains, as I alluded to in Chapter 2. This disconnect provides fertile ground for future research.

I believe that the CRN tools that my colleagues and I have developed can be broadly applied outside of battery electrolyte degradation. Indeed, we designed our CRN construction and analysis tools to be highly general and flexible, accommodating diverse species and (electro)chemical reactions. I will not enumerate all of the areas where our methods should be applied, but it is worth providing a short list of examples, noting important similarities to electrolyte degradation and interphase formation, where appropriate.

Electrochemical Synthesis

Most chemical and material synthesis today is thermochemical, requiring elevated temperature to drive reactions forward towards desired products.[380, 381] In particular, many commodity compounds, including steel, cement, and ammonia, are extremely energy intensive[382] and rely on fossil fuels for power.

Electrochemical synthesis offers an alternative to conventional thermochemical methods. Using an applied potential unlocks new reaction pathways that may not be accessible thermochemically, enabling energy-efficient synthesis under relatively mild conditions.[383] And since electrochemical synthesis only requires an electrical current, it is in general straightforward to drive the synthesis using renewable electrical energy from e.g. solar and wind sources rather than fossil fuels.

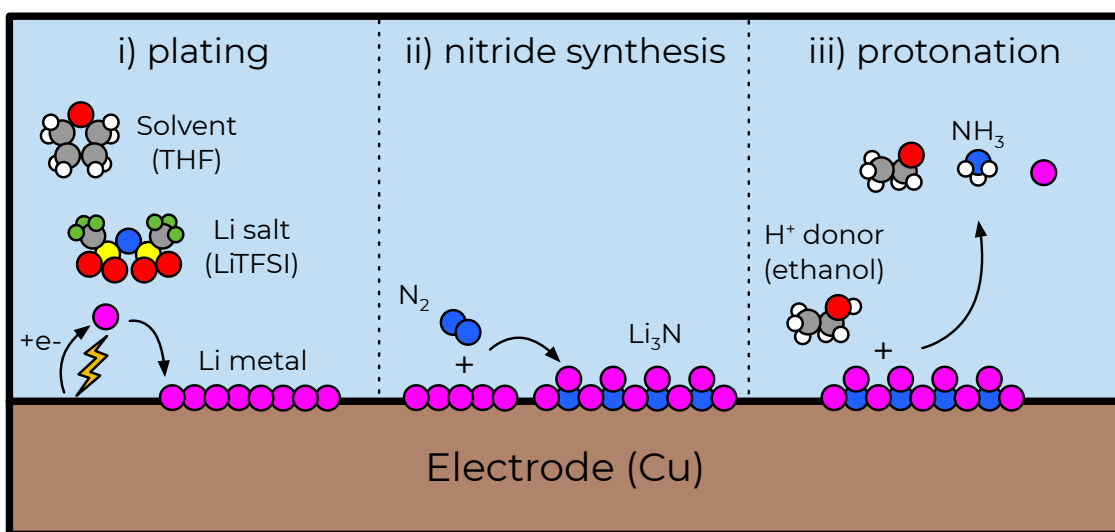


Figure 8.1: Stages of LMEAS: i) electrochemical lithium plating; ii) chemical reaction of lithium and N₂ to form Li₃N; iii) protonation of Li₃N to form NH₃. In this example, the electrode is copper (Cu) the solvent is tetrahydrofuran (THF), the salt is lithium bistriflimide (LiTFSI), and the proton donor is ethanol.

As I have emphasized earlier in this Dissertation, electrochemistry is often characterized by reaction cascade processes, the mechanisms of which are poorly understood. In general, this makes electrochemical synthesis an ideal application of CRN-based approaches such as those described in previous chapters. One particularly attractive target of study is ammonia (NH₃) synthesis. (NH₃) is currently produced almost exclusively using the Haber-Bosch process, which requires high temperatures (~ 500 C) and pressures (~ 100 bar) to drive the reaction $N_2 + 3 H_2 \longrightarrow 2 NH_3$.[384] In this reaction, nitrogen comes from air, while hydrogen comes from petrochemical cracking. Because NH₃ synthesis is so energy intensive and NH₃ is

one of the most widely used chemicals on Earth, with 185 million tons produced per year as of 2020,[385] the Haber-Bosch process accounts for roughly 1% of global energy consumption and 1.4% of global greenhouse gas emissions.[386]

Lithium-mediated electrochemical ammonia synthesis (LMEAS) is an alternative to Haber-Bosch that works by i) electrochemically plating Li; ii) chemically reacting Li with N₂ to form Li₃N; iii) reacting Li₃N with a proton donor (e.g. ethanol) to form NH₃ and reform dissolved Li⁺ (Figure 8.1). As in LIBs, electrolytes in LMEAS decompose to form interphases.[387] In this case, a functional SEI has not only low electronic conductivity and high Li⁺ conductivity but is also selectively permeable to N₂ and protons or proton donors, allowing the gas to access plated Li. While it is now recognized that a functional SEI is essential to efficient LMEAS,[388] the composition and structure of these SEI layers have not been well characterized by experiment or theory, to say nothing of the electrolyte decomposition mechanisms. The similarities between LMEAS and LIB SEI formation make it natural to apply CRNs in this domain. Following the progression that I have demonstrated in this Dissertation, studies should begin with predicting the products of electrolyte degradation and their formation mechanisms, followed by microkinetic studies that enable analysis of how SEI composition depends on variables such as applied potential, location relative to the working electrode, and time.

Wastewater Valorization

Wastewater includes pollutants derived from homes, industrial buildings, and other sources such as runoff from rain. While many of these pollutants are inherently harmful, including heavy metals[389] and microbial pathogens,[390] there are opportunities to extract dissolved pollutants and use or re-use them industrially. In particular, wastewater is often rich in nitrogen and phosphorus,[391] which are valuable for their utility as ingredients in agricultural fertilizers. As I have already mentioned, nitrogenous fertilizers based on ammonia have a considerable environmental impact, while phosphorus resources are at risk of depletion if circular recovery and reuse efforts are not implemented.[392] Recovering nitrogen and phosphorus would further limit eutrophication, in which nutrient overabundance causes environmentally detrimental and toxic algae blooms.[393]

A variety of chemical methods have been proposed to extract phosphorus and nitrogen from wastewater,[394, 395] and in particular to convert the dissolved nitrogen and phosphorus nutrients (e.g. NO₃⁻ or PO₄⁻³) to more valuable compounds such as NH₃.[396] By its nature, wastewater is a highly impure mixture, so valorization efforts again need to be highly tolerant to a wide range of impurity species. As I have demonstrated (see especially Chapter 6), CRNs can elucidate impurity effects in reaction cascades, especially when dynamical simulations are performed. I believe CRNs could aid in the design of highly selective (electro)catalysts for water remediation and valorization of aqueous waste.

Circular plastic recycling

More than half of all plastics produced are discarded,[397] leading to plastic waste being found essentially everywhere on Earth, from the depths of the ocean to human tissue and the very air we breathe.[398–400] Conventional recycling based on mechanical grinding fails to meaningfully address this waste crisis, producing plastics with inferior properties[401] that rapidly reenter the waste stream.[397] Chemical recycling could completely avoid waste by depolymerizing plastics to short-chain oligomers and monomers.[402] Recent years have seen huge advances in circular chemical recycling methods for plastics, including the development of new, recyclable chemistries like poly(diketoenamines)[403, 404] and methods to recycle existing plastics such as poly(ethylene terephthalate).[405]

However, significant work is still required to realize a truly circular plastic economy. For instance, polyolefins such as polyethylene and polypropylene, which make up more than half of all plastic waste,[397] are notoriously difficult to chemically recycle because they are composed entirely of unreactive C-H and C-C bonds. Recent work has shown that organometallic homogeneous catalysis could enable efficient and selective polyolefin depolymerization via mechanisms including hydrogenolysis, ethenolysis, and hydrolysis,[406–410] but the field of polyolefin depolymerization remains in its infancy.

The organic chemistry underlying polymer (de)polymerization is well understood compared to battery electrochemistry. Nonetheless, the design of depolymerization reactions is not at all straightforward. Care must be taken to select catalysts that react selectively with the polymers of interest and do not react promiscuously with other polymers, plasticizers, and additives. Catalyst stability is another considerable challenge. For chemical recycling to be economically competitive, costs must be kept low, requiring catalysts that stay active for long times. CRNs could assist in the design of catalytic depolymerization reactions, providing an understanding of catalyst degradation pathways and possible side reactions with e.g. plasticizers. Through dynamical simulations, it would also be possible to predict the distribution of products, aiding in the selection of catalysts and reaction conditions that favor the production of monomers (e.g. ethylene and propylene) over diverse oligomers.

8.4 Final Reflections

I have been told repeatedly from several sources that I consider to be knowledgable that “no one will read [my] dissertation”. This may be true. But if someone does decide to read through this tome that I’ve constructed, I want it to be worth the time spent. I want you, dear Reader, to get as much wisdom as I can reasonably share. Here, in the last pages that I write, I will list some thoughts, more or less disconnected from the main ideas of this thesis, that have nonetheless been critical to the research that I have performed.

- Ignore disciplinary labels: My academic training is entirely in materials science, and upon entering my doctoral studies, I had little formal knowledge of chemistry, chemical engineering, or computer science. My doctoral research, however, required strong

attention to all of these fields, not to mention some comfort with applied mathematics and a healthy understanding of electrochemistry. From time to time, I have thought about why I was able to make progress in the field of electrochemical reactivity and batteries, why my colleagues and I were able to answer questions that in some cases had eluded the field for many years. Part of it is certainly timing — modern high-performance computing facilities made my work considerably easier than it might have been previously — but the main conclusion that I came to was that, perhaps, no one else wanted to. Or, more plainly, no one else wanted to combine the ideas and fields that were necessary to do the work that my colleagues and I ended up doing. I do not think that it is a coincidence that my close collaborators include a mathematician and several physicists. My wandering into new territories, picking up stray bits of information here and there, and working with people far outside of my field of study were all deeply valuable to my scientific process and progress.

- Read the old literature: At least in the conversations that I have been witness to, in-person and online, it has become fashionable to say that it is not important to read the literature, and in particular, that the articles that are most important are the ones written most recently, in the preceding five to ten years. In my own experience, many of the most important ideas for my work came from interactions with old articles. Without reading some of Marcus' original papers on quasiclassical electron transfer theory,[338] I would have had no idea how to treat electrochemical reactions in my own simulations. I became comfortable with potential energy surface exploration — critical for computational geometry optimization, transition-state searches, etc. — by reading early works by Bernhard Schlegel and his contemporaries.[411–416] And so on. It can be daunting to search through the literature, and especially to look for papers from 20, 30, 50, or even more years ago. It can feel like a waste of time to wade through ideas from the past when certainly (one might think) something better has been devised since the early papers were written. And yet, I must insist that these excursions into the past can be far more illuminating than skimming the latest abstracts in hot journals.
- Give up: During my doctoral studies, I had to learn to step away from projects that were succeeding and failing. When a project goes well, I have noticed a tendency in many scientists towards perfection. Keep making the outcome — code, a paper, a presentation — better and better. Leave no loose ends, no flaws, no lingering questions. But perfection is unachievable, and the pursuit of perfection not only hurts the individual researcher — leading them down a road of potential misery and madness — but can also hurt the research community. If a preprint or paper is delayed by a year or longer because it is not yet “perfect”, that means that the field cannot build on that work for that long or longer! On the other hand, I have struggled to give up on projects that were floundering. In my own experience, I do not believe that any of these projects were doomed. None of them went against the laws of physics or

demanded more than modern-day technology could allow. However, these projects required a different approach, a new perspective, more hands, or more time. Sometimes, I realized, I just didn't have the resources to give to make the project successful, and the only way that I could finish my other projects was to let the failing ones go. I cannot give any hard and fast rules for when a project must be stopped, successful or failing, but any aspiring researcher must take pains to discover when to give up, and to be willing to make the choice when necessary.

Appendix A

Data Availability

A.1 Data associated with Chapter 3¹

We have distributed data for Chapter 3 as a JavaScript Object Notation (JSON)-formatted file `pfx_named_data.json` on Figshare (DOI:10.6084/m9.figshare.21583581.v1).[417] `pfx_named_data.json` contains the structures (as serialized Pymatgen[316] `Molecule` objects) and thermochemical properties of the reaction endpoints and TS reported in this work. The key for each key-value pair in `pfx_named_data.json` is the name of the species as reported in the main text or this Supporting Information. For instance, the data for TS_{11} would be found under the key “ $\text{TS}11$ ”. For reactions where species, namely LiF, HF, and CO_2 , are removed (for details, see Appendix B.1), two entries for the relevant endpoint are provided. The species with LiF, HF, and/or CO_2 present are named “ Mn ”, where n is the appropriate index; the species with the species removed are named “ $\text{Mn-}x$ ”, where x is the species that is removed. Where multiple species are removed, the name takes the form “ $\text{Mn-}x\text{-}y$ ”, where x and y are the species removed.

To load this data in Python, use monty (<https://github.com/materialsvirtuallab/monty>):

```
from monty.serialization import loadfn

data = loadfn("pfx_named_data.json")
```

¹This section is closely adapted from Ref [216]: Spotte-Smith*, E.W.C.; Petrocelli*, T.B; Patel, H.D.; Blau, S.M.; Persson, K.A. Elementary decomposition mechanisms of lithium hexafluorophosphate in battery electrolytes and interphases. *ACS Energy Letters* **2023**, 8(1), 347–355.

A.2 Data associated with Chapter 5²

Data for 17,190 molecules generated using an ω B97X-V/def2-TZVPPD/SMD level of theory are provided in a Figshare repository.[418] The data, including optimized 3D coordinates, partial charges and spins (from Mulliken population analysis,[419] the Restrained Electrostatic Potential (RESP) method,[420] and Critic2), molecular connectivity information, vibrational information (frequencies, vibrational mode vectors, IR intensities), and thermodynamic quantities (energy, enthalpy, entropy, Gibbs free energy), are contained in a single JSON-formatted file, `libe.json`. Molecules for which calculations failed or which otherwise failed the tests described in the Validation section of Chapter 5 are not included in this collection.

All data used to construct mechanisms (molecular structures, thermodynamics, vibrational frequencies, and frequency modes) are also provided in JSON format in the supplementary file “`reaction_pathways.json`”.

A.3 Data associated with Chapter 7³

The computational data used in this study is publicly available in a Figshare repository (DOI: 10.6084/m9.figshare.22189810.v1). Two Javascript Object Notation (JSON) files are included in this repository. `madeira.json` includes the properties (including structural, electronic, bonding, vibrational, and thermodynamic properties) of the 11,502 species in the MADEIRA dataset. `pathway_data.json` includes a more limited set of structural and thermodynamic properties calculated for all minima and transition-states reported in this work, labeled as they are in Figures 7.3 and 7.4 in Chapter 7.

²This chapter is adapted from the following references: [253]: Spotte-Smith*, E.W.C.; Blau*, S.M.; Xie, X.; Patel, H.D.; Wen, M.; Wood, B; Dwaraknath, S.; Persson, K.A. Quantum chemical calculations of lithium-ion battery electrolyte and interphase species. *Scientific Data* **2021**, *8*(203); [254]: Barter*, D.; Spotte-Smith*, E.W.C.; Redkar, N.S.; Khanwale, A.; Dwaraknath, S; Persson, K.A.; Blau, S.M. Predictive stochastic analysis of massive filter-based electrochemical reaction networks. *Digital Discovery* **2023**, *2*, 123–137.

³This chapter is adapted from reference [358]: Spotte-Smith, E.W.C., Blau, S.M., Barter, D., Leon, N.J., Hahn, N.T., Redkar, N.S., Zavadil, K.R., Liao, C., Persson, K.A. *Journal of the American Chemical Society* **145**(22), 12181–12192.

Appendix B

Additional Methods

B.1 Methods associated with Chapter 3¹

Transition-states (TS) were identified using the AutoTS algorithm[421] which relies on the Jaguar electronic structure code.[422] In cases where AutoTS could not identify a TS, the single-ended growing string method (SE-GSM)[423] was used. Specifically, the pyGSM implementation of SE-GSM [424] was used with the Q-Chem electronic structure code version 5.4.2 as the back-end.[265] TS identified using pyGSM were re-optimized in Jaguar to ensure consistency. To reduce computational costs, these calculations were conducted using the range-separated hybrid generalized gradient approximation (GGA) density functional ω B97X-D,[425] def2-SVPD basis set,[300, 301] and Conductor-like Screening Model (COSMO)[426, 427] implementation of the polarizable continuum model (PCM)[304] with water as the solvent. In Jaguar, all basis functions representing f and higher orbitals were removed to further reduce cost, making the basis more precisely def2-SVPD(-f). All TS were confirmed to have one imaginary frequency and to connect to the expected endpoints. The electronic energies of all TS and reaction endpoints (reactants and products) were corrected with single-point energy evaluations in Jaguar using range-separated hybrid meta-GGA functional ω B97M-V with the def2-TZVPD basis set in COSMO. Note that ω B97X-D and ω B97M-V density functionals perform excellently on benchmarks of reaction energies and energy barriers.[135]

In general, reaction free energies ΔG and energy barriers ΔG^\ddagger are reported using the calculated Gibbs free energies of the optimized reaction entrance and exit complexes (as opposed to the isolated reactants and products at infinite separation). Some exceptions are made, for instance in the case where optimization of an endpoint fails due to multiple fragments flying away towards infinite separation. In all reported reaction mechanisms, species not prefixed by “M” - for example, LiPF₂O₂ + PF₅ in Figure 3.4 - indicate that an

¹This section is closely adapted from Ref [216]: Spotte-Smith*, E.W.C.; Petrocelli*, T.B; Patel, H.D.; Blau, S.M.; Persson, K.A. Elementary decomposition mechanisms of lithium hexafluorophosphate in battery electrolytes and interphases. *ACS Energy Letters* **2023**, 8(1), 347–355.

infinite separation approximation was used.

In the energy diagrams shown in Chapter 3, there are several reactions where species are removed. For example, in Figure 3.1 of the main text, HF is removed in the reaction $M_2 \longrightarrow M_3$, and in Figure 3.2 of the main text, LiF is removed in the reactions $M_8 \longrightarrow M_9$ and $M_{12} \longrightarrow M_{13}$. In all such cases, we assume that the removal of those dissociated species from the reacting complex is isergonic ($\Delta G = 0.0$ eV), and we do not show the complex without the removed species in the energy diagrams. However, as we note above (see Appendix A), we always performed optimizations on the associated reaction endpoints with and without the removed species (HF, LiF, and/or CO₂) as part of our process to verify TS.

For correlation plots between reaction energy and partial charge, partial charges were obtained using the Natural Bonding Orbital (NBO)[428] program version 7.0.[429] For the species considered in Chapter 3 (Li₂CO₃, LiHCO₃, and H₂CO₃), single-point energy evaluations were performed on structures from the LIBE dataset[253] (see Chapter 5 using the ωB97X-V range-separated hybrid GGA functional,[298] def2-TZVPPD basis set,[301] and SMD implicit solvent model[302] (with EC/EMC as the solvent)). Unless otherwise noted, only the partial charges of the most negatively charged oxygen atoms are reported.

Rate coefficients are calculated using the Eyring equation:

$$k = \frac{k_B T}{h} \exp\left(\frac{-\Delta G^\ddagger}{k_B T}\right) \quad (\text{B.1})$$

where k_B is the Boltzmann constant, h is the Planck constant, ΔG^\ddagger is the reaction energy barrier, and T is the absolute temperature.

B.2 Methods associated with Chapter 5²

Identification of Bonding In Molecules

Much of the HiPRGen method of CRN generation relies on bonding - to identify coordimers, to filter species, and to filter reactions (more details below). It is therefore worthwhile to describe how bonds are identified in HiPRGen.

In this work, HiPRGen took as input entries from the LIBE dataset. Two possible modifications can be made to the LIBE-defined bonding. First, in rare cases, molecules in LIBE contain hydrogen atoms with two covalent bonds. Where this occurs, we discard the longer of the two bonds. Second, we re-assess coordinate bonds. In addition to any coordinate bonds present in the molecular graph representation in LIBE, we include any coordinate bonds between Li⁺ and an atom X if

²This chapter is adapted from Ref [254]: Barter*, D.; Spotte-Smith*, E.W.C.; Redkar, N.S.; Khanwale, A.; Dwarakanath, S; Persson, K.A.; Blau, S.M. Predictive stochastic analysis of massive filter-based electrochemical reaction networks. *Digital Discovery* **2023**, 2, 123–137.

1. X has a partial charge less than 0, as calculated by either the Mulliken or Restrained Electrostatic Potential (RESP) methods
2. The distance between Li^+ and X is less than or equal to 2.4 Å (note that the distance cutoff in LIBE is slightly larger, at 2.5 Å).

Modifying Species Thermodynamics

All calculations on the species present in LIBE were conducted in an implicit solvation environment. While implicit solvation is generally accurate enough for the calculation of properties such as the solvation energy[320] and redox potentials of organic molecules,[322] we have found that even highly accurate implicit solvation methods severely underestimate the stabilization of small ions, especially metal ions, by solvent. This means that species in LIBE containing Li^+ ions with many coordination bonds are in many cases vastly more stable according to DFT than those with fewer coordination bonds, even if the corresponding species without lithium present are significantly less stable. As an example, we show LEDC (Figure B.1). In previous molecular dynamics studies,[133, 155, 156] it has generally been found that LEDC prefers a roughly linear conformation both when ordered in the solid state and when present in an amorphous SEI or liquid electrolyte. However, when using SMD with DFT, a “puckered” conformation is preferred by 0.68 eV because each Li^+ has 3 coordinate bonds (compared to only two in the linear LEDC conformation). As further evidence that this result is based solely on the insufficient stabilization of the Li^+ , upon removing the Li^+ from the puckered conformation, the structure optimizes to a roughly linear conformation. When the solvation correction is applied, the linear conformer is identified as the more stable by 0.68 eV. The insufficient stabilization of Li^+ leads to unreasonable structures and should be expected to result in inaccurate thermodynamics for reactions where the overall charge of the system was constant but the number of coordinate bonds changed (non-redox reactions).

To correct for the inaccurate Li^+ stabilization of SMD, we sought to approximate the stabilizing effect of a solvation shell comprised of ethylene carbonate (EC). Specifically, we assume that all species in our CRN are sufficiently stable such that all Li^+ ions have full solvation shells consisting of four coordinate bonds (either from solvent or other coordinating species). To correct for insufficient metal ion stabilization, we optimized $\text{Li}^+ \text{EC}_n$ clusters at the $\omega\text{B97X-D}/\text{def2-SVPD}/\text{PCM} // \omega\text{B97X-V}/\text{def2-TZVPPD}/\text{SMD}$ level of theory, with $n \in 0, 1, 2, 3, 4$ to estimate the stabilizing effect of each solvent molecule on Li^+ . The lower level of theory ($\omega\text{B97X-D}/\text{def2-SVPD}/\text{PCM}$, $\epsilon = 18.5$) was used for optimization due to the considerable computational cost of optimizing large clusters. The relative stabilization was calculated as

$$\Delta E = E_{\text{Li}^+ \text{EC}_n} - E_{\text{Li}^+} - nE_{\text{EC}} \quad (\text{B.2})$$

Performing this calculation with $n = 0, 1, 2, 3, 4$, we obtain a roughly linear trend (Figure B.2) with slope -0.746 eV/(molecule EC) ($R^2 = 0.994$). When free energy is accounted for, this solvent correction to the electronic energy (-0.746 eV per missing coordinate bond) actually results in the coordination of Li^+ with EC being slightly endergonic. We therefore

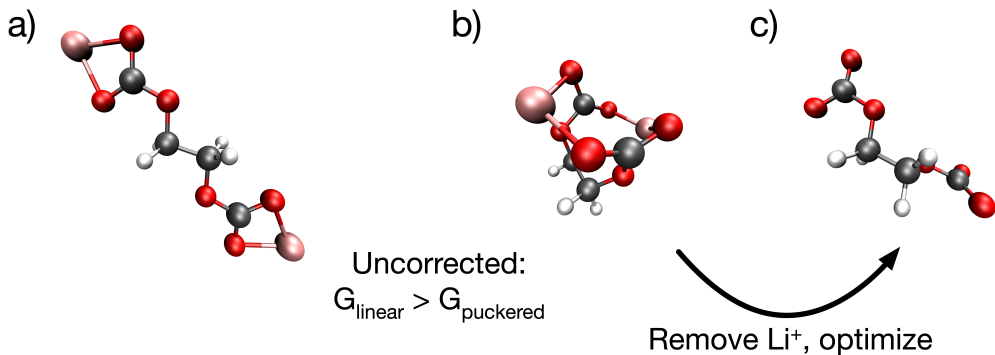


Figure B.1: Conformations of LEC. The linear conformer (libe-115795, **a**) is less stable than the puckered conformer (libe-652486, **b**) by 0.68 eV, although the linear conformer is more commonly observed in all-atom molecular dynamics simulations. When the Li^+ are removed from the puckered conformer and the structure is re-optimized (charge -2), a roughly linear conformer is again obtained (**c**), indicating that the puckered conformer is only preferred because of the insufficient stabilization of Li^+ in implicit solvent.

alter this value to -0.68 eV, at which point the coordination of Li^+ with EC is essentially isergonic (-0.01 eV).

For reactions where the number of coordination bonds does not change (Figure B.3a), the same correction is applied to the reactants and the products, so there is no net effect on the reaction thermodynamics. However, if there is a change in the number of coordinate bonds between reactants and products (Figure B.3b), then the solvation correction alters the reaction free energy ($\Delta\Delta G = 0.68(\Delta n_c)$), where Δn_c is the change in the number of coordinate bonds in the reaction ($\Delta n_c = n_{c,\text{products}} - n_{c,\text{reactants}}$). In some cases, this change can make reactions that are endergonic without a solvation correction exergonic, and vice versa.

When Not to Apply a Solvation Correction

Redox reactions: Initially, we applied a solvation correction to all reactions, including reduction and oxidation reactions. However, based on previous studies that showed that SMD can be used for the accurate prediction of redox potentials,[322] we evaluated this choice using a small benchmark, comparing the uncorrected redox potentials calculated using the data in LIBE to experiment.

The experimental data relevant to molecules in lithium-ion battery electrolytes is relatively scarce. While some redox potentials for common electrolyte species have been reported in the literature, even comparing to this data must be done with caution because there can be considerable uncertainty and disagreement between measurements. For instance, the reduction potential of EC has been measured to be as low as +0.35V[430] and as high as

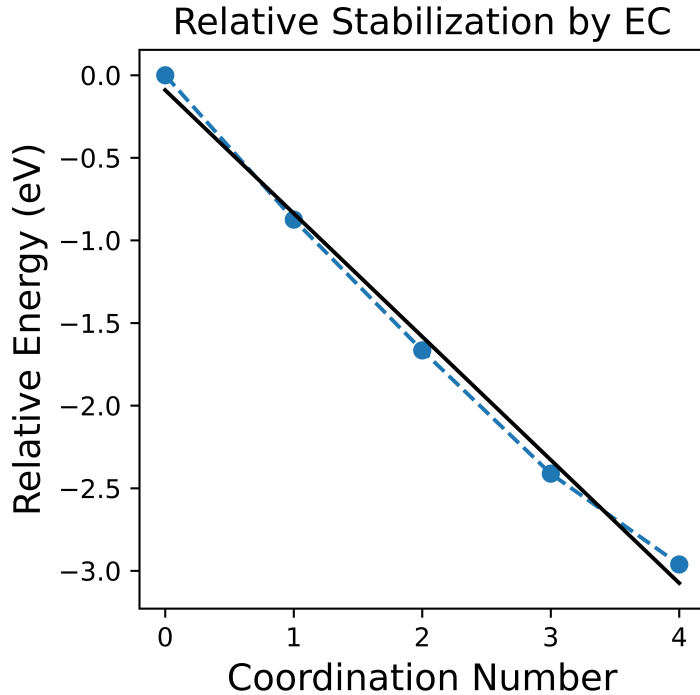


Figure B.2: Relative stabilization of Li^+ by increasing numbers of EC.

$+1.36\text{V}$ [431] vs. Li/Li^+ (though the most common value seen in the literature is around $+0.75\text{V}$). Moreover, side reactions like the trans-esterification of linear carbonates[432] make the interpretation of experimental data challenging. We calculate reduction potentials as

$$E(\text{Li}/\text{Li}^+) = -(G_{\text{reduced}} - G_{\text{non-reduced}}) - 1.4 \text{ V} \quad (\text{B.3})$$

and oxidation potentials as

$$E(\text{Li}/\text{Li}^+) = (G_{\text{oxidized}} - G_{\text{non-oxidized}}) - 1.4 \text{ V} \quad (\text{B.4})$$

where all free energies are given in units of eV. The scaling factor of $\sim -1.4 \text{ V}$, derived from the difference between the energy of an electron in vacuum (-4.44 eV) and the absolute potential of a Li electrode (-3.05 eV),[20] converts the calculated reduction potential to be relative to a Li/Li^+ reference electrode, which is standard in the lithium-ion battery community.

As can be seen, our calculations tend to somewhat underestimate reduction potentials (except for EMC, which we note has a somewhat more approximate experimental reduction potential). However, we are generally quantitatively close to the experimental value (within roughly 0.2V), and we correctly capture trends - for instance, that the electrolyte additives

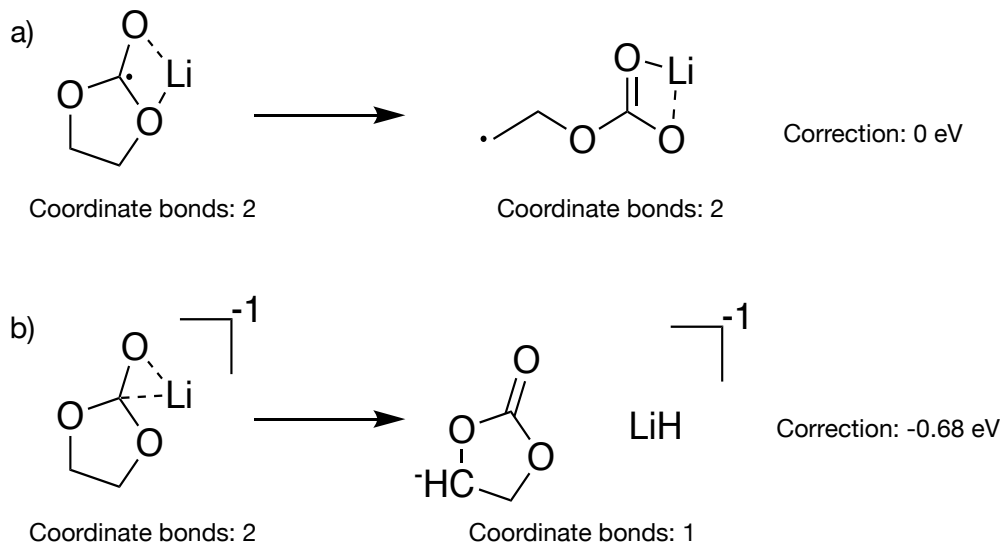


Figure B.3: Solvation corrections applied to reactions with bonds changing. a) When the number of coordinate bonds in the reactants and the products are the same, then the correction to the reaction free energy is 0 eV. b) However, when there is a change in the number of coordinate bonds (here, there are two coordinate bonds in the reactants and only one in the products), then the reaction free energy changes based on the change in coordinate bonds.

Molecule	ID (non-reduced)	ID (reduced)	E_{red} (V) (calc)	E_{red} (V) (exp)
LiEC	libe-115918	libe-115782	0.65	0.75[348]
LiVC	libe-115855	libe-120798	0.87	1.0[348], 1.1[433]
LiFEC	libe-135858	libe-140687	0.97	0.9, 1.15[348]
LiDEC	libe-173831	libe-173906	0.60	0.71 - 0.90[434]
LiEMC	libe-173686	libe-173778	0.62	\approx 0.45[348]

Table B.1: : Comparison of computed and experimental reduction potentials for lithium-ion battery electrolyte solvents coordinated with Li^+ .

FEC and VC should reduce before EC, and that cyclic carbonates are in general easier to reduce than linear carbonates. With the exception of EC, for which we significantly overestimate the oxidation potential, our calculated E_{ox} are in excellent agreement with experiment. Because of this generally good agreement, we chose not to include a solvation correction for redox reactions.

Full Mechanisms: Perhaps surprisingly, we only apply a solvation correction to reactions where energy barriers are unknown. The reason is based on the initial assumption of the solvation correction - that at all points, Li^+ has a full solvation shell. This is effectively

Molecule	ID (non-oxidized)	ID (oxidized)	E_{ox} (V) (calc)	E_{ox} (V) (exp)
EC	libe-115834	libe-115879	6.98	6.2[435]
DMC	libe-202458	libe-202592	6.84	6.7[435]
DEC	libe-175140	libe-175285	6.69	6.7[435]
EMC	libe-185427	libe-186936	6.74	6.7[435, 436]

Table B.2: : Comparison of computed and experimental oxidation potentials for lithium-ion battery electrolyte solvents.

an equilibrium or quasi-equilibrium argument. At any particular moment in time, fluctuations in the electrolyte may cause Li^+ to have either less than or more than the preferred number of coordinate bonds. These fluctuations should be relatively rare, however, and on average we expect the coordination number of Li^+ to be four.

This argument breaks down at the TS. TS are inherently points of instability that are typically occupied for vanishingly small times. Moreover, at the TS, bonds are commonly in a state of rearrangement - forming and breaking. While it is possible that all Li^+ might be fully coordinated at a TS, there is no reason why this should be so in general. Rather than try to apply an equilibrium argument to a non-equilibrium point of the potential energy surface, we choose not to apply a solvation correction at TS. To be consistent with this choice, when reporting full mechanisms, all free energies are uncorrected. We note that devising reasonable corrections for the energy or free energy of full reaction mechanisms in solution, including TS, is a topic for future research.

Species Filtering

In the HiPRGen package (see Appendix), we implement a number of filters that remove undesirable species. These filters take as input an object containing information about a molecule, including its species, coordinates, charge, spin multiplicity, partial charges, connectivity, and thermodynamics. Each filter, based on this information, can discard the molecule or pass it onto the next filter. For terminal filters, if the molecule passes, then it is included in the final filtered set $\mathbf{S}_{filtered}$. For this work, we applied the following filters:

- 1. Metal non-cation filter:** Remove species with a lithium atom with an NBO partial charge less than 0.1. We assume that if a Li^+ ion is reduced, it should rapidly desolvate and either plate or intercalate. Therefore, we do not want to include any species containing Li^0 or Li^- in the CRN.
- 2. Molecule not connected:** Remove species that do not have a connected full molecule graph as defined by both covalent and coordinate bonding. This indicates that the structure contains separate molecules and should not be treated as a single species in the CRN. Each network species being an individual molecule is essential for bounding

complexity. If a species is allowed to be composed of multiple molecules, the number of species grows substantially without any benefit, e.g. [A, B, C] becomes [A, B, C, A+B, A+C, B+C, A+A, B+B, C+C, etc]. Meanwhile, the number of reactions similarly grows without encoding any new information, e.g. “A and B react to form C” ends up being represented additionally as “A+B reacts to form C” and “A and B+C reacts to form C+C” and “A+B and C reacts to form C+C” and “A+A and B react to form A+C”, etc.

3. **Metal-centric complex:** Remove species which only have a connected full molecule graph due to the presence of a metal ion, e.g. A — Li⁺ — B. Since metal coordinate bonds are electrostatic interactions that are typically much weaker than covalent bonds, such a species is effectively disconnected A and B molecules which can in principle participate in all of the same reactions that A or B or Li⁺A or Li⁺B could participate in individually. Therefore, for the same reasons stated above, such species must be removed. Chemically, this is equivalent to assuming that non-solvent molecules exist in sufficiently low concentration that each Li⁺ is always coordinated to at most one non-solvent molecule. In the future, we will explore situations where this approximation breaks down, but it is presently necessary.

In addition to these filters, which define types of molecules to be excluded from the final network, we further reduce the molecules in the network by removing redundant species. In LIBE, all molecules are unique based on the combination of their charge, spin multiplicity, and molecular connectivity. This means that there could be several molecules that differ only by spin multiplicity, or that differ only by the coordination environment of Li⁺ ions (what we call “coordiners”). When this occurs (when there are multiple molecules with the same *covalent* connectivity and charge but potentially with different coordination environments or spin multiplicities), we include only that species with the lowest solvation-corrected free energy in the final filtered set of species $\mathbf{S}_{\text{filtered}}$.

We emphasize that these filters are particular to the chemistry being studied in this work, but that HiPRGen has been engineered to enable straightforward addition, removal, or modification of filters in order to be easily applied across diverse chemical applications.

Reaction Filtering

Reaction filters take as input a reaction, defined by a collection of reactants and a collection of products, and either discard the reaction or pass it onto the next filter until a terminal filter is reached. While chemical examples and TS from our specific system motivate and justify some of the filters developed, we believe the filters are generally applicable as a starting point to model a diverse range of complex reactivity. Further, HiPRGen has been intentionally engineered to enable the straightforward addition of new filters as well as the modification or removal of any of the filters employed in this work in order to be easily customized to suit any system of interest. The following types of reactions were filtered out in this work:

1. **Redox reactions**, as defined by a change in total charge between reactants and products:

- a) **Too many reactants or products**: Remove redox reactions with more than one reactant or more than one product. This partially enforces the assumption that redox reactions occur separately from covalent bond breakage/formation. While there are known dissociative redox reactions, in which a redox process occurs simultaneous with a covalent bond breakage,[437] they are uncommon, and thus we exclude them in general.
- b) **Reactant and product not covalent isomorphic**: Remove redox reactions with one reactant and one product where the covalent bonds of the reactant and product are not equivalent. In combination with the previous filter, this completes enforcement of the assumption that redox reactions occur separately from covalent bond breakage/formation. Note that Li^+ coordinate bonds are allowed to change during a redox reaction as long as there is at least one coordinate bond in both the reactant and the product.
- c) **Change in charge too large**: Remove redox reactions involving the simultaneous addition or removal of two electrons. As above, there are known simultaneous two-electron redox processes, but they are very rare, and thus we exclude them in general.

2. **Both redox and non-redox reactions**:

- a) **ΔG above threshold**: Remove all reactions with $\Delta G > 0$ eV. If we include endergonic reactions over even a very small range - e.g. corresponding to the expected magnitude of DFT uncertainty or what would be thermally accessible - then we introduce loops into our CRN, as the corresponding exergonic reverse reactions will also be present. Such loops are detrimental to pathfinding, as trajectories become filled with unimportant back-and-forth processes. This in turn obscures network product identification which depends on meaningful counts of species formation and consumption. Such values are only rigorously well-defined when trajectories are all guaranteed to run to completion, which is only guaranteed when the network contains no loops. Therefore, at present, we enforce the approximation that the network is composed of only exergonic reactions.

3. **Non-redox reactions**:

- a) **Star count difference above threshold**:

A molecule can be characterized by its “stars”, where a star is defined by the identity of a central atom and the identity of the neighboring atom(s) it is bonding with. Each atom in a molecule will be the center of a star, and thus a molecule will have the same number of stars as it has atoms. For example, the molecule CH_3OH (methanol) will have six stars:

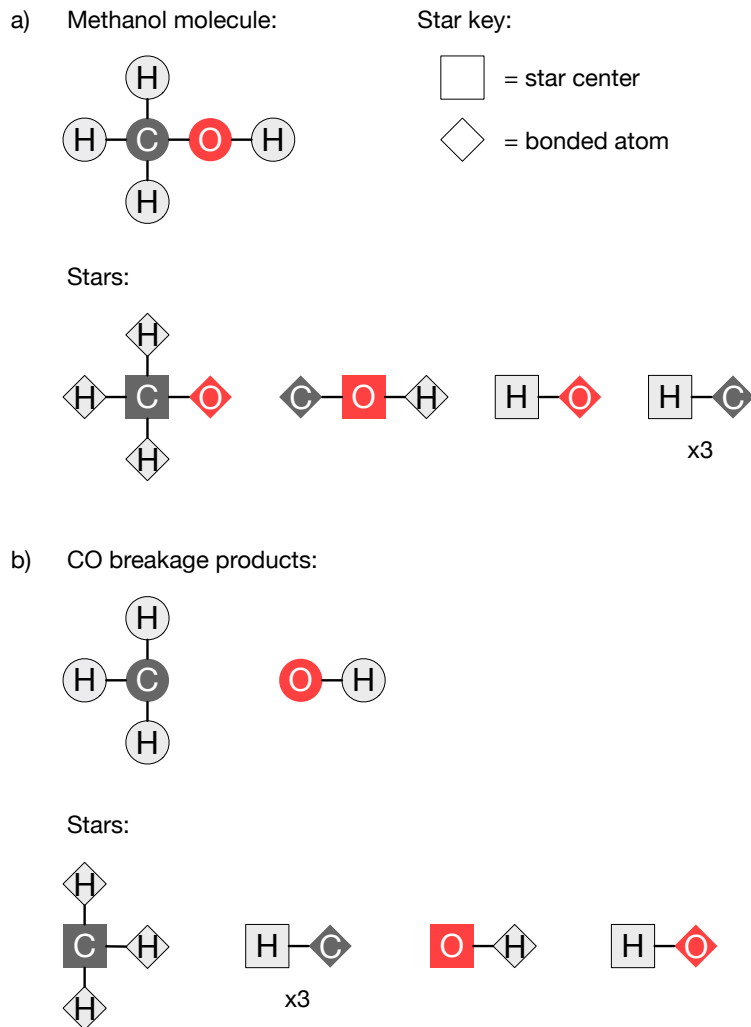


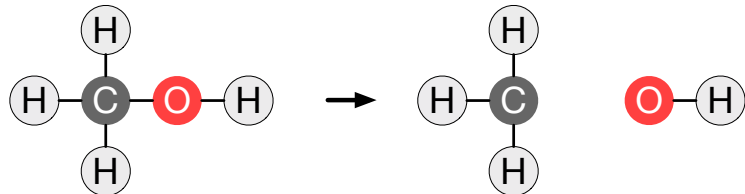
Figure B.4: Star examples. a) The stars of methanol. b) The stars of two product molecules following the breakage of the CO bond in methanol.

- Center: C, bonded atoms: H, H, H, O
- Center: O, bonded atoms: H, C
- Center: H, bonded atoms: O
- (Center: H, bonded atoms: C) x3

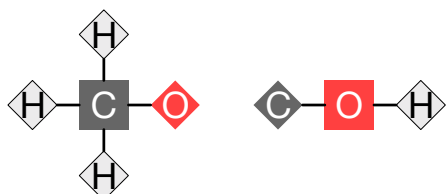
shown graphically in Figure B.4a. If we break the C-O bond in methanol, the product stars would be:

- Center: C, bonded atoms: H, H, H
- Center: O, bonded atoms: H

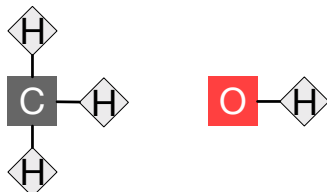
Reaction:



Stars which are only in the reactant and not in the products:



Stars which are only in the products and not in the reactant:



$$\text{Star count difference} = 2+2 = 4$$

Figure B.5: The star count difference of the reaction breaking the CO bond in methanol.

- Center: H, bonded atoms: O
- (Center: H, bonded atoms: C) x3

shown graphically in Figure B.4b. As could be expected, both the C-centric and the O-centric stars are different than they were previously. Therefore, as shown in Figure B.5, the total star count difference of this reaction is four; there are two stars in the reactant that are not found in the products, and there are two stars in the products not found in the reactant.

We pre-compute the stars of each molecule during species filtering and are able to rapidly compute the number of stars that are different between reactant(s) and product(s) in a given reaction during reaction filtering. Our goal is to remove reactions involving the simultaneous breakage/formation of more than two bonds in total or which are break-1-form-1 but do not have a reaction center involved in both the breakage and formation, as such reactions are unlikely to occur in a single

concerted step. This is based on the concept that reactions involving fewer bonds changing should be more likely to occur in a single step and more energetically favorable, in general, than those involving many bonds changing.[323] We note that there are well known examples of mechanisms which are outside of our stated scope, including E2 reactions (most often break-2-form-1) and hydrolysis reactions (up to break-2-form-2). We continue to consider possibilities for how to include such unique mechanisms in our approach in the future.

We remove all reactions where the stars contained in the reactants and products differ by more than a user-defined threshold. Throughout this work, we use a threshold of six. In order to explain our cutoff of six, we will use a simplified model system of elements [A, B, C, D] which can each form two bonds. Some example reactions and star count differences:

- $AB \rightarrow A + B$, star count difference of 4 which is accepted. This is a break-1 reaction like the example above.
- $AB + C \rightarrow A + BC$, star count difference of 6 which is accepted. This is a break-1-form-1 reaction where B is the reaction center as it is participating in both the bond being broken and the bond being formed.
- $ABC + D \rightarrow AB + CD$, star count difference of 6 which is accepted. This is also a break-1-form-1 reaction, and C is the reaction center.
- $ABC + D \rightarrow A + BCD$, star count difference of 8 which is not accepted. This is a break-1-form-1 reaction without a reaction center. A and B are participating in the bond breakage, but C and D are participating in the bond formation.
- $ABC + D \rightarrow CABD$, star count difference of 8 which is not accepted. This is a break-1-form-2 reaction, where the BC bond is breaking, the CA bond is forming, and the BD bond is forming.

For molecules composed entirely of uniquely distinguishable atoms, a star count difference cutoff of six is 100% effective at enforcing the removal of only reactions without a reaction center or those involving the breakage/formation of more than two covalent bonds. However, once a molecule contains multiple indistinguishable atoms, this cutoff becomes only partially effective. In the examples below, I bold atoms whose stars cannot be matched to an equivalent star on the other side of the reaction. Therefore, the star count difference is the total number of bolded atoms:

- $\mathbf{ABCAB} + \mathbf{A} \rightarrow \mathbf{ABA} \mathbf{ABC} \mathbf{A}$, star count difference of 6 which is accepted. This is a break-1-form-2 reaction, where the CA bond is breaking, the BA bond is forming, and the CA bond is forming.
- $\mathbf{ABAAC} + \mathbf{AB} \rightarrow \mathbf{ABA} + \mathbf{ACAB}$, star count difference of 6 which is accepted. This is a break-1-form-1 reaction without a reaction center, where the AA bond is breaking and the CA bond is forming.

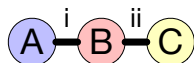
Therefore, while the star filter is useful in that it is extremely performant and removes all reactions which are unambiguously violating our stated goal, a later filter that is more computationally intensive - the fragment filter - will be necessary to remove most of the remaining ambiguous but undesirable reactions.

- b) **Covalently decomposable:** Remove reactions of the form $A + B \rightarrow A + C$ as the reaction is covalently decomposable and the presence of A has no impact on the ΔG . We note that in this type of scenario A could be acting catalytically, which could non-trivially impact the reaction kinetics, but that does not need to be considered until we are attempting to kinetically refine a given reaction or pathway.
- c) **Concerted metal coordination:** Remove reactions in which a bare metal ion is coordinated or uncoordinated simultaneous with covalent bond breakage and/or formation since these processes occur on different timescales and are very unlikely to happen simultaneously.
- d) **Fragment filter:** Remove reactions without a viable fragment matching. As stated previously, our goal at present is to remove reactions in which more than two covalent bonds are breaking/forming simultaneously or which do not have a reaction center involved in both the breakage and formation. We achieve this by precomputing and saving the fragments corresponding to the breaking of each individual bond in a molecule and then systematically comparing those fragments between reactant(s) and product(s) during reaction filtering.

Figure B.6 shows a graphical example of this process. The ABC molecule has two sets of fragments: A+BC, from breaking the A-B bond (labeled i), and AB+C, from breaking the B-C bond (labeled ii). In the context of a reaction $R_1 + R_2 \rightarrow P_1 + P_2$, we obtain reactant fragment entries by taking the precomputed fragments from R_1 and adding them to the full molecule R_2 and vice versa. Thus each reactant fragment set defines the fragments that would be obtained from breaking one bond. We do the same for the products. In this case, there are only two reactant fragment sets because the two reactants are identical, but there are four product fragment entries corresponding to the four distinct bonds that can be broken. We then compare each reactant fragment set to each product fragment set. If there is a match, that means that one bond can be broken in the reactants and one bond can be broken in the products and the identical fragments are obtained. In other words, the reaction is a break-1-form-1 reaction. A similar but simplified procedure is used to identify break-1 and form-1 reactions as well. As currently implemented, our procedure enforces that only break-1, form-1, or break-1-form-1 non-redox reactions are allowed. In the near future it will also be possible to include break-2 reactions or form-2 reactions, such as Diels-Alder reactions.

The fragment filter is both the most important and by far the most computationally intensive filter. Even with all of the filters beforehand, it could still be

Molecule:



Molecule fragments:



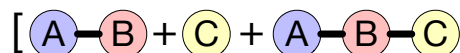
i breakage

ii breakage

Reaction:

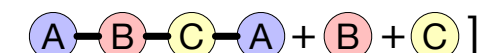
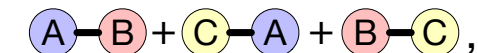
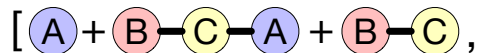


Reactant fragments:



Only two entries because reactants are identical

Product fragments:



Match! Reaction
is break-1-form-1
and is accepted

Figure B.6: Generating fragments from the breakage of one bond for a molecule and then comparing reactant and product fragments for a reaction.

performed hundreds of millions of times or more, so it must be extremely fast. Comparing fragment sets involves many operations checking whether two graphs are isomorphic. Standard graph isomorphism operations are fairly slow and must be accelerated for our purposes.

We achieve this using a graph hashing function. Graph hashing functions take graphs and return strings (with a fixed length) such that isomorphic graphs are assigned identical strings. Like all hash functions, graph hash functions have collisions, but for a well defined hashing functions, such collisions will be extremely rare. In HiPRGen, we use the Weisfeiler-Lehman graph hash [438], which is implemented in networkx [439]. During species filtering, we perform fragmentation and graph hashing pre-computation and store the hashes so that they can be referred back to during reaction filtering, as described above.

We restate the procedure for fragment filtering here in terms of hashes in order to be precise: for each molecule, for each bond, we remove the bond and hash the resulting connected components. If the bond was part of a ring, there may be only one component. We call the list of hashes associated with the removal of one bond a fragment hash list. We also store the hash of the whole molecule which we call the total hash. Then, in the fragment filter, a reaction is break-1-form-1 if there is a way of choosing one bond in the reactants and one bond in the products such that the fragment hash list + total hash is the same on the left and the right (up to permutation). Searching for such a hash matching is quadratic in the expected number of bonds. While over 99% of the reactions being filtered are $A + B \rightarrow C + D$, for reactions with only one reactant or only one product, a similar procedure is used to also identify and accept break-1 and form-1 reactions.

Returning to the final two model examples discussed in the context of the star count filter, the $ABCAB + A \rightarrow ABABCA$ reaction will be successfully removed by the fragment filter because there is no way to either just break one bond on the right or break one bond on the left and one bond on the right and obtain matching sets of fragments. In contrast, the $ABAAC + AB \rightarrow ABAACAB$ reaction will not be filtered out as breaking the AA bond on the left and the CA bond on the right does yield a matching set of fragments, consistent with the fact that the reaction is break-1-form-1 despite not having a reaction center. Thus, while this filter does effectively remove reactions involving more than two bonds simultaneously breaking and/or forming, it does not enforce that a reaction center must be present. Molecular symmetry has thus far prevented us from tractably filtering out all reactions without a reaction center which make it past the star count filter, but none have yet been observed during pathfinding analysis.

- e) **$A \rightarrow B$ non-hydrogen transfer:** Remove break-1-form-1 $A \rightarrow B$ reactions involving the movement of a non-hydrogen fragment within a molecule. While single step intramolecular hydrogen transfer is not uncommon, the concerted movement of e.g. a CO_2 fragment from one end of a molecule to another seemed extremely unlikely in general, for instance in the reaction shown below in Figure B.7 which frequently showed up in paths to LEDC.

Given that all evidence from TS searching indicated that this reaction and similar reactions do not occur in a single step, we constructed this filter to remove such mechanisms in general.

- f) **$A \rightarrow B + C$ ring closing:** Remove break-1-form-1 $A \rightarrow B + C$ reactions in which the number of reactants and products necessitates that the bond being formed is a ring-closing. Ring closing reactions in general are known to be highly entropically unfavorable. For a ring closing to occur simultaneous with another bond breaking should thus be extremely unlikely, such as in the reaction shown below in Figure B.8 in which LEDC is able to decompose into lithium carbonate while reforming the EC ring.

As with the previous filter, evidence from TS searching indicated that this reaction and similar reactions cannot occur in a single step, motivating the construction of this filter to remove such mechanisms in general.

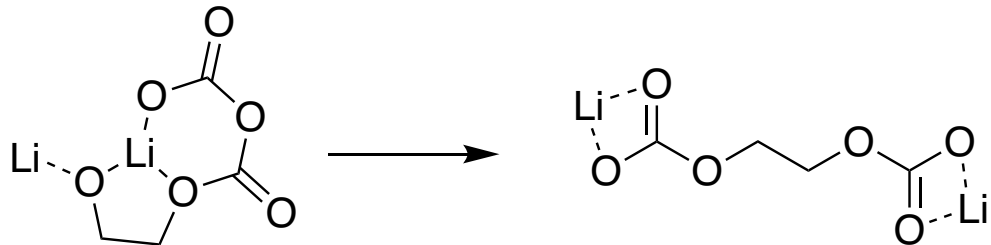


Figure B.7: Unphysical single step formation of LEDC that motivated the non-hydrogen transfer filter.

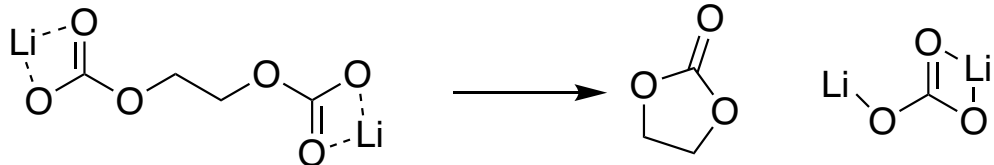


Figure B.8: Unphysical single step decomposition of LEDC that motivated the ring closing filter.

We note that for the size of the species collection presented in this work, some filters are necessary to obtain a tractable number of reactions in the final collection. For thousands of species, it is further necessary to filter reactions in parallel and for each filter to be computationally efficient in order to allow filtering to complete in a reasonable amount of time (hours to days).

Monte Carlo Methods

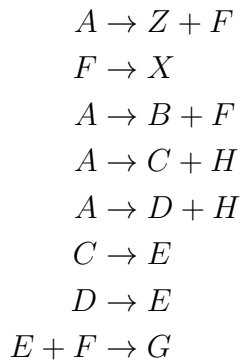
We developed a high-performance implementation of Gillespie's direct method [188], with dependency graph and logarithmically scaling sampler optimizations [291], which we call Reaction Network Monte Carlo (RNMC). RNMC is very closely based on the Stochastic Parallel Particle Kinetic Simulator (SPPARKS) package[343, 440] but with modifications to allow simulating networks with hundreds of millions of reactions and thousands of species. RNMC shares the reaction network and dependency graph between all running simulators

and uses a lockless data structure for the dependency graph that allows it to be computed dynamically by all of the simulators in parallel.

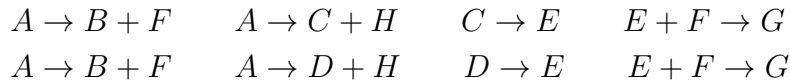
Using RNMC, we performed 100,000 simulations under each of the four chosen conditions (+0.0V without CO₂, +0.0V with CO₂, +0.5V without CO₂, and +0.5V with CO₂). For simulations without CO₂, the initial state consisted of 30 Li⁺ and 30 EC; for those with CO₂, the initial state also included 30 CO₂. Because all reactions were exergonic and no energy barriers were considered, all rate coefficients were constant and equal (discussed in Stochastic Network Analysis). Each simulation was conducted to “completion” – that is, until there were no further reactions available for further simulation. Due to the relatively small number of initial species, most simulations took between roughly 200 and 500 steps. We reiterate that simulating to completion – especially with so few simulation steps – is only possible because the system contains only exergonic reactions and therefore contains no loops. The elimination of loops is critical to adequately sample the reactive space in a tractable number of simulations, as we discussed in 4.2.

Identification of Thermodynamic Reaction Pathways

A reaction network consists of a set of species and a set of reactions linking them. Given a chemical system, we are interested in exploring the reaction pathways which produce particular species of interest. Stochastic trajectories are a useful tool for approaching the problem because they can be simulated efficiently, even when the network has hundreds of millions of reactions. [440] Unfortunately, since we collapse all spatial aspects of the system, identical molecules become indistinguishable (in reality, identical molecules can be distinguished by their locations in space). This creates the following problem: Suppose we are interested in the production of species *G* from *A* and have the following simulation trajectory:



It is impossible to decide between the two pathways



If our model had a spacial aspect, we would be able to trace the specific E used back to either a C or a D . Fundamentally, this ambiguity is caused by sequence



which is called a deficiency loop.[295] To avoid this problem, we extract a pathway which produces the target in the following way: Take the first reaction x which produces the target molecule. Then recursively, take the first reactions which produced the reactants of x . If a reactant is a starting molecule, then stop. Applying the procedure to the above sequence gives the pathway



Intuitively, this procedure is producing pathways which don't take into account competition, since there is no guarantee that the first molecule which is produced is not immediately consumed by some competing reaction. Since, in this work, we identify pathways using Monte Carlo simulation with thermodynamically bounded rate coefficients, the problem is not as bad as it seems. Since all reactions have the same rate coefficient, the only thing which can cause one reaction to out-compete another is relative abundance of reactant species. Reaction pathways do not get shut down by some competing reaction with a much higher rate coefficient, so if we have two reactions $A + B \rightarrow C$ and $A + D \rightarrow E$, if the number of B s and D s have equalized, then both reactions are equally likely to fire.

Since we collapse trajectories to pathways in this way and then rank them using the cost function $\Phi_{total} = \sum_x \Phi_x = \sum_x 1 + \exp(\Delta G_x / k_B T)$, where the sum is over all reactions and ΔG_x is the free energy of reaction x , [211] frequently occurring pathways do not necessarily have low costs, and visa versa. This means we are not guaranteed to find the lowest cost pathway via exhaustively sampling for large networks. In practice, we do not believe that this is an issue, as our approach nonetheless produces many low-cost, chemically reasonable paths.

To verify that our stochastic approach, while not theoretically guaranteed to identify the shortest pathway, nonetheless can, we applied it to a previously constructed network of roughly 4.5 million reactions.[211] We note that this network was not constructed using the High-Performance Reaction Generation (HiPRGen) method, but rather as described by Blau et al. For this network, our stochastic method finds exactly the same top pathways to LEDC as our previously published method which used graph-based pathfinding algorithms that are guaranteed to find the shortest paths.

In general, we are not interested in a single reaction pathway but rather the myriad pathways to the species of interest. Therefore, for each species of interest, we repeat the pathway identification procedure above for each trajectory, collecting all unique pathways. We then rank these pathways by the cost function Φ_{total} . We note that, because all reactions included in our network are exergonic, the constant term tends to dominate, though this cost function retains a preference for highly exergonic reactions over those that are only slightly exergonic.

Identification of Network Products

After all simulations have completed, the resulting trajectories are analyzed to determine product species. Products are defined by three criteria: the ratio of formation and consumption, relative accumulation, and availability of low-cost pathways.

To determine the ratio of formation and consumption, each trajectory was interrogated to find all reactions involving each species. If a given species is a reactant of an identified reaction, then that means it was consumed; if it is a product of the reaction, then that means it was formed. If the ratio of the total number of instances of formation across all trajectories to the total number of instances of consumption across all trajectories is greater than some threshold (here chosen as 1.5, meaning that three of the species are produced for every two consumed), then it could be a network product.

For relative accumulation, we take the average of all trajectories. The expected value of a species is the average of the final state – how many of the molecule will persist once the average simulation has completed. If this expected value is greater than some threshold (here 0.1, meaning that one of this species is produced and is present in the final state for every ten simulations), then that species could be a product.

Finally, for those species with formation/consumption ratios and expected values that pass the chosen thresholds, we perform pathfinding analysis. If the pathway with the lowest cost has a cost less than some threshold (here 10.0), then we consider the species to be a product of the network.

The species reported in Figure 5.2 are network products in at least one – but not necessarily all – of the four conditions considered (see Supplementary Information for details). We note that we add one additional constraint to the products reported here: spin multiplicity. While open-shell species can be products of the network, they are highly unlikely to be stable or meta-stable (long-lived radicals are generally rare). In the hopes of extracting useful chemical insights from network products, we therefore only consider network products that are singlets.

Kinetic Refinement of Reaction Mechanisms

The thermodynamic reaction pathways obtained via stochastic analysis were interrogated to determine the actual elementary steps. For the network products considered here (LFEO and bi-dioxolylidene), several low-cost thermodynamic reaction pathways were selected. For each elementary step along these pathways – excluding coordination reactions and redox reactions – we attempted to locate the TS using the AutoTS workflow[421] with the ω B97X-D/def2-SVPD(-f)/PCM level of theory[301, 304, 425] and water as the solvent, as described in B.1. In some cases, for reactions involving two bonds changing, AutoTS identified two TS (for instance, one to form a bond and one to break a bond); these were optimized separately.

In cases where AutoTS was unable to find a TS for a given reaction, we searched using the single-ended growing string method (SE-GSM), as implemented in the pyGSM code.[441] SE-GSM calculations were conducted with a Q-Chem backend (version 5.3.2) at the ω B97X-

D/def2-SVPD/PCM level of theory.[265] To be as consistent as possible, TS found using SE-GSM in Q-Chem were re-optimized in Jaguar at the ω B97X-D/def2-SVPD(-f)/PCM level of theory.

For each TS, we confirmed that the optimized structure possessed one imaginary frequency and confirmed that it connected the expected endpoints. For cases where the endpoints consist of two molecules that are not covalently bound (typically bound only by coordination to Li^+), we allow small imaginary frequencies (less than 75i cm^{-1}). These small imaginary modes can prove extremely difficult to remove using conventional geometry optimization methods, especially when they involve the motion of Li^+ ions, and typically do not significantly affect the free energy. We note that in some cases, the barriers that we report are based on the difference between the TS and the reactants or products at infinite separation, rather than the entrance or exit complex. The electronic energies of all optimized structures (TS and endpoints) were corrected using a single-point calculation at a higher level of theory (ω B97X-V/def2-TZVPPD/SMD) in Q-Chem. The SMD parameters used were the same used for the construction of the LIBE dataset.[253] We note that we used Q-Chem for these calculations, rather than Jaguar, because the SMD implicit solvent model is not implemented in Jaguar at the time of this writing.

All AutoTS and pyGSM calculations were automated using workflows that we have implemented in the MPcat code (see C). These workflows are designed for high-throughput TS searches and reaction pathway analysis. Note that we use a fork of the original pyGSM code for SE-GSM.

B.3 Methods associated with Chapter 6³

Density Functional Theory

The properties (including molecular geometries, electronic energies, enthalpies, entropies, and free energies) of most molecules were taken from the LIBE dataset.[253] For molecules not included in LIBE, these properties were calculated with the methods used to generate LIBE. Specifically, the ω B97X-V density functional,[298] def2-TZVPPD basis set,[300, 301] and SMD implicit solvent model[302] as implemented in the Q-Chem electronic structure code[265] were used for all calculations.

Transition-states were initially identified using the AutoTS algorithm[421] powered by the Jaguar molecular electronic structure code,[422] as well as the single-ended growing string method[423] (using the pyGSM package[424] with a Q-Chem back-end). As in previous Chapters, these calculations were conducted using the ω B97X-D density functional,[425] def2-SVPD basis set,[300, 301] and Conductor-like Screening Model (COSMO)[426, 427] implementation of the polarizable continuum model (PCM)[304] with water as the solvent. All

³This chapter is adapted from reference [330]: Spotte-Smith*, E.W.C., Kam*, R.L., Barter, D., Xie, X., Hou, T., Dwaraknath, S., Blau, S.M., Persson, K.A. Toward a Mechanistic Model of Solid-Electrolyte Interphase Formation and Evolution in Lithium-Ion Batteries. *ACS Energy Letters* 7(4), 1446–1453.

transition-states were confirmed to have one imaginary frequency (or two imaginary frequencies, if the second imaginary frequencies has a magnitude less than 75 cm^{-1}) and to connect to the expected endpoints. Generally, transition-states were re-optimized at the $\omega\text{B97X-V/def2-TZVPPD/SMD}$ level of theory. In a small set of cases, transition-states identified at the $\omega\text{B97X-D/def2-SVPD/PCM}$ level of theory could not be optimized at the $\omega\text{B97X-V/def2-TZVPPD/SMD}$ level of theory. In such cases, reaction energy barriers were calculated using the optimized geometries, enthalpies, and entropies calculated with $\omega\text{B97X-D/def2-SVPD/PCM}$, with the electronic energy calculated at $\omega\text{B97X-V/def2-TZVPPD/SMD}$. We have found through small benchmarks studies that the difference in energy barriers calculated using $\omega\text{B97X-V/def2-TZVPPD/SMD}$ and $\omega\text{B97X-V/def2-TZVPPD/SMD//}\omega\text{B97X-D/def2-SVPD/PCM}$ are typically small, so this difference in level of theory should not significantly affect the results of our kinetic simulations. We note that both the $\omega\text{B97X-V}$ and $\omega\text{B97X-D}$ density functionals perform excellently on benchmarks of reaction energies and energy barriers.[135]

Electron Transfer Rates

Marcus theory[442] is used to calculate the kinetics of reduction and oxidation barriers. Specifically, it is assumed that all redox reactions occur heterogeneously, with electrons transferred from the electrode[338]. The energy barrier for a reduction or oxidation reaction is

$$\Delta G^\ddagger = \frac{\lambda}{4} [1 + \frac{\Delta G}{\lambda}]^2 \quad (\text{B.5})$$

where ΔG is the reaction free energy and λ is the reorganization energy, which can be decomposed into an inner-shell reorganization energy λ_{in} and a bulk outer-shell reorganization energy λ_{out} ($\lambda = \lambda_{in} + \lambda_{out}$). The four-point method of Nelsen[443] is used to approximate the inner-shell electron reorganization energy, while Marcus' expression is used for the outer shell term:

$$\lambda_{out} = \frac{(\Delta e)^2}{8\pi\varepsilon_0} \left(\frac{1}{r} - \frac{1}{2D} \right) \left(\frac{1}{n^2} - \frac{1}{\varepsilon} \right) \quad (\text{B.6})$$

where e is the fundamental charge, ε_0 is the permittivity of the vacuum, r is the radius of the reacting molecule and its first solvation shell, D is the molecule-electrode distance (in our case, the effective SEI thickness), n is the index of refraction of the solvent (here $n = 1.415$), and ε is the relative permittivity of the solvent (here $\varepsilon = 18.5$).[253] The geometries of the molecules included in our model have not been calculated with full explicit solvent shells. More critically, it is not at all obvious how the solvent shell of a molecule might change in proximity to either a bare electrode or an existing SEI. Therefore, we assume a fixed radius $r = 5.0\text{ \AA}$ for all molecules.

It is assumed that the electron tunneling rate from the electrode to the electrolyte decays exponentially with distance; that is, for a rate equation

$$k = \kappa \frac{k_B T}{h} \exp\left[\frac{-\Delta G^\ddagger}{k_B T}\right] \quad (\text{B.7})$$

the transmission coefficient decays exponentially with SEI thickness ($\kappa = \exp(-\beta D)$),[444] with a decay coefficient $\beta = 1.2 \text{ \AA}^{-1}$.

Li-ion (Re)coordination Dynamics

Li coordination reactions of the type $A + M \rightarrow AM$ and re-coordination reactions of the type $AM + B \rightarrow A + BM$ were included in order to simulate the changing solvation environment near the electrolyte-electrode interface during early SEI formation. Coordination reactions are generally assumed to be barrierless in the forwards direction. Effective free energy barriers for these re-coordination reactions are based on the residence time of Li ions in electrolyte solvation shells. Recent MD simulations found that in LIB electrolytes, the residence time of Li^+ with EC at standard temperature is $\approx 5\text{ns}$.[145] Here we assume that this residence time is generally applicable, and that the minimum residence time of Li with any specie is 5ns at 298.15K ; this is used to define a minimum Li re-coordination free energy barrier $\Delta G_{recoord}^\ddagger = 0.266\text{eV}$. For reactions with $\Delta G \leq \Delta G_{recoord}^\ddagger$, $\Delta G_{recoord}^\ddagger$ is used as the effective free energy barrier to calculate the rate constant. For reactions with $\Delta G > \Delta G_{recoord}^\ddagger$, the reaction free energy ΔG is used.

Selection of Reaction Mechanisms

To identify reaction pathways to SEI products and gases of interest (LEDC, LEMC, DLEMC, Li_2CO_3 , $\text{Li}_2\text{C}_2\text{O}_4$, H_2 , C_2H_4 , and CO), we perform thermodynamically bounded Monte Carlo simulations on the CRN described in 5 and B.2 under an applied potential of $+0.0\text{V}$ vs. Li/Li^+ . To broadly sample potentially important reaction pathways, we conduct these simulations under various initial conditions: beginning with Li^+ and EC; Li^+ EC, and CO_2 ; Li^+ EC, H, and OH^- ; and Li^+ EC, CO_2 , H, and OH^- . For simulations not including water, we calculated 100,000 Monte Carlo trajectories. Because the systems containing water in the initial state involve more possible species and reactions, the computational cost of performing simulations to completion is much greater. As a result, we calculated only 20,000 trajectories in these cases; because we still observe smoothing in the average trajectory, we nonetheless believe that we have adequately sampled these systems.

All unique reactions from the top 10 pathways under all conditions considered were analyzed using AutoTS and pyGSM, yielding 345 unique transition-states corresponding to elementary reaction steps. We intend to publish these elementary reaction steps as part of a larger collection of reaction data in the near future.

From the set of mechanisms identified, a set of reactions were selected to populate the microkinetic model. In order to reduce model complexity, reactions were chosen to minimize the number of intermediates and byproducts that must be considered while maximizing the number of kinetically viable pathways included. The former consideration is important because the number of possible reactions increases roughly combinatorially with the number of species; the latter is critical to ensure that there is adequate competition between pathways. Since the reaction pathways identified from reaction network analysis were for the formation

of SEI products, additional reactions were added to account for SEI product decomposition. Reactions that are known to be barrierless with no transition-state were also added. We intend to improve our methods to allow for the fully automated construction of comprehensive microkinetic models in future work.

After a set of reactions involving covalent bond changes were selected, all possible lithium coordination and re-coordination reactions (as defined above) were between all species were added, as well as all possible one-electron reduction and oxidation reactions between species.

Kinetic Monte Carlo

The Reaction Network Monte Carlo (**RNMC**) code (see C) is used to simulate the evolution of the system state over time via the Gillespie algorithm. As a baseline, initial conditions included 9,000 EC, 600 Li⁺, 50 CO₂, 10 H, and 10 OH⁻. These conditions represent a small volume (1,000 nm³) with an approximate 1M Li⁺ concentration and 15M EC concentration. The CO₂ concentration corresponds approximately to the maximum solubility in EC at $T = 298.15\text{K}$ ($\approx 5\text{ppt}$),[445] while the H and OH⁻ concentrations are elevated (1,000ppm) compared to rigorously dried laboratory electrolytes (<10ppm). Additional simulations were conducted with an elevated initial quantity (500) of CO₂; For simulations of SEI decomposition, an initial state of 500 molecules of Li⁺EC, LEDC, LEMC, Li₂CO₃, and Li₂C₂O₄ was used. Most simulations were conducted at 298.15 K; simulations of SEI decomposition were conducted at 423.15 K.

B.4 Methods associated with Chapter 7⁴

Computational Methods

Species and Molecular Property Dataset

A dataset of species relevant to Mg(TFSI)₂/G2 electrolyte decomposition and interphase formation, the **M**Agnesium **D**ataset of **E**lectrolyte and **I**nterphase **R**eAagents (MADEIRA), was constructed using high-throughput DFT. The approach taken for the construction of this dataset was similar to that used to develop the LIBE dataset.[253] Electrolyte species (including G2, TFSI⁻, and related complexes with Mg ions) and known or suspected products were broken down into a set of fragment molecules. Due to limited experimental characterization, the products included were only inorganic species (e.g. MgSO₃) and small molecule gases (e.g. H₂). For each fragment, we obtained an optimized geometry, Gibbs free energy, and other properties (including atomic partial charges and atomic partial spin) using DFT with the $\omega\text{B97X-V}$ density functional,[298] def2-TZVPPD basis set,[301] and solvent model with density (SMD)[302] with solvent parameters for G2.[306] We denote this level of theory

⁴This chapter is adapted from reference [358]: Spotte-Smith, E.W.C., Blau, S.M., Barter, D., Leon, N.J., Hahn, N.T., Redkar, N.S., Zavadil, K.R., Liao, C., Persson, K.A. *Journal of the American Chemical Society* 145(22), 12181–12192.

ω B97X-V/def2-TZVPPD/SMD(G2). Additional species were included based on selective recombination of the fragments. All calculations were conducted using the Q-Chem electronic structure code version 5,[265] and calculations were conducted in high throughput using the `atomate`[446] and `custodian`[316, 447] libraries.

The complete dataset obtained using this procedure is available on Figshare (see A.3). We note that, because few products — and essentially no organic or polymeric products — of Mg(TFSI)₂/G2 electrolyte decomposition have been positively identified, we were not able to use knowledge of such products to improve the coverage of the dataset. As a result, the set of species obtained by this fragmentation-recombination procedure is almost certainly incomplete, with key species relevant to electrolyte decomposition and SEI formation likely missing. Work to expand this dataset is ongoing.

CRN Generation

Solvation Correction: While implicit solvation methods such as SMD are suitable for solution-phase calculations involving neutral and charged organic species, they severely underestimate the stabilizing effect of solvent on metal ions.[254]

To correct the (free) energies of species with undercoordinated Mg ions in our reaction network, we calculated the average effect of each coordinate bond on the Mg²⁺ and Mg¹⁺ ions. We optimized Mg²⁺(G₂)_n and Mg¹⁺(G₂)_n clusters using DFT in Q-Chem, with $n \in \{0, 1, 2\}$. To lower the cost of these calculations, we optimized the clusters at the ω B97X-D/def2-SVPD/PCM[301, 425, 427] ($\varepsilon = 7.23$) level of theory, with single-point energy corrections performed at the ω B97X-V/def2-TZVPPD/SMD(G2) level of theory as described above. We found (Figure H.7 in Appendix H) that each Mg-O coordinate bond stabilized Mg²⁺ by 1.37 eV, while Mg¹⁺ was stabilized by 0.49 eV for each coordinate bond. In network construction, these values were modified slightly to 1.49 and 0.56 eV, respectively, in order to make expected coordination reactions slightly exergonic.

If any Mg ions are undercoordinated, then the free energy is lowered by the correction factors for each “missing” coordinate bond. We use partial charges obtained from Natural Bonding Orbital (NBO) version 5.0[448] analysis to determine the charge state of each Mg ion in order to apply the appropriate correction. When determining the number of “missing coordinate bonds”, we assume that Mg²⁺ generally prefers a 6-fold coordination and Mg¹⁺ prefers a 5-fold coordination.

As in our previous study,[254] when calculating reaction free energies for oxidation or reduction reactions, we used an uncorrected free energy. This is especially important for reduction reactions involving Mg due to the different preferred coordination environments of Mg²⁺ and Mg¹⁺. In addition, we do not apply a solvation correction when calculating energy barriers. The assumptions implicit in performing a correction for metal-ion solvation — namely, that the ion is always in an equilibrium solvation structure — break down when considering TS, which are inherently non-equilibrium structures.

Species Filtering: We used HiPRGen to automatically construct CRNs from an initial set of species and their properties. HiPRGen is designed for cases where potential energy

surface (PES) exploration techniques (stochastic surface walking,[275] AIMD, etc.) are too expensive to thoroughly capture the reactivity of a system and where reaction patterns are not sufficiently well understood to allow the use of prescriptive reaction templates.

Instead of using PES exploration or templates, HiPRGen constructs CRNs using extensible filters. For this work, the following types of species were excluded:

- Molecules containing neutral or negative metal ions, where the charges are calculating by applying NBO to a single-point energy calculation at the ω B97X-V/def2-TZVPPD/SMD(G2) level of theory.
- Molecules composed of two or more disconnected fragments
- Metal-centric complexes, where two or more non-metal fragments are connected only by coordinate bonds to Mg ions
- Molecules with charge less than -2 or greater than 2

In addition to these filters, we ensure that there are no redundant species. That is, if there exist multiple molecules with the same charge, spin multiplicity, and structure (neglecting coordinate bonds with metal ions), we include only the molecule with the lowest solvation-corrected free energy. Using these filters, an initial set of 11,502 species was reduced to 6,469 species.

Reaction Filtering

After the species have been filtered, HiPRGen enumerates all possible stoichiometrically valid unimolecular or bimolecular reactions between these species. Because we are interested in electrochemical processes, where the electrolyte system is open to electrons, these stoichiometrically valid reactions conserve mass but do not necessarily conserve charge. Then, the stoichiometrically valid reactions are filtered in much the same way as the species are filtered. For this work, we used the same set of reaction filters that we have previously reported (see Appendix B.2 above). As some examples, we remove:

- Endergonic reactions with $\Delta G > 0$ eV.
- Reduction or oxidation reactions involving more than one electron ($|\Delta q| > 1$)
- Reactions involving spectators that do not directly participate
- Reactions involving more than two covalent bonds changing simultaneously

In total, we obtained 92,812,997 unique reactions using this filtering procedure.

Identification of CRN Products

We employed the Gillespie algorithm,[189, 190] a stochastic method, to sample the reactive space defined by the HiPRGen-generated CRN. In order to explore as many diverse reaction pathways as possible, we conducted simulations with various initial states:

- 30 Mg²⁺, 30 G2, and 30 TFSI⁻
- 30 Mg²⁺, 30 G2, 30 TFSI⁻, and 30 CO₂
- 30 Mg²⁺, 30 G2, 30 TFSI⁻, and 30 OH⁻
- 30 Mg²⁺, 30 G2, 30 TFSI⁻, 30 OH⁻, and 30 H[•]
- 30 Mg²⁺, 30 G2, 30 TFSI⁻, 30 CO₂, 30 OH⁻, and 30 H[•]

The choice to include 30 of each initial species is arbitrary and was determined empirically. Simulations involving too few molecules in the initial state will not allow many reactions to be sampled, while simulations involving many molecules will complete more slowly.

For each initial state, 50,000 trajectories of at most 250 steps were conducted. For each of the five sets of simulations, we obtained the stepwise average trajectories. The smoothing of the average trajectories (Figures E.6–E.10 in Appendix E.3) indicates convergence to the exact expected behavior and confirms that we have sampled sufficiently. All simulations were conducted at the equilibrium potential of Mg (0V vs. Mg/Mg²⁺).

Using the average trajectories, we automatically identified the CRN products. These CRN products are not necessarily the products of the corresponding real chemical system, but we have previously found (see Chapter 5) significant overlap between CRN products and experimentally observed products in battery electrolyte systems. CRN products are defined using three heuristics described in Appendix B.2. Specifically, a CRN product has a formation:consumption ratio of at least 1.5 (the species must be formed three times as a product of a reaction for every two times it is consumed as a reactant), has an average amount of at least 0.1 in the final state (at least one of the species remains at the end of every ten trajectories), and can be formed via a pathway with cost lower than 10, where the cost of a reaction is $\Phi = \exp(\Delta G/k_B T) + 1$ and the cost of a pathway is the sum of the costs of the elementary steps involved. We further remove CRN products that are open-shell, as we generally believe that radical species should be short-lived. The CRN products vary depending on the initial conditions. A description of all predicted CRN products can be found in Figures H.8–H.10 in Appendix H.

Discovery of Elementary Reaction Mechanisms

We identified elementary reaction mechanisms using the AutoTS workflow,[421] which is powered by the Jaguar electronic structure code.[422] All initial transition-state searches were conducted using the ω B97X-D density functional with the def2-SVPD(-f) basis set and

the PCM implicit solvent model with water as a solvent. A single-point energy correction was then applied using the ω B97M-V functional[449] with a larger def2-TZVPD basis set and the PCM implicit solvent model. All transition-states were validated by confirming that they connect the expected reaction endpoints. All energy barriers reported in this work are based on an infinite-separation approximation; that is, the free energies of reaction reactants and products are calculated from the free energies of individual isolated species, rather than reaction entrance or exit complexes.

Calculation of Reduction Potentials

When constructing and analyzing CRNs, we intentionally remove clusters with multiple molecules bound to Mg ions, as we described above. In part, this is necessary in order to limit the size of the CRN. However, this means that essentially all Mg ions in our dataset are undercoordinated. As we note, for chemical reactions, we can account for this undercoordination via a simple linear correction to the free energy, but the same correction cannot easily be applied to reduction reactions, especially if Mg ions are being reduced.

Here we report reduction potentials based on calculations in implicit solvent at the ω B97X-D/def2-SVPD(-f)/PCM// ω B97M-V/def2-TZVPD/PCM level of theory. From the Gibbs free energies of the reduced and non-reduced species, the reduction potential is calculated as

$$EV) = -(G_{reduced} - G_{non-reduced}) - 2.08 \quad (\text{B.8})$$

where the Gibbs free energies are reported in eV and the shift by 2.08 V is necessary in order to report potentials referenced to a Mg/Mg²⁺ electrode. In Appendix H, we also calculate reduction potentials where Mg ions are fully solvated by an explicit solvent shell.

Estimation of Solubility in Diglyme

We calculate the liquid-vapor solubility limits of CRN products in G2 S_{G2} via

$$S_{G2} = \frac{VP}{P_0} \exp\left[\frac{-\Delta G_{solv}}{RT}\right] \quad (\text{B.9})$$

where VP is the vapor pressure of the solute (in atmospheres or atm), P_0 is the pressure of a standard-state (1M) ideal gas at room temperature (24.45 atm), R is the ideal gas constant (8.314 J mol⁻¹ K⁻¹), T is the absolute temperature (298.15 K for room temperature), and ΔG_{solv} is the free energy of solvation. This equation assumes that the solutes of interest behave ideally in both the gas and the solution phase. We also neglect the effect of the dissolved salt in G2 and treat the solvent as a pure organic liquid. We predict the vapor pressure of CRN products using the SIMPOL[450] group contribution method (as implemented in UManSysProp),[451] and we calculate the free energy of solvation using SMD (specifically, via DFT calculations at the ω B97X-V/def2-TZVPPD/SMD(G2) level of theory). Because SIMPOL is specifically designed for multifunctional organic compounds, we instead provide experimental vapor pressures at room temperature for H₂ and H₂O.

We note that *ab initio* prediction of gas solubility limits is deeply challenging and an area of ongoing research. The method employed here was chosen for its ease and simplicity, rather than for its accuracy. While we believe it is sufficiently accurate to distinguish between species which should or should not evolve as gases from an electrolyte, we do not expect quantitatively accurate predictions of solubility limits.

Experimental Methods

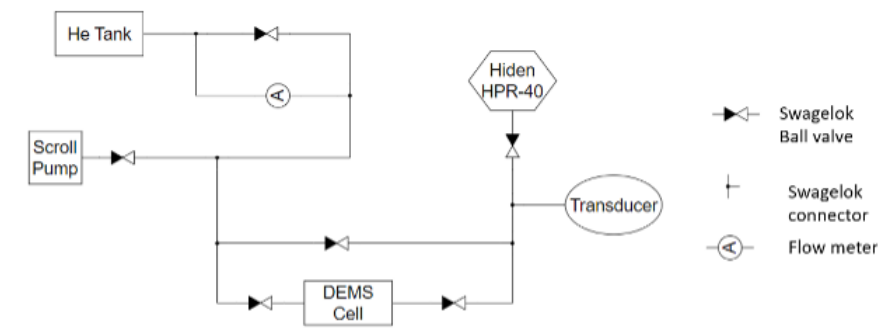


Figure B.9: Schematic drawing of the OEMS system used in this study.

Electrolyte Preparation

All reagents and solvents were prepared using a Schlenk line or glovebox (with < 1 ppm of O₂ and < 1 ppm H₂O) under an argon atmosphere. Mg(TFSI)₂ (99.5%, Solvionic) was dried under vacuum at 170 °C for 24 - 48 hours prior to use. G2 (anhydrous, 99%, Sigma-Aldrich) was distilled over calcium hydride and stored on 3 Å and 4 Å molecular sieves. The distilled G2 had a water content of < 5 ppm H₂O as measured by a Karl-Fischer Coulometer Titrator. Mg(TFSI)₂/G2 solutions were prepared in a glovebox with a volumetric flask charged with the appropriate amount of pre-dried Mg(TFSI)₂ powder dissolved in distilled G2 solvent.

Online Electrochemical Mass Spectrometry

Device Configuration

Online electrochemical mass spectrometry (OEMS), one category of the differential electrochemical mass spectrometry (DEMS), was used for the instantaneous and quantitative analysis of the gaseous species generated during electrochemical experiments. A schematic of our OEMS experimental setup is provided in the Supporting Information (Figure B.9).

In our work, a modified capillary OEMS was used, which consisted of a supporting inert gas as a flow carrier (He) and capillary inlet for mass spectroscopy. It has a moderate response time of 16s, and the flow rate was controlled at ~ 20 μL/min by a flow meter.

Other features in our OEMS include: 1) the ability to evacuate and flush the system with He after the DEMS cell was assembled inside the glovebox; 2) calibration to quantify the gaseous generation amount in real-time; and 3) flow system to enable detection of a small amount of gas production.

An FMA-2600/FVL-2600 SERIES Mass and Volumetric from OMEGA was used to control the flow rate of a He tank. The Hiden HPR-40 DEMS system was equipped with a quadrupole mass spectrometer and a QIC UF microflow capillary inlet (type 303452) with a flow rate of 12 $\mu\text{L}/\text{min}$. A PX409-015GUSBH (Pressure Sensor, 15 psi, Digital, Gauge, 1/16") transducer was used to measure the real-time pressure in order to quantify gaseous species. A total of five manual Swagelok ball valves (SS-41GS1) were incorporated into the system to allow evacuation of the gas line and control of the flow rate/testing. An ECC-DEMS cell from El-cell was used.

Electrochemical Measurements

A two-electrode setup was used for the experiments, with polished Mg metal as the Counter Electrode (CE) and reference electrode (RE) and a gold disc ($\Phi = 8 \text{ mm}$, Au, Aldrich, 99.99%, 0.1 mm thick) as the Working Electrode (WE). We note that Au can alloy with Mg, but under typical electrochemical experimental conditions, the extent of alloying is minimal, with only nanoscale alloy regions.[452] We therefore expect that Au will not significantly affect the electrochemistry and reactivity of plated Mg.

OEMS Calibration

A calibration and conversion is required in order to report OEMS measured intensities in terms of either partial pressure or molar flow. The relative signal intensity of a species with mass-to-charge ratio M/Z ($x_{M/Z}$) is calculated as

$$x_{M/Z} = S_{M/Z} \frac{I_{M/Z} - B_{M/Z}}{I_{total}} \quad (\text{B.10})$$

where $S_{M/Z}$ is a machine-specific sensitivity factor, $B_{M/Z}$ is the background intensity, $I_{M/Z}$ is the measured intensity at the mass-to-charge ratio of interest, and I_{total} is the total measured intensity.

Using the cell pressure P_{total} , the relative signal intensity $x_{M/Z}$ can be converted to a partial pressure

$$P_{M/Z} = P_{total} x_{M/Z} \quad (\text{B.11})$$

From there, the quantity of gas detected (in mols) can be obtained using the ideal gas law:

$$n_{M/Z} = \frac{P_{M/Z} V}{RT} \quad (\text{B.12})$$

where R is the ideal gas constant, T is the absolute gas in Kelvin, and V is the head space volume in the DEMS cell.

X-Ray Photoelectron Spectroscopy and Scanning Electron Microscopy

Mg cycling and deposition for ex-situ analyses were performed on planar Pt (111) textured substrates in a custom-built Teflon cell containing a Mg rod CE, Mg wire RE, and a WE area of 0.2 cm^2 . These substrates were prepared by evaporation of the noble metal onto Ti-coated Si wafers and were cleaned prior to use with acetone, 3:1 $\text{H}_2\text{SO}_4:\text{H}_2\text{O}_2$ (piranha solution), and deionized water, successively. Deposited Mg films were successively rinsed in G2 and 1,2-dimethoxyethane. Samples were transferred for X-ray photoelectron spectroscopy (XPS) using an inert transfer capsule. XPS was performed on a Kratos Axis Ultra spectrometer using a monochromatic Al K- α source. Analyses were performed on films after 10s Ar^+ sputtering, and quantification was performed using CasaXPS software. SEM was performed on a FEI Magellan microscope.

Appendix C

Software Availability¹

C.1 LIBE Usage Notes

The `libe.json` file provided on Figshare[418] can be analyzed by any code capable of parsing JSON documents. The “molecule” and “molecule_graph” keys (see Table 5.2) are JSON representations of Python objects, and so Python-based analysis tools may be most convenient; however, the data stored in these objects is redundant, so this choice is not necessary.

We have created a software repository, `deliberate`, to aid in the use and analysis of the LIBE dataset. It includes the following files:

- `plotting.py`: Contains a utility function for making categorical bar plots and histograms
- `filters.py`: Contains functions for filtering the dataset
- `recombination.py`: Contains some basic code for molecular recombination
- `data_generation.ipynb`: A Jupyter Notebook providing a basic example of a fragmentation and recombination scheme to generate molecules from an initial set of principal molecules
- `dataset_composition.ipynb`: A Jupyter Notebook analyzing the composition of the LIBE dataset in some basic dimensions (bond types, molecule charge, molecule spin multiplicity, etc.)
- `filters.ipynb`: A Jupyter Notebook employing the filters in `filters.py`, which might be useful to tailor the dataset to a particular application

¹This chapter is adapted from the following references: [253]: Spotte-Smith*, E.W.C.; Blau*, S.M.; Xie, X.; Patel, H.D.; Wen, M.; Wood, B; Dwaraknath, S.; Persson, K.A. Quantum chemical calculations of lithium-ion battery electrolyte and interphase species. *Scientific Data* **2021**, *8*(203); [254]: Barter*, D.; Spotte-Smith*, E.W.C.; Redkar, N.S.; Khanwale, A.; Dwaraknath, S; Persson, K.A.; Blau, S.M. Predictive stochastic analysis of massive filter-based electrochemical reaction networks. *Digital Discovery* **2023**, *2*, 123–137.

C.2 Generating LIBE

Our computational infrastructure for high-throughput and automated DFT calculations using the Q-Chem electronic structure code is implemented in existing open-source Python packages developed by the Materials Project, namely `pymatgen`,^[316] `custodian`, and `atomate`.^[446] The modules in these codes used specifically for Q-Chem, along with their purposes, are described in Figure C.1a.

The basic functionality to generate, process, analyze, and manipulate molecules is included in `pymatgen`. We have added functionality to read and write Q-Chem input files and to parse Q-Chem output files. In addition, we have developed a number of “sets”, pre-defined collections of input parameters appropriate for common types of calculations. While these sets can be used with any level of theory available in Q-Chem, it is especially facile to use the advanced level of theory used for the LIBE dataset (ω B97X-V/def2-TZVPPD/SMD).

The `custodian` Q-Chem module defines the interface between Q-Chem and our automation framework in `atomate`. It can execute arbitrary Q-Chem jobs and can automatically check for, detect, and correct errors in Q-Chem calculations. `custodian` also handles the logic for FFOpt calculations.

The Q-Chem module in `atomate` combines the Q-Chem input and output modules in `pymatgen` and the Q-Chem interface and error handlers in `custodian` to perform Q-Chem jobs and analyze their data in a high-throughput fashion. An example calculation, or Firework, for a single-point optimization is shown schematically in Figure C.1b. First, based on some input parameters, a Q-Chem input file for a geometry optimization calculation is written. Then, the optimization job is run, with `custodian` waiting for completion and, upon completion, checking for errors. If the job completes without errors, then the output is parsed and stored in a database. Individual Q-Chem calculations, represented in `atomate` by Fireworks like `SinglePointFW`, can be combined to form more complex workflows.

Other than Q-Chem itself, all the necessary code used to generate and analyze the LIBE dataset can be found on Github:

- `pymatgen`: <http://github.com/materialsproject/pymatgen>
- `custodian`: <http://github.com/materialsproject/custodian>
- `atomate`: <http://github.com/hackingmaterials/atomate>
- `deliberate`: <http://github.com/espottesmith/deliberate>

C.3 CRN generation and reaction pathways

All codes discussed in Chapters 4 and 5 (HiPRGen, RNMC, MPcat, and pyGSM) are released open source on Github. A Python implementation of the HiPRGen method can be found at <https://github.com/BlauGroup/HiPRGen>. RNMC, a performant kinetic Monte Carlo code in C++ and based on SPPARKS, can be found at <https://github.com/BlauGroup/RNMC>.

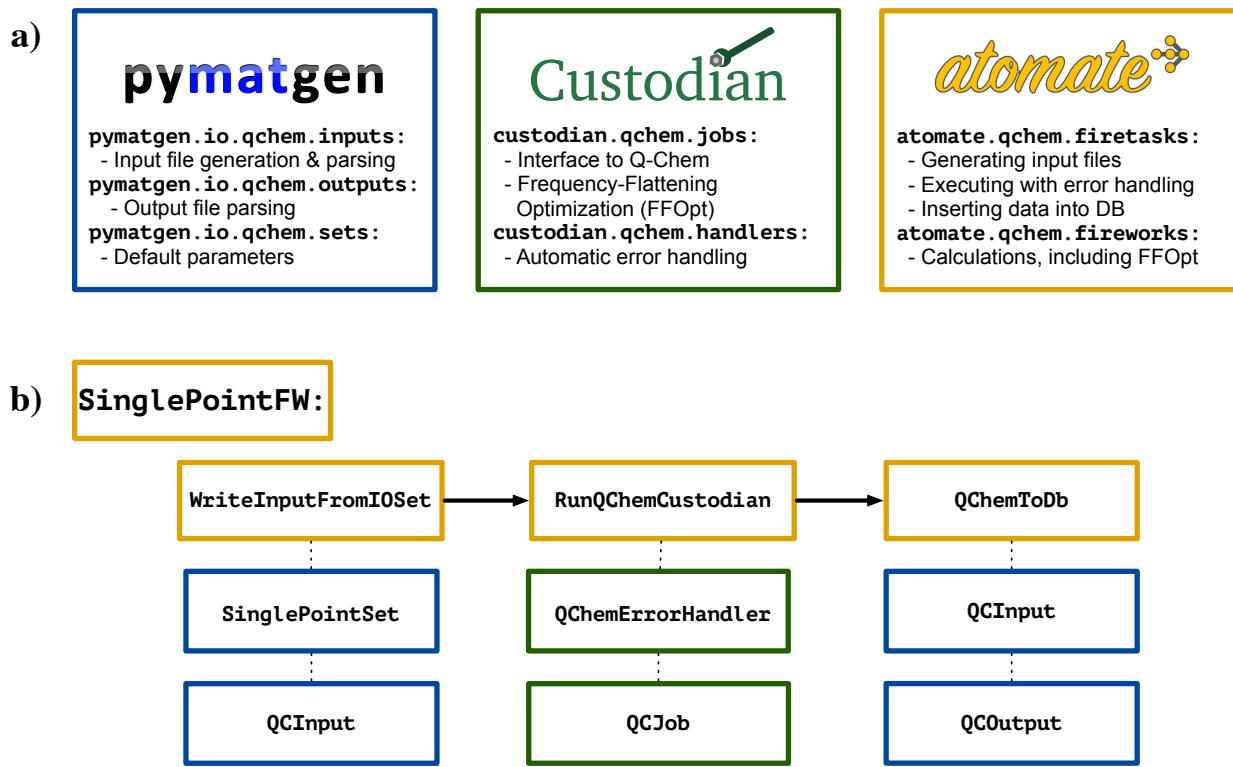


Figure C.1: An overview of our automated high-throughput molecular DFT framework, as implemented in **pymatgen** (blue), **custodian** (green), and **atomate** (yellow) (a); an example calculation (Firework) for geometry optimization (b), indicating the different steps and the ways in which **pymatgen**, **custodian**, and **atomate** interact. First, the input file is written using default parameters defined in **pymatgen**. Then, the geometry optimization calculation is performed using the Q-Chem interface in **custodian** and an automated error handler. Finally, once the calculation is finished, the input and output files are parsed using **pymatgen**, and the results from the calculation are added to a database.

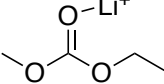
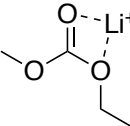
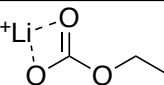
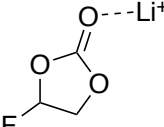
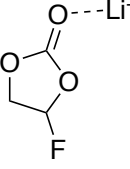
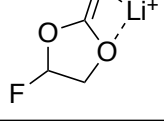
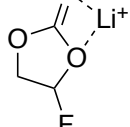
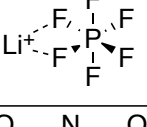
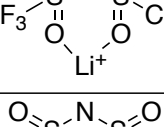
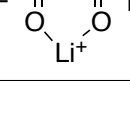
AutoTS and SE-GSM calculations were performed using the automated workflows defined in MPcat, which can be found at <https://github.com/espottesmith/MPcat>. SE-GSM calculations used a fork of the original pyGSM code, which can be found at <https://github.com/espottesmith/pyGSM/tree/c8cd99fcac451b1584f3f75e676f9d325e7ad6d4>.

Appendix D

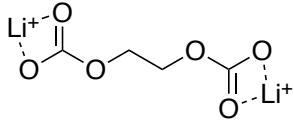
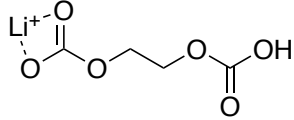
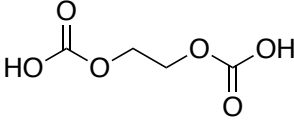
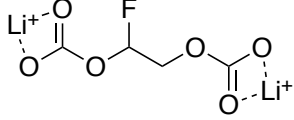
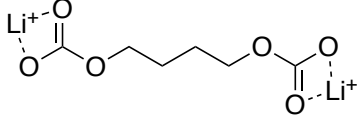
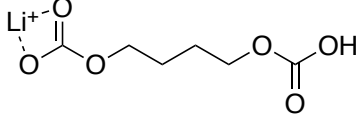
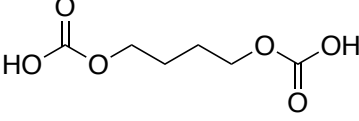
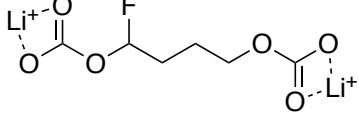
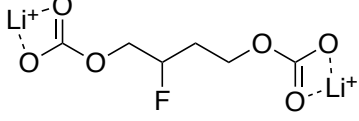
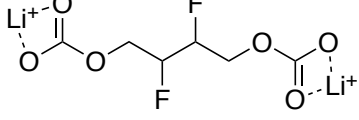
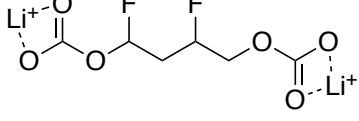
Principal Molecules Used to Generate LIBE

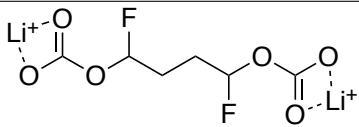
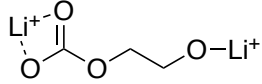
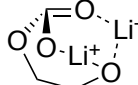
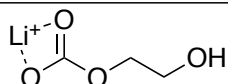
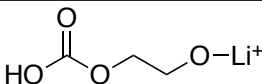
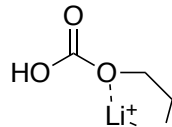
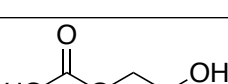
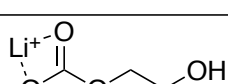
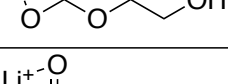
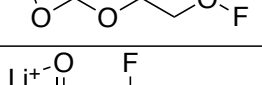
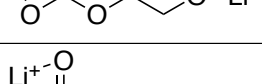
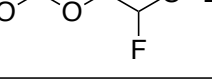
Molecule Number	Structure	Fragmentation Steps
1		MAX
2		MAX
3		MAX
4		MAX
5		MAX
6		MAX

⁰This chapter is adapted from Ref [253]: Spotte-Smith*, E.W.C.; Blau*, S.M.; Xie, X.; Patel, H.D.; Wen, M.; Wood, B; Dwaraknath, S.; Persson, K.A. Quantum chemical calculations of lithium-ion battery electrolyte and interphase species. *Scientific Data* **2021**, 8(203)

7		MAX
8		MAX
9		MAX
10		MAX
11		MAX
12		MAX
13		MAX
14		MAX
15		MAX
16		MAX

17		MAX
18		MAX
19		MAX
20		MAX
21		MAX
22		MAX
23		MAX
24	$\text{Li}-\text{OH}$	MAX
25	$\text{Li}-\text{O}^-\text{Li}$	MAX
26	$\text{Li}-\text{F}$	MAX
27	O_2	MAX
28	H_2	MAX
29	F_2	MAX
30	$\text{O}=\text{C}=\text{O}$	MAX
31		MAX
32		MAX
33		MAX
34	H_3O	MAX
35	HF	MAX

36		MAX
37		MAX
38		MAX
39		MAX
40		3
41		3
42		3
43		2
44		2
45		2
46		2

47		2
48		MAX
49		MAX
50		MAX
51		MAX
52		MAX
53		MAX
54		MAX
55		MAX
56		MAX
57		MAX
58		MAX
59		MAX

60		MAX
61		MAX
62		MAX
63		MAX
64		MAX
65		MAX
66		MAX
67		MAX
68		MAX
69		MAX
70		MAX
71		MAX
72		MAX
73		MAX
74		MAX
75		MAX

76		MAX
77		MAX
78		MAX
79		MAX
80		MAX
81		MAX
82		MAX
83		MAX
84		MAX
85		MAX
86		MAX
87		4

Table D.1: Principal molecules used for fragmentation, including depth of fragmentation. A fragmentation depth of “MAX” indicates that all possible combinations of bonds were broken during fragmentation.

Appendix E

Average Monte Carlo Trajectories

E.1 Trajectories associated with Chapter 5¹

If we plot a single trajectory of a reaction network simulation, it is a step function. On the other hand, the expected values of the species counts satisfy a rate equation, so the average trajectory should be smooth as demonstrated in Figures E.1, E.2, E.3, E.4. For the purpose of identifying proposed products, we need to sample until the average trajectory smooths out and no longer looks like a step function, which is indicative of sampling convergence.

E.2 Average trajectory associated with Chapter 6²

The plots shown in Chapter 6 only the average final state of kMC simulations, with no notion of time evolution. While this is the most important observable for this study, which focuses primarily on compositional variation in the SEI, kMC simulations most directly simulate time dynamics. In Figure E.5, we show the average trajectory for one set of simulations, namely those conducted with an applied potential of +0.0V vs. Li/Li⁺ in the regime far from the negative electrode.

E.3 Trajectories associated with Chapter 7³

¹This chapter is adapted from Ref [254]: Barter*, D.; Spotte-Smith*, E.W.C.; Redkar, N.S.; Khanwale, A.; Dwaraknath, S; Persson, K.A.; Blau, S.M. Predictive stochastic analysis of massive filter-based electrochemical reaction networks. *Digital Discovery* **2023**, *2*, 123–137.

²This chapter is adapted from reference [330]: Spotte-Smith*, E.W.C., Kam*, R.L., Barter, D., Xie, X., Hou, T., Dwaraknath, S., Blau, S.M., Persson, K.A. Toward a Mechanistic Model of Solid-Electrolyte Interphase Formation and Evolution in Lithium-Ion Batteries. *ACS Energy Letters* **7**(4), 1446–1453.

³This chapter is adapted from Ref [358]: Spotte-Smith, E.W.C., Blau, S.M., Barter, D., Leon, N.J., Hahn, N.T., Redkar, N.S., Zavadil, K.R., Liao, C., Persson, K.A. *Journal of the American Chemical Society* **145**(22), 12181–12192.

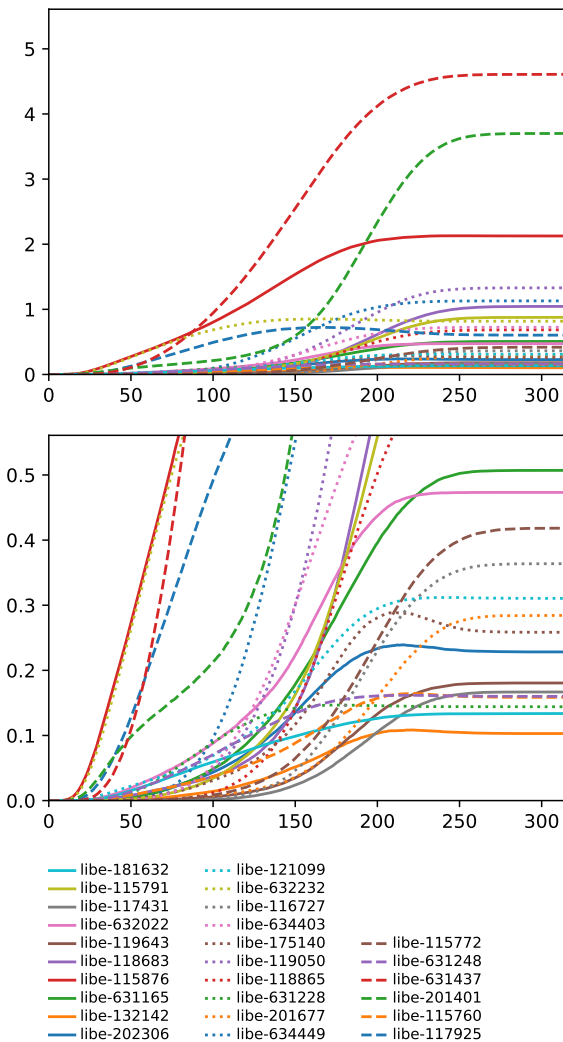


Figure E.1: Average trajectory from 100,000 stochastic trajectories of our network with electron free energy -1.4 and initial condition 30 Li^+ ions and 30 EC. Only network products are shown.

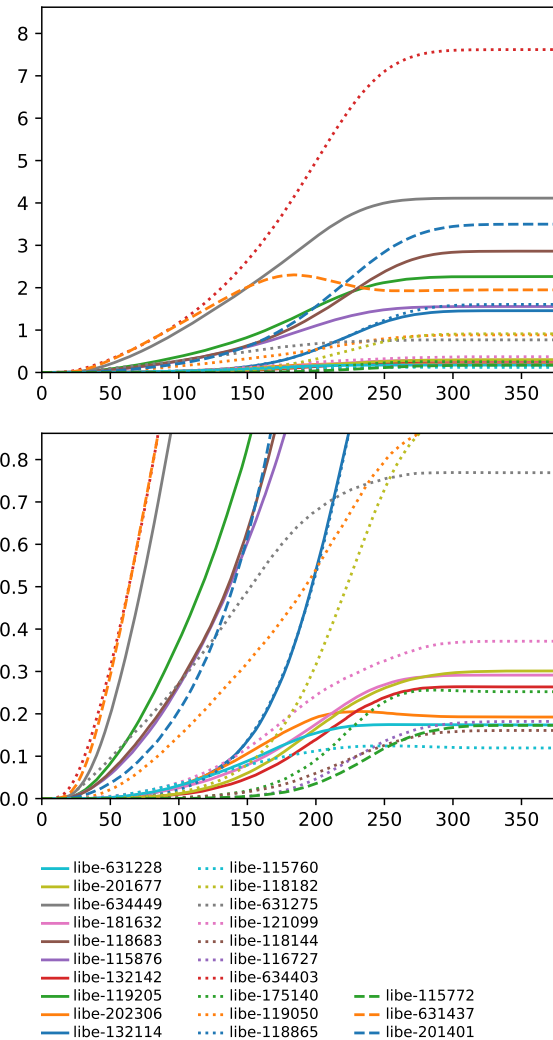


Figure E.2: Average trajectory from 100,000 stochastic trajectories of our network with electron free energy -1.4 and initial condition 30 Li^+ ions, 30 EC and 30 CO_2 . Only network products are shown.

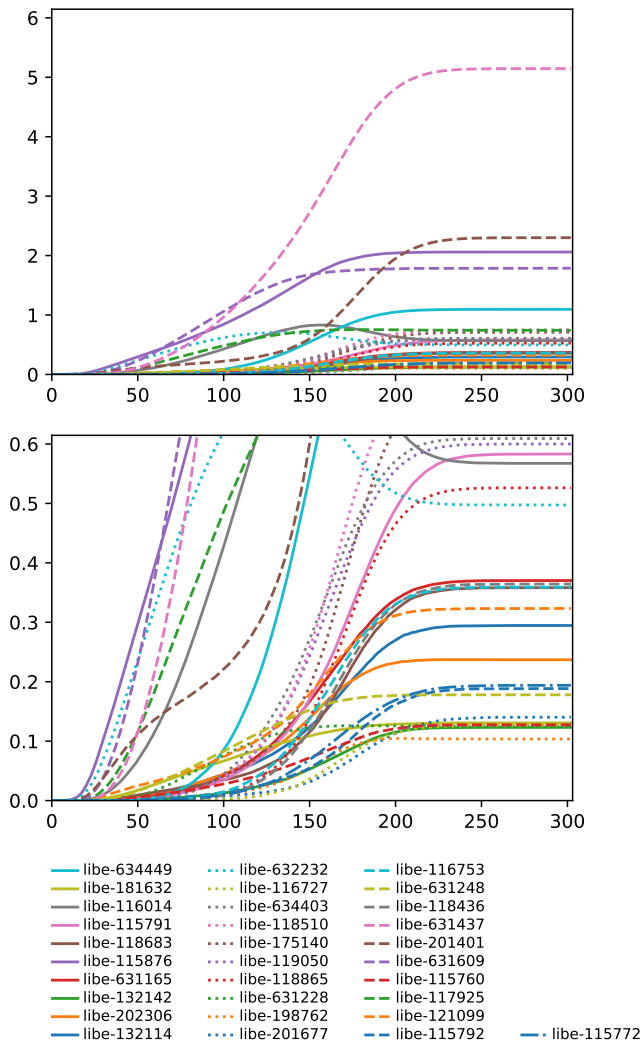


Figure E.3: Average trajectory from 100,000 stochastic trajectories of our network with electron free energy -1.9 and initial condition 30 Li⁺ ions and 30 EC. Only network products are shown.

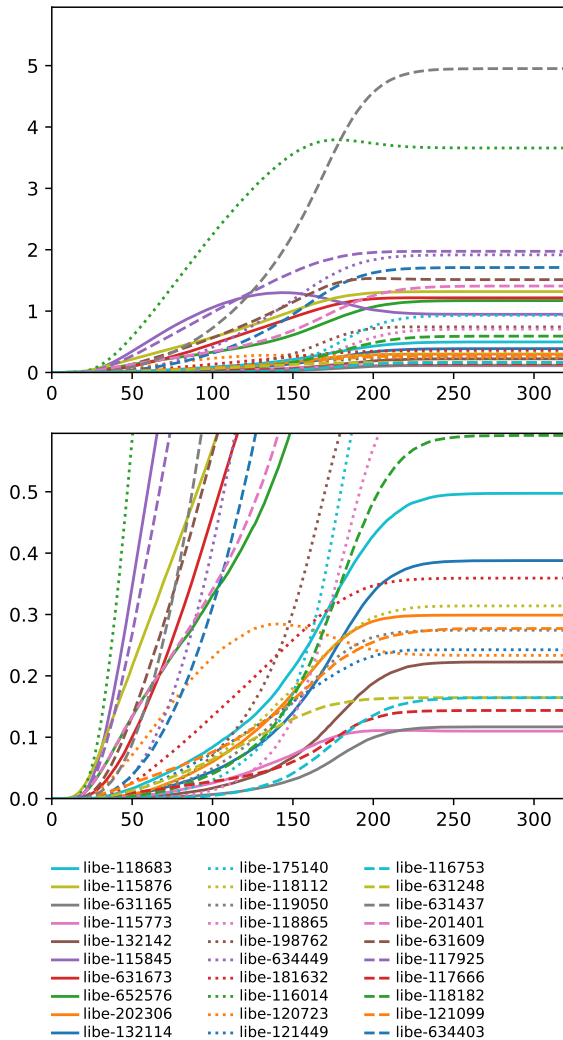


Figure E.4: Average trajectory from 100,000 stochastic trajectories of our network with electron free energy -1.9 and initial condition 30 Li^+ ions, 30 EC and 30 CO_2 . Only network products are shown.

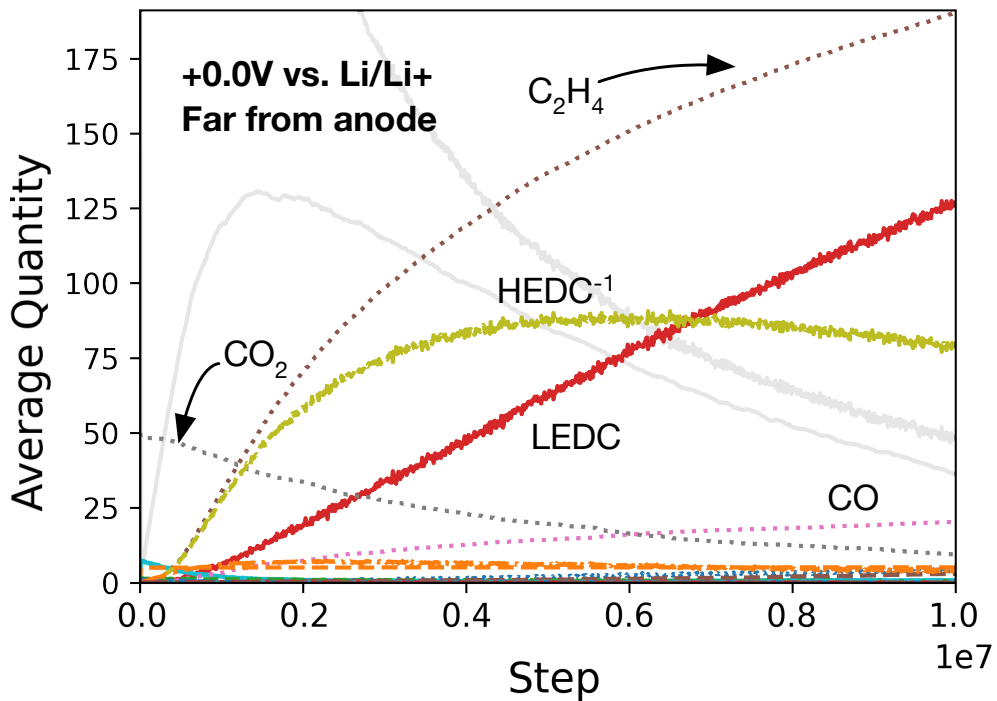


Figure E.5: Average trajectory for simulations conducted at an applied potential of +0.0 V vs. Li/Li⁺ with a tunneling barrier $D = 10.0 \text{ \AA}$, simulating a regime far from the negative electrode. It can be seen that starting species such as CO₂ are consumed over time, leading to the formation of SEI products, such as LEDC, as well as gases, such as C₂H₄ and CO.

Figures E.6 – E.10 show the average trajectories for the five sets of parameters considered in Chapter 7. As with the previous examples, it can be seen that the average trajectories are all smooth, indicating that we have sampled sufficiently.

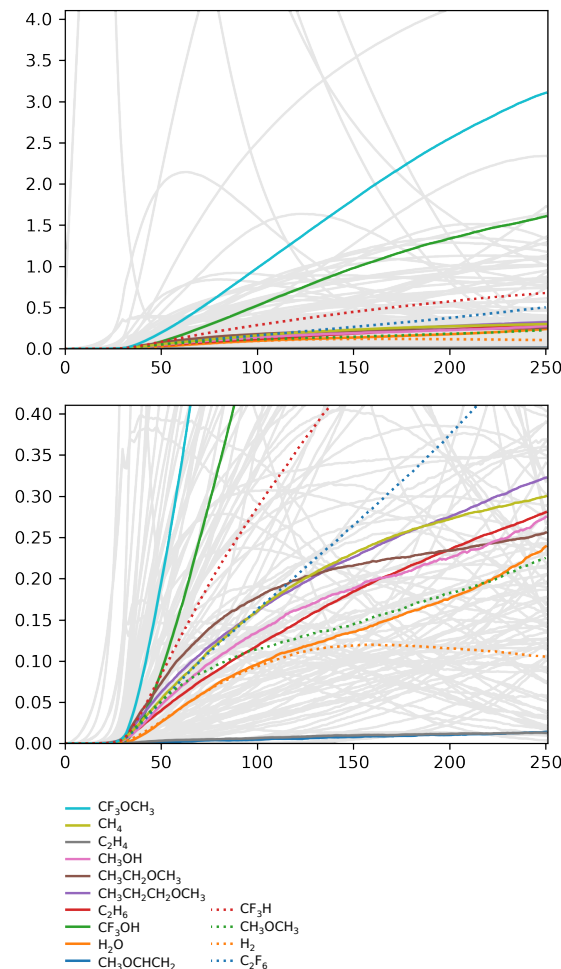


Figure E.6: Average of 50,000 Monte Carlo trajectories beginning with Mg^{2+} , G2, and TFSI^- subjected to a potential of 0V vs. Mg/Mg^{2+} . Predicted gaseous products are highlighted.

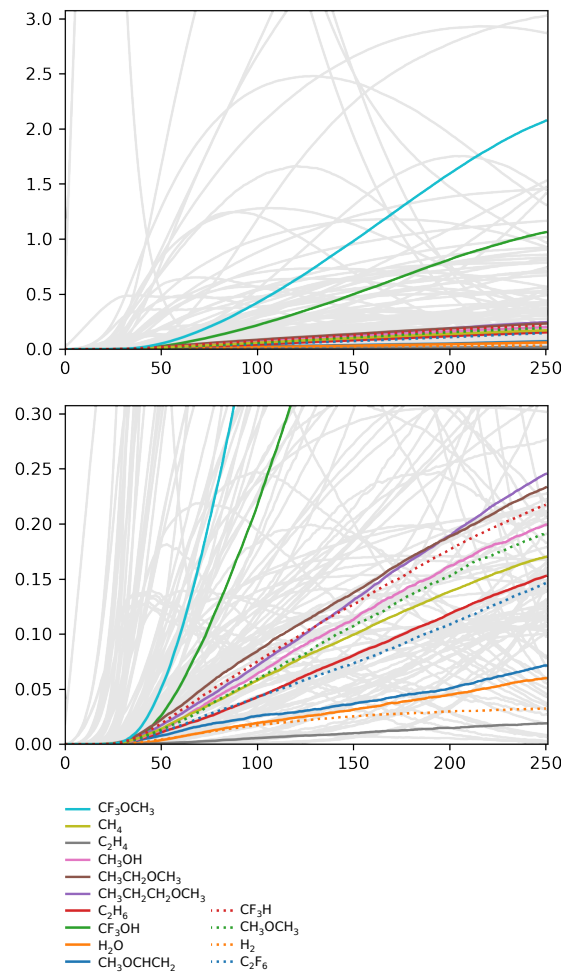


Figure E.7: Average of 50,000 Monte Carlo trajectories beginning with Mg^{2+} , G2, TFSI⁻, and CO_2 subjected to a potential of 0V vs. Mg/Mg^{2+} . Predicted gaseous products are highlighted.

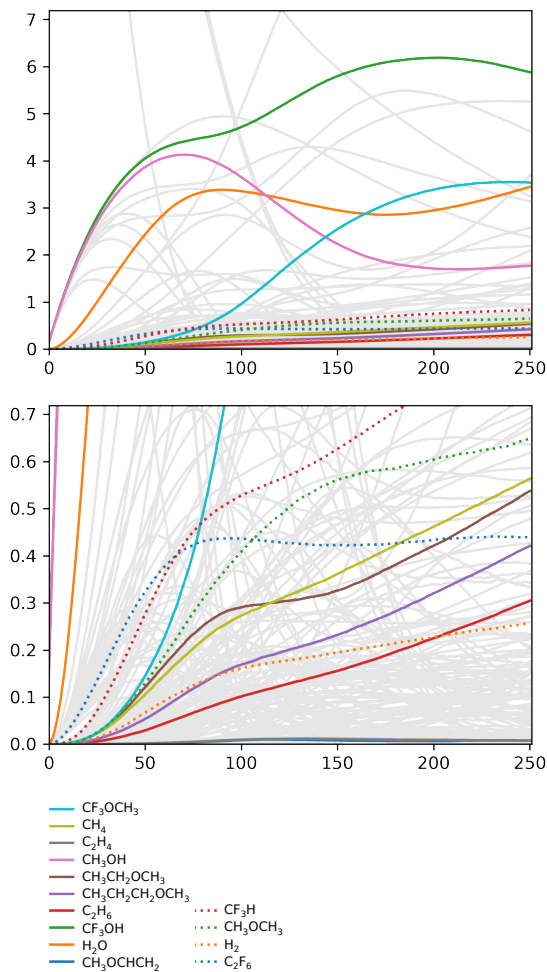


Figure E.8: Average of 50,000 Monte Carlo trajectories beginning with Mg^{2+} , G2, TFSI⁻, and OH⁻ subjected to a potential of 0V vs. Mg/Mg²⁺. Predicted gaseous products are highlighted.

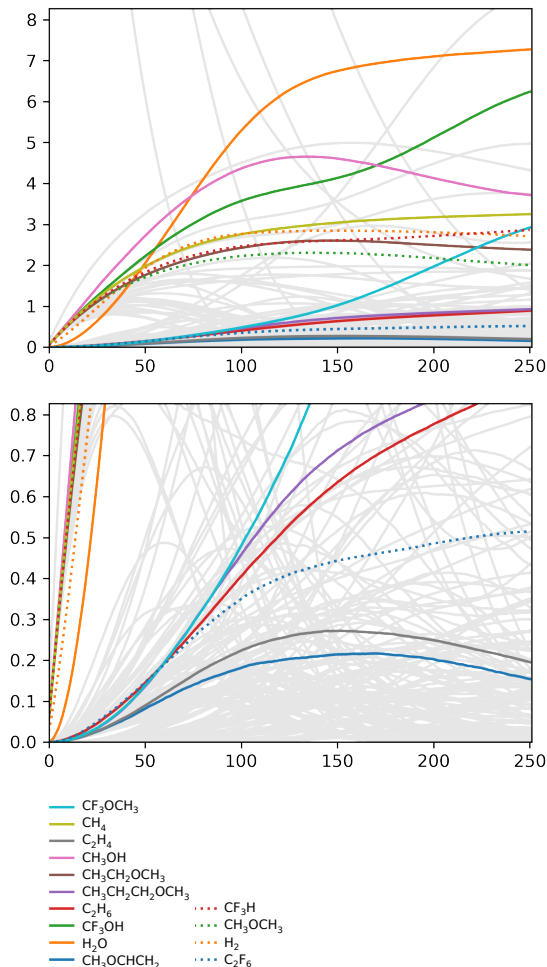


Figure E.9: Average of 50,000 Monte Carlo trajectories beginning with Mg^{2+} , G2, TFSI^- , OH^- , and H^\bullet subjected to a potential of 0V vs. Mg/Mg^{2+} . Predicted gaseous products are highlighted.

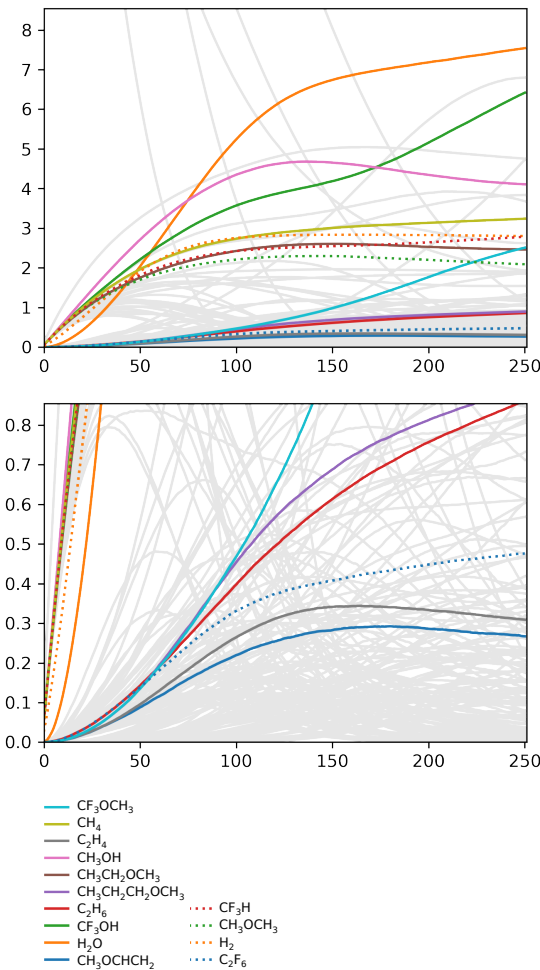


Figure E.10: Average of 50,000 Monte Carlo trajectories beginning with Mg^{2+} , G2, TFSI⁻, CO_2 , OH^- , and H^\bullet subjected to a potential of 0V vs. Mg/Mg^{2+} . Predicted gaseous products are highlighted.

Appendix F

Understanding Differences in SEI Formation¹

Within the class of EC-based electrolytes, the existing evidence seems to indicate that similar products form in the SEI regardless of the electrode chemistry (ignoring SiO_xF_y and other silicon-containing species that form on silicon negative electrodes)[453]. Inorganic species include Li_2CO_3 , $\text{Li}_2\text{C}_2\text{O}_4$, LiF (deriving from PF_6^- or other fluorinated salts, rather than the EC solvent), and Li_2O . Major organic products include LEDC and possibly LEMC,[29, 116] while the major oligomeric species are predominantly PEO and PEC. Observed gas species generally include CO , C_2H_4 , CO_2 (possibly formed at the cathode[29] due to solvent oxidation), and H_2 (from hydrolysis[344] or solvent oxidation at the cathode[454]). These same species have been widely observed in batteries with graphite, Li metal, and Si negative electrodes, as noted in Supporting Information Table F.1. Moreover, a wide range of theoretical studies have demonstrated remarkably consistent reaction pathways. For instance, three major pathways to LEDC have been proposed, shown in Figure 6.1. Paths forming C_2H_4 and CO have been observed in MD and AIMD studies.[155, 166, 236] The C_2H_4 -forming paths have also been more recently identified in computational studies using automated analysis of chemical reaction networks.[211] Evidence for the CO -forming pathway has been essentially universal in studies using AIMD, having been observed at graphite,[166] Si,[337] Li metal, Ca, and Al negative electrodes.[237] Given the consistency of these observations, a general mechanistic model capable of elucidating SEI formation processes in a wide range of LIB chemistries seems not only desirable, but plausible.

However, in spite of the consistent experimental and theoretical observations of SEI products, it is well known that there is no universal SEI, and specifically, that identical electrolytes can form interphases with vastly different behavior depending on the electrode chemistry. The inclusion of explicit negative electrode surface effects is outside of the scope of this work and will be the subject of future studies. However, it is worth noting some

¹This chapter is adapted from reference [330]: Spotte-Smith*, E.W.C., Kam*, R.L., Barter, D., Xie, X., Hou, T., Dwarakanath, S., Blau, S.M., Persson, K.A. Toward a Mechanistic Model of Solid-Electrolyte Interphase Formation and Evolution in Lithium-Ion Batteries. *ACS Energy Letters* 7(4), 1446–1453.

plausible explanations for the differences between negative electrodes - here we consider graphite (Gr), lithium metal (Li), and silicon (Si) - and how they align with the results presented here.

Lithium plating occurs at 0V vs. Li/Li⁺, while the intercalation of lithium into Gr[346] and Si[347] occurs at a range of applied potentials, as these intercalating electrodes reach several intermediate phases. The cutoff potentials used for these electrodes are also different, though those for Gr and Si are similar.[478] We have found that SEI composition can vary with relatively small changes in applied potential (for example, see the difference between +0.7V and +0.5V vs. Li/Li⁺ in Figure 1 a, c of the main text, between +0.5V and +0.3V in Figure 1 b, d of the main text, between +0.5V and +0.3V in Figure 3 of the main text). It is plausible that the different voltage profiles necessary to charge batteries with various negative electrode chemistries would cause variations in composition but also potentially thickness (if lower applied potentials are used, the reactivity of the negative electrode will increase, and more SEI products could be expected to form).

More significantly, it has been widely noted that the SEI is prone to mechanical cracking in batteries with Li[471, 479–481] and Si negative electrodes[472, 482–484] due to electrode volume expansion during charging. SEI cracking exposes fresh surface, allowing for reduction with a greatly reduced or even eliminated tunneling barrier. This in turn leads to uncontrolled SEI growth and electrolyte degradation.[52, 485] The propensity of Li negative electrodes to form dendrites[486–489] should also contribute to this uncontrolled SEI formation mechanism, as dendrites serve as fresh surfaces for SEI formation.

Finally, a “breathing” mechanism has been recognized[94] in Si negative electrode batteries. The Si SEI appears to grow upon lithiation and shrink upon delithiation.[490] However, the exact mechanism of SEI breathing is not well understood. Hasa et al.[462] suggest that LEDC may dissolve into the SEI. This does not seem likely given that LEDC has previously been found to be essentially insoluble in EC-based electrolytes,[491] although SEI dissolution might increase at higher temperatures.[492] It seems clear that the breathing mechanism is not reactive in nature, as Hasa et al. also showed that SEI products such as LEDC do not re-oxidize and convert to other products at elevated applied potential. This could imply that the underlying reaction pathways do not change in Si compared to Gr or Li, but that they happen upon every cycle as the SEI continually reforms.

SEI Species	Graphite	Li Metal	Silicon
LEDC	[23, 24, 29, 96, 116, 215, 225, 355, 455–457]	[23, 354, 458] [313]	[47, 459–462] [463]
LEMC	[29, 116, 212]		
Li_2CO_3	[23, 29, 225, 230, 355, 455, 457] [96, 225, 230, 355]	[30, 464] [52, 230, 465, 466]	[41, 47, 94, 138, 453, 459, 462, 467–469]
LiF		[30]	[462]
$\text{Li}_2\text{C}_2\text{O}_4$	[29, 355]		
Li_2O	[24, 470]	[466, 471]	[41, 453, 472]
PEO	[225, 242]	[473]	[41, 138, 462]
PEC	[242, 433, 457]	[466, 474]	[430]
CO	[29, 119, 225, 335, 433, 475]	[31, 313]	[32, 468]
C_2H_4	[29, 119, 225, 335, 433, 475]	[313]	[468, 476]
H_2	[119, 225, 335, 475, 477]	[31, 313]	[32, 468, 476]
CO_2	[29, 119, 225, 335, 475, 477]	[31, 313]	[32, 468, 476]

Table F.1: SEI species commonly identified in the experimental literature from EC-based electrolytes at graphite, lithium metal, and silicon negative electrodes.

Appendix G

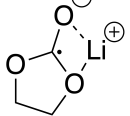
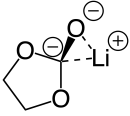
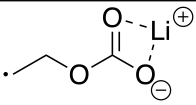
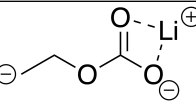
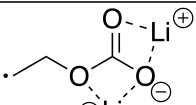
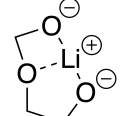
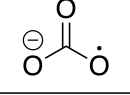
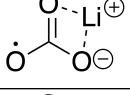
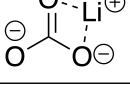
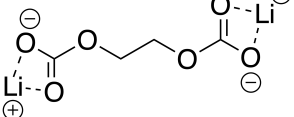
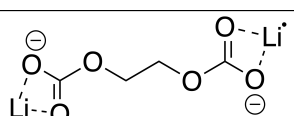
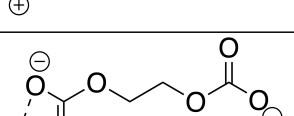
Species and Reactions for kMC in Chapter 6¹

G.1 Molecules Included in kMC Simulations

All molecules included in our kMC simulations are listed in Table G.1. We note that, when reporting the quantity of different types of molecules, we aggregate the final quantities of several similar molecules. Specifically, molecules are defined to be similar if they have identical covalent bonding but different number or coordination of Li^+ , or if they have identical covalent bonding other than the substitution of lithium for hydrogen. As an example, “inorganic carbonates” include Li_2CO_3 but also LiCO_3^- , LiCO_3 , LiHCO_3 , HCO_3^- , and CO_3^{2-} .

Index	Molecular structure	LIBE ID (if applicable)
1		libe-115834
2		libe-120806
3		libe-115880

¹This chapter is adapted from reference [330]: Spotte-Smith*, E.W.C., Kam*, R.L., Barter, D., Xie, X., Hou, T., Dwaraknath, S., Blau, S.M., Persson, K.A. Toward a Mechanistic Model of Solid-Electrolyte Interphase Formation and Evolution in Lithium-Ion Batteries. *ACS Energy Letters* 7(4), 1446–1453.

Index	Molecular structure	LIBE ID (if applicable)
4		libe-115782
5		libe-631254
6		libe-115781
7		libe-116879
8		libe-119754
9		libe-116884
10		libe-117493
11		libe-115878
12		libe-115887
13		libe-115795
14		libe-224228
15		libe-120759

Index	Molecular structure	LIBE ID (if applicable)
16		libe-115794
17		libe-120875
18		libe-121494
19		libe-115786
20		libe-120828
21		libe-117666
22		libe-115787
23		libe-120831
24		libe-119054
25		libe-118619
26		libe-118546
27		libe-117463
28		libe-116877
29		libe-115775

Index	Molecular structure	LIBE ID (if applicable)
30	\equiv	libe-115876
31	CO	libe-116014
32	CO ₂	libe-115765
33	$\text{O}^{\ominus}\text{C}=\text{O}$	libe-118669
34	$\text{O}=\text{C}=\text{O}^{\cdot-}\text{Li}^{\oplus}$	libe-118558
35	$\text{O}^{\ominus}\text{C}=\text{O}$ Li^{\oplus}	libe-118556
36	OH^{\ominus}	libe-116013
37	$\dot{\text{O}}\text{H}$	libe-116011
38	H ₂ O	libe-115768
39	H ₂ O $^{\cdot-}$	libe-115896
40	H ₂	libe-115760
41	LiOH	libe-115766
42	$\text{Li}^{\oplus}\text{O}=\text{C}(\text{OH})^{\ominus}$	libe-115770
43	$\text{O}^{\ominus}\text{C}(=\text{O})\text{OH}$	libe-118683
44	$\text{Li}^{\oplus}\text{O}=\text{C}(\text{OH})^{\cdot-}\text{Li}^{\oplus}$	libe-116846
45	$\text{Li}^{\oplus}\text{O}=\text{C}(\text{O}^{\cdot-})\text{Li}^{\oplus}$	libe-115771
46	$\text{Li}^{\oplus}\text{O}^{\ominus}\text{CH}_2\text{O}^{\ominus}\text{Li}^{\oplus}$	libe-115776
47	Li^{\oplus}	libe-116001
48	H $^{\cdot}$	libe-116003

Index	Molecular structure	LIBE ID (if applicable)
49		libe-634449
50		libe-634403
51		N/A
52		N/A
53		N/A
54		N/A
55		N/A
56		N/A
57		N/A
58		N/A

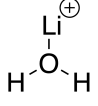
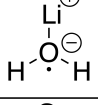
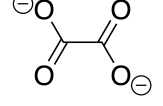
Index	Molecular structure	LIBE ID (if applicable)
59		N/A
60		N/A
61		N/A
62		N/A

Table G.1: Molecules included in kMC simulations. For molecules included in the LIBE dataset, molecule IDs are provided.

G.2 Reactions Included in kMC Simulations

Reactants	Products	ΔG (eV)	λ_i (eV)
2	1	0.866	1.206
1	2	-0.866	1.206
4	3	2.170	1.131
3	4	-2.170	1.131
5	4	1.769	0.821
4	5	-1.769	0.821
7	6	2.897	0.608
6	7	-2.897	0.608
12	11	4.878	0.410
11	12	-4.878	0.410
14	13	1.425	0.501
13	14	-1.425	0.501
17	16	1.441	0.024
16	17	-1.441	0.024
20	19	1.424	0.025
19	20	-1.424	0.025
23	22	1.486	0.010
22	23	-1.486	0.010
27	26	-3.879	0.125

Reactants	Products	ΔG (eV)	λ_i (eV)
26	27	3.879	0.125
29	28	5.694	0.322
28	29	-5.694	0.322
33	32	1.842	1.396
32	33	-1.842	1.396
35	34	3.161	1.575
34	35	-3.161	1.575
37	36	-4.411	0.006
36	37	4.411	0.006
39	38	0.614	0.018
38	39	-0.614	0.018
45	44	6.554	0.982
44	45	-6.554	0.982
52	51	1.436	0.798
51	52	-1.436	0.798
54	53	2.039	0.012
53	54	-2.039	0.012
55	21	0.391	0.023
21	55	-0.391	0.023
60	59	2.079	0.004
59	60	-2.079	0.004
61	10	3.080	0.202
10	61	-3.080	0.202

Table G.2: Reduction and oxidation reactions included in kMC simulations. The Gibbs free energy ΔG reported here does not account for the electron free energy, which will vary with potential; energy barriers and rate constants, which also depend on potential, are not reported. However, the inner reorganization energy, λ_{in} is independent of potential, and so is general to all simulations. Where relevant, all values are calculated at $T = 298.15K$.

Reactants	Products	ΔG (eV)	ΔG^\ddagger (eV)	k
3	1 47	0.573	0.573	1.276e+03
1 47	3	-0.573	0.000	6.212e+12
4	2 47	1.876	1.876	1.193e-19
2 47	4	-1.876	0.000	6.212e+12
8	6 47	0.983	0.983	1.531e-04
6 47	8	-0.983	0.000	6.212e+12
11	10 47	1.395	1.395	1.659e-11
10 47	11	-1.395	0.000	6.212e+12
15 47	13	-1.888	0.000	6.212e+12
13	15 47	1.888	1.888	7.441e-20
18 47	16	-1.840	0.000	6.212e+12
16	18 47	1.840	1.840	4.861e-19
21 47	19	-1.884	0.000	6.212e+12
19	21 47	1.884	1.884	9.019e-20
24 47	22	-2.209	0.000	6.212e+12
22	24 47	2.209	2.209	2.885e-25
28	27 47	0.432	0.432	3.117e+05
27 47	28	-0.432	0.000	6.212e+12
29	26 47	2.247	2.247	6.373e-26
26 47	29	-2.247	0.000	6.212e+12
34	32 47	0.046	0.046	1.022e+12
32 47	34	-0.046	0.000	6.212e+12
35	33 47	1.366	1.366	5.129e-11
33 47	35	-1.366	0.000	6.212e+12
41	36 47	2.313	2.313	5.024e-27
36 47	41	-2.313	0.000	6.212e+12
43 47	42	-1.860	0.000	6.212e+12
42	43 47	1.860	1.860	2.243e-19
44	11 47	0.626	0.626	1.644e+02
11 47	44	-0.626	0.000	6.212e+12
45	12 47	2.301	2.301	7.811e-27
12 47	45	-2.301	0.000	6.212e+12
46	25 47	1.343	1.343	1.212e-10
25 47	46	-1.343	0.000	6.212e+12
47 50	49	-2.209	0.000	6.212e+12
49	47 50	2.209	2.209	2.873e-25
51	13 47	0.959	0.959	3.789e-04
13 47	51	-0.959	0.000	6.212e+12
52	14 47	0.970	0.970	2.497e-04

Reactants	Products	ΔG (eV)	ΔG^\ddagger (eV)	k
14 47	52	-0.970	0.000	6.212e+12
53	19 47	0.604	0.604	3.904e+02
19 47	53	-0.604	0.000	6.212e+12
54	20 47	1.219	1.219	1.548e-08
20 47	54	-1.219	0.000	6.212e+12
47 55	20	-2.916	0.000	6.212e+12
20	47 55	2.916	2.916	3.141e-37
57	17 47	0.566	0.566	1.711e+03
17 47	57	-0.566	0.000	6.212e+12
59	38 47	0.578	0.578	1.062e+03
38 47	59	-0.578	0.000	6.212e+12
60	39 47	2.043	2.043	1.849e-22
39 47	60	-2.043	0.000	6.212e+12
47 61	12	-3.193	0.000	6.212e+12
12	47 61	3.193	3.193	6.635e-42
47 62	50	-2.801	0.000	6.212e+12
50	47 62	2.801	2.801	2.824e-35
1 4	2 3	1.303	1.303	5.811e-10
2 3	1 4	-1.303	0.266	1.981e+08
1 8	3 6	0.409	0.409	7.456e+05
3 6	1 8	-0.409	0.266	1.981e+08
1 11	3 10	0.821	0.821	8.078e-02
3 10	1 11	-0.821	0.266	1.981e+08
1 13	3 15	1.315	1.315	3.623e-10
3 15	1 13	-1.315	0.266	1.981e+08
1 16	3 18	1.267	1.267	2.367e-09
3 18	1 16	-1.267	0.266	1.981e+08
1 19	3 21	1.310	1.310	4.392e-10
3 21	1 19	-1.310	0.266	1.981e+08
1 22	3 24	1.635	1.635	1.405e-15
3 24	1 22	-1.635	0.266	1.981e+08
1 28	3 27	-0.141	0.266	1.981e+08
3 27	1 28	0.141	0.266	1.981e+08
1 29	3 26	1.674	1.674	3.103e-16
3 26	1 29	-1.674	0.266	1.981e+08
1 34	3 32	-0.527	0.266	1.981e+08
3 32	1 34	0.527	0.527	7.754e+03
1 35	3 33	0.792	0.792	2.497e-01
3 33	1 35	-0.792	0.266	1.981e+08

Reactants	Products	ΔG (eV)	ΔG^\ddagger (eV)	k
1 41	3 36	1.740	1.740	2.447e-17
3 36	1 41	-1.740	0.266	1.981e+08
1 42	3 43	1.287	1.287	1.092e-09
3 43	1 42	-1.287	0.266	1.981e+08
1 44	3 11	0.053	0.266	1.981e+08
3 11	1 44	-0.053	0.266	1.981e+08
1 45	3 12	1.728	1.728	3.803e-17
3 12	1 45	-1.728	0.266	1.981e+08
1 46	3 25	0.770	0.770	5.903e-01
3 25	1 46	-0.770	0.266	1.981e+08
1 49	3 50	1.636	1.636	1.399e-15
3 50	1 49	-1.636	0.266	1.981e+08
1 51	3 13	0.386	0.386	1.845e+06
3 13	1 51	-0.386	0.266	1.981e+08
1 52	3 14	0.397	0.397	1.216e+06
3 14	1 52	-0.397	0.266	1.981e+08
1 53	3 19	0.030	0.266	1.981e+08
3 19	1 53	-0.030	0.266	1.981e+08
1 54	3 20	0.646	0.646	7.539e+01
3 20	1 54	-0.646	0.266	1.981e+08
1 20	3 55	2.343	2.343	1.530e-27
3 55	1 20	-2.343	0.266	1.981e+08
1 57	3 17	-0.008	0.266	1.981e+08
3 17	1 57	0.008	0.266	1.981e+08
1 59	3 38	0.005	0.266	1.981e+08
3 38	1 59	-0.005	0.266	1.981e+08
1 60	3 39	1.469	1.469	9.006e-13
3 39	1 60	-1.469	0.266	1.981e+08
1 12	3 61	2.620	2.620	3.231e-32
3 61	1 12	-2.620	0.266	1.981e+08
1 50	3 62	2.228	2.228	1.375e-25
3 62	1 50	-2.228	0.266	1.981e+08
2 8	4 6	-0.894	0.266	1.981e+08
4 6	2 8	0.894	0.894	4.842e-03
2 11	4 10	-0.482	0.266	1.981e+08
4 10	2 11	0.482	0.482	4.469e+04
2 13	4 15	0.012	0.266	1.981e+08
4 15	2 13	-0.012	0.266	1.981e+08
2 16	4 18	-0.036	0.266	1.981e+08

Reactants	Products	ΔG (eV)	ΔG^\ddagger (eV)	k
4 18	2 16	0.036	0.266	1.981e+08
2 19	4 21	0.007	0.266	1.981e+08
4 21	2 19	-0.007	0.266	1.981e+08
2 22	4 24	0.332	0.332	1.502e+07
4 24	2 22	-0.332	0.266	1.981e+08
2 28	4 27	-1.444	0.266	1.981e+08
4 27	2 28	1.444	1.444	2.378e-12
2 29	4 26	0.371	0.371	3.318e+06
4 26	2 29	-0.371	0.266	1.981e+08
2 34	4 32	-1.830	0.266	1.981e+08
4 32	2 34	1.830	1.830	7.253e-19
2 35	4 33	-0.511	0.266	1.981e+08
4 33	2 35	0.511	0.511	1.446e+04
2 41	4 36	0.436	0.436	2.616e+05
4 36	2 41	-0.436	0.266	1.981e+08
2 42	4 43	-0.016	0.266	1.981e+08
4 43	2 42	0.016	0.266	1.981e+08
2 44	4 11	-1.251	0.266	1.981e+08
4 11	2 44	1.251	1.251	4.510e-09
2 45	4 12	0.425	0.425	4.066e+05
4 12	2 45	-0.425	0.266	1.981e+08
2 46	4 25	-0.533	0.266	1.981e+08
4 25	2 46	0.533	0.533	6.116e+03
2 49	4 50	0.332	0.332	1.496e+07
4 50	2 49	-0.332	0.266	1.981e+08
2 51	4 13	-0.917	0.266	1.981e+08
4 13	2 51	0.917	0.917	1.957e-03
2 52	4 14	-0.906	0.266	1.981e+08
4 14	2 52	0.906	0.906	2.969e-03
2 53	4 19	-1.273	0.266	1.981e+08
4 19	2 53	1.273	1.273	1.899e-09
2 54	4 20	-0.657	0.266	1.981e+08
4 20	2 54	0.657	0.657	4.789e+01
2 20	4 55	1.040	1.040	1.635e-05
4 55	2 20	-1.040	0.266	1.981e+08
2 57	4 17	-1.311	0.266	1.981e+08
4 17	2 57	1.311	1.311	4.333e-10
2 59	4 38	-1.299	0.266	1.981e+08
4 38	2 59	1.299	1.299	6.981e-10

Reactants	Products	ΔG (eV)	ΔG^\ddagger (eV)	k
2 60	4 39	0.166	0.266	1.981e+08
4 39	2 60	-0.166	0.266	1.981e+08
2 12	4 61	1.317	1.317	3.454e-10
4 61	2 12	-1.317	0.266	1.981e+08
2 50	4 62	0.924	0.924	1.470e-03
4 62	2 50	-0.924	0.266	1.981e+08
6 11	8 10	0.412	0.412	6.731e+05
8 10	6 11	-0.412	0.266	1.981e+08
6 13	8 15	0.906	0.906	3.019e-03
8 15	6 13	-0.906	0.266	1.981e+08
6 16	8 18	0.858	0.858	1.972e-02
8 18	6 16	-0.858	0.266	1.981e+08
6 19	8 21	0.901	0.901	3.660e-03
8 21	6 19	-0.901	0.266	1.981e+08
6 22	8 24	1.226	1.226	1.171e-08
8 24	6 22	-1.226	0.266	1.981e+08
6 28	8 27	-0.551	0.266	1.981e+08
8 27	6 28	0.551	0.551	3.051e+03
6 29	8 26	1.265	1.265	2.586e-09
8 26	6 29	-1.265	0.266	1.981e+08
6 34	8 32	-0.936	0.266	1.981e+08
8 32	6 34	0.936	0.936	9.306e-04
6 35	8 33	0.383	0.383	2.081e+06
8 33	6 35	-0.383	0.266	1.981e+08
6 41	8 36	1.330	1.330	2.039e-10
8 36	6 41	-1.330	0.266	1.981e+08
6 42	8 43	0.878	0.878	9.102e-03
8 43	6 42	-0.878	0.266	1.981e+08
6 44	8 11	-0.357	0.266	1.981e+08
8 11	6 44	0.357	0.357	5.787e+06
6 45	8 12	1.319	1.319	3.169e-10
8 12	6 45	-1.319	0.266	1.981e+08
6 46	8 25	0.361	0.361	4.918e+06
8 25	6 46	-0.361	0.266	1.981e+08
6 49	8 50	1.226	1.226	1.166e-08
8 50	6 49	-1.226	0.266	1.981e+08
6 51	8 13	-0.023	0.266	1.981e+08
8 13	6 51	0.023	0.266	1.981e+08
6 52	8 14	-0.013	0.266	1.981e+08

Reactants	Products	ΔG (eV)	ΔG^\ddagger (eV)	k
8 14	6 52	0.013	0.266	1.981e+08
6 53	8 19	-0.379	0.266	1.981e+08
8 19	6 53	0.379	0.379	2.436e+06
6 54	8 20	0.236	0.266	1.981e+08
8 20	6 54	-0.236	0.266	1.981e+08
6 20	8 55	1.934	1.934	1.274e-20
8 55	6 20	-1.934	0.266	1.981e+08
6 57	8 17	-0.417	0.266	1.981e+08
8 17	6 57	0.417	0.417	5.560e+05
6 59	8 38	-0.405	0.266	1.981e+08
8 38	6 59	0.405	0.405	8.957e+05
6 60	8 39	1.060	1.060	7.504e-06
8 39	6 60	-1.060	0.266	1.981e+08
6 12	8 61	2.210	2.210	2.692e-25
8 61	6 12	-2.210	0.266	1.981e+08
6 50	8 62	1.818	1.818	1.146e-18
8 62	6 50	-1.818	0.266	1.981e+08
10 13	11 15	0.494	0.494	2.786e+04
11 15	10 13	-0.494	0.266	1.981e+08
10 16	11 18	0.446	0.446	1.820e+05
11 18	10 16	-0.446	0.266	1.981e+08
10 19	11 21	0.489	0.489	3.378e+04
11 21	10 19	-0.489	0.266	1.981e+08
10 22	11 24	0.814	0.814	1.080e-01
11 24	10 22	-0.814	0.266	1.981e+08
10 28	11 27	-0.963	0.266	1.981e+08
11 27	10 28	0.963	0.963	3.306e-04
10 29	11 26	0.853	0.853	2.387e-02
11 26	10 29	-0.853	0.266	1.981e+08
10 34	11 32	-1.348	0.266	1.981e+08
11 32	10 34	1.348	1.348	1.008e-10
10 35	11 33	-0.029	0.266	1.981e+08
11 33	10 35	0.029	0.266	1.981e+08
10 41	11 36	0.918	0.918	1.882e-03
11 36	10 41	-0.918	0.266	1.981e+08
10 42	11 43	0.466	0.466	8.401e+04
11 43	10 42	-0.466	0.266	1.981e+08
10 44	11 11	-0.769	0.266	1.981e+08
11 11	10 44	0.769	0.769	6.270e-01

Reactants	Products	ΔG (eV)	ΔG^\ddagger (eV)	k
10 45	11 12	0.907	0.907	2.925e-03
11 12	10 45	-0.907	0.266	1.981e+08
10 46	11 25	-0.051	0.266	1.981e+08
11 25	10 46	0.051	0.266	1.981e+08
10 49	11 50	0.814	0.814	1.076e-01
11 50	10 49	-0.814	0.266	1.981e+08
10 51	11 13	-0.435	0.266	1.981e+08
11 13	10 51	0.435	0.435	2.720e+05
10 52	11 14	-0.425	0.266	1.981e+08
11 14	10 52	0.425	0.425	4.127e+05
10 53	11 19	-0.791	0.266	1.981e+08
11 19	10 53	0.791	0.791	2.640e-01
10 54	11 20	-0.176	0.266	1.981e+08
11 20	10 54	0.176	0.266	1.981e+08
10 20	11 55	1.522	1.522	1.176e-13
11 55	10 20	-1.522	0.266	1.981e+08
10 57	11 17	-0.829	0.266	1.981e+08
11 17	10 57	0.829	0.829	6.024e-02
10 59	11 38	-0.817	0.266	1.981e+08
11 38	10 59	0.817	0.817	9.705e-02
10 60	11 39	0.648	0.648	6.926e+01
11 39	10 60	-0.648	0.266	1.981e+08
10 12	11 61	1.798	1.798	2.485e-18
11 61	10 12	-1.798	0.266	1.981e+08
10 50	11 62	1.406	1.406	1.057e-11
11 62	10 50	-1.406	0.266	1.981e+08
15 16	13 18	-0.048	0.266	1.981e+08
13 18	15 16	0.048	0.266	1.981e+08
15 19	13 21	-0.005	0.266	1.981e+08
13 21	15 19	0.005	0.266	1.981e+08
15 22	13 24	0.320	0.320	2.409e+07
13 24	15 22	-0.320	0.266	1.981e+08
15 28	13 27	-1.457	0.266	1.981e+08
13 27	15 28	1.457	1.457	1.483e-12
15 29	13 26	0.359	0.359	5.321e+06
13 26	15 29	-0.359	0.266	1.981e+08
15 34	13 32	-1.842	0.266	1.981e+08
13 32	15 34	1.842	1.842	4.522e-19
15 35	13 33	-0.523	0.266	1.981e+08

Reactants	Products	ΔG (eV)	ΔG^\ddagger (eV)	k
13 33	15 35	0.523	0.523	9.013e+03
15 41	13 36	0.424	0.424	4.195e+05
13 36	15 41	-0.424	0.266	1.981e+08
15 42	13 43	-0.028	0.266	1.981e+08
13 43	15 42	0.028	0.266	1.981e+08
15 44	11 13	-1.263	0.266	1.981e+08
11 13	15 44	1.263	1.263	2.812e-09
15 45	12 13	0.413	0.413	6.521e+05
12 13	15 45	-0.413	0.266	1.981e+08
15 46	13 25	-0.545	0.266	1.981e+08
13 25	15 46	0.545	0.545	3.813e+03
15 49	13 50	0.320	0.320	2.399e+07
13 50	15 49	-0.320	0.266	1.981e+08
15 51	13 13	-0.929	0.266	1.981e+08
13 13	15 51	0.929	0.929	1.220e-03
15 52	13 14	-0.918	0.266	1.981e+08
13 14	15 52	0.918	0.918	1.851e-03
15 53	13 19	-1.285	0.266	1.981e+08
13 19	15 53	1.285	1.285	1.184e-09
15 54	13 20	-0.670	0.266	1.981e+08
13 20	15 54	0.670	0.670	2.986e+01
15 20	13 55	1.028	1.028	2.623e-05
13 55	15 20	-1.028	0.266	1.981e+08
15 57	13 17	-1.323	0.266	1.981e+08
13 17	15 57	1.323	1.323	2.702e-10
15 59	13 38	-1.311	0.266	1.981e+08
13 38	15 59	1.311	1.311	4.353e-10
15 60	13 39	0.154	0.266	1.981e+08
13 39	15 60	-0.154	0.266	1.981e+08
12 15	13 61	1.304	1.304	5.540e-10
13 61	12 15	-1.304	0.266	1.981e+08
15 50	13 62	0.912	0.912	2.358e-03
13 62	15 50	-0.912	0.266	1.981e+08
18 19	16 21	0.043	0.266	1.981e+08
16 21	18 19	-0.043	0.266	1.981e+08
18 22	16 24	0.368	0.368	3.688e+06
16 24	18 22	-0.368	0.266	1.981e+08
18 28	16 27	-1.408	0.266	1.981e+08
16 27	18 28	1.408	1.408	9.686e-12

Reactants	Products	ΔG (eV)	ΔG^\ddagger (eV)	k
18 29	16 26	0.407	0.407	8.145e+05
16 26	18 29	-0.407	0.266	1.981e+08
18 34	16 32	-1.794	0.266	1.981e+08
16 32	18 34	1.794	1.794	2.954e-18
18 35	16 33	-0.475	0.266	1.981e+08
16 33	18 35	0.475	0.475	5.888e+04
18 41	16 36	0.472	0.472	6.422e+04
16 36	18 41	-0.472	0.266	1.981e+08
18 42	16 43	0.020	0.266	1.981e+08
16 43	18 42	-0.020	0.266	1.981e+08
18 44	11 16	-1.214	0.266	1.981e+08
11 16	18 44	1.214	1.214	1.837e-08
18 45	12 16	0.461	0.461	9.983e+04
12 16	18 45	-0.461	0.266	1.981e+08
18 46	16 25	-0.497	0.266	1.981e+08
16 25	18 46	0.497	0.497	2.491e+04
18 49	16 50	0.368	0.368	3.672e+06
16 50	18 49	-0.368	0.266	1.981e+08
18 51	13 16	-0.881	0.266	1.981e+08
13 16	18 51	0.881	0.881	7.970e-03
18 52	14 16	-0.870	0.266	1.981e+08
14 16	18 52	0.870	0.870	1.209e-02
18 53	16 19	-1.237	0.266	1.981e+08
16 19	18 53	1.237	1.237	7.734e-09
18 54	16 20	-0.621	0.266	1.981e+08
16 20	18 54	0.621	0.621	1.951e+02
18 20	16 55	1.076	1.076	4.015e-06
16 55	18 20	-1.076	0.266	1.981e+08
18 57	16 17	-1.275	0.266	1.981e+08
16 17	18 57	1.275	1.275	1.765e-09
18 59	16 38	-1.262	0.266	1.981e+08
16 38	18 59	1.262	1.262	2.843e-09
18 60	16 39	0.202	0.266	1.981e+08
16 39	18 60	-0.202	0.266	1.981e+08
12 18	16 61	1.353	1.353	8.481e-11
16 61	12 18	-1.353	0.266	1.981e+08
18 50	16 62	0.961	0.961	3.609e-04
16 62	18 50	-0.961	0.266	1.981e+08
21 22	19 24	0.325	0.325	1.987e+07

Reactants	Products	ΔG (eV)	ΔG^\ddagger (eV)	k
19 24	21 22	-0.325	0.266	1.981e+08
21 28	19 27	-1.452	0.266	1.981e+08
19 27	21 28	1.452	1.452	1.797e-12
21 29	19 26	0.364	0.364	4.389e+06
19 26	21 29	-0.364	0.266	1.981e+08
21 34	19 32	-1.837	0.266	1.981e+08
19 32	21 34	1.837	1.837	5.482e-19
21 35	19 33	-0.518	0.266	1.981e+08
19 33	21 35	0.518	0.518	1.093e+04
21 41	19 36	0.429	0.429	3.461e+05
19 36	21 41	-0.429	0.266	1.981e+08
21 42	19 43	-0.023	0.266	1.981e+08
19 43	21 42	0.023	0.266	1.981e+08
21 44	11 19	-1.258	0.266	1.981e+08
11 19	21 44	1.258	1.258	3.409e-09
21 45	12 19	0.418	0.418	5.380e+05
12 19	21 45	-0.418	0.266	1.981e+08
21 46	19 25	-0.540	0.266	1.981e+08
19 25	21 46	0.540	0.540	4.623e+03
21 49	19 50	0.325	0.325	1.979e+07
19 50	21 49	-0.325	0.266	1.981e+08
21 51	13 19	-0.924	0.266	1.981e+08
13 19	21 51	0.924	0.924	1.479e-03
21 52	14 19	-0.914	0.266	1.981e+08
14 19	21 52	0.914	0.914	2.244e-03
21 53	19 19	-1.280	0.266	1.981e+08
19 19	21 53	1.280	1.280	1.435e-09
21 54	19 20	-0.665	0.266	1.981e+08
19 20	21 54	0.665	0.665	3.619e+01
20 21	19 55	1.033	1.033	2.164e-05
19 55	20 21	-1.033	0.266	1.981e+08
21 57	17 19	-1.318	0.266	1.981e+08
17 19	21 57	1.318	1.318	3.275e-10
21 59	19 38	-1.306	0.266	1.981e+08
19 38	21 59	1.306	1.306	5.276e-10
21 60	19 39	0.159	0.266	1.981e+08
19 39	21 60	-0.159	0.266	1.981e+08
12 21	19 61	1.309	1.309	4.570e-10
19 61	12 21	-1.309	0.266	1.981e+08

Reactants	Products	ΔG (eV)	ΔG^\ddagger (eV)	k
21 50	19 62	0.917	0.917	1.945e-03
19 62	21 50	-0.917	0.266	1.981e+08
24 28	22 27	-1.777	0.266	1.981e+08
22 27	24 28	1.777	1.777	5.749e-18
24 29	22 26	0.039	0.266	1.981e+08
22 26	24 29	-0.039	0.266	1.981e+08
24 34	22 32	-2.162	0.266	1.981e+08
22 32	24 34	2.162	2.162	1.754e-24
24 35	22 33	-0.843	0.266	1.981e+08
22 33	24 35	0.843	0.843	3.495e-02
24 41	22 36	0.104	0.266	1.981e+08
22 36	24 41	-0.104	0.266	1.981e+08
24 42	22 43	-0.348	0.266	1.981e+08
22 43	24 42	0.348	0.348	7.990e+06
24 44	11 22	-1.583	0.266	1.981e+08
11 22	24 44	1.583	1.583	1.090e-14
24 45	12 22	0.093	0.266	1.981e+08
12 22	24 45	-0.093	0.266	1.981e+08
24 46	22 25	-0.865	0.266	1.981e+08
22 25	24 46	0.865	0.865	1.479e-02
24 49	22 50	0.000	0.266	1.981e+08
22 50	24 49	-0.000	0.266	1.981e+08
24 51	13 22	-1.249	0.266	1.981e+08
13 22	24 51	1.249	1.249	4.731e-09
24 52	14 22	-1.239	0.266	1.981e+08
14 22	24 52	1.239	1.239	7.177e-09
24 53	19 22	-1.605	0.266	1.981e+08
19 22	24 53	1.605	1.605	4.591e-15
24 54	20 22	-0.990	0.266	1.981e+08
20 22	24 54	0.990	0.990	1.158e-04
20 24	22 55	0.708	0.708	6.764e+00
22 55	20 24	-0.708	0.266	1.981e+08
24 57	17 22	-1.643	0.266	1.981e+08
17 22	24 57	1.643	1.643	1.048e-15
24 59	22 38	-1.631	0.266	1.981e+08
22 38	24 59	1.631	1.631	1.688e-15
24 60	22 39	-0.166	0.266	1.981e+08
22 39	24 60	0.166	0.266	1.981e+08
12 24	22 61	0.984	0.984	1.429e-04

Reactants	Products	ΔG (eV)	ΔG^\ddagger (eV)	k
22 61	12 24	-0.984	0.266	1.981e+08
24 50	22 62	0.592	0.592	6.080e+02
22 62	24 50	-0.592	0.266	1.981e+08
27 29	26 28	1.816	1.816	1.270e-18
26 28	27 29	-1.816	0.266	1.981e+08
27 34	28 32	-0.385	0.266	1.981e+08
28 32	27 34	0.385	0.385	1.895e+06
27 35	28 33	0.934	0.934	1.022e-03
28 33	27 35	-0.934	0.266	1.981e+08
27 41	28 36	1.881	1.881	1.001e-19
28 36	27 41	-1.881	0.266	1.981e+08
27 42	28 43	1.428	1.428	4.470e-12
28 43	27 42	-1.428	0.266	1.981e+08
27 44	11 28	0.194	0.266	1.981e+08
11 28	27 44	-0.194	0.266	1.981e+08
27 45	12 28	1.870	1.870	1.556e-19
12 28	27 45	-1.870	0.266	1.981e+08
27 46	25 28	0.912	0.912	2.416e-03
25 28	27 46	-0.912	0.266	1.981e+08
27 49	28 50	1.777	1.777	5.725e-18
28 50	27 49	-1.777	0.266	1.981e+08
27 51	13 28	0.527	0.527	7.551e+03
13 28	27 51	-0.527	0.266	1.981e+08
27 52	14 28	0.538	0.538	4.976e+03
14 28	27 52	-0.538	0.266	1.981e+08
27 53	19 28	0.172	0.266	1.981e+08
19 28	27 53	-0.172	0.266	1.981e+08
27 54	20 28	0.787	0.787	3.085e-01
20 28	27 54	-0.787	0.266	1.981e+08
20 27	28 55	2.484	2.484	6.260e-30
28 55	20 27	-2.484	0.266	1.981e+08
27 57	17 28	0.134	0.266	1.981e+08
17 28	27 57	-0.134	0.266	1.981e+08
27 59	28 38	0.146	0.266	1.981e+08
28 38	27 59	-0.146	0.266	1.981e+08
27 60	28 39	1.611	1.611	3.685e-15
28 39	27 60	-1.611	0.266	1.981e+08
12 27	28 61	2.761	2.761	1.322e-34
28 61	12 27	-2.761	0.266	1.981e+08

Reactants	Products	ΔG (eV)	ΔG^\ddagger (eV)	k
27 50	28 62	2.369	2.369	5.627e-28
28 62	27 50	-2.369	0.266	1.981e+08
26 34	29 32	-2.201	0.266	1.981e+08
29 32	26 34	2.201	2.201	3.873e-25
26 35	29 33	-0.882	0.266	1.981e+08
29 33	26 35	0.882	0.882	7.720e-03
26 41	29 36	0.065	0.266	1.981e+08
29 36	26 41	-0.065	0.266	1.981e+08
26 42	29 43	-0.387	0.266	1.981e+08
29 43	26 42	0.387	0.387	1.765e+06
26 44	11 29	-1.622	0.266	1.981e+08
11 29	26 44	1.622	1.622	2.409e-15
26 45	12 29	0.054	0.266	1.981e+08
12 29	26 45	-0.054	0.266	1.981e+08
26 46	25 29	-0.904	0.266	1.981e+08
25 29	26 46	0.904	0.904	3.266e-03
26 49	29 50	-0.039	0.266	1.981e+08
29 50	26 49	0.039	0.266	1.981e+08
26 51	13 29	-1.288	0.266	1.981e+08
13 29	26 51	1.288	1.288	1.045e-09
26 52	14 29	-1.277	0.266	1.981e+08
14 29	26 52	1.277	1.277	1.585e-09
26 53	19 29	-1.644	0.266	1.981e+08
19 29	26 53	1.644	1.644	1.014e-15
26 54	20 29	-1.029	0.266	1.981e+08
20 29	26 54	1.029	1.029	2.557e-05
20 26	29 55	0.669	0.669	3.062e+01
29 55	20 26	-0.669	0.266	1.981e+08
26 57	17 29	-1.682	0.266	1.981e+08
17 29	26 57	1.682	1.682	2.314e-16
26 59	29 38	-1.670	0.266	1.981e+08
29 38	26 59	1.670	1.670	3.728e-16
26 60	29 39	-0.205	0.266	1.981e+08
29 39	26 60	0.205	0.266	1.981e+08
12 26	29 61	0.946	0.946	6.468e-04
29 61	12 26	-0.946	0.266	1.981e+08
26 50	29 62	0.553	0.553	2.753e+03
29 62	26 50	-0.553	0.266	1.981e+08
32 35	33 34	1.319	1.319	3.117e-10

Reactants	Products	ΔG (eV)	ΔG^\ddagger (eV)	k
33 34	32 35	-1.319	0.266	1.981e+08
32 41	34 36	2.266	2.266	3.054e-26
34 36	32 41	-2.266	0.266	1.981e+08
32 42	34 43	1.814	1.814	1.363e-18
34 43	32 42	-1.814	0.266	1.981e+08
32 44	11 34	0.579	0.579	9.991e+02
11 34	32 44	-0.579	0.266	1.981e+08
32 45	12 34	2.255	2.255	4.747e-26
12 34	32 45	-2.255	0.266	1.981e+08
32 46	25 34	1.297	1.297	7.368e-10
25 34	32 46	-1.297	0.266	1.981e+08
32 49	34 50	2.162	2.162	1.746e-24
34 50	32 49	-2.162	0.266	1.981e+08
32 51	13 34	0.913	0.913	2.303e-03
13 34	32 51	-0.913	0.266	1.981e+08
32 52	14 34	0.924	0.924	1.518e-03
14 34	32 52	-0.924	0.266	1.981e+08
32 53	19 34	0.557	0.557	2.373e+03
19 34	32 53	-0.557	0.266	1.981e+08
32 54	20 34	1.173	1.173	9.409e-08
20 34	32 54	-1.173	0.266	1.981e+08
20 32	34 55	2.870	2.870	1.909e-36
34 55	20 32	-2.870	0.266	1.981e+08
32 57	17 34	0.519	0.519	1.040e+04
17 34	32 57	-0.519	0.266	1.981e+08
32 59	34 38	0.531	0.531	6.455e+03
34 38	32 59	-0.531	0.266	1.981e+08
32 60	34 39	1.996	1.996	1.124e-21
34 39	32 60	-1.996	0.266	1.981e+08
12 32	34 61	3.147	3.147	4.033e-41
34 61	12 32	-3.147	0.266	1.981e+08
32 50	34 62	2.754	2.754	1.716e-34
34 62	32 50	-2.754	0.266	1.981e+08
33 41	35 36	0.947	0.947	6.086e-04
35 36	33 41	-0.947	0.266	1.981e+08
33 42	35 43	0.495	0.495	2.717e+04
35 43	33 42	-0.495	0.266	1.981e+08
33 44	11 35	-0.740	0.266	1.981e+08
11 35	33 44	0.740	0.740	1.938e+00

Reactants	Products	ΔG (eV)	ΔG^\ddagger (eV)	k
33 45	12 35	0.936	0.936	9.461e-04
12 35	33 45	-0.936	0.266	1.981e+08
33 46	25 35	-0.022	0.266	1.981e+08
25 35	33 46	0.022	0.266	1.981e+08
33 49	35 50	0.843	0.843	3.480e-02
35 50	33 49	-0.843	0.266	1.981e+08
33 51	13 35	-0.406	0.266	1.981e+08
13 35	33 51	0.406	0.406	8.409e+05
33 52	14 35	-0.396	0.266	1.981e+08
14 35	33 52	0.396	0.396	1.276e+06
33 53	19 35	-0.762	0.266	1.981e+08
19 35	33 53	0.762	0.762	8.161e-01
33 54	20 35	-0.147	0.266	1.981e+08
20 35	33 54	0.147	0.266	1.981e+08
20 33	35 55	1.551	1.551	3.805e-14
35 55	20 33	-1.551	0.266	1.981e+08
33 57	17 35	-0.800	0.266	1.981e+08
17 35	33 57	0.800	0.800	1.862e-01
33 59	35 38	-0.788	0.266	1.981e+08
35 38	33 59	0.788	0.788	3.000e-01
33 60	35 39	0.677	0.677	2.240e+01
35 39	33 60	-0.677	0.266	1.981e+08
12 33	35 61	1.827	1.827	8.038e-19
35 61	12 33	-1.827	0.266	1.981e+08
33 50	35 62	1.435	1.435	3.420e-12
35 62	33 50	-1.435	0.266	1.981e+08
36 42	41 43	-0.453	0.266	1.981e+08
41 43	36 42	0.453	0.453	1.391e+05
36 44	11 41	-1.687	0.266	1.981e+08
11 41	36 44	1.687	1.687	1.899e-16
36 45	12 41	-0.011	0.266	1.981e+08
12 41	36 45	0.011	0.266	1.981e+08
36 46	25 41	-0.969	0.266	1.981e+08
25 41	36 46	0.969	0.969	2.575e-04
36 49	41 50	-0.104	0.266	1.981e+08
41 50	36 49	0.104	0.266	1.981e+08
36 51	13 41	-1.353	0.266	1.981e+08
13 41	36 51	1.353	1.353	8.238e-11
36 52	14 41	-1.343	0.266	1.981e+08

Reactants	Products	ΔG (eV)	ΔG^\ddagger (eV)	k
14 41	36 52	1.343	1.343	1.250e-10
36 53	19 41	-1.709	0.266	1.981e+08
19 41	36 53	1.709	1.709	7.995e-17
36 54	20 41	-1.094	0.266	1.981e+08
20 41	36 54	1.094	1.094	2.016e-06
20 36	41 55	0.604	0.604	3.884e+02
41 55	20 36	-0.604	0.266	1.981e+08
36 57	17 41	-1.747	0.266	1.981e+08
17 41	36 57	1.747	1.747	1.824e-17
36 59	38 41	-1.735	0.266	1.981e+08
38 41	36 59	1.735	1.735	2.939e-17
36 60	39 41	-0.270	0.266	1.981e+08
39 41	36 60	0.270	0.270	1.688e+08
12 36	41 61	0.880	0.880	8.205e-03
41 61	12 36	-0.880	0.266	1.981e+08
36 50	41 62	0.488	0.488	3.491e+04
41 62	36 50	-0.488	0.266	1.981e+08
43 44	11 42	-1.234	0.266	1.981e+08
11 42	43 44	1.234	1.234	8.478e-09
43 45	12 42	0.441	0.441	2.163e+05
12 42	43 45	-0.441	0.266	1.981e+08
43 46	25 42	-0.517	0.266	1.981e+08
25 42	43 46	0.517	0.517	1.150e+04
43 49	42 50	0.349	0.349	7.956e+06
42 50	43 49	-0.349	0.266	1.981e+08
43 51	13 42	-0.901	0.266	1.981e+08
13 42	43 51	0.901	0.901	3.678e-03
43 52	14 42	-0.890	0.266	1.981e+08
14 42	43 52	0.890	0.890	5.581e-03
43 53	19 42	-1.257	0.266	1.981e+08
19 42	43 53	1.257	1.257	3.570e-09
43 54	20 42	-0.641	0.266	1.981e+08
20 42	43 54	0.641	0.641	9.002e+01
20 43	42 55	1.056	1.056	8.699e-06
42 55	20 43	-1.056	0.266	1.981e+08
43 57	17 42	-1.295	0.266	1.981e+08
17 42	43 57	1.295	1.295	8.145e-10
43 59	38 42	-1.282	0.266	1.981e+08
38 42	43 59	1.282	1.282	1.312e-09

Reactants	Products	ΔG (eV)	ΔG^\ddagger (eV)	k
43 60	39 42	0.182	0.266	1.981e+08
39 42	43 60	-0.182	0.266	1.981e+08
12 43	42 61	1.333	1.333	1.838e-10
42 61	12 43	-1.333	0.266	1.981e+08
43 50	42 62	0.941	0.941	7.820e-04
42 62	43 50	-0.941	0.266	1.981e+08
11 45	12 44	1.676	1.676	2.952e-16
12 44	11 45	-1.676	0.266	1.981e+08
11 46	25 44	0.718	0.718	4.581e+00
25 44	11 46	-0.718	0.266	1.981e+08
11 49	44 50	1.583	1.583	1.086e-14
44 50	11 49	-1.583	0.266	1.981e+08
11 51	13 44	0.333	0.333	1.432e+07
13 44	11 51	-0.333	0.266	1.981e+08
11 52	14 44	0.344	0.344	9.438e+06
14 44	11 52	-0.344	0.266	1.981e+08
11 53	19 44	-0.022	0.266	1.981e+08
19 44	11 53	0.022	0.266	1.981e+08
11 54	20 44	0.593	0.593	5.851e+02
20 44	11 54	-0.593	0.266	1.981e+08
11 20	44 55	2.291	2.291	1.187e-26
44 55	11 20	-2.291	0.266	1.981e+08
11 57	17 44	-0.060	0.266	1.981e+08
17 44	11 57	0.060	0.266	1.981e+08
11 59	38 44	-0.048	0.266	1.981e+08
38 44	11 59	0.048	0.266	1.981e+08
11 60	39 44	1.417	1.417	6.990e-12
39 44	11 60	-1.417	0.266	1.981e+08
11 12	44 61	2.567	2.567	2.508e-31
44 61	11 12	-2.567	0.266	1.981e+08
11 50	44 62	2.175	2.175	1.067e-24
44 62	11 50	-2.175	0.266	1.981e+08
12 46	25 45	-0.958	0.266	1.981e+08
25 45	12 46	0.958	0.958	4.003e-04
12 49	45 50	-0.093	0.266	1.981e+08
45 50	12 49	0.093	0.266	1.981e+08
12 51	13 45	-1.342	0.266	1.981e+08
13 45	12 51	1.342	1.342	1.281e-10
12 52	14 45	-1.331	0.266	1.981e+08

Reactants	Products	ΔG (eV)	ΔG^\ddagger (eV)	k
14 45	12 52	1.331	1.331	1.943e-10
12 53	19 45	-1.698	0.266	1.981e+08
19 45	12 53	1.698	1.698	1.243e-16
12 54	20 45	-1.082	0.266	1.981e+08
20 45	12 54	1.082	1.082	3.134e-06
12 20	45 55	0.615	0.615	2.498e+02
45 55	12 20	-0.615	0.266	1.981e+08
12 57	17 45	-1.736	0.266	1.981e+08
17 45	12 57	1.736	1.736	2.836e-17
12 59	38 45	-1.724	0.266	1.981e+08
38 45	12 59	1.724	1.724	4.569e-17
12 60	39 45	-0.259	0.266	1.981e+08
39 45	12 60	0.259	0.266	1.981e+08
12 12	45 61	0.892	0.892	5.278e-03
45 61	12 12	-0.892	0.266	1.981e+08
12 50	45 62	0.499	0.499	2.246e+04
45 62	12 50	-0.499	0.266	1.981e+08
25 49	46 50	0.865	0.865	1.472e-02
46 50	25 49	-0.865	0.266	1.981e+08
25 51	13 46	-0.384	0.266	1.981e+08
13 46	25 51	0.384	0.384	1.987e+06
25 52	14 46	-0.374	0.266	1.981e+08
14 46	25 52	0.374	0.374	3.016e+06
25 53	19 46	-0.740	0.266	1.981e+08
19 46	25 53	0.740	0.740	1.929e+00
25 54	20 46	-0.125	0.266	1.981e+08
20 46	25 54	0.125	0.266	1.981e+08
20 25	46 55	1.573	1.573	1.610e-14
46 55	20 25	-1.573	0.266	1.981e+08
25 57	17 46	-0.778	0.266	1.981e+08
17 46	25 57	0.778	0.778	4.401e-01
25 59	38 46	-0.766	0.266	1.981e+08
38 46	25 59	0.766	0.766	7.091e-01
25 60	39 46	0.699	0.699	9.478e+00
39 46	25 60	-0.699	0.266	1.981e+08
12 25	46 61	1.849	1.849	3.401e-19
46 61	12 25	-1.849	0.266	1.981e+08
25 50	46 62	1.457	1.457	1.447e-12
46 62	25 50	-1.457	0.266	1.981e+08

Reactants	Products	ΔG (eV)	ΔG^\ddagger (eV)	k
50 51	13 49	-1.249	0.266	1.981e+08
13 49	50 51	1.249	1.249	4.710e-09
50 52	14 49	-1.239	0.266	1.981e+08
14 49	50 52	1.239	1.239	7.147e-09
50 53	19 49	-1.605	0.266	1.981e+08
19 49	50 53	1.605	1.605	4.571e-15
50 54	20 49	-0.990	0.266	1.981e+08
20 49	50 54	0.990	0.990	1.153e-04
20 50	49 55	0.708	0.708	6.793e+00
49 55	20 50	-0.708	0.266	1.981e+08
50 57	17 49	-1.643	0.266	1.981e+08
17 49	50 57	1.643	1.643	1.043e-15
50 59	38 49	-1.631	0.266	1.981e+08
38 49	50 59	1.631	1.631	1.681e-15
50 60	39 49	-0.166	0.266	1.981e+08
39 49	50 60	0.166	0.266	1.981e+08
12 50	49 61	0.984	0.984	1.435e-04
49 61	12 50	-0.984	0.266	1.981e+08
50 50	49 62	0.592	0.592	6.106e+02
49 62	50 50	-0.592	0.266	1.981e+08
13 52	14 51	0.011	0.266	1.981e+08
14 51	13 52	-0.011	0.266	1.981e+08
13 53	19 51	-0.356	0.266	1.981e+08
19 51	13 53	0.356	0.356	6.029e+06
13 54	20 51	0.260	0.266	1.981e+08
20 51	13 54	-0.260	0.266	1.981e+08
13 20	51 55	1.957	1.957	5.150e-21
51 55	13 20	-1.957	0.266	1.981e+08
13 57	17 51	-0.394	0.266	1.981e+08
17 51	13 57	0.394	0.394	1.376e+06
13 59	38 51	-0.381	0.266	1.981e+08
38 51	13 59	0.381	0.381	2.217e+06
13 60	39 51	1.083	1.083	3.032e-06
39 51	13 60	-1.083	0.266	1.981e+08
12 13	51 61	2.234	2.234	1.088e-25
51 61	12 13	-2.234	0.266	1.981e+08
13 50	51 62	1.841	1.841	4.630e-19
51 62	13 50	-1.841	0.266	1.981e+08
14 53	19 52	-0.366	0.266	1.981e+08

Reactants	Products	ΔG (eV)	ΔG^\ddagger (eV)	k
19 52	14 53	0.366	0.366	3.974e+06
14 54	20 52	0.249	0.266	1.981e+08
20 52	14 54	-0.249	0.266	1.981e+08
14 20	52 55	1.946	1.946	7.814e-21
52 55	14 20	-1.946	0.266	1.981e+08
14 57	17 52	-0.404	0.266	1.981e+08
17 52	14 57	0.404	0.404	9.067e+05
14 59	38 52	-0.392	0.266	1.981e+08
38 52	14 59	0.392	0.392	1.461e+06
14 60	39 52	1.073	1.073	4.601e-06
39 52	14 60	-1.073	0.266	1.981e+08
12 14	52 61	2.223	2.223	1.651e-25
52 61	12 14	-2.223	0.266	1.981e+08
14 50	52 62	1.831	1.831	7.024e-19
52 62	14 50	-1.831	0.266	1.981e+08
19 54	20 53	0.615	0.615	2.463e+02
20 53	19 54	-0.615	0.266	1.981e+08
19 20	53 55	2.313	2.313	4.998e-27
53 55	19 20	-2.313	0.266	1.981e+08
19 57	17 53	-0.038	0.266	1.981e+08
17 53	19 57	0.038	0.266	1.981e+08
19 59	38 53	-0.026	0.266	1.981e+08
38 53	19 59	0.026	0.266	1.981e+08
19 60	39 53	1.439	1.439	2.943e-12
39 53	19 60	-1.439	0.266	1.981e+08
12 19	53 61	2.589	2.589	1.056e-31
53 61	12 19	-2.589	0.266	1.981e+08
19 50	53 62	2.197	2.197	4.493e-25
53 62	19 50	-2.197	0.266	1.981e+08
20 20	54 55	1.697	1.697	1.261e-16
54 55	20 20	-1.697	0.266	1.981e+08
20 57	17 54	-0.653	0.266	1.981e+08
17 54	20 57	0.653	0.653	5.621e+01
20 59	38 54	-0.641	0.266	1.981e+08
38 54	20 59	0.641	0.641	9.056e+01
20 60	39 54	0.824	0.824	7.421e-02
39 54	20 60	-0.824	0.266	1.981e+08
12 20	54 61	1.974	1.974	2.663e-21
54 61	12 20	-1.974	0.266	1.981e+08

Reactants	Products	ΔG (eV)	ΔG^\ddagger (eV)	k
20 50	54 62	1.582	1.582	1.133e-14
54 62	20 50	-1.582	0.266	1.981e+08
55 57	17 20	-2.351	0.266	1.981e+08
17 20	55 57	2.351	2.351	1.141e-27
55 59	20 38	-2.339	0.266	1.981e+08
20 38	55 59	2.339	2.339	1.838e-27
55 60	20 39	-0.874	0.266	1.981e+08
20 39	55 60	0.874	0.874	1.055e-02
12 55	20 61	0.277	0.277	1.312e+08
20 61	12 55	-0.277	0.266	1.981e+08
50 55	20 62	-0.116	0.266	1.981e+08
20 62	50 55	0.116	0.266	1.981e+08
17 59	38 57	0.012	0.266	1.981e+08
38 57	17 59	-0.012	0.266	1.981e+08
17 60	39 57	1.477	1.477	6.715e-13
39 57	17 60	-1.477	0.266	1.981e+08
12 17	57 61	2.627	2.627	2.409e-32
57 61	12 17	-2.627	0.266	1.981e+08
17 50	57 62	2.235	2.235	1.025e-25
57 62	17 50	-2.235	0.266	1.981e+08
38 60	39 59	1.465	1.465	1.082e-12
39 59	38 60	-1.465	0.266	1.981e+08
12 38	59 61	2.615	2.615	3.882e-32
59 61	12 38	-2.615	0.266	1.981e+08
38 50	59 62	2.223	2.223	1.652e-25
59 62	38 50	-2.223	0.266	1.981e+08
12 39	60 61	1.150	1.150	2.229e-07
60 61	12 39	-1.150	0.266	1.981e+08
39 50	60 62	0.758	0.758	9.485e-01
60 62	39 50	-0.758	0.266	1.981e+08
50 61	12 62	-0.392	0.266	1.981e+08
12 62	50 61	0.392	0.392	1.460e+06

Reactants	Products	ΔG (eV)	ΔG^\ddagger (eV)	k
-----------	----------	-----------------	--------------------------	---

Table G.3: Coordination and re-coordination reactions included in kMC simulations. For coordination reactions, if the reaction is exergonic ($\Delta G < 0$), then the reaction is taken to be barrierless; otherwise, the free energy defines the effective barrier. For re-coordination reactions, there is a minimum energy barrier, which we take in most simulations to be $\Delta G_{recoord}^\ddagger = 0.266$ eV. The units of the rate constant k depend on if the reaction is unimolecular or bimolecular. Where relevant, all values are calculated at $T = 298.15K$.

Reactants	Products	ΔG (eV)	ΔG^\ddagger (eV)	k
41 32	42	-0.809	0.000	6.212e+12
42	41 32	0.809	0.809	1.307e-01
33 35	12 31	-2.115	0.000	6.212e+12
12 31	33 35	2.115	2.115	1.089e-23
35 35	45 31	-3.051	0.000	6.212e+12
45 31	35 35	3.051	3.051	1.659e-39
33 33	61 31	-0.288	0.000	6.212e+12
61 31	33 33	0.288	0.288	8.420e+07
33 35	50	-3.082	0.000	6.212e+12
50	33 35	3.082	3.082	4.917e-40
35 35	49	-3.925	0.000	6.212e+12
49	35 35	3.925	3.925	2.754e-54
33 33	62	-1.647	0.000	6.212e+12
62	33 33	1.647	1.647	8.931e-16
58	16 36	-2.654	0.000	6.212e+12
16 36	58	2.654	2.654	8.492e-33
19 36	38 24	-0.285	0.000	6.212e+12
38 24	19 36	0.285	0.285	9.532e+07
36 32	43	-1.262	0.000	6.212e+12
43	36 32	1.262	1.262	2.926e-09
39	36 48	1.017	0.000	6.212e+12
36 48	39	-1.017	0.000	6.212e+12
60	41 48	0.747	0.000	6.212e+12
41 48	60	-0.747	0.000	6.212e+12
46 32	23	-2.342	0.000	6.212e+12
23	46 32	2.342	2.342	1.586e-27
25 32	24	0.009	0.000	6.212e+12

Reactants	Products	ΔG (eV)	ΔG^\ddagger (eV)	k
22 32	13	-0.696	0.000	6.212e+12
13	22 32	0.696	0.696	1.056e+01
24 32	15	-1.016	0.000	6.212e+12
15	24 32	1.016	1.016	4.096e-05
6 6	13 30	-2.676	0.000	6.212e+12
13 30	6 6	2.676	2.676	3.561e-33
48 48	40	-4.157	0.000	6.212e+12
40	48 48	4.157	4.157	3.297e-58
42 24	12 19	-0.743	0.000	6.212e+12
12 19	42 24	0.743	0.743	1.712e+00
20 48	24 40	-2.616	0.000	6.212e+12
24 40	20 48	2.616	2.616	3.795e-32
6 42	57	2.344	0.000	6.212e+12
57	6 42	-2.344	0.000	6.212e+12

Table G.4: Barrierless reactions included in kMC simulations. These reactions either have no transition-state (as reported from the literature and confirmed at the ω B97X-V/def2-TZVPPD/SMD level of theory) or a transition-state was found and the calculated free energy barrier was negative in one or both directions. In general, the effective free energy barrier is calculated from the reaction free energy ΔG . However, for select reactions (such as the dissociation of water, which occurs essentially barrierlessly on a bare surface but not in solution),[212] the barrier was set to 0 by fiat. All values are calculated at $T = 298.15K$.

Reactants	Products	ΔG (eV)	ΔG^\ddagger (eV)	k
4	6	-1.208	0.400 ^a	1.076e+06
6	4	1.208	1.893	6.351e-20
6	11 30	0.370	1.076	4.010e-06
11 30	6	-0.370	0.706	7.258e+00
7	12 30	-1.611	0.130	3.936e+10
12 30	7	1.611	1.741	2.299e-17
52	6 45	-1.737	0.590	6.706e+02
6 45	52	1.737	2.327	2.869e-27
20	6 36	0.552	1.671	3.545e-16
6 36	20	-0.552	1.119	7.672e-07
54	22 48	0.552	0.803	1.675e-01

Reactants	Products	ΔG (eV)	ΔG^\ddagger (eV)	k
22 48	54	-0.552	0.251	3.595e+08
55	26 33	-0.370	1.315	3.615e-10
26 33	55	0.370	1.685	2.042e-16
56	13 36	-0.493	0.245	4.446e+08
13 36	56	0.493	0.739	2.038e+00
14	6 12	-0.406	1.780	4.990e-18
6 12	14	0.406	2.186	6.826e-25
14	7 11	1.575	1.780	4.990e-18
7 11	14	-1.575	0.205	2.115e+09
9	25 31	-0.202	0.089	1.955e+11
25 31	9	0.202	0.291	7.403e+07
13	3 12	1.546	1.866	1.754e-19
3 12	13	-1.546	0.321	2.363e+07
15	1 12	0.230	1.339	1.442e-10
1 12	15	-0.230	1.109	1.133e-06
19	3 36	2.506	2.506	2.700e-30
3 36	19	-2.506	0.000	6.127e+12
20	29 33	0.299	1.526	9.940e-14
29 33	20	-0.299	1.227	1.139e-08
20	26 35	1.181	1.526	9.940e-14
26 35	20	-1.181	0.345	9.169e+06
23	33 46	0.500	1.736	2.802e-17
33 46	23	-0.500	1.236	8.021e-09
23	25 35	0.478	1.736	2.802e-17
25 35	23	-0.478	1.258	3.394e-09
14	24 35	1.123	1.512	1.694e-13
24 35	14	-1.123	0.390	1.602e+06
14	22 33	0.280	1.512	1.694e-13
22 33	14	-0.280	1.233	9.013e-09
56	22 43	-1.059	0.157	1.383e+10
22 43	56	1.059	1.216	1.756e-08
56	24 42	-0.710	0.157	1.383e+10
24 42	56	0.710	0.867	1.366e-02
22 43	12 19	-0.395	0.088	2.022e+11
12 19	22 43	0.395	0.483	4.333e+04
13 36	12 19	-0.960	1.344	1.168e-10
12 19	13 36	0.960	2.304	6.937e-27
43 48	10 40	-0.370	0.793	2.404e-01
10 40	43 48	0.370	1.163	1.345e-07

Reactants	Products	ΔG (eV)	ΔG^\ddagger (eV)	k
5	9	-1.674	0.087	2.093e+11
9	5	1.674	1.761	1.064e-17
4 36	20	-1.760	0.470	7.077e+04
20	4 36	1.760	2.230	1.269e-25
1 43	18	0.380	1.388	2.168e-11
18	1 43	-0.380	1.007	5.828e-05
3 43	16	-0.887	0.588	7.193e+02
16	3 43	0.887	1.475	7.367e-13
17	6 43	-1.049	1.088	2.564e-06
6 43	17	1.049	2.137	4.748e-24
16 36	19 43	-1.619	0.962	3.403e-04
19 43	16 36	1.619	2.581	1.464e-31
58	19 43	-1.447	0.422	4.610e+05
19 43	58	1.447	1.869	1.598e-19

Table G.5: Other reactions included in kMC simulations.

All values are calculated at $T = 298.15K$. ^a this value is modified from the calculated value of 0.685 eV.

Appendix H

Supplemental Information for Chapter 7¹

H.1 Demonstration of Reversible Mg Plating and Stripping

Figure H.1 shows data from a cyclic voltammetry (CV) experiment conducted on the same MIB cell used for OEMS measurements. A scan of 100 mV s^{-1} was applied to the cell with Au WE, Mg RE, and a 0.5 M solution of $\text{Mg}(\text{TFSI})_2$ dissolved in G2. Four cycles are shown. All cycles demonstrate reversible Mg plating and stripping. This confirms that, during the OEMS experiment in which the cell voltage was held at -1.0 V, Mg was constantly plated.

¹This chapter is adapted from Ref [358]: Spotte-Smith, E.W.C., Blau, S.M., Barter, D., Leon, N.J., Hahn, N.T., Redkar, N.S., Zavadil, K.R., Liao, C., Persson, K.A. *Journal of the American Chemical Society* 145(22), 12181–12192.

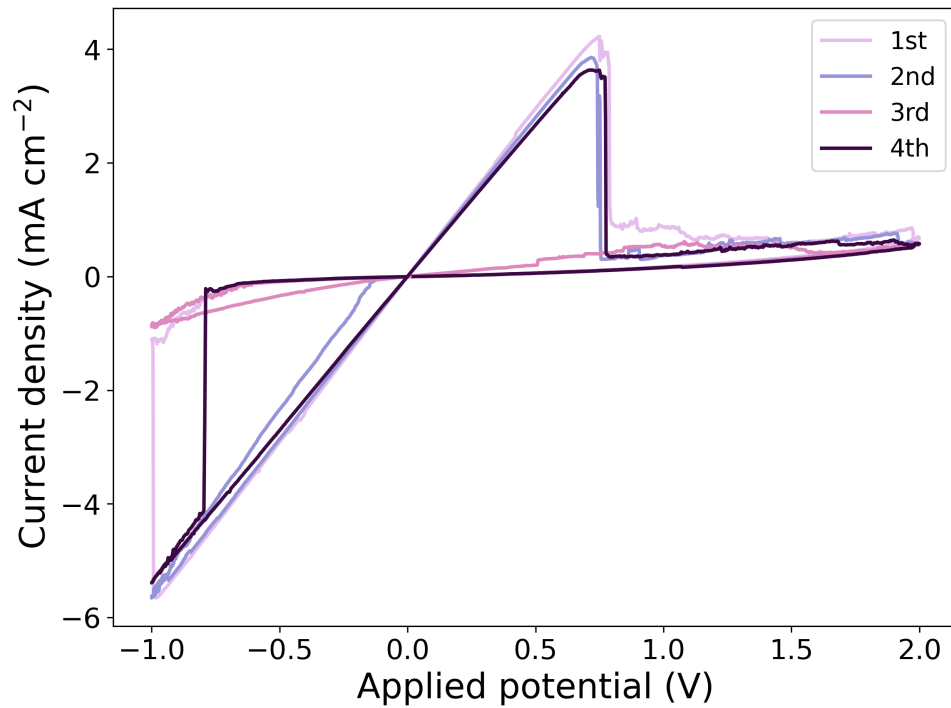


Figure H.1: Cyclic voltammogram showing two plating-stripping cycles for a DEMS cell containing a 0.5M Mg(TFSI)₂/G2 electrolyte, an Au working electrode, and Mg foil reference electrode. The scan rate was 100 mV s⁻¹.

H.2 Snapshot OEMS Spectra

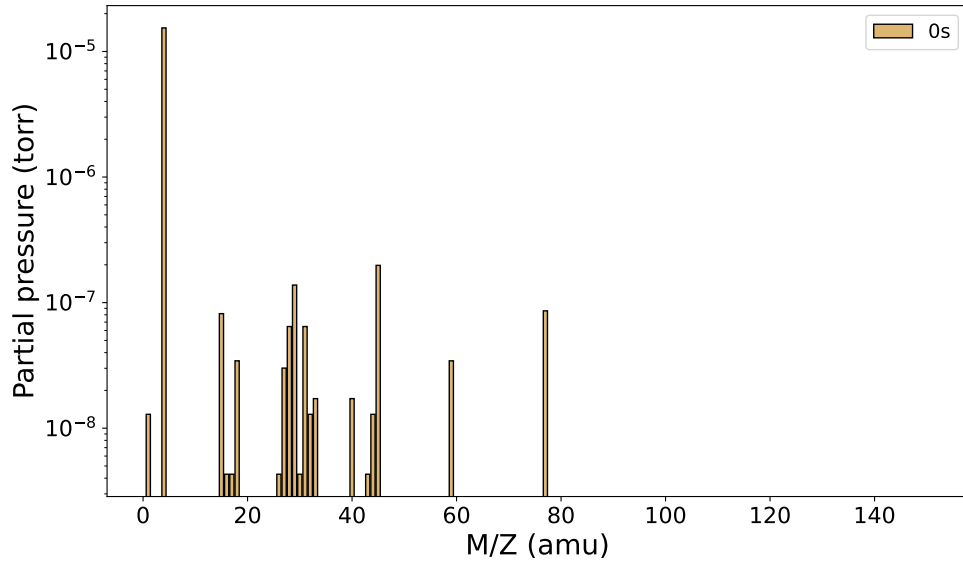


Figure H.2: Snapshot OEMS spectrum taken at the beginning of a potentiostatic experiment.

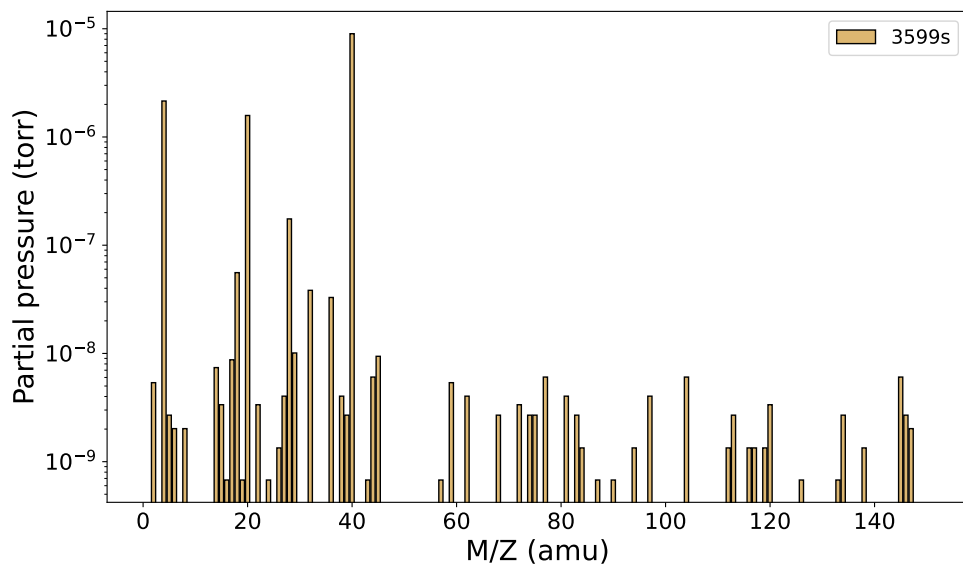


Figure H.3: Snapshot OEMS spectrum taken one hour into a potentiostatic experiment.

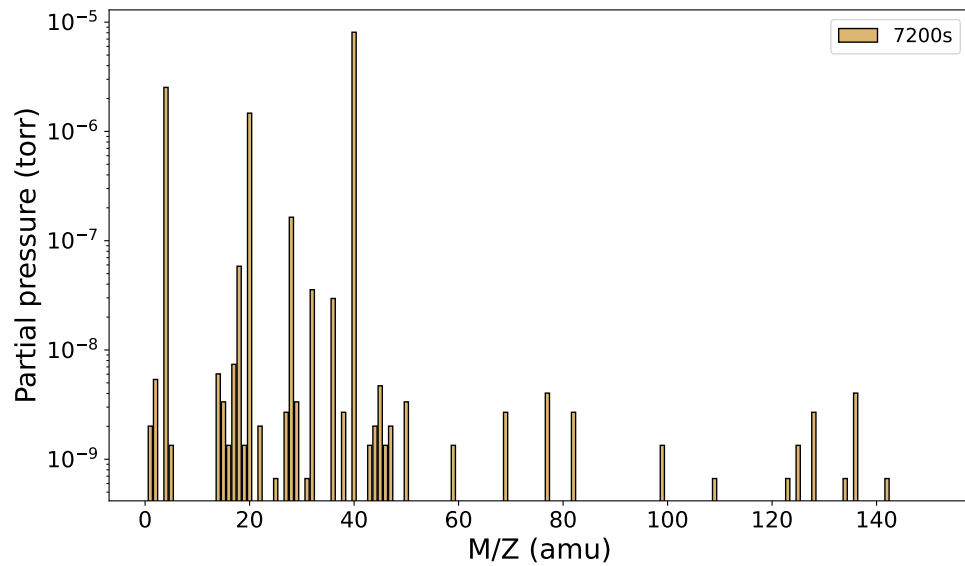


Figure H.4: Snapshot OEMS spectrum taken two hours into a potentiostatic experiment.

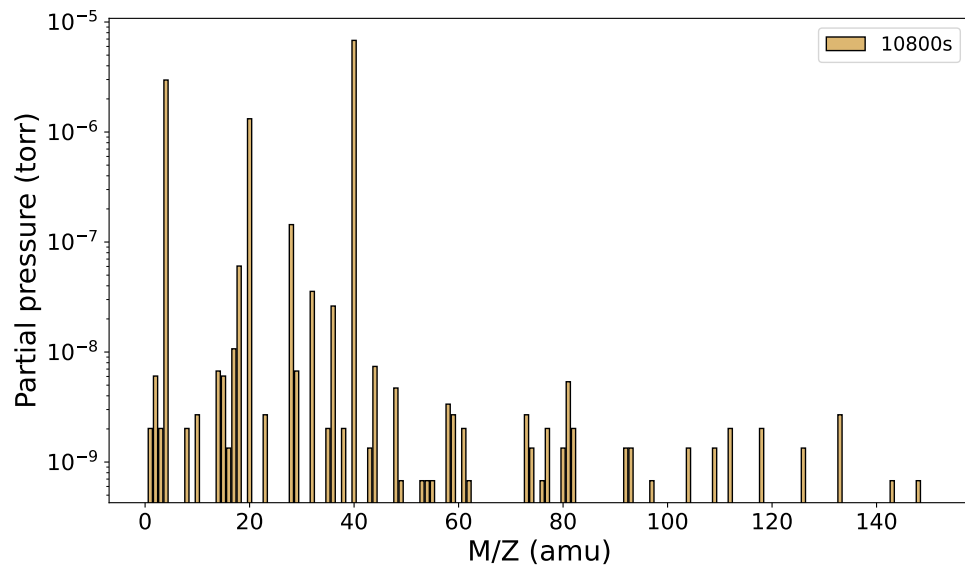


Figure H.5: Snapshot OEMS spectrum taken three hours into a potentiostatic experiment.

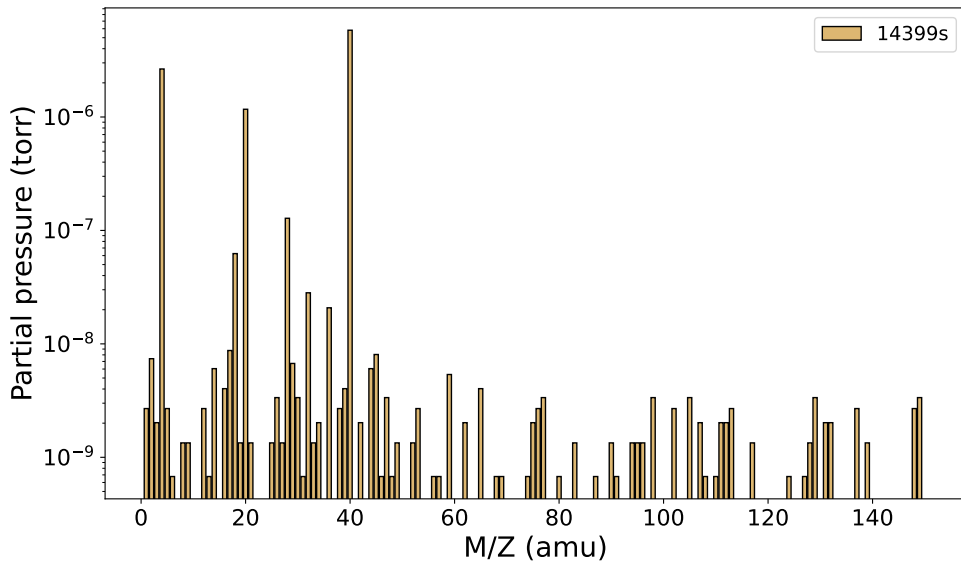


Figure H.6: Snapshot OEMS spectrum taken four hours into a potentiostatic experiment.

H.3 Solvation Correction

We optimized clusters with variable numbers of G2 as well as dimethoxyethane (DME) coordinating Mg^{2+} and Mg^{1+} ions in Q-Chem at the ω B97X-D/def2-SVPD/PCM// ω B97X-V/def2-TZVPPD/SMD level of theory[298, 301, 302, 425, 427]. From these clusters, we can calculate the relative stabilization of the ion as

$$\Delta E_{stabilization} = E_{S_n} - E_{S_0} - nE_S \quad (\text{H.1})$$

where E_{S_n} is the electronic energy of the ion surrounded by n solvent molecules S , E_{S_0} is the electronic energy of the ion without any explicit solvent molecules, and E_S is the electronic energy of the uncoordinated solvent molecule.

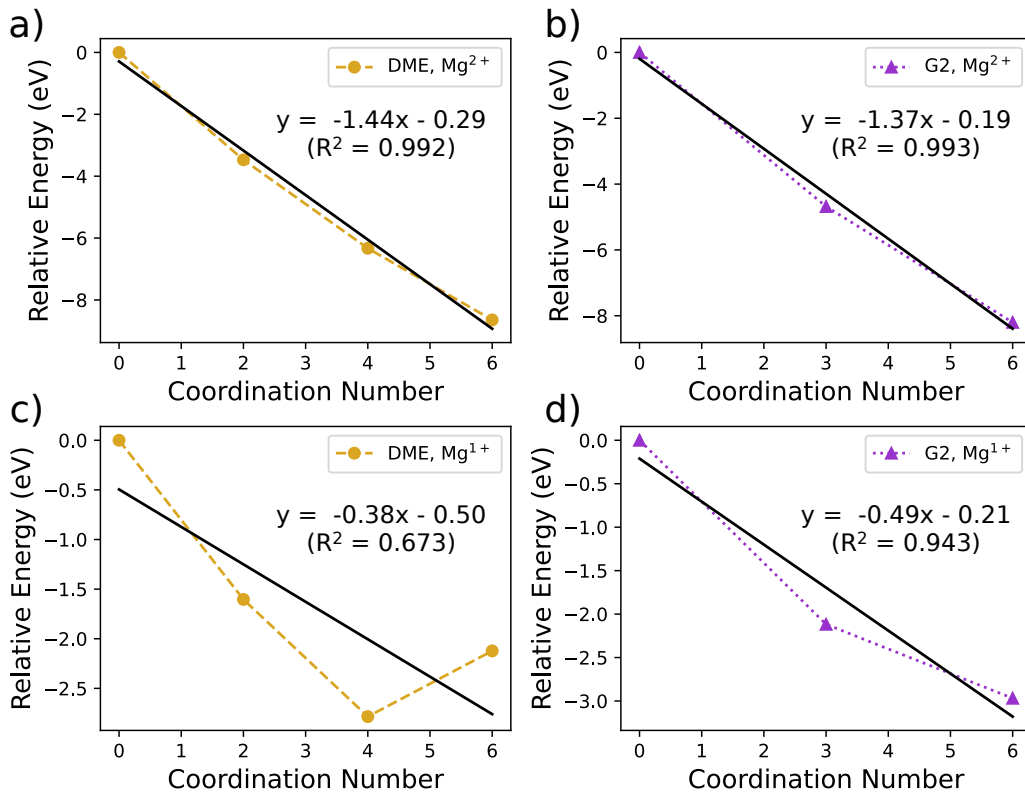


Figure H.7: Relative stabilization of Mg ions (Mg^{2+} , a-b; Mg^{1+} , c-d) by dimethoxyethane (DME) (a, c) and G2 (b, d) in terms of electronic energy (in eV). Equations for lines of best fit (solid black lines) are provided.

By performing linear regression on the relative stabilization of the Mg ions as a function of the coordination number of the ion (Figure H.7), we can find an effective solvation correction to apply during CRN construction. We note that the comparatively poor linear trend seen with Mg^{1+} ions reflects the preference of these ions for 5-fold coordination. The addition of a sixth coordinate bond is somewhat energetically unfavorable with DME as a solvent (the stabilization decreases when a third DME molecule, increasing the coordination number from 4 to 6, is added), and the addition of a second G2 molecule (increasing the coordination number from 3 to 6) leads to a much lower stabilization than the first G2.

H.4 Reduction Potentials

We considered redox potentials of Mg-coordinated species with and without full explicit solvent shells (Table H.1). It can be seen that the inclusion of explicit solvent can dramatically affect the reduction potential, in some cases changing the calculated value by $\sim 2\text{V}$. For the

reduction of Mg-coordinated G2 ($M_1 \longrightarrow M_2$), the predictions of reduction potentials in implicit solvent and explicit solvent are in qualitative disagreement. In implicit solvent, Mg^{2+} is expected to reduce significantly before the Mg plating potential (0.64 V vs. Mg/Mg^{2+}), while when a full explicit solvent shell is included, the reduction potential is significantly below the plating potential (-1.32 V vs. Mg/Mg^{2+}).

Reaction	Eimplicit (V)	Eexplicit (V)
$M_1 \longrightarrow M_2$	0.64	-1.32
$M_4 \longrightarrow M_7$	3.51	3.26*
$M_6^+Mg^{2+} \longrightarrow M_8$	3.89	1.62

Table H.1: Reduction potentials of Mg-coordinated species with and without explicit solvation. All potentials are reported referenced to the reduction potential of Mg. * = The reduced molecule dissociated during geometry optimization.

Without conducting additional dynamic simulations in the presence of explicit electrified interfaces, it is challenging to know in detail either the solvation behavior or the reduction behavior of Mg ions. In Chapter 7, we report reduction potentials without explicit solvent, as we expect that Mg ions will at least partially desolvate when in close proximity to an electrode or interphase surface. This is also supported by the preference of Mg^{1+} ions for lower coordination numbers than Mg^{2+} (see Section H.3 above). Nonetheless, we expect nontrivial error in our reported reduction potentials.

H.5 Network Products

Of the 6,469 species included in our CRN, 85 are identified as network products. Of these 85, 14 have sufficiently low predicted solubility in G2 that they can be considered as possible gaseous products. The remaining 71 species are shown in Figures H.8-H.10.

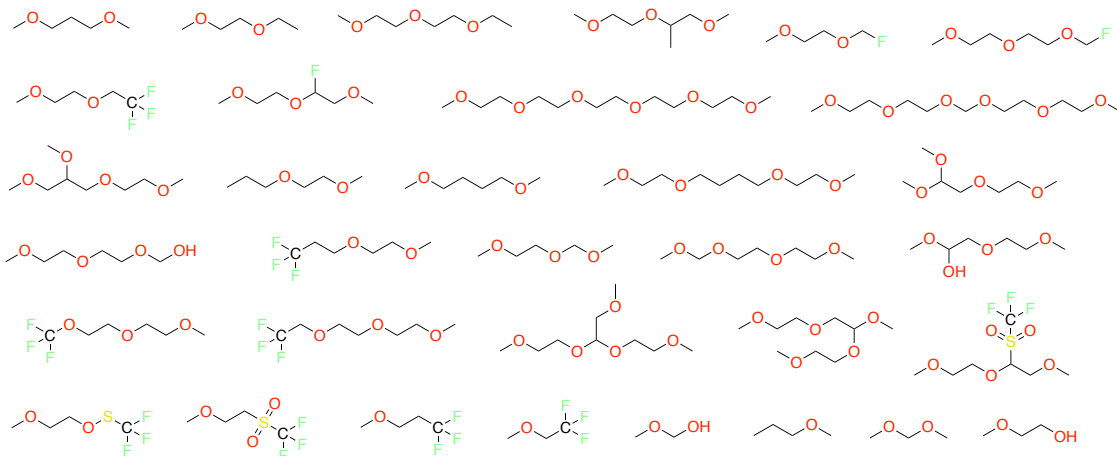


Figure H.8: Oligomer and other chain hydrocarbon network products.

Thirty-three of the predicted products (Figure H.8) have chain hydrocarbon backbones, in most cases with ether moieties. Many are oligomeric, including several branched oligomers. Considering these predicted network products alongside the propensity for G2 to decompose and form radical and anionic intermediates, we suggest that G2 should polymerize during MIB charging and SEI formation.

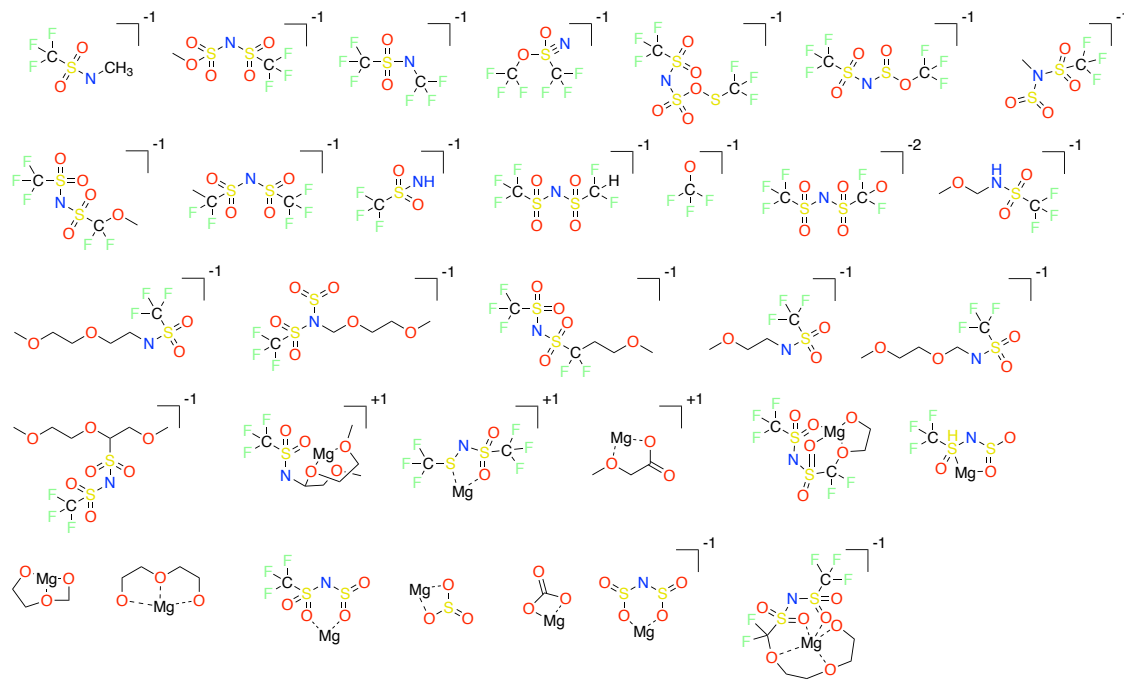


Figure H.9: Salt network products.

An additional 32 network products contain non-magnesium ions or are magnesium salts (Figure H.9). Without further experimental characterization, we cannot say much about most of these products and whether they are likely to emerge during MIB SEI formation. We suspect that many of these species are not likely stable and may continue to degrade (the decomposition products may be missing from the network). However, we do note that several salt products - namely MgCO_3 [54, 364] and MgSO_3 [55] - have been observed by experimental spectroscopy.

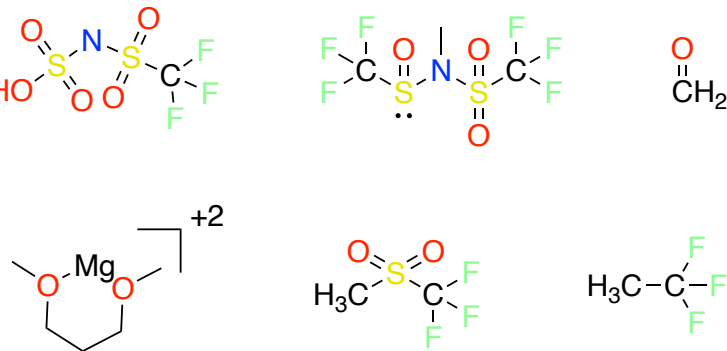


Figure H.10: Other network products.

H.6 Scanning Electron Microscopy

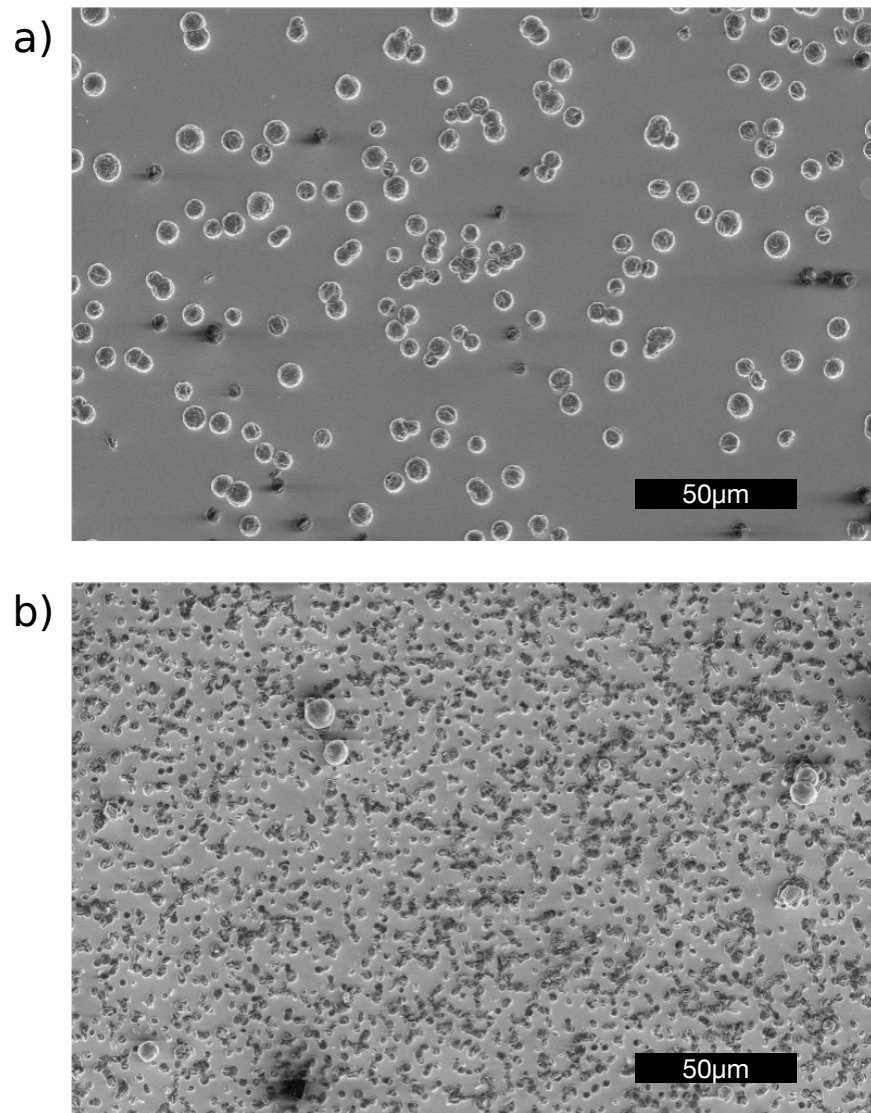


Figure H.11: SEM images of remnant Mg and electrolyte (TFSI^- and G2) decomposition products after 1 (a) and 10 (b) deposition and stripping cycles.

Bibliography

- (1) Padhi, A. K.; Nanjundaswamy, K. S.; Goodenough, J. B. *Journal of The Electrochemical Society* **1997**, *144*, 1188.
- (2) Liu, Z.; Yu, A.; Lee, J. Y. *Journal of Power Sources* **1999**, *81-82*, 416–419.
- (3) *Electrolytes for Lithium and Lithium-Ion Batteries*; Jow, T. R., Xu, K., Borodin, O., Ue, M., Eds.; Modern Aspects of Electrochemistry, Vol. 58; Springer New York: New York, NY, 2014.
- (4) Harlow, J. E.; Ma, X.; Li, J.; Logan, E.; Liu, Y.; Zhang, N.; Ma, L.; Glazier, S. L.; Cormier, M. M. E.; Genovese, M.; Buteau, S.; Cameron, A.; Stark, J. E.; Dahn, J. R. *Journal of The Electrochemical Society* **2019**, *166*, A3031.
- (5) S. Ziegler, M.; E. Trancik, J. *Energy & Environmental Science* **2021**, *14*, 1635–1651.
- (6) Ma, H.; Cheng, F.; Chen, J.-Y.; Zhao, J.-Z.; Li, C.-S.; Tao, Z.-L.; Liang, J. *Advanced Materials* **2007**, *19*, 4067–4070.
- (7) Lang, J.; Qi, L.; Luo, Y.; Wu, H. *Energy Storage Materials* **2017**, *7*, 115–129.
- (8) Wang, R.; Li, X.; Liu, L.; Lee, J.; Seo, D.-H.; Bo, S.-H.; Urban, A.; Ceder, G. *Electrochemistry Communications* **2015**, *60*, 70–73.
- (9) Lun, Z.; Ouyang, B.; Kitchaev, D. A.; Clément, R. J.; Papp, J. K.; Balasubramanian, M.; Tian, Y.; Lei, T.; Shi, T.; McCloskey, B. D.; Lee, J.; Ceder, G. *Advanced Energy Materials* **2019**, *9*, 1802959.
- (10) Sun, X.; Hao, H.; Hartmann, P.; Liu, Z.; Zhao, F. *Materials Today Energy* **2019**, *14*, 100347.
- (11) Wen, J.; Yu, Y.; Chen, C. *Materials Express* **2012**, *2*, 197–212.
- (12) Maxwell, P.; Mora, M. *Mineral Economics* **2020**, *33*, 57–71.
- (13) Sanchez-Lopez, M. D. *Latin American Policy* **2023**, *14*, 22–45.
- (14) Wu, X.; Song, K.; Zhang, X.; Hu, N.; Li, L.; Li, W.; Zhang, L.; Zhang, H. *Frontiers in Energy Research* **2019**, *7*.
- (15) Campion, C. L.; Li, W.; Lucht, B. L. *Journal of The Electrochemical Society* **2005**, *152*, A2327.
- (16) Anderson, D. L., *New Theory of the Earth*; Cambridge University Press: 2007.

- (17) Ponrouch, A.; Bitenc, J.; Dominko, R.; Lindahl, N.; Johansson, P.; Palacin, M. R. *Energy Storage Materials* **2019**, *20*, 253–262.
- (18) Park, M.-S.; Kim, J.-G.; Kim, Y.-J.; Choi, N.-S.; Kim, J.-S. *Israel Journal of Chemistry* **2015**, *55*, 570–585.
- (19) Xiao, J.; Li, Q.; Bi, Y.; Cai, M.; Dunn, B.; Glossmann, T.; Liu, J.; Osaka, T.; Sugiura, R.; Wu, B.; Yang, J.; Zhang, J.-G.; Whittingham, M. S. *Nature Energy* **2020**, *5*, 561–568.
- (20) Trasatti, S. *Pure and Applied Chemistry* **1986**, *58*, 955–966.
- (21) Kasavajjula, U.; Wang, C.; Appleby, A. J. *Journal of Power Sources* **2007**, *163*, 1003–1039.
- (22) Li, Y.; Lu, Y.; Adelhelm, P.; Titirici, M.-M.; Hu, Y.-S. *Chemical Society Reviews* **2019**, *48*, 4655–4687.
- (23) Aurbach, D. *Journal of The Electrochemical Society* **1996**, *143*, 3809.
- (24) Aurbach, D.; Levi, M. D.; Levi, E.; Schechter, A. *The Journal of Physical Chemistry B* **1997**, *101*, 2195–2206.
- (25) Michan, A. L.; Parimalam, B. S.; Leskes, M.; Kerber, R. N.; Yoon, T.; Grey, C. P.; Lucht, B. L. *Chemistry of Materials* **2016**, *28*, 8149–8159.
- (26) Parimalam, B. S.; Lucht, B. L. *Journal of The Electrochemical Society* **2018**, *165*, A251.
- (27) Vetter, J.; Novák, P.; Wagner, M. R.; Veit, C.; Möller, K. .-.; Besenhard, J. O.; Winter, M.; Wohlfahrt-Mehrens, M.; Vogler, C.; Hammouche, A. *Journal of Power Sources* **2005**, *147*, 269–281.
- (28) Wohlfahrt-Mehrens, M.; Vogler, C.; Garche, J. *Journal of Power Sources* **2004**, *127*, 58–64.
- (29) Rinkel, B. L. D.; Hall, D. S.; Temprano, I.; Grey, C. P. *Journal of the American Chemical Society* **2020**, *142*, 15058–15074.
- (30) Etxebarria, A.; Yun, D.-J.; Blum, M.; Ye, Y.; Sun, M.; Lee, K.-J.; Su, H.; Muñoz-Márquez, M. Á.; Ross, P. N.; Crumlin, E. J. *ACS Applied Materials & Interfaces* **2020**, *12*, 26607–26613.
- (31) Jusys, Z.; Binder, M.; Schnaitt, J.; Behm, R. J. *Electrochimica Acta* **2019**, *314*, 188–201.
- (32) Seitzinger, C. L.; Sacci, R. L.; Coyle, J. E.; Apblett, C. A.; Hays, K. A.; Armstrong, R. R.; Rogers, A. M.; Armstrong, B. L.; Bennet, T. H.; Neale, N. R.; Veith, G. M. *Chemistry of Materials* **2020**, *32*, 3199–3210.
- (33) Lee, K. H.; Song, E. H.; Lee, J. Y.; Jung, B. H.; Lim, H. S. *Journal of Power Sources* **2004**, *132*, 201–205.

- (34) Sahore, R.; Dogan, F.; Bloom, I. D. *Chemistry of Materials* **2019**, *31*, 2884–2891.
- (35) Jayawardana, C.; Rodrigo, N.; Parimalam, B.; Lucht, B. L. *ACS Energy Letters* **2021**, *6*, 3788–3792.
- (36) Freiberg, A. T. S.; Roos, M. K.; Wandt, J.; de Vivie-Riedle, R.; Gasteiger, H. A. *The Journal of Physical Chemistry A* **2018**, *122*, 8828–8839.
- (37) Liu, M.; Vatamanu, J.; Chen, X.; Xing, L.; Xu, K.; Li, W. *ACS Energy Letters* **2021**, *6*, 2096–2102.
- (38) Ha, Y.; Stetson, C.; Harvey, S. P.; Teeter, G.; Tremolet de Villers, B. J.; Jiang, C.-S.; Schnabel, M.; Stradins, P.; Burrell, A.; Han, S.-D. *ACS Applied Materials & Interfaces* **2020**, *12*, 49563–49573.
- (39) Verma, P.; Maire, P.; Novák, P. *Electrochimica Acta* **2010**, *55*, 6332–6341.
- (40) Ishikawa, M.; Takaki, Y.; Morita, M.; Matsuda, Y. *Journal of The Electrochemical Society* **1997**, *144*, L90–L92.
- (41) Chan, C. K.; Ruffo, R.; Hong, S. S.; Cui, Y. *Journal of Power Sources* **2009**, *189*, 1132–1140.
- (42) Nadimpalli, S. P. V.; Sethuraman, V. A.; Dalavi, S.; Lucht, B.; Chon, M. J.; Shenoy, V. B.; Guduru, P. R. *Journal of Power Sources* **2012**, *215*, 145–151.
- (43) Attias, R.; Salama, M.; Hirsch, B.; Goffer, Y.; Aurbach, D. *Joule* **2019**, *3*, 27–52.
- (44) Zhao, Q.; Stalin, S.; Archer, L. A. *Joule* **2021**, *5*, 1119–1142.
- (45) Peled, E. *Journal of The Electrochemical Society* **1979**, *126*, 2047.
- (46) Peled, E.; Yamin, H. *Israel Journal of Chemistry* **1979**, *18*, 131–135.
- (47) Nie, M.; Abraham, D. P.; Chen, Y.; Bose, A.; Lucht, B. L. *The Journal of Physical Chemistry C* **2013**, *117*, 13403–13412.
- (48) Mogensen, R.; Brandell, D.; Younesi, R. *ACS Energy Letters* **2016**, *1*, 1173–1178.
- (49) Wang, H.; Zhai, D.; Kang, F. *Energy & Environmental Science* **2020**, *13*, 4583–4608.
- (50) Zhou, Y. et al. *Nature Nanotechnology* **2020**, *15*, 224–230.
- (51) Song, H.; Su, J.; Wang, C. *Advanced Materials* **2021**, *33*, 2006141.
- (52) Cheng, X.-B.; Zhang, R.; Zhao, C.-Z.; Wei, F.; Zhang, J.-G.; Zhang, Q. *Advanced Science* **2016**, *3*, 1500213.
- (53) Arthur, T. S.; Glans, P.-A.; Singh, N.; Tutusaus, O.; Nie, K.; Liu, Y.-S.; Mizuno, F.; Guo, J.; Alsem, D. H.; Salmon, N. J.; Mohtadi, R. *Chemistry of Materials* **2017**, *29*, 7183–7188.
- (54) Gao, T.; Hou, S.; Huynh, K.; Wang, F.; Eidson, N.; Fan, X.; Han, F.; Luo, C.; Mao, M.; Li, X.; Wang, C. *ACS Applied Materials & Interfaces* **2018**, *10*, 14767–14776.

- (55) Jay, R.; Tomich, A. W.; Zhang, J.; Zhao, Y.; De Gorostiza, A.; Lavallo, V.; Guo, J. *ACS Applied Materials & Interfaces* **2019**, *11*, 11414–11420.
- (56) Lau, K.-C.; Seguin, T. J.; Carino, E. V.; Hahn, N. T.; Connell, J. G.; Ingram, B. J.; Persson, K. A.; Zavadil, K. R.; Liao, C. *Journal of The Electrochemical Society* **2019**, *166*, A1510.
- (57) Leon, N. J.; Xie, X.; Yang, M.; Driscoll, D. M.; Connell, J. G.; Kim, S.; Seguin, T.; Vaughey, J. T.; Balasubramanian, M.; Persson, K. A.; Liao, C. *The Journal of Physical Chemistry C* **2022**, *126*, 13579–13584.
- (58) Forero-Saboya, J.; Davoisne, C.; Dedryvère, R.; Yousef, I.; Canepa, P.; Ponrouch, A. *Energy & Environmental Science* **2020**, *13*, 3423–3431.
- (59) Xiao, J.; Zhang, X.; Fan, H.; Zhao, Y.; Su, Y.; Liu, H.; Li, X.; Su, Y.; Yuan, H.; Pan, T.; Lin, Q.; Pan, L.; Zhang, Y. *Advanced Materials* **2022**, *34*, 2203783.
- (60) Winter, M. *Zeitschrift für Physikalische Chemie* **2009**, *223*, 1395–1406.
- (61) Nicolaou, K. C.; Edmonds, D. J.; Bulger, P. G. *Angewandte Chemie International Edition* **2006**, *45*, 7134–7186.
- (62) Blank, S.; Nguyen, Z.; Boucher, D. G.; Minteer, S. D. *Current Opinion in Electrochemistry* **2022**, *35*, 101049.
- (63) Xing, L.; Zheng, X.; Schroeder, M.; Alvarado, J.; von Wald Cresce, A.; Xu, K.; Li, Q.; Li, W. *Accounts of Chemical Research* **2018**, *51*, 282–289.
- (64) Melin, T.; Lundström, R.; Berg, E. J. *Advanced Materials Interfaces* **2022**, *9*, 2101258.
- (65) Xu, K. *Chemical Reviews* **2014**, *114*, 11503–11618.
- (66) Giffin, G. A. *Nature Communications* **2022**, *13*, 5250.
- (67) Sun, X.; Duffort, V.; Mehdi, B. L.; Browning, N. D.; Nazar, L. F. *Chemistry of Materials* **2016**, *28*, 534–542.
- (68) Stich, M.; Pandey, N.; Bund, A. *Journal of Power Sources* **2017**, *364*, 84–91.
- (69) Yang, Z.; Yang, M.; Hahn, N. T.; Connell, J.; Bloom, I.; Liao, C.; Ingram, B. J.; Trahey, L. *Frontiers in Chemistry* **2022**, *10*.
- (70) Huang, X.; Wang, Z.; Knibbe, R.; Luo, B.; Ahad, S. A.; Sun, D.; Wang, L. *Energy Technology* **2019**, *7*, 1801001.
- (71) Kim, T.; Choi, W.; Shin, H.-C.; Choi, J.-Y.; Kim, J. M.; Park, M.-S.; Yoon, W.-S. *Journal of Electrochemical Science and Technology* **2020**, *11*, 14–25.
- (72) Andre, D.; Meiler, M.; Steiner, K.; Wimmer, C.; Soczka-Guth, T.; Sauer, D. U. *Journal of Power Sources* **2011**, *196*, 5334–5341.
- (73) Belharouak, I., *Lithium Ion Batteries: New Developments*; BoD – Books on Demand: 2012.
- (74) Iurilli, P.; Brivio, C.; Wood, V. *Journal of Power Sources* **2021**, *505*, 229860.

- (75) An, S. J.; Li, J.; Daniel, C.; Mohanty, D.; Nagpure, S.; Wood, D. L. *Carbon* **2016**, *105*, 52–76.
- (76) Muldoon, J.; Bucur, C. B.; Gregory, T. *Angewandte Chemie International Edition* **2017**, *56*, 12064–12084.
- (77) Wang, A.; Kadam, S.; Li, H.; Shi, S.; Qi, Y. *npj Computational Materials* **2018**, *4*, 1–26.
- (78) Horstmann, B.; Single, F.; Latz, A. *Current Opinion in Electrochemistry* **2019**, *13*, 61–69.
- (79) Gavilán-Arriazu, E. M.; Mercer, M. P.; Barraco, D. E.; Hoster, H. E.; Leiva, E. P. M. *Progress in Energy* **2021**, *3*, 042001.
- (80) Wu, J.; Ihsan-Ul-Haq, M.; Chen, Y.; Kim, J.-K. *Nano Energy* **2021**, *89*, 106489.
- (81) Hollander, J. M.; Jolly, W. L. *Accounts of chemical research* **1970**, *3*, 193–200.
- (82) Fadley, C. S. *Journal of Electron Spectroscopy and Related Phenomena* **2010**, *178-179*, 2–32.
- (83) Akai, T.; Ota, H.; Namita, H.; Yamaguchi, S.; Nomura, M. *Physica Scripta* **2005**, *2005*, 408.
- (84) Guo, R.; Wang, D.; Zuin, L.; Gallant, B. M. *ACS Energy Letters* **2021**, *6*, 877–885.
- (85) Oyakhire, S. T.; Gong, H.; Cui, Y.; Bao, Z.; Bent, S. F. *ACS Energy Letters* **2022**, *7*, 2540–2546.
- (86) Nandasiri, M. I.; Camacho-Forero, L. E.; Schwarz, A. M.; Shutthanandan, V.; Thevuthasan, S.; Balbuena, P. B.; Mueller, K. T.; Murugesan, V. *Chemistry of Materials* **2017**, *29*, 4728–4737.
- (87) Yan, P.; Zheng, J.; Gu, M.; Xiao, J.; Zhang, J.-G.; Wang, C.-M. *Nature Communications* **2017**, *8*, 14101.
- (88) Fan, X.; Hu, G.; Zhang, B.; Ou, X.; Zhang, J.; Zhao, W.; Jia, H.; Zou, L.; Li, P.; Yang, Y. *Nano Energy* **2020**, *70*, 104450.
- (89) Dollé, M.; Sannier, L.; Beaudoin, B.; Trentin, M.; Tarascon, J.-M. *Electrochemical and Solid-State Letters* **2002**, *5*, A286.
- (90) Tang, C.-Y.; Dillon, S. J. *Journal of The Electrochemical Society* **2016**, *163*, A1660.
- (91) Keyzer, E. N.; Glass, H. F. J.; Liu, Z.; Bayley, P. M.; Dutton, S. E.; Grey, C. P.; Wright, D. S. *Journal of the American Chemical Society* **2016**, *138*, 8682–8685.
- (92) Fan, X.; Chen, L.; Borodin, O.; Ji, X.; Chen, J.; Hou, S.; Deng, T.; Zheng, J.; Yang, C.; Liou, S.-C.; Amine, K.; Xu, K.; Wang, C. *Nature Nanotechnology* **2018**, *13*, 715–722.
- (93) Nagarajan, S.; Weiland, C.; Hwang, S.; Balasubramanian, M.; Arava, L. M. R. *Chemistry of Materials* **2022**, *34*, 4587–4601.

- (94) Veith, G. M.; Doucet, M.; Baldwin, J. K.; Sacci, R. L.; Fears, T. M.; Wang, Y.; Browning, J. F. *The Journal of Physical Chemistry C* **2015**, *119*, 20339–20349.
- (95) Andriunas, I.; Milojevic, Z.; Wade, N.; Das, P. K. *Journal of Power Sources* **2022**, *525*, 231126.
- (96) Nie, M.; Chalasani, D.; Abraham, D. P.; Chen, Y.; Bose, A.; Lucht, B. L. *The Journal of Physical Chemistry C* **2013**, *117*, 1257–1267.
- (97) Betz, J.; Brinkmann, J.-P.; Nölle, R.; Lürenbaum, C.; Kolek, M.; Stan, M. C.; Winter, M.; Placke, T. *Advanced Energy Materials* **2019**, *9*, 1900574.
- (98) Li, Y.; Li, Y.; Pei, A.; Yan, K.; Sun, Y.; Wu, C.-L.; Joubert, L.-M.; Chin, R.; Koh, A. L.; Yu, Y.; Perrino, J.; Butz, B.; Chu, S.; Cui, Y. *Science* **2017**, *358*, 506–510.
- (99) Huang, W.; Boyle, D. T.; Li, Y.; Li, Y.; Pei, A.; Chen, H.; Cui, Y. *ACS Nano* **2019**, *13*, 737–744.
- (100) Zhang, J.; Liu, J.; Wang, M.; Zhang, Z.; Zhou, Z.; Chen, X.; Du, A.; Dong, S.; Li, Z.; Li, G.; Cui, G. *Energy & Environmental Science* **2023**, *16*, 1111–1124.
- (101) Griffiths, P. R. In *Handbook of Vibrational Spectroscopy*; John Wiley & Sons, Ltd: 2007.
- (102) Kraka, E.; Zou, W.; Tao, Y. *WIREs Computational Molecular Science* **2020**, *10*, e1480.
- (103) Choquette, S. J.; Chesler, S. N.; Duewer, D. L.; Wang, S.; O'Haver, T. C. *Analytical Chemistry* **1996**, *68*, 3525–3533.
- (104) Giles, J. H.; Gilmore, D. A.; Denton, M. B. *Journal of Raman Spectroscopy* **1999**, *30*, 767–771.
- (105) Allen, J. L.; Borodin, O.; Seo, D. M.; Henderson, W. A. *Journal of Power Sources* **2014**, *267*, 821–830.
- (106) Giorgini, M. G.; Futamatagawa, K.; Torii, H.; Musso, M.; Cerini, S. *The Journal of Physical Chemistry Letters* **2015**, *6*, 3296–3302.
- (107) T. Pekarek, R.; Affolter, A.; L. Baranowski, L.; Coyle, J.; Hou, T.; Sivonxay, E.; A. Smith, B.; D. McAuliffe, R.; A. Persson, K.; Key, B.; Apblett, C.; M. Veith, G.; R. Neale, N. *Journal of Materials Chemistry A* **2020**, *8*, 7897–7906.
- (108) Hy, S.; Felix; Chen, Y.-H.; Liu, J.-y.; Rick, J.; Hwang, B.-J. *Journal of Power Sources* **2014**, *256*, 324–328.
- (109) Gajan, A.; Lecourt, C.; Bautista, B. E. T.; Fillaud, L.; Demeaux, J.; Lucas, I. T. *ACS Energy Letters* **2021**, *7*.
- (110) Bovey, F. A.; Mirau, P. A.; Gutowsky, H. S., *Nuclear Magnetic Resonance Spectroscopy*; Elsevier: 1988.
- (111) B. Gunnarsdóttir, A.; Vema, S.; Menkin, S.; E. Marbella, L.; P. Grey, C. *Journal of Materials Chemistry A* **2020**, *8*, 14975–14992.

- (112) Kitz, P. G.; Lacey, M. J.; Novák, P.; Berg, E. J. *Journal of Power Sources* **2020**, *477*, 228567.
- (113) Märker, K.; Xu, C.; Grey, C. P. *Journal of the American Chemical Society* **2020**, *142*, 17447–17456.
- (114) D. Rinkel, B. L.; Padmanabhan Vivek, J.; Garcia-Araez, N.; P. Grey, C. *Energy & Environmental Science* **2022**, DOI: 10.1039/D1EE04053G.
- (115) Leskes, M.; Kim, G.; Liu, T.; Michan, A. L.; Aussénac, F.; Dorffer, P.; Paul, S.; Grey, C. P. *The Journal of Physical Chemistry Letters* **2017**, *8*, 1078–1085.
- (116) Wang, L.; Menakath, A.; Han, F.; Wang, Y.; Zavalij, P. Y.; Gaskell, K. J.; Borodin, O.; Iuga, D.; Brown, S. P.; Wang, C.; Xu, K.; Eichhorn, B. W. *Nature Chemistry* **2019**, *11*, 789–796.
- (117) Gao, L.; Chen, J.; Chen, Q.; Kong, X. *Science Advances* **2022**, *8*, eabm4606.
- (118) Lambert, J. B.; Mazzola, E. P.; Ridge, C. D., *Nuclear Magnetic Resonance Spectroscopy: An Introduction to Principles, Applications, and Experimental Methods*; John Wiley & Sons: 2019.
- (119) Onuki, M.; Kinoshita, S.; Sakata, Y.; Yanagidate, M.; Otake, Y.; Ue, M.; Deguchi, M. *Journal of The Electrochemical Society* **2008**, *155*, A794.
- (120) Gachot, G.; Ribière, P.; Mathiron, D.; Grugeon, S.; Armand, M.; Leriche, J.-B.; Pilard, S.; Laruelle, S. *Analytical Chemistry* **2011**, *83*, 478–485.
- (121) Shi, B.; Liu, K.; Lee, E.; Liao, C. **2021**, 5–1.
- (122) Self, J.; Aiken, C. P.; Petibon, R.; Dahn, J. R. *Journal of The Electrochemical Society* **2015**, *162*, A796.
- (123) Xiong, D. J.; Petibon, R.; Nie, M.; Ma, L.; Xia, J.; Dahn, J. R. *Journal of The Electrochemical Society* **2016**, *163*, A546.
- (124) McCloskey, B. D.; Bethune, D. S.; Shelby, R. M.; Girishkumar, G.; Luntz, A. C. *The Journal of Physical Chemistry Letters* **2011**, *2*, 1161–1166.
- (125) Kreth, F. A.; Hess, L. H.; Balducci, A. *Energy Storage Materials* **2023**, *56*, 192–204.
- (126) Fang, C.; Tran, T.-N.; Zhao, Y.; Liu, G. *Electrochimica Acta* **2021**, *399*, 139362.
- (127) Fang, C.; Lau, J.; Hubble, D.; Khomein, P.; Dailing, E. A.; Liu, Y.; Liu, G. *Joule* **2021**, *5*, 415–428.
- (128) Lee, C. W.; Cho, N. H.; Im, S. W.; Jee, M. S.; Hwang, Y. J.; Min, B. K.; Nam, K. T. *Journal of Materials Chemistry A* **2018**, *6*, 14043–14057.
- (129) Hohenberg, P.; Kohn, W. *Physical Review* **1964**, *136*, B864–B871.
- (130) Kohn, W.; Sham, L. J. *Physical Review* **1965**, *140*, A1133–A1138.
- (131) Born, M.; Oppenheimer, R. *Annalen der Physik* **1927**, *389*, 457–484.

- (132) Bryantsev, V. S.; Blanco, M. *The Journal of Physical Chemistry Letters* **2011**, *2*, 379–383.
- (133) Borodin, O.; Zhuang, G. V.; Ross, P. N.; Xu, K. *The Journal of Physical Chemistry C* **2013**, *117*, 7433–7444.
- (134) Debnath, S.; Neufeld, V. A.; Jacobson, L. D.; Rudshteyn, B.; Weber, J. L.; Berkelbach, T. C.; Friesner, R. A. Accurate quantum chemical reaction energies for lithium-mediated electrolyte decomposition and evaluation of density functional approximations, ChemRxiv preprint; DOI: 10.26434/chemrxiv-2023-d4mq1-v2, 2023.
- (135) Mardirossian, N.; Head-Gordon, M. *Molecular Physics* **2017**, *115*, 2315–2372.
- (136) Hou, T.; Yang, G.; Rajput, N. N.; Self, J.; Park, S.-W.; Nanda, J.; Persson, K. A. *Nano Energy* **2019**, *64*, 103881.
- (137) Clément, R. J.; Middlemiss, D. S.; Seymour, I. D.; Ilott, A. J.; Grey, C. P. *Chemistry of Materials* **2016**, *28*, 8228–8239.
- (138) Michan, A. L.; Leskes, M.; Grey, C. P. *Chemistry of Materials* **2016**, *28*, 385–398.
- (139) Bursch, M.; Mewes, J.-M.; Hansen, A.; Grimme, S. *Angewandte Chemie International Edition* **2022**, *61*, e202205735.
- (140) Islam, M. M.; Kolesov, G.; Verstraelen, T.; Kaxiras, E.; van Duin, A. C. T. *Journal of Chemical Theory and Computation* **2016**, *12*, 3463–3472.
- (141) Piquemal, J.-P.; Cisneros, G. A.; Reinhardt, P.; Gresh, N.; Darden, T. A. *The Journal of Chemical Physics* **2006**, *124*, 104101.
- (142) Gabrieli, A.; Sant, M.; Demontis, P.; Suffritti, G. B. *The Journal of Physical Chemistry C* **2016**, *120*, 26309–26319.
- (143) Bin Faheem, A.; Kim, J.-Y.; Bae, S.-E.; Lee, K.-K. *Journal of Molecular Liquids* **2021**, *337*, 116579.
- (144) Ringsby, A. J.; Fong, K. D.; Self, J.; Bergstrom, H. K.; McCloskey, B. D.; Persson, K. A. *Journal of The Electrochemical Society* **2021**, *168*, 080501.
- (145) Hou, S.; Ji, X.; Gaskell, K.; Wang, P.-f.; Wang, L.; Xu, J.; Sun, R.; Borodin, O.; Wang, C. *Science* **2021**, *374*, 172–178.
- (146) Self, J.; Fong, K. D.; Persson, K. A. *ACS Energy Letters* **2019**, *4*, 2843–2849.
- (147) Fong, K. D.; Self, J.; Diederichsen, K. M.; Wood, B. M.; McCloskey, B. D.; Persson, K. A. *ACS Central Science* **2019**, *5*, 1250–1260.
- (148) Wu, Q.; McDowell, M. T.; Qi, Y. *Journal of the American Chemical Society* **2023**, *145*, 2473–2484.
- (149) Muralidharan, A.; Chaudhari, M. I.; Pratt, L. R.; Rempe, S. B. *Scientific Reports* **2018**, *8*, 10736.

- (150) Van Duin, A. C. T.; Dasgupta, S.; Lorant, F.; Goddard, W. A. *The Journal of Physical Chemistry A* **2001**, *105*, 9396–9409.
- (151) Senftle, T. P.; Hong, S.; Islam, M. M.; Kylasa, S. B.; Zheng, Y.; Shin, Y. K.; Junkermeier, C.; Engel-Herbert, R.; Janik, M. J.; Aktulga, H. M.; Verstraelen, T.; Grama, A.; van Duin, A. C. T. *npj Computational Materials* **2016**, *2*, 1–14.
- (152) Yun, K.-S.; Pai, S. J.; Yeo, B. C.; Lee, K.-R.; Kim, S.-J.; Han, S. S. *The Journal of Physical Chemistry Letters* **2017**, *8*, 2812–2818.
- (153) Wang, Y.; Liu, Y.; Tu, Y.; Wang, Q. *The Journal of Physical Chemistry C* **2020**, *124*, 9099–9108.
- (154) Hossain, M. J.; Pawar, G.; Liaw, B.; Gering, K. L.; Dufek, E. J.; van Duin, A. C. T. *The Journal of Chemical Physics* **2020**, *152*, 184301.
- (155) Bedrov, D.; Smith, G. D.; van Duin, A. C. T. *The Journal of Physical Chemistry A* **2012**, *116*, 2978–2985.
- (156) Alzate-Vargas, L.; Blau, S. M.; Spotte-Smith, E. W. C.; Allu, S.; Persson, K. A.; Fattebert, J.-L. *The Journal of Physical Chemistry C* **2021**, *125*, 18588–18596.
- (157) Deringer, V. L.; Caro, M. A.; Csányi, G. *Advanced Materials* **2019**, *31*, 1902765.
- (158) Batzner, S.; Musaelian, A.; Sun, L.; Geiger, M.; Mailoa, J. P.; Kornbluth, M.; Molinari, N.; Smidt, T. E.; Kozinsky, B. *Nature Communications* **2022**, *13*, 2453.
- (159) Batatia, I.; Kovacs, D. P.; Simm, G.; Ortner, C.; Csanyi, G. *Advances in Neural Information Processing Systems* **2022**, *35*, 11423–11436.
- (160) Musaelian, A.; Batzner, S.; Johansson, A.; Sun, L.; Owen, C. J.; Kornbluth, M.; Kozinsky, B. *Nature Communications* **2023**, *14*, 579.
- (161) Liao, Y.-L.; Smidt, T. Equiformer: Equivariant Graph Attention Transformer for 3D Atomistic Graphs, arXiv preprint; DOI: 10.48550/arXiv.2206.11990, 2023.
- (162) Liao, Y.-L.; Wood, B.; Das, A.; Smidt, T. EquiformerV2: Improved Equivariant Transformer for Scaling to Higher-Degree Representations, arXiv preprint; DOI: 10.48550/arXiv.2306.12059, 2023.
- (163) Kim, K.; Dive, A.; Grieder, A.; Adelstein, N.; Kang, S.; Wan, L. F.; Wood, B. C. *The Journal of Chemical Physics* **2022**, *156*, 221101.
- (164) Tuckerman, M. E. *Journal of Physics: Condensed Matter* **2002**, *14*, R1297.
- (165) Tse, J. S. *Annual Review of Physical Chemistry* **2002**, *53*, 249–290.
- (166) Leung, K.; Budzien, J. L. *Physical Chemistry Chemical Physics* **2010**, *12*, 6583–6586.
- (167) Benitez, L.; Cristancho, D.; Seminario, J. M.; Martinez de la Hoz, J. M.; Balbuena, P. B. *Electrochimica Acta* **2014**, *140*, 250–257.
- (168) Agarwal, G.; Howard, J. D.; Prabhakaran, V.; Johnson, G. E.; Murugesan, V.; Mueller, K. T.; Curtiss, L. A.; Assary, R. S. *ACS Applied Materials & Interfaces* **2021**, *13*, 38816–38825.

- (169) Kuai, D.; Balbuena, P. B. *ACS Applied Materials & Interfaces* **2022**, *14*, 2817–2824.
- (170) Galvez-Aranda, D. E.; Seminario, J. M. *Journal of The Electrochemical Society* **2022**, *169*, 030502.
- (171) Sundararaman, R.; Vigil-Fowler, D.; Schwarz, K. *Chemical Reviews* **2022**, *122*, 10651–10674.
- (172) Shibuta, Y.; Maruyama, S. *Chemical Physics Letters* **2003**, *382*, 381–386.
- (173) Klein, M. L.; Shinoda, W. *Science* **2008**, *321*, 798–800.
- (174) Wood, D. L.; Li, J.; Daniel, C. *Journal of Power Sources* **2015**, *275*, 234–242.
- (175) Berkes, B. B.; Schiele, A.; Sommer, H.; Brezesinski, T.; Janek, J. *Journal of Solid State Electrochemistry* **2016**, *20*, 2961–2967.
- (176) Kalaga, K.; Rodrigues, M.-T. F.; Trask, S. E.; Shkrob, I. A.; Abraham, D. P. *Electrochimica Acta* **2018**, *280*, 221–228.
- (177) Bi, Y.; Wang, T.; Liu, M.; Du, R.; Yang, W.; Liu, Z.; Peng, Z.; Liu, Y.; Wang, D.; Sun, X. *RSC Advances* **2016**, *6*, 19233–19237.
- (178) Lowe, J. S.; Siegel, D. J. *ACS Applied Materials & Interfaces* **2020**, *12*, 46015–46026.
- (179) Kuwata, H.; Matsui, M.; Imanishi, N. *Journal of The Electrochemical Society* **2017**, *164*, A3229.
- (180) Shin, S.; Kwak, J. H.; Oh, S. H.; Kim, H.-S.; Yu, S.-H.; Lim, H.-D. *ACS Applied Materials & Interfaces* **2023**, *15*, 28684–28691.
- (181) He, Y.; Piper, D. M.; Gu, M.; Travis, J. J.; George, S. M.; Lee, S.-H.; Genc, A.; Pullan, L.; Liu, J.; Mao, S. X.; Zhang, J.-G.; Ban, C.; Wang, C. *ACS Nano* **2014**, *8*, 11816–11823.
- (182) Christensen, J.; Newman, J. *Journal of The Electrochemical Society* **2004**, *151*, A1977.
- (183) Colclasure, A. M.; Smith, K. A.; Kee, R. J. *Electrochimica Acta* **2011**, *58*, 33–43.
- (184) Deshpande, R. D.; Bernardi, D. M. *Journal of The Electrochemical Society* **2017**, *164*, A461.
- (185) Deng, J.; Wagner, G. J.; Muller, R. P. *Journal of The Electrochemical Society* **2013**, *160*, A487.
- (186) Yurkiv, V.; Foroozan, T.; Ramasubramanian, A.; Shahbazian-Yassar, R.; Mashayek, F. *Electrochimica Acta* **2018**, *265*, 609–619.
- (187) Katrašnik, T.; Mele, I.; Zelić, K. *Energy Conversion and Management* **2021**, *236*, 114036.
- (188) Gillespie, D. T. *Journal of Computational Physics* **1976**, *22*, 403–434.
- (189) Gillespie, D. T. *The Journal of Physical Chemistry* **1977**, *81*, 2340–2361.

- (190) Gillespie, D. T. *Annual Review of Physical Chemistry* **2007**, *58*, 35–55.
- (191) Mason, D. R.; Hudson, T. S.; Sutton, A. P. *Computer Physics Communications* **2005**, *165*, 37–48.
- (192) Leetmaa, M.; Skorodumova, N. V. *Computer Physics Communications* **2014**, *185*, 2340–2349.
- (193) Pineda, M.; Stamatakis, M. *The Journal of Chemical Physics* **2022**, *156*, 120902.
- (194) Snyder, M. A.; Chatterjee, A.; Vlachos, D. G. *Computers & Chemical Engineering* **2005**, *29*, 701–712.
- (195) Esmailpour, M.; Jana, S.; Li, H.; Soleymanibrojeni, M.; Wenzel, W. *Advanced Energy Materials* **2023**, *13*, 2203966.
- (196) Hao, F.; Liu, Z.; Balbuena, P. B.; Mukherjee, P. P. *The Journal of Physical Chemistry C* **2017**, *121*, 26233–26240.
- (197) Röder, F.; Braatz, R. D.; Krewer, U. In *Computer Aided Chemical Engineering*, Kravanja, Z., Bogataj, M., Eds.; 26 European Symposium on Computer Aided Process Engineering, Vol. 38; Elsevier: 2016, pp 157–162.
- (198) Röder, F.; Laue, V.; Krewer, U. *Batteries & Supercaps* **2019**, *2*, 248–265.
- (199) Gerasimov, M.; Soto, F. A.; Wagner, J.; Baakes, F.; Guo, N.; Ospina-Acevedo, F.; Röder, F.; Balbuena, P. B.; Krewer, U. *The Journal of Physical Chemistry C* **2023**, *127*, 4872–4886.
- (200) Wen, M.; Spotte-Smith, E. W. C.; Blau, S. M.; McDermott, M. J.; Krishnapriyan, A. S.; Persson, K. A. *Nature Computational Science* **2023**, *3*, 12–24.
- (201) Maeda, S.; Morokuma, K. *Journal of Chemical Theory and Computation* **2012**, *8*, 380–385.
- (202) Unsleber, J. P.; Reiher, M. *Annual Review of Physical Chemistry* **2020**, *71*, 121–142.
- (203) Ismail, I.; Chantreau Majerus, R.; Habershon, S. *The Journal of Physical Chemistry A* **2022**, *126*, 7051–7069.
- (204) Gothard, C. M.; Soh, S.; Gothard, N. A.; Kowalczyk, B.; Wei, Y.; Baytekin, B.; Grzybowski, B. A. *Angewandte Chemie* **2012**, *124*, 8046–8051.
- (205) Szymkuć, S.; Gajewska, E. P.; Klucznik, T.; Molga, K.; Dittwald, P.; Startek, M.; Bajczyk, M.; Grzybowski, B. A. *Angewandte Chemie International Edition* **2016**, *55*, 5904–5937.
- (206) Schilling, C. H.; Palsson, B. O. *Proceedings of the National Academy of Sciences* **1998**, *95*, 4193–4198.
- (207) Warne, D. J.; Baker, R. E.; Simpson, M. J. *Journal of The Royal Society Interface* **2019**, *16*, 20180943.

- (208) Wołos, A.; Roszak, R.; Żadło-Dobrowolska, A.; Beker, W.; Mikulak-Klucznik, B.; Spólnik, G.; Dygas, M.; Szymkuć, S.; Grzybowski, B. A. *Science* **2020**, *369*, eaaw1955.
- (209) Van Geem, K. M.; Pyl, S. P.; Marin, G. B.; Harper, M. R.; Green, W. H. *Industrial & Engineering Chemistry Research* **2010**, *49*, 10399–10420.
- (210) Pio, G.; Dong, X.; Salzano, E.; Green, W. H. *Combustion and Flame* **2022**, *241*, 112080.
- (211) Blau, S. M.; Patel, H. D.; Spotte-Smith, E. W. C.; Xie, X.; Dwaraknath, S.; Persson, K. A. *Chemical science* **2021**, *12*, 4931–4939.
- (212) Xie, X.; Clark Spotte-Smith, E. W.; Wen, M.; Patel, H. D.; Blau, S. M.; Persson, K. A. *Journal of the American Chemical Society* **2021**, *143*, 13245–13258.
- (213) Dijkstra, E. W. *Numerische Mathematik* **1959**, *1*, 269–271.
- (214) Yen, J. Y. *Quarterly of Applied Mathematics* **1970**, *27*, 526–530.
- (215) Zhuang, G. V.; Xu, K.; Yang, H.; Jow, T. R.; Ross, P. N. *The Journal of Physical Chemistry B* **2005**, *109*, 17567–17573.
- (216) Spotte-Smith, E. W. C.; Petrocelli, T. B.; Patel, H. D.; Blau, S. M.; Persson, K. A. *ACS Energy Letters* **2023**, *8*, 347–355.
- (217) Blomgren, G. E. *Journal of Power Sources* **1999**, *81-82*, 112–118.
- (218) Zhang, S. S.; Jow, T. R.; Amine, K.; Henriksen, G. L. *Journal of Power Sources* **2002**, *107*, 18–23.
- (219) Xu, K. *Chemical Reviews* **2004**, *104*, 4303–4418.
- (220) Wagner, R.; Preschitschek, N.; Passerini, S.; Leker, J.; Winter, M. *Journal of Applied Electrochemistry* **2013**, *43*, 481–496.
- (221) Stich, M.; Göttlinger, M.; Kurniawan, M.; Schmidt, U.; Bund, A. *The Journal of Physical Chemistry C* **2018**, *122*, 8836–8842.
- (222) Seo, D. M.; Reininger, S.; Kutcher, M.; Redmond, K.; Euler, W. B.; Lucht, B. L. *The Journal of Physical Chemistry C* **2015**, *119*, 14038–14046.
- (223) Agubra, V.; Fergus, J. *Materials* **2013**, *6*, 1310–1325.
- (224) Agubra, V. A.; Fergus, J. W. *Journal of Power Sources* **2014**, *268*, 153–162.
- (225) Heiskanen, S. K.; Kim, J.; Lucht, B. L. *Joule* **2019**, *3*, 2322–2333.
- (226) Xue, W.; Shi, Z.; Huang, M.; Feng, S.; Wang, C.; Wang, F.; Lopez, J.; Qiao, B.; Xu, G.; Zhang, W.; Dong, Y.; Gao, R.; Shao-Horn, Y.; A. Johnson, J.; Li, J. *Energy & Environmental Science* **2020**, *13*, 212–220.
- (227) Philippe, B.; Dedryvère, R.; Gorgoi, M.; Rensmo, H.; Gonbeau, D.; Edström, K. *Journal of the American Chemical Society* **2013**, *135*, 9829–9842.
- (228) McBrayer, J. D. et al. *Nature Energy* **2021**, *6*, 866–872.

- (229) Boyle, D. T.; Huang, W.; Wang, H.; Li, Y.; Chen, H.; Yu, Z.; Zhang, W.; Bao, Z.; Cui, Y. *Nature Energy* **2021**, *6*, 487–494.
- (230) Aurbach, D.; Ein-Eli, Y.; Markovsky, B.; Zaban, A.; Luski, S.; Carmeli, Y.; Yamin, H. *Journal of The Electrochemical Society* **1995**, *142*, 2882.
- (231) Aurbach, D.; Zaban, A.; Schechter, A.; Ein-Eli, Y.; Zinigrad, E.; Markovsky, B. *Journal of The Electrochemical Society* **1995**, *142*, 2873.
- (232) Rowden, B.; Garcia-Araez, N. *Energy Reports* **2020**, *6*, 10–18.
- (233) Zhao, H.; Wang, J.; Shao, H.; Xu, K.; Deng, Y. *Energy & Environmental Materials* **2022**, *5*, 327–336.
- (234) Ma, Y.; Balbuena, P. B. *Journal of The Electrochemical Society* **2014**, *161*, E3097.
- (235) Gibson, L. D.; Pfaendtner, J. *Physical Chemistry Chemical Physics* **2020**, *22*, 21494–21503.
- (236) Soto, F. A.; Ma, Y.; Martinez de la Hoz, J. M.; Seminario, J. M.; Balbuena, P. B. *Chemistry of Materials* **2015**, *27*, 7990–8000.
- (237) Young, J.; Kulick, P. M.; Juran, T. R.; Smeu, M. *ACS Applied Energy Materials* **2019**, *2*, 1676–1684.
- (238) Sloop, S. E.; Pugh, J. K.; Wang, S.; Kerr, J. B.; Kinoshita, K. *Electrochemical and Solid-State Letters* **2001**, *4*, A42.
- (239) Kawamura, T.; Okada, S.; Yamaki, J.-i. *Journal of Power Sources* **2006**, *156*, 547–554.
- (240) Yang, H.; Zhuang, G. V.; Ross, P. N. *Journal of Power Sources* **2006**, *161*, 573–579.
- (241) Wiemers-Meyer, S.; Winter, M.; Nowak, S. *Physical Chemistry Chemical Physics* **2016**, *18*, 26595–26601.
- (242) Henschel, J.; Peschel, C.; Klein, S.; Horsthemke, F.; Winter, M.; Nowak, S. *Angewandte Chemie* **2020**, *132*, 6184–6193.
- (243) Botte, G. G.; White, R. E.; Zhang, Z. *Journal of Power Sources* **2001**, *97-98*, 570–575.
- (244) Lux, S. F.; Lucas, I. T.; Pollak, E.; Passerini, S.; Winter, M.; Kostecki, R. *Electrochemistry Communications* **2012**, *14*, 47–50.
- (245) Aurbach, D.; Talyosef, Y.; Markovsky, B.; Markevich, E.; Zinigrad, E.; Asraf, L.; Gnanaraj, J. S.; Kim, H.-J. *Electrochimica Acta* **2004**, *50*, 247–254.
- (246) Wagner, R.; Korth, M.; Streipert, B.; Kasnatscheew, J.; Gallus, D. R.; Brox, S.; Amereller, M.; Cekic-Laskovic, I.; Winter, M. *ACS Applied Materials & Interfaces* **2016**, *8*, 30871–30878.
- (247) Okamoto, Y. *Journal of The Electrochemical Society* **2013**, *160*, A404.

- (248) Gebala, A. E.; Jones, M. M. *Journal of Inorganic and Nuclear Chemistry* **1969**, *31*, 771–776.
- (249) Cao, C.; Pollard, T. P.; Borodin, O.; Mars, J. E.; Tsao, Y.; Lukatskaya, M. R.; Kasse, R. M.; Schroeder, M. A.; Xu, K.; Toney, M. F.; Steinrück, H.-G. *Chemistry of Materials* **2021**, *33*, 7315–7336.
- (250) Parimalam, B. S.; MacIntosh, A. D.; Kadam, R.; Lucht, B. L. *The Journal of Physical Chemistry C* **2017**, *121*, 22733–22738.
- (251) Leung, K. *Chemical Physics Letters* **2013**, *568-569*, 1–8.
- (252) Jayawardana, C.; Rodrigo, N. D.; Rynearson, L.; Lucht, B. L. *Journal of The Electrochemical Society* **2022**, *169*, 060509.
- (253) Spotte-Smith, E. W. C.; Blau, S. M.; Xie, X.; Patel, H. D.; Wen, M.; Wood, B.; Dwaraknath, S.; Persson, K. A. *Scientific Data* **2021**, *8*, 203.
- (254) Barter, D.; Spotte-Smith, E. W. C.; Redkar, N. S.; Khanwale, A.; Dwaraknath, S.; Persson, K. A.; Blau, S. M. *Digital Discovery* **2023**, *2*, 123–137.
- (255) O’Boyle, N. M.; Banck, M.; James, C. A.; Morley, C.; Vandermeersch, T.; Hutchison, G. R. *Journal of Cheminformatics* **2011**, *3*, 1–14.
- (256) O’Boyle, N. M.; Morley, C.; Hutchison, G. R. *Chemistry Central Journal* **2008**, *2*, 1–7.
- (257) Sayle, R. *MUG 2001* **2001**.
- (258) Skarmoutsos, I.; Ponnuchamy, V.; Vetere, V.; Mossa, S. *The Journal of Physical Chemistry C* **2015**, *119*, 4502–4515.
- (259) Chapman, N.; Borodin, O.; Yoon, T.; Nguyen, C. C.; Lucht, B. L. *The Journal of Physical Chemistry C* **2017**, *121*, 2135–2148.
- (260) Otero-de-la-Roza, A.; Blanco, M. A.; Pendás, A. M.; Luaña, V. *Computer Physics Communications* **2009**, *180*, 157–166.
- (261) Otero-de-la-Roza, A.; Johnson, E. R.; Luaña, V. *Computer Physics Communications* **2014**, *185*, 1007–1018.
- (262) Van Voorhis, T.; Head-Gordon, M. *Molecular Physics* **2002**, *100*, 1713–1721.
- (263) Pulay, P. *Chemical Physics Letters* **1980**, *73*, 393–398.
- (264) Pulay, P. *Journal of Computational Chemistry* **1982**, *3*, 556–560.
- (265) Epifanovsky, E. et al. *The Journal of Chemical Physics* **2021**, *155*, 084801.
- (266) Schlegel, H. B. *WIREs Computational Molecular Science* **2011**, *1*, 790–809.
- (267) Gallagher, N.; Zhang, H.; Junghoefer, T.; Giangrisostomi, E.; Ovsyannikov, R.; Pink, M.; Rajca, S.; Casu, M. B.; Rajca, A. *Journal of the American Chemical Society* **2019**, *141*, 4764–4774.

- (268) Klán, P.; Wirz, J. *Photochemistry of organic compounds: from concepts to practice*; John Wiley & Sons: 2009.
- (269) Shavitt, I. *Tetrahedron* **1985**, *41*, 1531–1542.
- (270) Herbert, J. M. *Reviews in Computational Chemistry* **2015**, *28*, 391–517.
- (271) Wen, M.; Blau, S. M.; Spotte-Smith, E. W. C.; Dwaraknath, S.; Persson, K. A. *Chemical Science* **2021**, *12*, 1858–1868.
- (272) Banks, J. L. et al. *Journal of Computational Chemistry* **2005**, *26*, 1752–1780.
- (273) Dewyer, A. L.; Argüelles, A. J.; Zimmerman, P. M. *WIREs Computational Molecular Science* **2018**, *8*, e1354.
- (274) Maeda, S.; Harabuchi, Y.; Takagi, M.; Taketsugu, T.; Morokuma, K. *The Chemical Record* **2016**, *16*, 2232–2248.
- (275) Shang, C.; Liu, Z.-P. *Journal of Chemical Theory and Computation* **2013**, *9*, 1838–1845.
- (276) Bannwarth, C.; Ehlert, S.; Grimme, S. *Journal of Chemical Theory and Computation* **2019**, *15*, 1652–1671.
- (277) Zhao, Q.; Savoie, B. M. *Nature Computational Science* **2021**, *1*, 479–490.
- (278) Kang, P.-L.; Shang, C.; Liu, Z.-P. *Accounts of Chemical Research* **2020**, *53*, 2119–2129.
- (279) Holmberg, N.; Laasonen, K. *The Journal of Physical Chemistry C* **2015**, *119*, 16166–16178.
- (280) Gao, C. W.; Allen, J. W.; Green, W. H.; West, R. H. *Computer Physics Communications* **2016**, *203*, 212–225.
- (281) Goldsmith, C. F.; West, R. H. *The Journal of Physical Chemistry C* **2017**, *121*, 9970–9981.
- (282) Rappoport, D.; Aspuru-Guzik, A. *Journal of Chemical Theory and Computation* **2019**, *15*, 4099–4112.
- (283) Liu, M.; Grinberg Dana, A.; Johnson, M. S.; Goldman, M. J.; Jocher, A.; Payne, A. M.; Grambow, C. A.; Han, K.; Yee, N. W.; Mazeau, E. J.; Blondal, K.; West, R. H.; Goldsmith, C. F.; Green, W. H. *Journal of Chemical Information and Modeling* **2021**, *61*, 2686–2696.
- (284) Kim, Y.; Kim, J. W.; Kim, Z.; Kim, W. Y. *Chemical Science* **2018**, *9*, 825–835.
- (285) Jia, X.; Lynch, A.; Huang, Y.; Danielson, M.; Lang’at, I.; Milder, A.; Ruby, A. E.; Wang, H.; Friedler, S. A.; Norquist, A. J.; Schrier, J. *Nature* **2019**, *573*, 251–255.
- (286) Calle-Vallejo, F.; Koper, M. T. M. *Electrochimica Acta* **2012**, *84*, 3–11.
- (287) Birdja, Y. Y.; Pérez-Gallent, E.; Figueiredo, M. C.; Göttle, A. J.; Calle-Vallejo, F.; Koper, M. T. M. *Nature Energy* **2019**, *4*, 732–745.

- (288) Bell, R. P.; Hinshelwood, C. N. *Proceedings of the Royal Society of London. Series A - Mathematical and Physical Sciences* **1936**, *154*, 414–429.
- (289) Evans, M. G.; Polanyi, M. *Transactions of the Faraday Society* **1936**, *32*, 1333–1360.
- (290) Segler, M. H. S.; Preuss, M.; Waller, M. P. *Nature* **2018**, *555*, 604–610.
- (291) Gibson, M. A.; Bruck, J. *The Journal of Physical Chemistry A* **2000**, *104*, 1876–1889.
- (292) Stocker, S.; Csányi, G.; Reuter, K.; Margraf, J. T. *Nature Communications* **2020**, *11*, 5505.
- (293) Plesniak, M. P.; Huang, H.-M.; Procter, D. J. *Nature Reviews Chemistry* **2017**, *1*, 1–16.
- (294) Yuan, Y.; Chen, Y.; Tang, S.; Huang, Z.; Lei, A. *Science Advances* **2018**, *4*, eaat5312.
- (295) Baez, J. C. *Advances in Mathematical Physics* **2018**, *2018*, e7676309.
- (296) Baez, J. C.; Biamonte, J. Quantum Techniques for Stochastic Mechanics, arXiv preprint; DOI: 10.48550/arXiv.1209.3632, 2019.
- (297) Dasgupta, S.; Herbert, J. M. *Journal of Computational Chemistry* **2017**, *38*, 869–882.
- (298) Mardirossian, N.; Head-Gordon, M. *Physical Chemistry Chemical Physics* **2014**, *16*, 9904–9924.
- (299) Vydrov, O. A.; Van Voorhis, T. *The Journal of Chemical Physics* **2010**, *133*, 244103.
- (300) Weigend, F.; Ahlrichs, R. *Physical Chemistry Chemical Physics* **2005**, *7*, 3297–3305.
- (301) Rappoport, D.; Furche, F. *The Journal of Chemical Physics* **2010**, *133*, 134105.
- (302) Marenich, A. V.; Cramer, C. J.; Truhlar, D. G. *The Journal of Physical Chemistry B* **2009**, *113*, 6378–6396.
- (303) Tomasi, J.; Mennucci, B.; Cammi, R. *Chemical Reviews* **2005**, *105*, 2999–3094.
- (304) Mennucci, B. *WIREs Computational Molecular Science* **2012**, *2*, 386–404.
- (305) Hall, D. S.; Self, J.; Dahn, J. R. *The Journal of Physical Chemistry C* **2015**, *119*, 22322–22330.
- (306) Qu, X.; Jain, A.; Rajput, N. N.; Cheng, L.; Zhang, Y.; Ong, S. P.; Brafman, M.; Maginn, E.; Curtiss, L. A.; Persson, K. A. *Computational Materials Science* **2015**, *103*, 56–67.
- (307) Solchenbach, S.; Metzger, M.; Egawa, M.; Beyer, H.; Gasteiger, H. A. *Journal of The Electrochemical Society* **2018**, *165*, A3022.
- (308) Kang, S.-J.; Park, K.; Park, S.-H.; Lee, H. *Electrochimica Acta* **2018**, *259*, 949–954.
- (309) Liu, S.; Zhang, Q.; Wang, X.; Xu, M.; Li, W.; Lucht, B. L. *ACS Applied Materials & Interfaces* **2020**, *12*, 33719–33728.

- (310) Xia, J.; Petibon, R.; Xiao, A.; Lamanna, W. M.; Dahn, J. R. *Journal of The Electrochemical Society* **2016**, *163*, A1637.
- (311) Xia, L.; Tang, B.; Yao, L.; Wang, K.; Cheris, A.; Pan, Y.; Lee, S.; Xia, Y.; Chen, G. Z.; Liu, Z. *ChemistrySelect* **2017**, *2*, 7353–7361.
- (312) Intan, N. N.; Pfaendtner, J. *ACS Applied Materials & Interfaces* **2021**, *13*, 8169–8180.
- (313) Hobold, G. M.; Khurram, A.; Gallant, B. M. *Chemistry of Materials* **2020**, *32*, 2341–2352.
- (314) Ribeiro, R. F.; Marenich, A. V.; Cramer, C. J.; Truhlar, D. G. *The Journal of Physical Chemistry B* **2011**, *115*, 14556–14562.
- (315) Grimme, S. *Chemistry – A European Journal* **2012**, *18*, 9955–9964.
- (316) Ong, S. P.; Richards, W. D.; Jain, A.; Hautier, G.; Kocher, M.; Cholia, S.; Gunter, D.; Chevrier, V. L.; Persson, K. A.; Ceder, G. *Computational Materials Science* **2013**, *68*, 314–319.
- (317) Chan, B.; Gill, P. M. W.; Kimura, M. *Journal of Chemical Theory and Computation* **2019**, *15*, 3610–3622.
- (318) Dohm, S.; Hansen, A.; Steinmetz, M.; Grimme, S.; Checinski, M. P. *Journal of Chemical Theory and Computation* **2018**, *14*, 2596–2608.
- (319) Yao, Y.; Kanai, Y. *Journal of Chemical Theory and Computation* **2018**, *14*, 884–893.
- (320) Marenich, A. V.; Cramer, C. J.; Truhlar, D. G. *The Journal of Physical Chemistry B* **2009**, *113*, 4538–4543.
- (321) Marenich, A. V.; Cramer, C. J.; Truhlar, D. G. *Journal of Chemical Theory and Computation* **2013**, *9*, 609–620.
- (322) Guerard, J. J.; Arey, J. S. *Journal of Chemical Theory and Computation* **2013**, *9*, 5046–5058.
- (323) Grambow, C. A.; Pattanaik, L.; Green, W. H. *Scientific Data* **2020**, *7*, 137.
- (324) Lin, Y.-S.; Li, G.-D.; Mao, S.-P.; Chai, J.-D. *Journal of Chemical Theory and Computation* **2013**, *9*, 263–272.
- (325) Mogi, R.; Inaba, M.; Iriyama, Y.; Abe, T.; Ogumi, Z. *Journal of Power Sources* **2003**, *119-121*, 597–603.
- (326) Nanda, J.; Yang, G.; Hou, T.; Voylov, D. N.; Li, X.; Ruther, R. E.; Naguib, M.; Persson, K.; Veith, G. M.; Sokolov, A. P. *Joule* **2019**, *3*, 2001–2019.
- (327) Tsubouchi, S.; Domi, Y.; Doi, T.; Ochida, M.; Nakagawa, H.; Yamanaka, T.; Abe, T.; Ogumi, Z. *Journal of The Electrochemical Society* **2012**, *159*, A1786.
- (328) Nie, M.; Abraham, D. P.; Seo, D. M.; Chen, Y.; Bose, A.; Lucht, B. L. *The Journal of Physical Chemistry C* **2013**, *117*, 25381–25389.

- (329) Nie, M.; Demeaux, J.; Young, B. T.; Heskett, D. R.; Chen, Y.; Bose, A.; Woicik, J. C.; Lucht, B. L. *Journal of The Electrochemical Society* **2015**, *162*, A7008–A7014.
- (330) Spotte-Smith, E. W. C.; Kam, R. L.; Barter, D.; Xie, X.; Hou, T.; Dwaraknath, S.; Blau, S. M.; Persson, K. A. *ACS Energy Letters* **2022**, *7*, 1446–1453.
- (331) Wang, Y.; Nakamura, S.; Ue, M.; Balbuena, P. B. *Journal of the American Chemical Society* **2001**, *123*, 11708–11718.
- (332) Eyring, H. *The Journal of Chemical Physics* **1935**, *3*, 107–115.
- (333) Boyer, M. J.; Hwang, G. S. *The Journal of Physical Chemistry C* **2019**, *123*, 17695–17702.
- (334) Peled, E.; Menkin, S. *Journal of The Electrochemical Society* **2017**, *164*, A1703–A1719.
- (335) Galushkin, N.; Yazvinskaya, N. N.; Galushkin, D. N. *Journal of The Electrochemical Society* **2019**, *166*, A897.
- (336) Wang, Y.; Balbuena, P. B. *International Journal of Quantum Chemistry* **2005**, *102*, 724–733.
- (337) Martinez de la Hoz, J. M.; Leung, K.; Balbuena, P. B. *ACS Applied Materials & Interfaces* **2013**, *5*, 13457–13465.
- (338) Marcus, R. A. *The Journal of Chemical Physics* **1965**, *43*, 679–701.
- (339) Methkar, R. N.; Northrop, P. W. C.; Chen, K.; Braatz, R. D.; Subramanian, V. R. *Journal of The Electrochemical Society* **2011**, *158*, A363.
- (340) Röder, F.; Braatz, R. D.; Krewer, U. *Journal of The Electrochemical Society* **2017**, *164*, E3335.
- (341) Hankins, K.; Kamphaus, E. P.; Balbuena, P. B. *Electrochimica Acta* **2021**, *397*, 139272.
- (342) Morgan, L. et al. *Progress in Energy* **2021**, DOI: 10.1088/2516-1083/ac3894.
- (343) Garcia Cardona, C.; Webb, E. B.; Wagner, G. J.; Tikare, V.; Holm, E. A.; Plimpton, S. J.; Thompson, A. P.; Slepoy, A.; Zhou, X. W.; Battaile, C. C.; Chandross, M. E. *Crossing the mesoscale no-mans land via parallel kinetic Monte Carlo*. Tech. rep. SAND2009-6226; Sandia National Laboratories, 2009.
- (344) Bernhard, R.; Metzger, M.; Gasteiger, H. A. *Journal of the Electrochemical Society* **2015**, *162*, A1984.
- (345) Yang, C.; Chen, J.; Qing, T.; Fan, X.; Sun, W.; von Cresce, A.; Ding, M. S.; Borodin, O.; Vatamanu, J.; Schroeder, M. A.; Eidson, N.; Wang, C.; Xu, K. *Joule* **2017**, *1*, 122–132.
- (346) Gallagher, K. G.; Dees, D. W.; Jansen, A. N.; Abraham, D. P.; Kang, S.-H. *Journal of The Electrochemical Society* **2012**, *159*, A2029.

- (347) Chandrasekaran, R.; Magasinski, A.; Yushin, G.; Fuller, T. F. *Journal of The Electrochemical Society* **2010**, *157*, A1139.
- (348) Xia, J.; Petibon, R.; Xiong, D.; Ma, L.; Dahn, J. R. *Journal of Power Sources* **2016**, *328*, 124–135.
- (349) Single, F.; Latz, A.; Horstmann, B. *ChemSusChem* **2018**, *11*, 1950–1955.
- (350) Zhang, S. S. *Journal of Power Sources* **2006**, *162*, 1379–1394.
- (351) Aurbach, D.; Chusid (Youngman), O. *Journal of The Electrochemical Society* **1993**, *140*, L155–L157.
- (352) Aurbach, D.; Ein-Eli, Y.; Chusid (Youngman), O.; Carmeli, Y.; Babai, M.; Yamin, H. *Journal of The Electrochemical Society* **1994**, *141*, 603–611.
- (353) Ein-Eli, Y.; Markovsky, B.; Aurbach, D.; Carmeli, Y.; Yamin, H.; Luski, S. *Electrochimica Acta* **1994**, *39*, 2559–2569.
- (354) Aurbach, D.; Ein-Ely, Y.; Zaban, A. *Journal of The Electrochemical Society* **1994**, *141*, L1.
- (355) Schwenke, K. U.; Solchenbach, S.; Demeaux, J.; Lucht, B. L.; Gasteiger, H. A. *Journal of The Electrochemical Society* **2019**, *166*, A2035.
- (356) Barré, A.; Deguilhem, B.; Grolleau, S.; Gérard, M.; Suard, F.; Riu, D. *Journal of Power Sources* **2013**, *241*, 680–689.
- (357) Ellis, L. D.; Allen, J. P.; Hill, I. G.; Dahn, J. R. *Journal of The Electrochemical Society* **2018**, *165*, A1529.
- (358) Spotte-Smith, E. W. C.; Blau, S. M.; Barter, D.; Leon, N. J.; Hahn, N. T.; Redkar, N. S.; Zavadil, K. R.; Liao, C.; Persson, K. A. *Journal of the American Chemical Society* **2023**, *145*, 12181–12192.
- (359) Olivetti, E. A.; Ceder, G.; Gaustad, G. G.; Fu, X. *Joule* **2017**, *1*, 229–243.
- (360) Brown, O. R.; McIntyre, R. *Electrochimica Acta* **1985**, *30*, 627–633.
- (361) Genders, J. D.; Pletcher, D. *Journal of Electroanalytical Chemistry and Interfacial Electrochemistry* **1986**, *199*, 93–100.
- (362) Shterenberg, I.; Salama, M.; Yoo, H. D.; Gofer, Y.; Park, J.-B.; Sun, Y.-K.; Aurbach, D. *Journal of The Electrochemical Society* **2015**, *162*, A7118.
- (363) Yu, Y.; Baskin, A.; Valero-Vidal, C.; Hahn, N. T.; Liu, Q.; Zavadil, K. R.; Eichhorn, B. W.; Prendergast, D.; Crumlin, E. J. *Chemistry of Materials* **2017**, *29*, 8504–8512.
- (364) Yoo, H. D.; Han, S.-D.; Bolotin, I. L.; Nolis, G. M.; Bayliss, R. D.; Burrell, A. K.; Vaughey, J. T.; Cabana, J. *Langmuir* **2017**, *33*, 9398–9406.
- (365) Nguyen, D.-T.; Eng, A. Y. S.; Ng, M.-F.; Kumar, V.; Sofer, Z.; Handoko, A. D.; Subramanian, G. S.; Seh, Z. W. *Cell Reports Physical Science* **2020**, *1*, 100265.

- (366) Rajput, N. N.; Qu, X.; Sa, N.; Burrell, A. K.; Persson, K. A. *Journal of the American Chemical Society* **2015**, *137*, 3411–3420.
- (367) Lowe, J. S.; Siegel, D. J. *The Journal of Physical Chemistry C* **2018**, *122*, 10714–10724.
- (368) Seguin, T. J.; Hahn, N. T.; Zavadil, K. R.; Persson, K. A. *Frontiers in Chemistry* **2019**, *7*, 175.
- (369) Novák, P.; Panitz, J. .-.; Joho, F.; Lanz, M.; Imhof, R.; Coluccia, M. *Journal of Power Sources* **2000**, *90*, 52–58.
- (370) Tsionvaras, N.; Meini, S.; Buchberger, I.; Gasteiger, H. A. *Journal of The Electrochemical Society* **2013**, *160*, A471.
- (371) Nie, K.; Wang, X.; Qiu, J.; Wang, Y.; Yang, Q.; Xu, J.; Yu, X.; Li, H.; Huang, X.; Chen, L. *ACS Energy Letters* **2020**, *5*, 826–832.
- (372) Connell, J. G.; Genorio, B.; Lopes, P. P.; Strmcnik, D.; Stamenkovic, V. R.; Markovic, N. M. *Chemistry of Materials* **2016**, *28*, 8268–8277.
- (373) Coplen, T. B.; Böhlke, J. K.; De Bievre, P.; Ding, T.; Holden, N.; Hopple, J.; Krouse, H.; Lamberty, A.; Peiser, H.; Revesz, K., et al. *Pure and Applied Chemistry* **2002**, *74*, 1987–2017.
- (374) Haynes, W. M., *CRC handbook of chemistry and physics*; CRC press: 2014.
- (375) Baskin, A.; Prendergast, D. *The Journal of Physical Chemistry C* **2016**, *120*, 3583–3594.
- (376) Michalak, B.; Berkes, B. B.; Sommer, H.; Bergfeldt, T.; Brezesinski, T.; Janek, J. *Analytical Chemistry* **2016**, *88*, 2877–2883.
- (377) Pritzl, D.; Solchenbach, S.; Wetjen, M.; Gasteiger, H. A. *Journal of The Electrochemical Society* **2017**, *164*, A2625.
- (378) Xu, G.; Wang, X.; Li, J.; Shangguan, X.; Huang, S.; Lu, D.; Chen, B.; Ma, J.; Dong, S.; Zhou, X.; Kong, Q.; Cui, G. *Chemistry of Materials* **2018**, *30*, 8291–8302.
- (379) Wang, Y.; Nakamura, S.; Tasaki, K.; Balbuena, P. B. *Journal of the American Chemical Society* **2002**, *124*, 4408–4421.
- (380) Chu, S.; Cui, Y.; Liu, N. *Nature Materials* **2017**, *16*, 16–22.
- (381) Tackett, B. M.; Gomez, E.; Chen, J. G. *Nature Catalysis* **2019**, *2*, 381–386.
- (382) Worrell, E.; Price, L.; Neelis, M.; Galitsky, C.; Zhou, N. *World best practice energy intensity values for selected industrial sectors*; tech. rep. LBNL-62806; Lawrence Berkeley National Laboratory, Berkeley, CA (United States), 2007.
- (383) Xia, R.; Overa, S.; Jiao, F. *JACS Au* **2022**, *2*, 1054–1070.
- (384) McPherson, I.; Zhang, J. *Joule* **2020**, *4*, 12–14.

- (385) International Energy Agency, *Ammonia Technology Roadmap: Towards more sustainable nitrogen fertiliser production*; OECD: 2021.
- (386) Capdevila-Cortada, M. *Nature Catalysis* **2019**, *2*, 1055–1055.
- (387) Li, K.; Shapel, S. G.; Hochfilzer, D.; Pedersen, J. B.; Kreml, K.; Andersen, S. Z.; Sažinas, R.; Saccoccio, M.; Li, S.; Chakraborty, D.; Kibsgaard, J.; Vesborg, P. C. K.; Nørskov, J. K.; Chorkendorff, I. *ACS Energy Letters* **2022**, *7*, 36–41.
- (388) Lazouski, N.; Steinberg, K. J.; Gala, M. L.; Krishnamurthy, D.; Viswanathan, V.; Manthiram, K. *ACS Catalysis* **2022**, *12*, 5197–5208.
- (389) Barakat, M. *Arabian journal of chemistry* **2011**, *4*, 361–377.
- (390) Gerardi, M. H.; Zimmerman, M. C., *Wastewater pathogens*; John Wiley & Sons: 2004.
- (391) Sedlak, R. I., *Phosphorus and nitrogen removal from municipal wastewater: principles and practice*; CRC press: 1991.
- (392) Reijnders, L. *Resources, conservation and recycling* **2014**, *93*, 32–49.
- (393) Conley, D. J.; Paerl, H. W.; Howarth, R. W.; Boesch, D. F.; Seitzinger, S. P.; Havens, K. E.; Lancelot, C.; Likens, G. E. *Controlling eutrophication: nitrogen and phosphorus*, 2009.
- (394) Tarpeh, W. A.; Chen, X. *Environmental Science and Ecotechnology* **2021**, *5*, 100078.
- (395) Kogler, A.; Farmer, M.; Simon, J. A.; Tilmans, S.; Wells, G. F.; Tarpeh, W. A. *ACS ES&T Engineering* **2021**, *1*, 662–684.
- (396) Miller, D. M.; Abels, K.; Guo, J.; Williams, K. S.; Liu, M. J.; Tarpeh, W. A. *Journal of the American Chemical Society* **2023**.
- (397) Geyer, R.; Jambeck, J. R.; Law, K. L. *Science advances* **2017**, *3*, e1700782.
- (398) Peng, G.; Bellerby, R.; Zhang, F.; Sun, X.; Li, D. *Water research* **2020**, *168*, 115121.
- (399) Ragusa, A.; Svelato, A.; Santacroce, C.; Catalano, P.; Notarstefano, V.; Carnevali, O.; Papa, F.; Rongioletti, M. C. A.; Baiocco, F.; Draghi, S., et al. *Environment international* **2021**, *146*, 106274.
- (400) Sridharan, S.; Kumar, M.; Singh, L.; Bolan, N. S.; Saha, M. *Journal of Hazardous Materials* **2021**, *418*, 126245.
- (401) Schyns, Z. O.; Shaver, M. P. *Macromolecular rapid communications* **2021**, *42*, 2000415.
- (402) Coates, G. W.; Getzler, Y. D. *Nature Reviews Materials* **2020**, *5*, 501–516.
- (403) Christensen, P. R.; Scheuermann, A. M.; Loeffler, K. E.; Helms, B. A. *Nature chemistry* **2019**, *11*, 442–448.
- (404) Helms, B. A. *Accounts of Chemical Research* **2022**, *55*, 2753–2765.
- (405) De Dios Caputto, M. D.; Navarro, R.; Valentín, J. L.; Marcos-Fernández, Á. *Journal of Polymer Science* **2022**, *60*, 3269–3283.

- (406) Kots, P. A.; Vance, B. C.; Vlachos, D. G. *Reaction Chemistry & Engineering* **2022**, *7*, 41–54.
- (407) Hancock, J. N.; Rorrer, J. E. *Applied Catalysis B: Environmental* **2023**, *338*, 123071.
- (408) Thevenon, A.; Vollmer, I. *Angewandte Chemie* **2023**, *135*, e202216163.
- (409) Bunescu, A.; Lee, S.; Li, Q.; Hartwig, J. F. *ACS central science* **2017**, *3*, 895–903.
- (410) Conk, R. J.; Hanna, S.; Shi, J. X.; Yang, J.; Ciccia, N. R.; Qi, L.; Bloomer, B. J.; Heuvel, S.; Wills, T.; Su, J., et al. *Science* **2022**, *377*, 1561–1566.
- (411) Schlegel, H. B. *Journal of Computational Chemistry* **1982**, *3*, 214–218.
- (412) Bernhard Schlegel, H. *Theoretica Chimica Acta* **1984**, *66*, 333–340.
- (413) Peng, C.; Schlegel, H. B. *Israel Journal of Chemistry* **1993**, *33*, 449–454.
- (414) Peng, C.; Ayala, P. Y.; Schlegel, H. B.; Frisch, M. J. *Journal of Computational Chemistry* **1996**, *17*, 49–56.
- (415) Ayala, P. Y.; Schlegel, H. B. *The Journal of Chemical Physics* **1997**, *107*, 375–384.
- (416) Farkas, Ö.; Schlegel, H. B. *The Journal of Chemical Physics* **1999**, *111*, 10806–10814.
- (417) Spotte-Smith, E. W. C.; Petrocelli, T. B.; Petal, H. D.; Blau, S. M.; Persson, K. A. Data for "Elementary Decomposition Mechanisms of Lithium Hexafluorophosphate in Battery Electrolytes and Interphases", DOI:10.6084/m9.figshare.21583581.v1, 2022.
- (418) Spotte-Smith, E. W. C.; Blau, S. M.; Xie, X.; Patel, H. D.; Wen, M.; Wood, B.; Dwaraknath, S.; Persson, K. A. Lithium-Ion Battery Electrolyte (LIBE) dataset, DOI: 10.6084/m9.figshare.14226464, 2021.
- (419) Mulliken, R. S. *The Journal of Chemical Physics* **1955**, *23*, 1833–1840.
- (420) Bayly, C. I.; Cieplak, P.; Cornell, W.; Kollman, P. A. *The Journal of Physical Chemistry* **1993**, *97*, 10269–10280.
- (421) Jacobson, L. D.; Bochevarov, A. D.; Watson, M. A.; Hughes, T. F.; Rinaldo, D.; Ehrlich, S.; Steinbrecher, T. B.; Vaiteeswaran, S.; Philipp, D. M.; Halls, M. D.; Friesner, R. A. *Journal of Chemical Theory and Computation* **2017**, *13*, 5780–5797.
- (422) Bochevarov, A. D.; Harder, E.; Hughes, T. F.; Greenwood, J. R.; Braden, D. A.; Philipp, D. M.; Rinaldo, D.; Halls, M. D.; Zhang, J.; Friesner, R. A. *International Journal of Quantum Chemistry* **2013**, *113*, 2110–2142.
- (423) Zimmerman, P. M. *Journal of Computational Chemistry* **2015**, *36*, 601–611.
- (424) Aldaz, C. Development of Reaction Discovery Tools in Photochemistry and Condensed Phases, Thesis, 2020.
- (425) Chai, J.-D.; Head-Gordon, M. *Physical Chemistry Chemical Physics* **2008**, *10*, 6615–6620.
- (426) Klamt, A.; Schüürmann, G. *Journal of the Chemical Society, Perkin Transactions 2* **1993**, *0*, 799–805.

- (427) Klamt, A. *WIREs Computational Molecular Science* **2011**, *1*, 699–709.
- (428) Glendening, E. D.; Landis, C. R.; Weinhold, F. *WIREs Computational Molecular Science* **2012**, *2*, 1–42.
- (429) Glendening, E. D.; Landis, C. R.; Weinhold, F. *Journal of Computational Chemistry* **2019**, *40*, 2234–2241.
- (430) Horowitz, Y.; Han, H.-L.; Ross, P. N.; Somorjai, G. A. *Journal of the American Chemical Society* **2016**, *138*, 726–729.
- (431) Zhang, X.; Kostecki, R.; Richardson, T. J.; Pugh, J. K.; Ross, P. N. *Journal of The Electrochemical Society* **2001**, *148*, A1341.
- (432) Ma, L.; Glazier, S. L.; Petibon, R.; Xia, J.; Peters, J. M.; Liu, Q.; Allen, J.; Doig, R. N. C.; Dahn, J. R. *Journal of The Electrochemical Society* **2016**, *164*, A5008.
- (433) Ota, H.; Sakata, Y.; Inoue, A.; Yamaguchi, S. *Journal of The Electrochemical Society* **2004**, *151*, A1659.
- (434) Haregewoin, A. M.; Leggesse, E. G.; Jiang, J.-C.; Wang, F.-M.; Hwang, B.-J.; Lin, S. D. *Electrochimica Acta* **2014**, *136*, 274–285.
- (435) Ue, M.; Takeda, M.; Takehara, M.; Mori, S. *Journal of The Electrochemical Society* **1997**, *144*, 2684–2688.
- (436) Xu, K.; Angell, C. A. *Journal of The Electrochemical Society* **1998**, *145*, L70.
- (437) Saveant, J. M. *Journal of the American Chemical Society* **1987**, *109*, 6788–6795.
- (438) Shervashidze, N.; Schweitzer, P.; van Leeuwen, E. J.; Mehlhorn, K.; Borgwardt, K. M. *Journal of Machine Learning Research* **2011**, *12*, 2539–2561.
- (439) Hagberg, A. A.; Schult, D. A.; Swart, P. J. In *Proceedings of the 7th Python in Science Conference*, ed. by Varoquaux, G.; Vaught, T.; Millman, J., Pasadena, CA USA, 2008, pp 11–15.
- (440) Plimpton, S.; Thompson, A.; Slepoy, A. *Stochastic Parallel PARticle Kinetic Simulator*; tech. rep. SPPARKS; Sandia National Lab. (SNL-NM), Albuquerque, NM (United States), 2008.
- (441) Aldaz, C.; A. Kammeraad, J.; M. Zimmerman, P. *Physical Chemistry Chemical Physics* **2018**, *20*, 27394–27405.
- (442) Marcus, R. A. *Reviews of Modern Physics* **1993**, *65*, 599–610.
- (443) Nelsen, S. F.; Blackstock, S. C.; Kim, Y. *Journal of the American Chemical Society* **1987**, *109*, 677–682.
- (444) Silverstein, T. P. *Journal of Chemical Education* **2012**, *89*, 1159–1167.
- (445) Anouti, M.; Dougassa, Y. R.; Tessier, C.; El Ouatani, L.; Jacquemin, J. *The Journal of Chemical Thermodynamics* **2012**, *50*, 71–79.
- (446) Mathew, K. et al. *Computational Materials Science* **2017**, *139*, 140–152.

- (447) Blau, S.; Spotte-Smith, E. W. C.; Wood, B.; Dwaraknath, S.; Persson, K. Accurate, Automated Density Functional Theory for Complex Molecules Using On-the-fly Error Correction, en, ChemRxiv preprint; DOI: 10.26434/chemrxiv.13076030.v1, 2020.
- (448) Weinhold, F.; Glendening, E. D. *Theoretical Chemistry Institute and Department of Chemistry, University of Wisconsin, Madison, WI 2001, 53706*.
- (449) Mardirossian, N.; Head-Gordon, M. *The Journal of Chemical Physics* **2016**, *144*, 214110.
- (450) Pankow, J. F.; Asher, W. E. *Atmospheric Chemistry and Physics* **2008**, *8*, 2773–2796.
- (451) Topping, D.; Barley, M.; Bane, M. K.; Higham, N.; Aumont, B.; Dingle, N.; McFig-gans, G. *Geoscientific Model Development* **2016**, *9*, 899–914.
- (452) Bachhav, M. N.; Hahn, N. T.; Zavadil, K. R.; Nelson, E. G.; Crowe, A. J.; Bartlett, B. M.; Chu, P.-W.; Araullo-Peters, V. J.; Marquis, E. A. *Journal of The Electrochemical Society* **2016**, *163*, D645.
- (453) Philippe, B.; Dedryvère, R.; Gorgoi, M.; Rensmo, H.; Gonbeau, D.; Edström, K. *Chemistry of Materials* **2013**, *25*, 394–404.
- (454) Metzger, M.; Strehle, B.; Solchenbach, S.; Gasteiger, H. A. *Journal of The Electrochemical Society* **2016**, *163*, A798–A809.
- (455) Aurbach, D.; Zaban, A.; Gofer, Y.; Ely, Y. E.; Weissman, I.; Chusid, O.; Abramson, O. *Journal of Power Sources* **1995**, *54*, 76–84.
- (456) Imhof, R.; Novák, P. *Journal of the Electrochemical Society* **1998**, *145*, 1081.
- (457) Nie, M.; Lucht, B. L. *Journal of The Electrochemical Society* **2014**, *161*, A1001–A1006.
- (458) Kominato, A.; Yasukawa, E.; Sato, N.; Ijuuin, T.; Asahina, H.; Mori, S. *Journal of Power Sources* **1997**, *68*, 471–475.
- (459) Etacheri, V.; Haik, O.; Goffer, Y.; Roberts, G. A.; Stefan, I. C.; Fasching, R.; Aurbach, D. *Langmuir* **2012**, *28*, 965–976.
- (460) Shi, F.; Ross, P. N.; Somorjai, G. A.; Komvopoulos, K. *The Journal of Physical Chemistry C* **2017**, *121*, 14476–14483.
- (461) Jin, Y.; Kneusels, N.-J. H.; Grey, C. P. *The Journal of Physical Chemistry Letters* **2019**, *10*, 6345–6350.
- (462) Hasa, I.; Haregewoin, A. M.; Zhang, L.; Tsai, W.-Y.; Guo, J.; Veith, G. M.; Ross, P. N.; Kostecki, R. *ACS Applied Materials & Interfaces* **2020**, *12*, 40879–40890.
- (463) Yin, Y.; Arca, E.; Wang, L.; Yang, G.; Schnabel, M.; Cao, L.; Xiao, C.; Zhou, H.; Liu, P.; Nanda, J., et al. *ACS Applied Materials & Interfaces* **2020**, *12*, 26593–26600.
- (464) Wu, H.; Jia, H.; Wang, C.; Zhang, J.-G.; Xu, W. *Advanced Energy Materials* **2021**, *11*, 2003092.

- (465) Togasaki, N.; Momma, T.; Osaka, T. *Journal of Power Sources* **2014**, *261*, 23–27.
- (466) Zheng, J.; Yan, P.; Mei, D.; Engelhard, M. H.; Cartmell, S. S.; Polzin, B. J.; Wang, C.; Zhang, J.-G.; Xu, W. *Advanced Energy Materials* **2016**, *6*, 1502151.
- (467) Michan, A. L.; Divitini, G.; Pell, A. J.; Leskes, M.; Ducati, C.; Grey, C. P. *Journal of the American Chemical Society* **2016**, *138*, 7918–7931.
- (468) Schiele, A.; Breitung, B.; Hatsukade, T.; Berkes, B. B.; Hartmann, P.; Janek, J.; Brezesinski, T. *ACS Energy Letters* **2017**, *2*, 2228–2233.
- (469) Veith, G. M.; Doucet, M.; Sacci, R. L.; Vacaliuc, B.; Baldwin, J. K.; Browning, J. F. *Scientific Reports* **2017**, *7*, 6326.
- (470) Lu, M.; Cheng, H.; Yang, Y. *Electrochimica Acta* **2008**, *53*, 3539–3546.
- (471) Cohen, Y. S.; Cohen, Y.; Aurbach, D. *The Journal of Physical Chemistry B* **2000**, *104*, 12282–12291.
- (472) Zhang, Y.; Du, N.; Yang, D. *Nanoscale* **2019**, *11*, 19086–19104.
- (473) Zhao, J.; Yu, H.; Ben, L.; Zhan, Y.; Wu, Y.; Huang, X.; Zhou, Z. *Journal of Materials Chemistry A* **2018**, *6*, 16818–16823.
- (474) Bae, J.; Qian, Y.; Li, Y.; Zhou, X.; B. Goodenough, J.; Yu, G. *Energy & Environmental Science* **2019**, *12*, 3319–3327.
- (475) Ellis, L.; Allen, J.; Thompson, L.; Harlow, J.; Stone, W.; Hill, I.; Dahn, J. *Journal of The Electrochemical Society* **2017**, *164*, A3518.
- (476) Schiele, A.; Breitung, B.; Mazilkin, A.; Schweidler, S.; Janek, J.; Gumbel, S.; Fleischmann, S.; Burakowska-Meise, E.; Sommer, H.; Brezesinski, T. *ACS Omega* **2018**, *3*, 16706–16713.
- (477) McShane, E. J.; Colclasure, A. M.; Brown, D. E.; Konz, Z. M.; Smith, K.; McCloskey, B. D. *ACS Energy Letters* **2020**, *5*, 2045–2051.
- (478) Nitta, N.; Wu, F.; Lee, J. T.; Yushin, G. *Materials Today* **2015**, *18*, 252–264.
- (479) Lin, D.; Liu, Y.; Liang, Z.; Lee, H.-W.; Sun, J.; Wang, H.; Yan, K.; Xie, J.; Cui, Y. *Nature Nanotechnology* **2016**, *11*, 626–632.
- (480) Lin, D.; Liu, Y.; Cui, Y. *Nature Nanotechnology* **2017**, *12*, 194–206.
- (481) Yoon, I.; Jurng, S.; Abraham, D. P.; Lucht, B. L.; Guduru, P. R. *Energy Storage Materials* **2020**, *25*, 296–304.
- (482) Kumar, R.; Tokranov, A.; Sheldon, B. W.; Xiao, X.; Huang, Z.; Li, C.; Mueller, T. *ACS Energy Letters* **2016**, *1*, 689–697.
- (483) Galvez-Aranda, D. E.; Seminario, J. M. *Journal of The Electrochemical Society* **2018**, *165*, A717.
- (484) Guo, K.; Kumar, R.; Xiao, X.; Sheldon, B. W.; Gao, H. *Nano Energy* **2020**, *68*, 104257.

- (485) Zuo, X.; Zhu, J.; Müller-Buschbaum, P.; Cheng, Y.-J. *Nano Energy* **2017**, *31*, 113–143.
- (486) Li, Z.; Huang, J.; Yann Liaw, B.; Metzler, V.; Zhang, J. *Journal of Power Sources* **2014**, *254*, 168–182.
- (487) Liu, B.; Zhang, J.-G.; Xu, W. *Joule* **2018**, *2*, 833–845.
- (488) Fang, C.; Wang, X.; Meng, Y. S. *Trends in Chemistry* **2019**, *1*, 152–158.
- (489) Zhang, X.; Wang, A.; Liu, X.; Luo, J. *Accounts of Chemical Research* **2019**, *52*, 3223–3232.
- (490) Ozanam, F.; Rosso, M. *Materials Science and Engineering: B* **2016**, *213*, 2–11.
- (491) Xu, K. *Journal of The Electrochemical Society* **2009**, *156*, A751.
- (492) Stetson, C.; Yin, Y.; Jiang, C.-S.; DeCaluwe, S. C.; Al-Jassim, M.; Neale, N. R.; Ban, C.; Burrell, A. *ACS Energy Letters* **2019**, *4*, 2770–2775.

ProQuest Number: 30816030

INFORMATION TO ALL USERS

The quality and completeness of this reproduction is dependent on the quality
and completeness of the copy made available to ProQuest.



Distributed by ProQuest LLC (2024).

Copyright of the Dissertation is held by the Author unless otherwise noted.

This work may be used in accordance with the terms of the Creative Commons license
or other rights statement, as indicated in the copyright statement or in the metadata
associated with this work. Unless otherwise specified in the copyright statement
or the metadata, all rights are reserved by the copyright holder.

This work is protected against unauthorized copying under Title 17,
United States Code and other applicable copyright laws.

Microform Edition where available © ProQuest LLC. No reproduction or digitization
of the Microform Edition is authorized without permission of ProQuest LLC.

ProQuest LLC
789 East Eisenhower Parkway
P.O. Box 1346
Ann Arbor, MI 48106 - 1346 USA